

Seismic Behaviour of Exterior Beam-Column Joints Reinforced with FRP Bars and Stirrups

by

MOHAMED HASSAN ABDELHAMED MADY

A Thesis submitted to the Faculty of Graduate Studies of

The University of Manitoba

in partial fulfillment of the requirements of the degree of

DOCTOR OF PHILOSOPHY

Department of Civil Engineering

University of Manitoba

Winnipeg, Manitoba, Canada

Copyright © 2011 by Mohamed H. A. Mady

ABSTRACT

Reinforced concrete beam-column joints are commonly used in structures such as parking garages, multi-storey industrial buildings and road overpasses, which might be exposed to extreme weathering conditions and the application of de-icing salts. The use of the non-corrodible fiber-reinforced polymer (FRP) reinforcing bars in such structures is beneficial to overcome the steel-corrosion problems. However, FRP materials exhibit linear-elastic stress-strain characteristics up to failure, which raises concerns on their performance in beam-column joints where energy dissipation, through plastic behaviour, is required. The objective of this research project is to assess the seismic behaviour of concrete beam-column joints reinforced with FRP bars and stirrups.

An experimental program was conducted at the University of Manitoba to participate in achieving this objective. Eight full-scale exterior T-shaped beam-column joint prototypes were constructed and tested under simulated seismic load conditions. The longitudinal and transversal reinforcement types and ratios for the beam and the columns were the main investigated parameters in the experimental study. The experimental results showed that the GFRP reinforced joints can successfully sustain a 4.0% drift ratio without any significant residual deformation. This indicates the feasibility of using GFRP bars and stirrups as reinforcement in the beam-column joints subjected to seismic-type loading. It was also concluded that, increasing the beam reinforcement ratio, while satisfying the strong column-weak beam concept, can enhance the ability of the joint to dissipate seismic energy.

An analytical investigation was conducted through constructing a finite element model using ANSYS-software. The model was verified against the experimental results

in this research. Then, a parametric study was performed on number of different parameters known to affect such joints including column axial load, concrete compressive strength, flexural strength ratio and joint transverse reinforcement. It was also concluded that 70% of the column axial load capacity can be recommended as an upper limit to the applied axial loads on the column to avoid damage occurrence within the joint. It was also concluded that a minimum flexural strength ratio of 1.50 is recommended to ensure the strong-column weak-beam mechanism. In addition, a minimum joint transverse reinforcement ratio of 0.60% is recommended to insure that the failure will not occur in the joint zone.

ACKNOWLEDGMENTS

In the name of ALLAH

The author would like to express his deepest and sincere gratitude to his supervisor Professor Ehab El-Salakawy, Ph.D., P.Eng., Canada Research Chair in Advanced Composite Materials and Monitoring of Civil Infrastructures in the Department of Civil Engineering at the University of Manitoba, for his guidance and continuous encouragement throughout the course of this research program. The patience and assistance of Dr. Amr El-Ragaby is also tremendously appreciated. In addition, the author expresses his gratitude to his colleagues specially Mr. Mohamed Hasaballa for the help and support during all experimental work stages.

The financial support provided by the Natural Science and Engineering Research Council of Canada (NSERC) through Discovery and Canada Research Chairs programs is gratefully acknowledged.

Many thanks to Chad Klowak, P.Eng., and Grant Whiteside, the technical staff of the McQuade Heavy Structures Laboratory in the Department of Civil Engineering at the University of Manitoba, for their technical assistance during the construction and testing of the specimens.

Finally, I would like to thank my parents and my wife who gave me invaluable support, financially and spiritually, that helped me to be here and finish my thesis.

Mohamed Mady

TABLE OF CONTENTS

ABSTRACT.....	i
ACKNOWLEDGMENTS	iii
TABLE OF CONTENTS.....	iv
LIST OF TABLES	ix
LIST OF FIGURES	x
NOTATIONS.....	xvi
CHAPTER 1: INTRODUCTION	1
1.1 GENERAL.....	1
1.2 PROBLEM DEFINITION.....	4
1.3 SCOPE.....	8
1.4 OBJECTIVES AND ORIGINALITY	8
1.5 METHODOLOGY	9
1.6 THESIS LAYOUT	10
CHAPTER 2: LITERATURE REVIEW	12
2.1 GENERAL.....	12
2.2 BEAM-COLUMN JOINTS REINFORCED WITH STEEL	13
2.2.1 Code Provisions and Formulae.....	13
2.2.1.1 ACI-ASCE committee 352-76.....	13
2.2.1.2 ACI-ASCE committee 352-85.....	15
2.2.1.3 ACI 318-08	16
2.2.1.4 CSA A23.3-04.....	17
2.2.2 Prediction Models.....	17
2.2.2.1 Shear mechanism model	18
2.2.2.2 Softened strut-and-tie model.....	23
2.2.2.3 Finite element modelling	27
2.2.3 Factors Affecting the Behaviour of Steel-RC Beam-Column Joints.....	33
2.2.3.1 Flexural strength ratio	33

2.2.3.2 Joint shear stresses	34
2.2.3.3 Concrete strength	35
2.2.3.4 Type and rate of loading	35
2.2.3.5 Location of developed plastic hinges.....	37
2.2.3.6 Effect of anchorage length	37
2.2.3.7 Role of joint reinforcement.....	38
2.2.3.8 Effect of diagonal bars existence within the joint.....	39
2.3 FRP COMPOSITE MATERIALS.....	40
2.3.1 Constituents	41
2.3.2 Manufacturing	43
2.3.3 Physical Properties	44
2.3.4 Mechanical Properties	44
2.4 BEAM-COLUMN JOINTS REINFORCED WITH FRP	46
2.4.1 FRP-RC Columns under Combined Axial and Lateral Loads	47
2.4.2 Experimental Testing.....	49
2.4.2.1 Aramid FRP-reinforced joints.....	49
2.4.2.2 Carbon FRP-reinforced joints	50
2.4.2.3 Glass FRP-reinforced joints.....	50
CHAPTER 3: EXPERIMENTAL PROGRAM.....	53
3.1 GENERAL.....	53
3.2 DESIGN STRATEGY OF FRP STRUCTURAL ELEMENTS	53
3.2.1 General.....	53
3.2.2 Beam Design.....	54
3.2.2.1 Design for flexure	54
3.2.2.2 Design for Shear	55
3.2.3 Column Design.....	58
3.2.3.1 Design for Axial Load-Moment Interaction	58
3.2.3.2 Design for Flexure	58
3.2.3.3 Design for Shear	59
3.2.3.4 Design for Lateral Confinement	59

3.2.4 Joint Design	60
3.3 MATERIAL PROPERTIES	61
3.3.1 Concrete	61
3.3.2 Reinforcement	62
3.4 TEST SPECIMENS	65
3.5 INSTRUMENTATIONS	70
3.6 TEST SET-UP AND PROCEDURE.....	75
CHAPTER 4: EXPERIMENTAL RESULTS	81
4.1 GENERAL.....	81
4.2 TEST RESULTS AND OBSERVATIONS	81
4.2.1 Cracking Pattern and Mode of Failure	81
4.2.1.1 Specimen SS03-B06-J06	81
4.2.1.2 Specimen GG12-B11-J12	83
4.2.1.3 Specimen GG17-B11-J12	84
4.2.1.4 Specimen GG29-B11-J12	85
4.2.1.5 Specimen GS17-B11-J12.....	87
4.2.1.6 Specimen GG17-B07-J12 and Specimen GG17-B11-J06.....	88
4.2.1.7 Specimen CG12-B11-J12	90
4.2.2 Hysteretic Behaviour	94
4.2.2.1 Specimen SS03-B06-J06	94
4.2.2.2 Specimen GG12-B11-J12	95
4.2.2.3 Specimen GG17-B11-J12	96
4.2.2.4 Specimen GG29-B11-J12	97
4.2.2.5 Specimen GS17-B11-J12.....	98
4.2.2.6 Specimen GG17-B07-J12 and Specimen GG17-B11-J06.....	99
4.2.3 Strain Measurements	103
4.2.4 Cumulative Energy Dissipation.....	112
4.2.5 Rotation Measurements	114
4.2.6 GFRP Bars under Reversed-Cyclic Loading.....	119
CHAPTER 5: NUMERICAL MODELLING.....	128

5.1 GENERAL.....	128
5.2 ANSYS FINITE ELEMENT MODEL.....	128
5.2.1 Material Properties	128
5.2.1.1 Concrete material	128
5.2.1.2 Reinforcement materials	132
5.2.1.3 Loading and bearing plates	135
5.2.1.4 Concrete-reinforcement interface	136
5.2.2 Geometry and Boundary Conditions	139
5.2.3 ANSYS Solution Control	143
5.3 MODEL VERIFICATION	144
5.3.1 Specimen SS03-B06-J06	144
5.3.2 Specimen GG17-B11-J12.....	148
5.3.3 Specimen GG29-B11-J12.....	151
5.4 REMARKS.....	154
CHAPTER 6: PARAMETRIC STUDY.....	155
6.1 GENERAL.....	155
6.2 STUDIED PARAMETERS.....	155
6.2.1 Column Axial Load	155
6.2.2 Concrete Compressive Strength	159
6.2.3 Flexural Strength Ratio.....	163
6.2.4 Joint Transverse Reinforcement	168
CHAPTER 7: SUMMARY AND CONCLUSIONS.....	176
7.1 SUMMARY.....	176
7.2 CONCLUSIONS	177
7.2.1 Conclusions from the Experimental Tests.....	177
7.2.2 Conclusions from the Numerical Modelling	179
7.3 FUTURE WORK.....	182

REFERENCES	183
APPENDICES	193
APPENDIX-A	A-1
APPENDIX-B.....	B-1
APPENDIX-C.....	C-1

LIST OF TABLES

Table 2.1: Typical coefficients of thermal expansion (Reproduced from <i>ACI, 2006</i>).....	44
Table 2.2: Typical densities of reinforcing bars (Reproduced from <i>ACI, 2006</i>).....	44
Table 2.3: Typical mechanical properties of FRP bars (Reproduced from <i>ISIS Canada, 2007</i>).....	46
Table 3.1: Concrete material properties.....	62
Table 3.2: Mechanical properties of the used steel bars and stirrups (Given by manufacturer).....	63
Table 3.3: Mechanical properties of the used FRP bars and stirrups (Given by manufacturer).....	64
Table 3.4: Specimens characteristics.....	67
Table 3.5: Specimens reinforcement details.....	68
Table 4.1: Summary of test results.....	93

LIST OF FIGURES

Figure 1.1: Strong column-weak beam mechanism.....	2
Figure 1.2: Weak column-strong beam mechanism.....	3
Figure 1.3: Typical Stress-Strain Relationship for steel and GFRP bars.....	5
Figure 1.4: Types of beam-column joints.....	7
Figure 2.1: Developed internal forces on a typical interior Beam column joint under seismic actions (Reproduced from <i>Paulay et al., 1978</i>).....	19
Figure 2.2: Joint shear resistant mechanisms (Reproduced from <i>Paulay et al., 1978</i>).....	20
Figure 2.3: Probable bond stress distributions in a joint core (Reproduced from <i>Paulay et al., 1978</i>).....	22
Figure 2.4: Joint shear resistant mechanisms (Reproduced from <i>Hwang and Lee, 1999</i>).....	23
Figure 2.5: Pultrusion process (Reproduced from <i>ISIS Canada, 2007</i>).....	43
Figure 2.6: Stress-strain curve for different reinforcing materials.....	45
Figure 3.1: FRP-reinforced specimen design flowchart.....	54
Figure 3.2: Geometry of beam-column joint specimens.....	67
Figure 3.3: Construction details of beam-column joint test prototypes.....	70
Figure 3.4: Position of strain gauges.....	71
Figure 3.5: Positions of LVDTs.....	73
Figure 3.6: Estimation of joint shear distortion.....	74

Figure 3.7: Positions of load cells.....	74
Figure 3.8: Test setup.....	76
Figure 3.9: Dynamic actuator photos.....	76
Figure 3.10: Hydraulic jack.....	77
Figure 3.11: Steel reaction frame.....	77
Figure 3.12: Column roller support.....	78
Figure 3.13: Loading history consequence.....	80
Figure 4.1: Cracking sequence of specimen SS03-B06-J06.....	82
Figure 4.2: Cracking sequence of specimen GG12-B11-J12.....	84
Figure 4.3: Cracking sequence of specimen GG17-B11-J12.....	85
Figure 4.4: Cracking sequence of specimen GG29-B11-J12.....	86
Figure 4.5: Cracking sequence of specimen GS17-B11-J12.....	88
Figure 4.6: Cracking sequence of specimen GG17-B07-J12.....	89
Figure 4.7: Cracking sequence of specimen GG17-B11-J06.....	90
Figure 4.8: Mode of failure of specimen CG12-B11-J12.....	91
Figure 4.9: Bond stress-slip relationship for CFRP bars.....	92
Figure 4.10: Stress-strain relationship for CFRP bars.....	92
Figure 4.11: Hysteretic load-drift ratio relationship of specimen SS03-B06-J06.....	95
Figure 4.12: Hysteretic load-drift ratio relationship of specimen GG12-B11-J12.....	96
Figure 4.13: Hysteretic load-drift ratio relationship of specimen GG17-B11-J12.....	97
Figure 4.14: Hysteretic load-drift ratio relationship of specimen GG29-B11-J12.....	98
Figure 4.15: Hysteretic load-drift ratio relationship of specimen GS17-B11-J12.....	99

Figure 5.7: SOLID45 3-D solid element (Reproduced from <i>ANSYS manual-Release 11, 2007</i>).....	135
Figure 5.8: Models for reinforced concrete element (Reproduced from <i>Wolanski, 2004</i>).....	136
Figure 5.9: Bond-slip curve for ripped steel bars embedded in concrete (Reproduced from <i>CEB-FIP Model Code, 1990</i>).....	138
Figure 5.10: Bond-slip curve for GFRP bars embedded in concrete (Reproduced from <i>Alves et al., 2011</i>).....	139
Figure 5.11: Finite element model dimensions.....	140
Figure 5.12: Boundary conditions for supports.....	141
Figure 5.13: Boundary conditions for plane of symmetry.....	142
Figure 5.14: Full view for the finite element ANSYS model.....	142
Figure 5.15: Full view for the internal reinforcement cage.....	143
Figure 5.16: Hysteretic behaviour comparison for specimen SS03-B06-J06.....	145
Figure 5.17: Load-drift relationship envelops for specimen SS03-B06-J06.....	146
Figure 5.18: Strain comparison of beam longitudinal bars for specimen SS03-B06-J06.....	147
Figure 5.19: Strain comparison of column longitudinal bars for specimen SS03-B06-J06.....	147
Figure 5.20: Hysteretic behaviour comparison for specimen GG17-B11-J12.....	148
Figure 5.21: Load-drift relationship envelops for specimen GG17-B11-J12.....	149
Figure 5.22: Strain comparison of beam longitudinal bars for specimen GG17-B11-J12.....	150

Figure 5.23: Strain comparison of column longitudinal bars for specimen GG17-B11-J12.....	150
Figure 5.24: Hysteretic behaviour comparison for specimen GG29-B11-J12.....	151
Figure 5.25: Load-drift relationship envelops for specimen GG29-B11-J12.....	152
Figure 5.26: Strain comparison of beam longitudinal bars for specimen GG29-B11-J12.....	153
Figure 5.27: Strain comparison of column longitudinal bars for specimen GG29-B11-J12.....	153
Figure 6.1: Load-drift relationship envelops under various column axial loads for specimen GG17-B11-J12.....	156
Figure 6.2: The mode of failure and the corresponding drift capacity for each column axial load ratio.....	157
Figure 6.3: Strain comparison of beam longitudinal bars under various column axial loads for specimen GG17-B11-J12.....	158
Figure 6.4: Strain comparison of column longitudinal bars under various column axial loads for specimen GG17-B11-J12.....	159
Figure 6.5: Load-drift relationship envelops under various column axial loads for specimen GG29-B11-J12.....	160
Figure 6.6: The mode of failure and the corresponding drift capacity for each concrete compressive strength.....	161
Figure 6.7: Strain comparison of beam longitudinal bars under various column axial loads for specimen GG29-B11-J12.....	162

Figure 6.8: Strain comparison of column longitudinal bars under various column axial loads for specimen GG29-B11-J12.....	163
Figure 6.9: Load-drift relationship envelops under various flexural strength ratios for specimen GG17-B11-J12.....	165
Figure 6.10: The mode of failure and the corresponding drift capacity for each flexural strength ratio.....	166
Figure 6.11: Strain comparison of beam longitudinal bars under various flexural strength ratios for specimen GG17-B11-J12.....	167
Figure 6.12: Strain comparison of column longitudinal bars under various flexural strength ratios for specimen GG17-B11-J12.....	167
Figure 6.13: Load-drift relationship envelops under various joint reinforcement ratios for specimen GG17-B11-J12.....	169
Figure 6.14: The mode of failure and the corresponding drift capacity for each joint reinforcement ratio.....	170
Figure 6.15: Strain comparison of beam longitudinal bars under various joint reinforcement ratios for specimen GG17-B11-J12.....	171
Figure 6.16: Strain comparison of column longitudinal bars under various joint reinforcement ratios for specimen GG17-B11-J12.....	171
Figure 6.17: Shear stresses distribution across the joint at failure.....	175

NOTATIONS

A_c	Core area of column measured to the centerline of the hoops, mm^2
A_{cv}	Joint cross-sectional effective area in shear, mm^2
$AFRP$	Aramid Fibre Reinforced Polymer
A_{FH}	Minimum transverse reinforcement for confinement purposes, mm^2
A_{frp}	The longitudinal FRP reinforcement area, mm^2
A_g	Total gross area of the column section, mm^2
A_j	Joint cross-sectional area; equal to column cross-sectional area, mm^2
A_{s1}	Beam top reinforcement area, mm^2
A_{s2}	Beam bottom reinforcement area, mm^2
A_{st}	Area of the steel stirrups, mm^2
A_v	The shear hoops area, mm^2
$A_{v,min}$	The minimum allowable shear hoops area, mm^2
a_b	Depth of the compression zones in the beam, mm
a_c	Depth of the compression zones in the column, mm
a_s	Diagonal strut thickness, mm
b	The width of the cross-section, mm
b_c	Cross-sectional dimension of column core measured center-to-center of outer legs of the transverse reinforcement, mm
b_j	The effective width of the joint, mm
b_s	The effective width of the diagonal strut, mm
c	Depth of neutral axis, mm

C_c	The compression force developed in concrete compression zone, N
C_s	The compression force developed in steel bars in compression side, N
$CFRP$	Carbon-Fibre Reinforced Polymer
d	The depth of the cross-section, mm
d_v	The effective shear depth; taken equal to $0.9d$, mm
d_b	Diameter of the hoop, mm
D	Diagonal shear mechanism force, N
D_c	Diagonal concrete strut magnitude, N
D_s	Capacity of the diagonal compression fields, N
E_c	The modulus of elasticity of concrete, MPa
E_{frp}	The tensile modulus of elasticity of FRP longitudinal bars, MPa
E_{frpc}	The compressive modulus of elasticity of FRP longitudinal bars, MPa
$E_{f,v}$	Tensile modulus of elasticity of FRP hoop reinforcement, MPa
f'_c	The concrete compressive strength after 28 days, MPa
f_{fb}	Bend strength of the hoop, MPa
$f_{uv,frp}$	Hoop design strength; taken equal to the smaller of $0.004E_{f,v}$ or hoop bend strength, MPa
f_{FH}	Equal to $0.004E_{f,v}$, MPa
f_{frpu}	The longitudinal FRP ultimate granted tensile strength, MPa
$f_{fu,v}$	Ultimate strength of the straight part in FRP hoop reinforcement, MPa
f_y	Yield strength of the steel bars, MPa
F_h	Horizontal shear mechanism force, N

F_v	Vertical shear mechanism force, N
FRP	Fibre-Reinforced Polymer
$GFRP$	Glass-Fibre Reinforced Polymer
h_c	Column core dimension of the direction under consideration, mm
M	The maximum anticipated bending moment, $N.m$
M_{col}	The actual moment acting on the column, $N.m$
M_{nb}	The beam nominal moment resistance, $N.m$
M_{nc}	The column nominal moment resistance, $N.m$
M_{pb}	The beam probable moment resistance, $N.m$
N_u	The minimum compressive axial column load, N
P_f	Actual applied axial load to the column, N
P_{ro}	The maximum column axial load resistance, N
P_y	Lateral load at the beam tip corresponding to the yielding of beam top or bottom longitudinal steel reinforcement, N
r_b	Radius of the hoop bend, mm
R_d	The ratio of the shear force resisted by the diagonal shear mechanism
R_h	The ratio of the shear force resisted by the horizontal shear mechanism
R_v	The ratio of the shear force resisted by the vertical shear mechanism
s	Spacing of transverse stirrups, mm
s_1	Spacing of tie legs in the cross-sectional plane of the column, mm
s_l	The corresponding slippage for any arbitrary bond stress τ , mm
S_{ze}	Crack spacing parameter

T'	Tension forces in steel reinforcement, N
T_b	The tensile force transferred to the joint from beam FRP bars, N
v_c	Concrete contribution to shear stresses, $N.m$
v_u	Nominal shear stresses acting on the joint, $N.m$
V	The developed shear force corresponding to maximum anticipated bending moment, N
V_c	The shear resisted by concrete, N
V_{ch}	The horizontal component of the diagonal compression strut force, N
V_{col}	Shear forces exerted on one side of the column, N
V'_{col}	Shear forces exerted on the opposite side of the column, N
V_F	The shear resisted by FRP hoops, N
V_j	Total shear force acting on the joint, N
V_{jh}	Maximum horizontal shear force in the joint core, N
V_{jr}	The maximum shear resistance of the exterior joint, N
V_{nc}	Shear force transferred by columns to the joint, N
V_{sh}	Horizontal shear resistance of the truss mechanism, N
α	Stress multiplier for the strain hardening effect of steel bars; a typical value is 1.25
α_1 and β_1	Concrete rectangular stress block coefficients
β	Diagonal concrete strut inclination, <i>degree</i>
β'	Factor reflecting loading to be imposed to the joint
β_v	Factor which depends on the ability of concrete to transmit tensile stresses

γ	Factor reflecting confinement of joint by lateral members
ν	Poisson's ratio
ε_c	Concrete compressive strain
ε_{cu}	The ultimate concrete compressive strain (crushing strain)
ε_{frpc}	The developed compressive strain in the longitudinal FRP bars
ε_{frp}	The developed tensile strain in the longitudinal FRP bars
ε_{frpu}	The ultimate tensile strain of the longitudinal FRP (rupture strain)
ε_o	Concrete compressive strain at the ultimate compressive strength f'_c
ε_r	The average transversal strain of cracked concrete
ε_x	Longitudinal strain at the mid-depth of the cross section
σ_v	The developed stresses in the shear hoops, <i>MPa</i>
$\sigma_{d,max}$	The maximum compressive stresses acting on the nodal zone, <i>MPa</i>
θ	Inclination of the shear cracks, <i>degree</i>
φ	Element reduction factor adopted by ACI standards
ϕ_c	Capacity reduction factor for concrete adopted by CSA standards
ϕ_F	Capacity reduction factor for FRP reinforcement adopted by CSA standards
τ	The bond stress between concrete and embedded steel bars, <i>MPa</i>
τ_{max}	Maximum bond strength for the steel bars embedded in concrete, <i>MPa</i>
λ	Concrete density factor; equal one for normal weight concrete
ζ	Concrete softening coefficient
ρ_{frp}	FRP bars reinforcement ratio

ρ_{frpb}	FRP bars balanced reinforcement ratio
δ	Design lateral drift ratio, shall not be less than 3%
Δ_y	Displacement at the beam tip corresponding to the yielding of beam top or bottom longitudinal steel reinforcement, <i>mm</i>
ΔT_c	Bond forces transmitted from the beam reinforcement to the joint core within the compression zone, <i>N</i>
ΔT_s	Bond forces transmitted from the beam reinforcement to the joint core outside the compression zone, <i>N</i>
ΣM_{nc}	The sum of nominal flexural strength of columns framing into the joint, evaluated at the faces of the joint, <i>N.m</i>
ΣM_{nb}	The sum of probable flexural strength of beams framing into the joint, evaluated at the faces of the joint, <i>N.m</i>

CHAPTER 1

INTRODUCTION

1.1 GENERAL

Many types of lateral loads can be involved in the analysis and design of a particular structure. Wind loads and earthquake ground motions represent the main two types of lateral loads considered during the design process. Therefore, reinforced concrete structures, especially those located in seismic active regions, should not be designed only according to the applied gravity loads. However, these structures have to be properly detailed and designed to accommodate the effect of lateral loads. Designers have to select one or more systems to resist such loads on the structure. Moment-resisting frames are one of the commonly used systems in most of the reinforced concrete structures. This research is dealing with the effect of the earthquake ground motions (seismic loads) on moment-resisting frames.

Moment-resisting frames are skeletal structures consisting of a combination of beams and columns, well detailed together in a standard way to be able to resist lateral (seismic) and gravity loads. The philosophy behind the seismic design for this type of frames is to provide them with sufficient ductility, by which these frames can dissipate the acting seismic energy. The structural ductility mainly comes from the ductility of the members; beams, columns and joints, which forming these frames.

Furthermore, in steel-reinforced concrete structures, the ductility of beams and columns is exhibited in the form of inelastic deformations (mainly rotations). During these inelastic deformations, the actual material properties are beyond the elastic range. The outcomes of these inelastic deformations what so-called plastic hinges. The plastic

hinges are definite regions located near the end of the beams or the columns where the structural damage is expected. In the seismic design, the plastic hinges are allowed to be formed in beams rather than in columns; strong column-weak beam behaviour, as shown in Figure 1.1. Therefore, it is possible for the structure to attain the desired inelastic response and in turn the sufficient ductility.

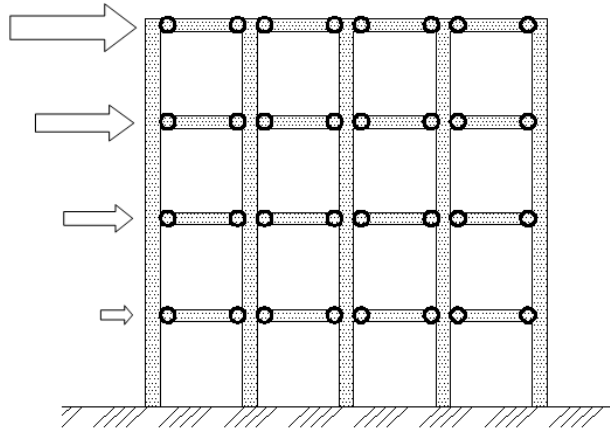


Figure 1.1: Strong column-weak beam mechanism

If plastic hinges are formed in columns, the mechanism is called column yielding or storey mechanism, as shown in Figure 1.2. One of the basic requirements of seismic design is that the columns above and below the beam should have sufficient flexural strength to ensure that possible hinging occurs in beams rather than in columns.

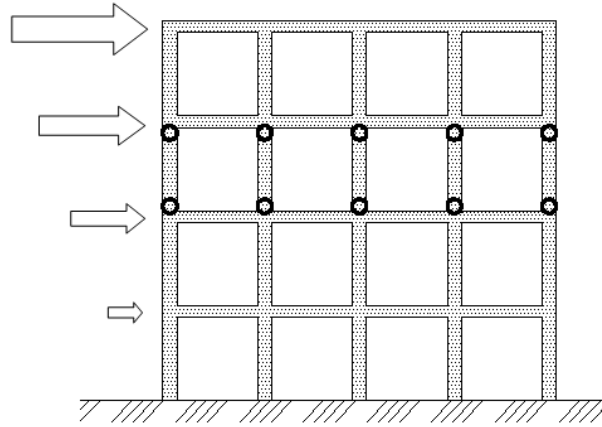


Figure 1.2: Weak column-strong beam mechanism

However, many earthquakes have demonstrated that even when the beams and columns in a reinforced concrete frame remain intact, the integrity of the whole structure is undermined if the “joint” fails (Saatcioglu 2001). The beam-column joints are simply defined by the zones of intersection of beams and columns. The main function of these joints is to enable the adjoining members to develop and sustain their ultimate capacity, which can be assured by having adequate strength and stiffness for the joint to resist the internal forces induced by the framing members. In addition, the joints degradation should not affect the capacity of the column in carrying its design loads, as well as limiting the joint deformation not to increase the storey drift (ACI-ASCE Committee 352 2002).

Obviously, beam-column joints or “connections” are playing an important role in governing the seismic behaviour of the moment-resisting frame structures. Therefore, the proper design and detailing of such joints are mandatory to ensure a satisfactory seismic performance for these structures.

1.2 PROBLEM DEFINITION

The corrosion problem of steel reinforcement is a major factor in limiting the life expectancy of reinforced concrete (RC) structures especially those exposed to harsh environments. Many of these structures contain moment-resisting frames such as parking garages, multi-storey industrial buildings and road overpasses. Corrosion of steel reinforcement causes concrete deterioration, which ultimately leads to loss of capacity, integrity and serviceability of RC structures.

Many alternatives are used to overcome the steel corrosion problem, such as coating the regular steel with some non-corrosive materials, using galvanized or stainless steel, increasing concrete cover, etc. However, all these attempts were not successful in preventing the corrosion phenomena completely. Furthermore, the repair cost in some cases can be twice as high as the original one (Yunovich and Thompson 2003).

The fibre reinforced polymer (FRP) reinforcement is currently being extensively used as an innovative material in new RC structures. The main driving force behind this effort is the superior performance of FRP in corrosive environments due to its non-corrodible nature. FRP reinforcements, in general, offer many other advantages over the conventional steel such as high strength-to-weight ratio, favourable fatigue performance and high electro-magnetic transparency. Three types of FRP reinforcements are commercially available, glass (GFRP), carbon (CFRP) and aramid (AFRP). However, due to its lower cost compared to other FRP types, GFRP reinforcements are more attractive to the construction industry. Therefore, the use of FRP reinforcement, especially GFRP, in moment-resisting frames within structures exposed to harsh environments is beneficial.

Furthermore, the mechanical and physical properties of FRP material are different from those of the steel reinforcement. As shown in Figure 1.3, the FRP material exhibits linear-elastic stress-strain characteristics up to failure with relatively low modulus of elasticity (40 - 50 GPa for glass FRP and 110 - 140 MPa for carbon FRP compared to 200 GPa for steel). Since inelastic behaviour is required for the moment-resisting frames as explained above, the use of the linear-elastic FRP (especially GFRP) in such elements needs to be investigated. In other words, an important question needs to be answered; can the large-elastic strains, exhibited by GFRP bars, replace the yielding behaviour of the steel reinforcement?

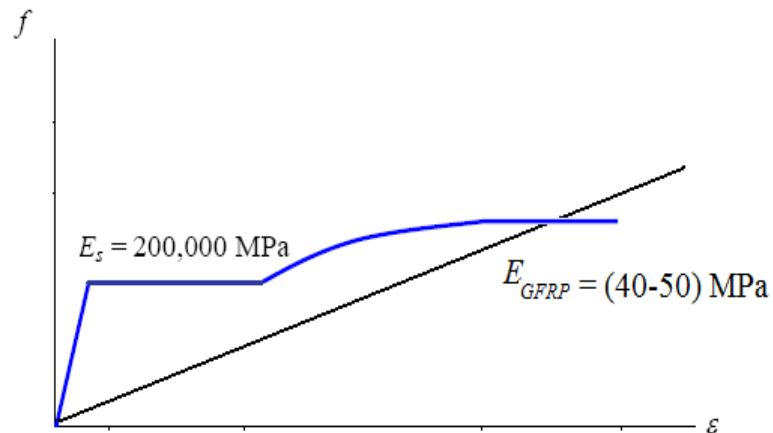


Figure 1.3: Typical stress-strain relationship for steel and GFRP bars

In addition, at the level of overall behaviour of FRP-reinforced frame structure, it is expected that the low modulus of elasticity for the GFRP reinforcement will lead to reducing the overall stiffness of the structure, which will result in attracting lower forces from the acting drifts. However, this lower stiffness will require higher displacement demand, which may reduce the expected base shear forces.

Moreover, the bond strength of sand-coated FRP reinforcement (the most commonly used FRP-reinforcement type) comes mainly from friction between the coating layer that covers the FRP reinforcement and concrete which is uniformly distributed along the bar surface. This results in having uniform distribution of bond stresses. However, for the deformed steel bars, the bond is mainly due to mechanical interlocking of concrete with the bar deformations (ribs), which results in having a bond stress concentration at the ribs' locations. As bond strength is related to developed crack pattern. This difference between the two bond behaviours will change the cracking pattern from few and wide cracks in the case of steel-reinforced elements to more uniformly distributed narrow cracks in the case of FRP-reinforced elements with the same reinforcement axial stiffness.

Although FRP bars can be bent in form of stirrups or bent bars while manufacturing, a strength reduction of 40 to 50% relative to the tensile strength of a straight bar is expected due to fibre bending and stress concentration (ACI 2006). In addition, the manufacturing process to fabricate a bent FRP bar is different (not pultrusion) and results in a strength reduction of the straight portion of the bent bar itself.

For a typical moment-resisting plane frame, as shown in Figure 1.4, three types of beam-column joints can be identified; interior, exterior and corner. The exterior beam-column joints are considered the most critical parts in the whole frame for the following reasons:

- Any damage occurs in the interior or exterior joints will affect the integrity of the whole frame, compared to the local influence of the corner joints;

- The interior joints have more confinement than the exterior ones due to larger numbers of beams and slabs connected to the joint;
- Less anchorage length is available for the straight FRP beam bars in the exterior joints, compared to the interior joints where the bars will continue through the joint.

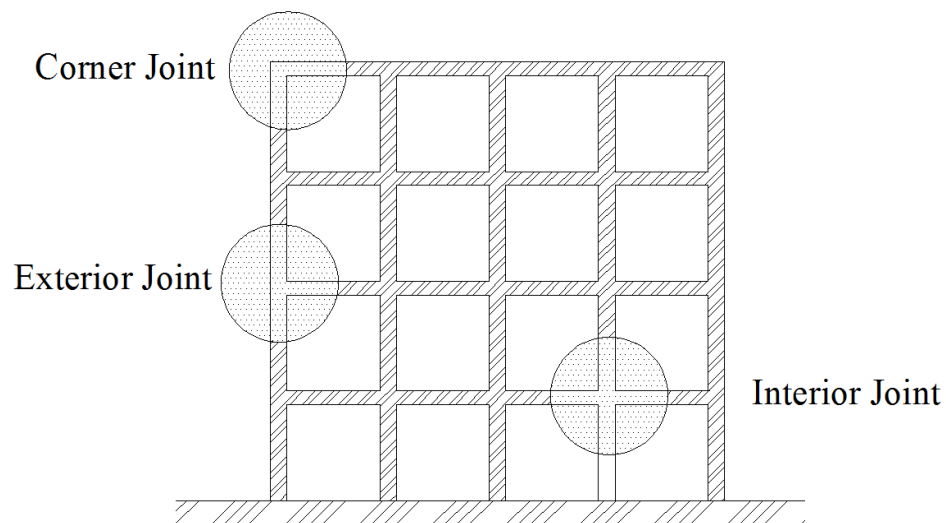


Figure 1.4: Types of beam-column joints

Therefore, investigating the possibility of using FRP reinforcement in exterior beam-column joints is more challenging while the results can be easily extended to the other types of joints.

Furthermore, several codes and guidelines for design and construction of concrete structures reinforced with FRP material have been recently published (CSA 2002; CSA 2009; ACI 2006). However, due to lack of data and test results, none of these codes and guidelines provides any recommendations on the seismic design of the moment-resisting

frames when FRP bars are used as primary reinforcement in both longitudinal and transversal directions.

1.3 SCOPE

Investigating the behaviour of beam-column joints subjected to seismic-type loading is a challenging task. As an integral part of a moment-resisting frame, beam-column joints can have variable geometries, reinforcement types and detailing, and can be subjected to different types of loading. This research is focussing on studying the behaviour of RC exterior beam-column sub-assemblies (joints) rather than the overall performance of a frame structure. The considered subassemblies are without transverse beams or slabs, which is more critical due to absence of confinement provided through these structural elements. Only sand-coated straight FRP bars and C-shaped stirrups, produced by a Canadian manufacturer, are used throughout this research. In addition, the seismic load was selected to be simulated by quasi-static cyclic loading.

1.4 OBJECTIVES AND ORIGINALITY

The use of FRP as reinforcement for concrete structures is rapidly increasing. Nevertheless, the seismic behaviour of beam-column joints reinforced with FRP bars and stirrups has not yet been explored. Several codes and design guidelines addressing FRP bars as primary reinforcement for concrete structures have been recently published (CSA 2002; CSA 2009; ACI 2006; ISIS Canada 2007). However, no seismic provisions are available due to lack of data and research in this area. Therefore, the main objective of this study is to contribute in fulfilling this gap by investigating the feasibility of using FRP bars and stirrups as reinforcement in exterior beam-column joints subjected to

simulated seismic loading. The specific objectives of this study can be summarized as follows:

- 1- Develop a design strategy for the beam-column joints reinforced with FRP material and subjected to seismic loading. This design strategy is a combination of selected formulae from the available design codes, manuals and previous research data.
- 2- Study the effect of different parameters that are known to affect the behaviour of these joints such as type of longitudinal and transverse reinforcement, beam longitudinal reinforcement ratio, beam transverse reinforcement ratio, joint reinforcement ratio and detailing, column axial load, concrete compressive strength and flexural strength ratio.
- 3- Investigate different detailing of the joint reinforcement.

1.5 METHODOLOGY

To achieve the above main and specific objectives, both experimental and analytical studies were conducted. Therefore, this research consists of two phases; experimental and analytical.

The experimental phase includes the construction and testing of eight full-scale exterior beam-column joint prototypes (T-shaped). Each prototype represents an exterior joint isolated from an end bay of a multi-storey structure, as shown in Figure 1-4, between the assumed points of contra-flexure located at the mid-height and mid-span of the column and the beam, respectively. Reversal lateral quasi-static cyclic loads are applied directly at the beam tip simulating seismic loading. Numbers of variables are investigated including type of longitudinal reinforcement bars (steel, GFRP and CFRP),

type of transverse reinforcement (steel and GFRP), beam longitudinal reinforcement ratio, beam transverse reinforcement ratio and joint reinforcement ratio and detailing.

The analytical phase consists of constructing a finite element model for the beam-column joints using ANSYS program (ANSYS, Release 11 2007). The model was validated against the experimental results. Then, the verified model was used to conduct a parametric study on number of different parameters known to affect such joints including column axial load, concrete compressive strength, flexural strength ratio and joint transverse reinforcement.

1.5 THESIS LAYOUT

This thesis consists of seven chapters. The contents of each chapter are as follows:

- Chapter one presents a brief introduction for the seismic behaviour of reinforced concrete frames, as well as the problem definition, work objectives and the followed methodology.
- Chapter two introduces a literature review on the code provisions and analytical models for the steel-reinforced beam-column joints, the factors affecting the behaviour of these joints, a brief introduction to the FRP materials, and finally the available research on beam-column joints reinforced with FRP reinforcement.
- Chapter three gives the details of the experimental research program including material properties, test specimens, instrumentations, test set-up and loading procedure. As well, the strategy followed in the design of these new joints is explained.

- Chapter four provides the analysis and discussion of test results in terms of cracking pattern and mode of failure, hysteretic behaviour, strain measurements, cumulative energy dissipation, rotation measurements and the reinforcement behaviour under reversed cyclic loading.
- Chapter five gives the details of the used finite element model including element types, material constitutive models, geometry and boundary conditions, and the solution control. The verification of the developed model against the experimental results is also presented.
- Chapter six presents the results of the finite element parametric study in terms of the hysteretic behaviour and the main reinforcement strain measurements.
- Chapter seven gives the conclusions obtained from this research and introduces the future research needs.

CHAPTER 2

LITERATURE REVIEW

2.1 GENERAL

During the past four decades, significant amount of research has been conducted to investigate the behaviour of steel-reinforced beam-column joints. These joints are studied due to its critical influence on the overall behaviour of RC moment-resisting frames subjected to seismic loads.

Hanson and Connor (1967) had conducted the first experiment on exterior beam-column joints reinforced with steel. Since then, many researchers have been involved in studying the behaviour of the beam-column connections through analytical models and experimental tests. These researchers were able to provide knowledge on how beam-column joints work and what are the main parameters that affect their performance.

However, there is a lack of data and test results still exists on such connections when they are totally reinforced with FRP reinforcement. Nevertheless, none of the available FRP codes or guidelines provides any recommendations on the seismic design of the moment-resisting frames reinforced with FRP.

In the following sections, summary of the basic analytical models, available code provisions and the main factors affecting the behaviour of steel-reinforced beam-column joints are discussed. Then, a brief introduction for the FRP material constituents, manufacturing and properties are presented. Also, the very few previous studies related to the beam-column joints reinforced with FRP material are reviewed.

2.2 BEAM-COLUMN JOINTS REINFORCED WITH STEEL

2.2.1 Code Provisions and Formulae

Nowadays, the behaviour of beam-column joints reinforced with steel bars and stirrups is well-established and defined. In addition, all the provisions and formulae related to the design and detailing of such joints can be found in the ACI-ASCE Committee 352-02 Report (2002), ACI 318-08 Code (2008) and CSA A23.3-04 Code (2004). These standards provide recommendations to satisfy strength and ductility requirements related to the function of the connection within a structural frame.

The first version of the ACI-ASCE 352-76 guideline was developed in 1976. However, since 1985, a number of updates have been published taking into account the observations, results and conclusions obtained from the laboratory tests and field studies performed since then.

The main difference between the first version of the ACI-ASCE 352 guideline and the following versions is the assumption of the shear resisting mechanisms and the role of the joint transverse reinforcement (stirrups) within the joint. More details about this difference and the related formulae of each code provision are described in the following sections. In addition, the formulae adopted by both ACI 318-08 (2008) and CSA A23.3-04 (2004), to determine the joint shear capacity, are also discussed.

2.2.1.1 ACI-ASCE committee 352-76 report

The ACI-ASCE committee 352-76 report was the first guideline developed for the design and detailing of beam-column joints. Since limited amount of research carried out before that date, there were not enough data to establish reliable formulae for the shear resistance of the joint. In that report, the assumption that the concrete and transverse reinforcement

in the joint act collectively to resist the shear forces in the joint was considered. In other words, the transverse reinforcement within the joint is not only for confining the column but also for resisting part of the shear force acting upon the joint area.

Accordingly, the ACI-ASCE 352-76 has recommended the use of equations derived for the flexural members subjected to shear forces. Concrete contribution to shear stresses (v_c) can be determined according to equation (2-1) that was available in the ACI 318-71 Code (1971) at that time:

$$v_c = 3.5 \beta \gamma \sqrt{f'_c (1 + 0.002 N_u / A_g)} \quad (2 - 1)$$

Where β is a factor reflecting loading to be imposed, γ is a factor reflecting confinement of joint by lateral members, and f'_c is the concrete compressive strength after 28 days. N_u is the minimum compressive axial column load and A_g is the gross cross-sectional area of the section perpendicular to the direction of the axial load.

For type 1 joints (subjected to monotonic loading), $\beta = 1.4$ and $N_u =$ actual compressive axial column load. However, for type 2 joints (subjected to seismic loading), $\beta = 1.0$ and $N_u =$ zero. The factor γ is taken equal to 1.4 if the joint is confined perpendicular to the loading direction, otherwise it should be taken equal to 1.0.

Then, the stirrups reinforcement area (A_{st}) required to carry the remaining amount of shear stresses acting on the joint can be determined according to equation (2-2):

$$A_{st} = \frac{(v_u - v_c) A_{cv} s}{f_y d_v} \quad (2 - 2)$$

Where v_u is the nominal shear stresses acting on the joint, A_{cv} is the cross-section of effective area in shear and s is the shear hoops spacing. f_y is the yield strength of the steel hoops and d_v is the effective joint depth in the direction of shear force.

2.2.1.2 ACI-ASCE committee 352-85 report

Between 1976 and 1985, the ACI-ASCE 352 Committee recommendations had been undergoing major revisions. The new philosophy adopted was that the contribution of both concrete and steel cannot be treated separately. It was believed that during anticipated earthquake, the joint can resist the acting shear forces if the concrete within the joint is adequately confined. To provide this confinement, recommended details for column longitudinal and transverse reinforcement in the joint region should be followed. In other words, the joint reinforcement plays an important role in confining the column in the joint area, so the column can be able to resist the total shear force acting on the joint, rather than contributing directly in resisting the acting loads.

Accordingly, the ACI-ASCE 352-85 (1985) has recommended satisfying equation (2-3), where the capacity of the concrete component of the column (V_c) should be checked to determine whether it is able to resist the acting shear forces on the joint (V_j) or not. If Eq. (2-3) is not satisfied, the dimensions of the column should be increased.

$$V_c = 0.083 \gamma \sqrt{f'_c} A_j \geq \frac{V_j}{\phi} \quad (2 - 3)$$

Where, A_j is the joint cross-sectional area and ϕ is the strength reduction factor; taken equal to 0.85. γ is the shear strength factor reflecting confinement of the joint by lateral members. The factor γ depends on both the type of the joint (interior, exterior, or

corner) and the type of loading (monotonic, type 1 or seismic, type 2). For type 1 joints, the factor γ should be taken equal to 24, 20 and 15 for interior, exterior and corner joints, respectively. While for types 2 joints, the corresponding values are 20, 15 and 12, respectively.

The stirrups reinforcement area required to confine the column is determined according to the larger value obtained by equations (2-4) and (2-5):

$$A_{st} = 0.30 s b_c \frac{f'_c}{f_y} \left[\frac{A_g}{A_c} - 1 \right] \quad (2 - 4)$$

$$A_{st} = 0.09 s b_c \frac{f'_c}{f_y} \quad (2 - 5)$$

Where b_c is the width of the column transverse to the direction of shear, A_g is the total gross area of the column and A_c is the core area of the column defined by hoop reinforcement.

After 1985, significant amount of research was carried out to verify the new concept, as well as to investigate the effect of other factors deemed to be affecting the behaviour of these joints. A brief summary for some of these researches are provided later in this chapter. It is worth mentioning that the latest version of ACI-ASCE 352 guidelines was developed in 2002. No changes in the concept of the joint shear resistance calculations were made in the new version. However, only the values of factor γ have been slightly modified.

2.2.1.3 ACI 318-08 code provisions

The ACI 318-08 (2008) adopted the same concept introduced by the ACI-ASCE 352-02 (2002). However, the formulae given in ACI 318-08 are slightly different in defining the

confinement coefficient. According to ACI 318-08 (Clause 21.7.4.1) the joint shear forces should not exceed the values shown in Equation (2-6) for normal weight concrete:

$$V_n = \begin{cases} 1.7\sqrt{f'_c}A_j & \text{for joints confined on all four faces} \\ 1.2\sqrt{f'_c}A_j & \text{for joints confined on three faces or} \\ & \text{two opposite faces} \\ 1.0\sqrt{f'_c}A_j & \text{for others} \end{cases} \quad (2-6)$$

Where V_n is the nominal shear strength of the joint.

2.2.1.4 CSA A23.3-04 code provisions

The CSA A23.3-04 (2004) introduced equations similar to those given by ACI 318-08 (2008). However, the Canadian Standard (CSA A23.3-04) allows higher confinement coefficient factors than those given by ACI 318-08 as shown in Equation (2-7); adopted from CSA A23.3-04 (Clause 21.5.4.1):

$$V_n = \begin{cases} 2.2 \lambda \phi_c \sqrt{f'_c} A_j & \text{for joints confined on all four faces} \\ 1.6 \lambda \phi_c \sqrt{f'_c} A_j & \text{for joints confined on three faces or} \\ & \text{two opposite faces} \\ 1.3 \lambda \phi_c \sqrt{f'_c} A_j & \text{for others} \end{cases} \quad (2-7)$$

Where λ is the factor for concrete density; equals one for normal weight concrete.

In fact, if the concrete resistance factor (ϕ_c) is eliminated, the CSA factors (Eq. 2-7) yield identical results to their ACI counterparts (Eq. 2-6).

2.2.2 Prediction Models

According to the method of analysis, structural models can be divided into two types; analytical and mathematical models. The analytical modelling always depends on applying the equilibrium and compatibility equations on a free-body diagram in order to

develop an equation or so-called “closed form solution”. However, the mathematical modelling depends on using finite element-based software to calculate the developed strains and stresses in the modelled elements.

Few analytical researches were carried out to model beam-column joints subjected to seismic loading. However, two famous analytical models investigating the shear resistance of these joints are described in the following sections; shear mechanism model (Paulay et al. 1978) and softened strut-and-tie model (Hwang and Lee 1999).

Contrary, reasonable amount of research has been carried out on reinforced concrete beam-column connections using finite element (FE) method. Few researchers had developed computer subroutines using FE to perform a non-linear analysis of RC structures (Tajima et al. 2004; Sagbas 2007; Supaviriyakit et al. 2008; Eligehausen et al. 2009). In the mean time, more researchers had used commercially-available software packages such as ANSYS, ABAQUS, DIANA, ATENA, or SBETA to carry out the FE analysis (Parvin and Granata 2000; Mostofinejad and Talaeitaba 2006; Bindhu and Jaya 2008 and 2010; Sritharan et al. 2000; Danesh et al. 2008; Li and Tran 2009; Kulkarni and Li 2009; Abdelwahed et al. 2005; Baglin and Scott 2000). In the following sections some of these researches are summarized.

2.2.2.1 Shear mechanism model

Paulay et al. (1978) were the first researchers to analytically investigate the behaviour of steel-reinforced beam-column joints. They believed that the concrete shear resisting mechanisms in a joint core are significantly different from those encountered in flexural members (ACI-ASCE 352-76 1976). Considering the seismic actions in equilibrium

acting on an interior joint, as shown in Figure 2.1-a, the locations and magnitudes of the resulting internal forces developed in the beams and columns can be determined accurately, as shown in Figure 2.1-b. The maximum horizontal shear force in the joint core (V_{jh}) can be expressed from Figure 2.1-b as follows:

$$V_{jh} = (A_{s1} + A_{s2}) \alpha f_y - V_{col} \quad (2 - 8)$$

Where A_{s1} and A_{s2} are the beam top and bottom reinforcement area, respectively. α is a stress multiplier; taken equal to 1.25 and V_{col} is the shear forces exerted on the column.

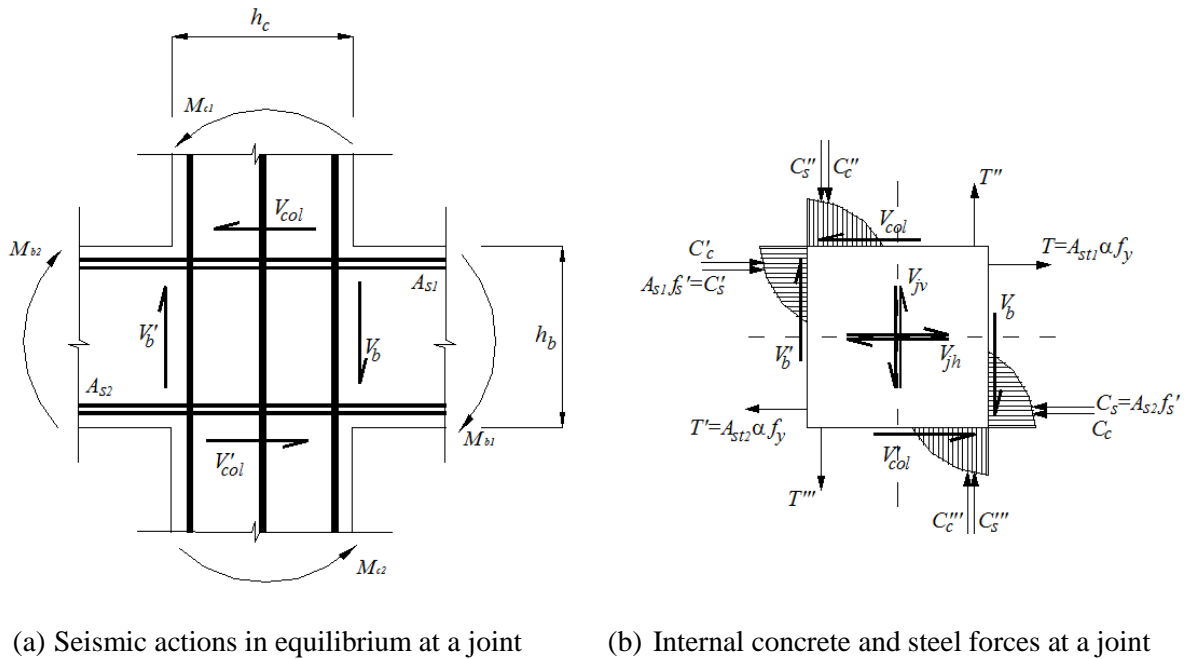


Figure 2.1: Developed internal forces on a typical interior Beam column joint under seismic actions (Reproduced from *Paulay et al., 1978*)

The authors showed that the joint shear resistance is coming from two major mechanisms; concrete strut and truss mechanism, as shown in Figure 2.2. These two mechanisms are discussed in details in the following sections.

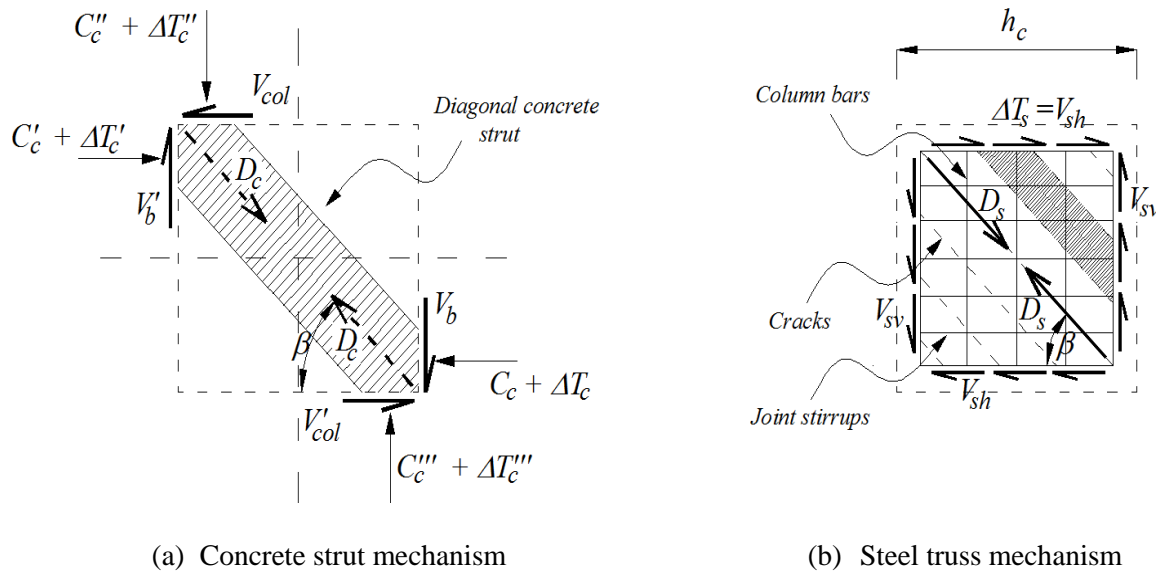


Figure 2.2: Joint shear resistant mechanisms (Reproduced from *Paulay et al., 1978*)

Concrete strut mechanism

Defining the bond forces transmitted from the beam reinforcement within the compression zone as ΔT_c , the internal concrete compression forces together with the column and beam shears and the force ΔT_c are forming a system in equilibrium. The principal component of this mechanism is a diagonal concrete strut with magnitude D_c at an angle β .

The horizontal component of the diagonal compression force (V_{ch}) can be defined, in terms of the forces at the lower right hand corner of the joint shown in Figure 2.1-b and Figure 2.2-a, as:

$$V_{ch} = D_c \cos \beta = C_c + \Delta T_c - V'_{col} \quad (2 - 9)$$

Where C_c is the compression force developed in concrete compression zone and V'_{col} is the corresponding shear forces exerted on the column at the bottom side of the joint as shown in Figure 2.2-a.

Truss mechanism

The bond forces induced within the joint core due to all the remaining longitudinal steel forces will introduce shear stresses. These shear stresses in turn will result in diagonal tension stresses on the joint core, which in most cases, are larger than the cracking tensile capacity of the joint core. Figure 2.2-b shows a truss mechanism that can be developed from the combination of the horizontal joint reinforcement, the vertical column bars and the diagonal concrete compression field between the developed cracks. Defining the capacity of the diagonal compression fields by D_s , the horizontal shear resistance of the developed truss mechanism (V_{sh}) can be calculated as:

$$V_{sh} = D_s \cos \beta = V_{jh} - V_{ch} = \Delta T_s \quad (2 - 10)$$

Where: ΔT_s is the bond forces transmitted from the beam reinforcement to the joint core outside the compression zone. This means that a combination of ΔT_c and ΔT_s will equal to the total forces developed in the beam reinforcement as shown in equation (2-11):

$$\Delta T_c + \Delta T_s = C_s + T' \quad (2 - 11)$$

Where C_s is the compression force developed in the beam steel reinforcement on one side of the joint and T' is the corresponding tension force in the beam steel reinforcement on the other side of the joint.

Bond distribution

It is recognized that the bond stress distribution on the beam reinforcement inside the joint area plays very important role in the joint performance. Hence, rational assumption for the bond transfer distribution within the joint is needed. The authors assumed three configurations for the probable bond stress distributions within the joint core depending on the state of stresses of the beam reinforcement stresses, as shown in Figure 2.3. It is worth mentioning that distance c in Figure 2.3 is the depth of the neutral axis in the column section just before yielding.

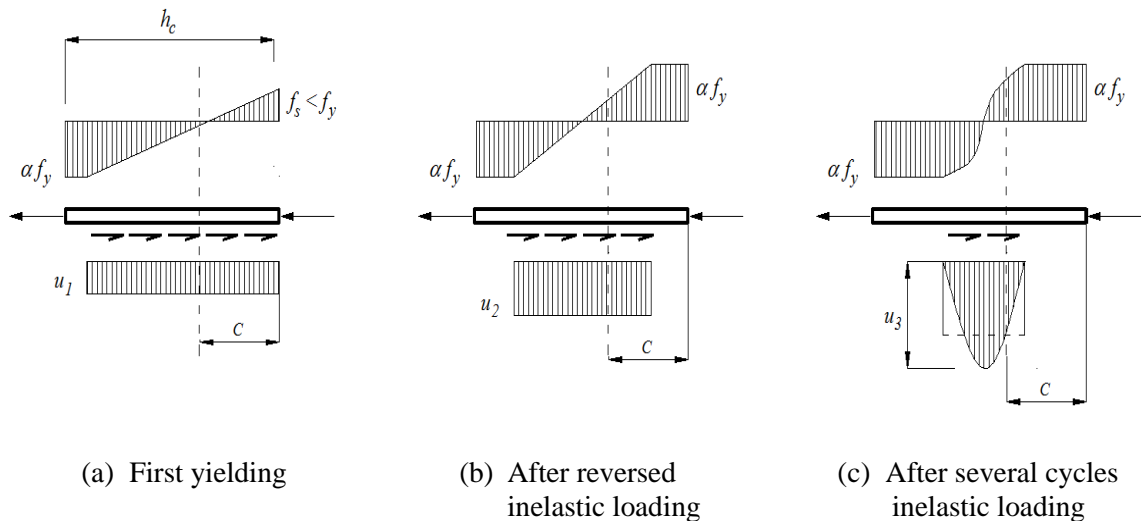


Figure 2.3: Probable bond stress distributions in a joint core (Reproduced from *Paulay et al., 1978*)

The most important part is what shown in Figure 2.3-c where some bond transfer is destroyed after a number of inelastic reversal cycles. Thus, the effective anchorage length of a beam bar is reduced, and a bond stress concentration is occurred near the center of the joint. Accordingly, after yield penetration, the concrete strut deteriorates ($\Delta T_c \approx 0$) and the major part of the joint shear force will be resisted by the truss mechanism.

2.2.2.2 Softened strut-and-tie model

Hwang and Lee (1999) had developed a new model for predicting the shear strength of the exterior beam-column joints under seismic loading; softened strut-and-tie model (SST), based on the same concept that was followed by Paulay et al. (1978). However, instead of having two mechanisms that are responsible to resist the joint shear forces, as mentioned before, the proposed strut-and-tie model consists of three mechanisms; the diagonal, horizontal and vertical mechanisms, as shown in Figure 2.4.

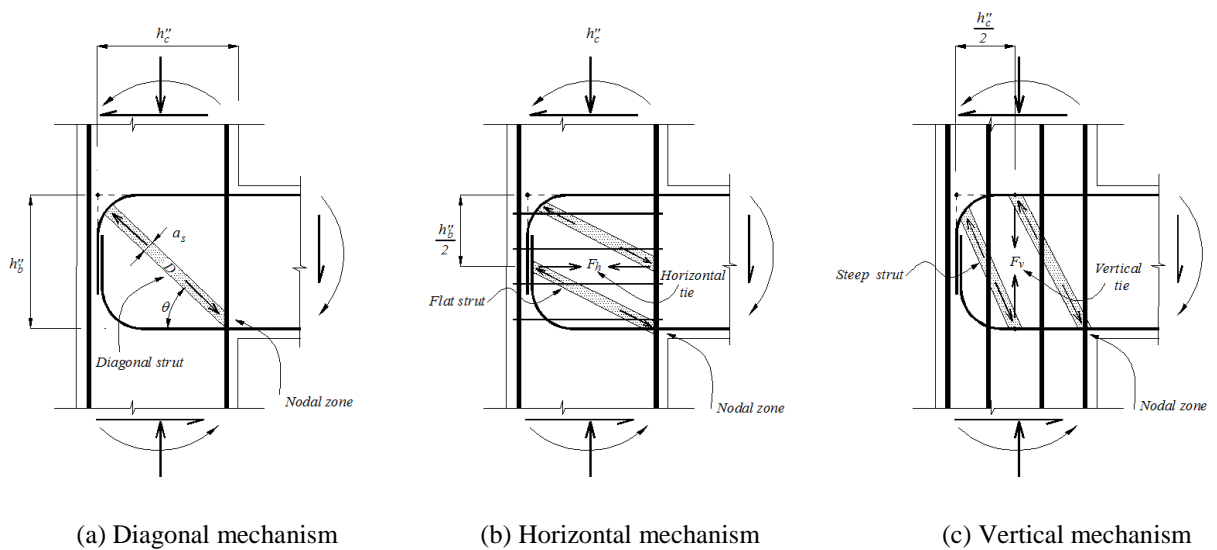


Figure 2.4: Joint shear resistant mechanisms (Reproduced from *Hwang and Lee, 1999*)

The purpose of this model is to detect the contribution of both the horizontal joint reinforcement and the vertical column reinforcement, separately, in resisting the shear forces acting on the joint.

Diagonal mechanism

The diagonal mechanism, as shown in Figure 2.4-a, is a single diagonal compression strut with an inclination angle $(\theta) = \tan^{-1}\left(\frac{h_b''}{h_c''}\right)$. The diagonal strut effective area (A_{str}) = $a_s \times b_s$, where b_s is the effective joint width and a_s can be calculated as:

$$a_s = \left\{ \begin{array}{ll} \sqrt{a_b^2 + a_c^2} & \text{without beam hinging occurred at the column face} \\ a_c & \text{beam hinging occurred at the column face} \end{array} \right\} \quad (2 - 12)$$

Where a_b and a_c are the depths of the compression zones in the beam and column, respectively.

Horizontal mechanism

The proposed horizontal mechanism consists of one horizontal tie and two flat struts, as shown in Figure 2.4-b. The horizontal tie represents the joint hoops area taking into account the unequal participation of these hoops in resisting shear forces. Fifty percent reduction in the hoops area located outside the middle half of the joint should be considered.

Vertical mechanism

The proposed vertical mechanism consists of one vertical tie and two steep struts, as shown in Figure 2.4-c. The vertical tie represents the area of the column intermediate bars taking into account the unequal participation of these bars similarly as in the horizontal mechanism.

Equilibrium equations

The strut-and-tie model can resist the horizontal joint shear forces V_{jh} through the contribution of the three mechanisms according to equation (2-13):

$$V_{jh} = D \cos \theta + F_h + F_v \cot \theta \quad (2 - 13)$$

Where D , F_h and F_v are the diagonal, horizontal and vertical shear mechanisms forces, respectively. Based on equation (2-13), the ratio of the three components can be expressed by:

$$D \cos \theta : F_h : F_v \cot \theta = R_d : R_h : R_v \quad (2 - 14)$$

Then, equation (2-14) could be re-written as:

$$D = \frac{1}{\cos \theta} \times \frac{R_d}{(R_d + R_h + R_v)} \times V_{jh} \quad (2 - 15)$$

$$F_h = \frac{R_h}{(R_d + R_h + R_v)} \times V_{jh} \quad (2 - 16)$$

$$F_v = \frac{1}{\cot \theta} \times \frac{R_v}{(R_d + R_h + R_v)} \times V_{jh} \quad (2 - 17)$$

Where R_d ; R_h ; and R_v are the ratios of the shear forces resisted by the three mechanisms. The authors defined the values of these ratios as:

$$R_d = \frac{(1 - \gamma_h)(1 - \gamma_v)}{1 - \gamma_h \gamma_v} \quad (2 - 18)$$

$$R_h = \frac{\gamma_h(1 - \gamma_v)}{1 - \gamma_h \gamma_v} \quad (2 - 19)$$

$$R_v = \frac{\gamma_v(1 - \gamma_h)}{1 - \gamma_h \gamma_v} \quad (2 - 20)$$

Where: $\gamma_h = \frac{2 \tan \theta - 1}{3}$ and $\gamma_v = \frac{2 \cot \theta - 1}{3}$ for $0 \leq \gamma_h$ and $\gamma_v \leq 1$

Finally, the maximum compression stress $\sigma_{d,max}$ acting on the nodal zone, shown in Figure (2.4) due to the three types of concrete struts (diagonal, flat and steep), can be calculated by:

$$\sigma_{d,max} = \frac{1}{A_{str}} \left[D + \frac{\cos \left(\theta - \tan^{-1} \left(\frac{h_b''}{2h_c''} \right) \right)}{\cos \left(\tan^{-1} \left(\frac{h_b''}{2h_c''} \right) \right)} F_h + \frac{\cos \left(\tan^{-1} \left(\frac{2h_b''}{h_c''} \right) - \theta \right)}{\sin \left(\tan^{-1} \left(\frac{2h_b''}{h_c''} \right) \right)} F_v \right] \quad (2 - 21)$$

Dealing with the assumption of cracked reinforced concrete, the maximum compressive stresses at the nodal zone, shown in Figure (2.4), should not exceed the maximum softened-compressive strength of concrete ($\zeta \cdot f'_c$). Where ζ is the softening coefficient and can be determined according to:

$$\zeta = \frac{5.8}{\sqrt{f'_c}} \frac{1}{\sqrt{1 + 400 \varepsilon_r}} \quad (2 - 22)$$

Where ε_r is the average transversal strain of cracked concrete subjected to compressive stresses equal to f'_c .

2.2.2.3 Finite element modelling

The finite element method is a powerful tool for the numerical solution of a wide range of engineering problems including solving for deformation and stress analysis of building and bridge structures. With the development in computer technology and CAD systems, complex problems can now be modelled easily and hence several alternative configurations can be tested on a computer. Several FE software packages are now commercially-available to facilitate the process of constructing and solving a model such as ANSYS, ABAQUS and DIANA.

In this section, a summary of the recently published work carried out on RC beam-column connections using finite element modelling is described. This summary is arranged with respect to the FE software that was used through each research.

ANSYS software:

Parvin and Granata (2000) studied the application of FRP composite laminates to exterior beam-column joints to increase their moment capacity. A three-dimensional model was created and analyzed. The concrete was modeled using an eight-node solid element specifically designed for concrete material (SOLID65). The concrete element is non-linear and requires an iterative solution. The reinforcing steel is modeled using a series of two node truss elements (LINK8) with bilinear stress-strain curve to account for plastic deformation and strain hardening of the steel reinforcing bars. The FRP laminate is modeled using an eight-node three-dimensional multi-layer solid element (SOLID45). Unlike the multi-layer shell element, the solid element (SOLID45) does not have mid

side nodes and therefore, the connectivity to the concrete element is enhanced. The authors ran a parametric study without calibrating their model against experimental data.

Mostofinejad and Talaeitaba (2006) attempted to introduce a comprehensive procedure for modeling FRP-strengthened RC exterior beam-column connections for non-linear FE analysis with ANSYS program. Similar to Parvin and Granata (2000), SOLID65, LINK8 and SOLID45 elements were used to model the concrete, longitudinal reinforcement and the FRP composite elements, respectively. However, the 5-parameter William-Warnke model was suggested to be used for concrete. This model is able to account for the cracking of concrete in tension and crushing of concrete in compression. Some of the important parameters to follow the failure envelope in the model are the shear transfer coefficients for crack opening and closing. These coefficients were suggested to be taken as 1.0 and 0.2 to 0.25 for closed and opened cracks, respectively. Furthermore, the crushing was eliminated from the concrete elements for better convergence in the analysis. An anisotropic material model was suggested to the FRP composites modelling. The authors connected the reinforcement nodes to the concrete nodes with non-linear spring elements (COMBIN39) to account for the anchorage slip and anchorage extension of the reinforcement. The authors concluded that a realistic non-linear analysis of RC connections with FRP overlays could be performed using ANSYS software. In addition, ignoring the anchorage slip of the longitudinal reinforcement of the beam embedded in the column in FE analysis may lead to underestimating the ultimate rotation of the joint up to 25%.

Bindhu and Jaya (2008 and 2010) investigated the effect of cross-inclined bars within the joint as confining reinforcement on the behaviour of RC exterior beam-column

joints subjected to seismic loading. The research included experimental part validated by FE modelling with ANSYS program. Again, SOLID65, LINK8 and SOLID45 elements were used to model the concrete, longitudinal reinforcement and the steel plates at the support locations, respectively. Half the system was modeled considering symmetry through the thickness. The authors found that the analytical load-displacement curves agreed quite well with the experimental data.

ABAQUS software:

Sritharan et al. (2000) studied the consequences of inadequate modeling of the strain penetration in finite element analysis of a bridge joint system. A finite element model of a bridge joint system in 2-D was created using eight-node bi-quadratic rectangular plane stress elements. Therefore, the confinement effect that transverse reinforcement has on the concrete behaviour was accounted for in the models by forcing its uni-axial stress-strain curve to follow that corresponding to a confined concrete response. Smearred-crack concept was adopted in this model. Reinforcing bars were represented with one-dimensional rebar elements, which can account for strain hardening, hysteresis and low cycle fatigue characteristics. Strength reduction of the system associated with bond slip is modeled by reducing the reinforcement strength as a function of dilatational strain in concrete normal to the bar. The authors concluded that this way of modelling does not take into account the effect of strain penetration and the accompanied bond slip. Therefore, additional array of double nodes along about $2/3$ of the column-to-joint interface with a series of tension and compression springs is required to provide

good predictions of the force flow across the joint region, and of overall force-displacement characteristics of the system.

Danesh et al. (2008) examined the effectiveness of using GFRP layers for joint shear strengthening of two-way corner beam-column connection through a 3-D finite element model. A solid element with eight nodes and three translational degrees of freedom at each ones, called C3D8R, was used to model concrete elements. Concrete-damaged plasticity model was used for defining concrete behaviour in plastic range. A truss element, called T3D2, was used to model reinforcement elements. This element has two nodes with three translational degrees of freedom at each node. A perfect bond assumption between steel and concrete nodes was made through this study. Four node shell elements, called S4R, with composite section were used for modeling the GFRP layers. The composite section enabled various materials to be defined in optional directions with various thicknesses. The authors concluded that the FE model used showed accepted agreement with the experimental results. However, compared to FE results, lower stiffness of the test specimen, in the initial loading steps, was observed.

DIANA software:

Li and Tran (2009) investigated the seismic behaviour of RC beam-column joints with vertically distributed longitudinal reinforcement layers along its beam. The study consisted of experimental part and a parametric study using FE modelling with DIANA program. Concrete was modeled using four-node isoparametric 2-D plane stress elements and the reinforcing steel bars were modeled as 2-node truss elements. The response of the concrete in compression was taken into account by an elastic-plastic model (isotropic

hardening), while uni-axial bilinear stress-strain relationship without strain hardening was used to describe the constitutive behaviour of the reinforcement. Bond-slip models were accounted between the reinforcement and surrounding concrete in order to simulate the bond deterioration along the beam and column longitudinal bars that was observed during experimental tests. Although the story shear forces of the analytical model for a few initial cycles were slightly higher than the experimental ones, comparison of the analytical and experimental results of all specimens showed that the lateral load-displacement hysteresis loops obtained from the FE analyses were quite similar to the experimental observations. The authors concluded that the FE modelling using DIANA software as a numerical tool to investigate the behaviour of RC Beam-column connections is feasible.

Kulkarni and Li (2009) investigated the behaviour of RC interior wide-beam-column joints subjected to seismic loading. The study consisted of experimental part and a parametric study using FE modelling with DIANA program. The concrete was modeled using 20-node, 3-D quadratic solid elements while the reinforcing bars were modeled as truss elements. The concrete model was based on nonlinear fracture theory to account for cracking and the plasticity model was used to account for the compression behaviour. The Von-Mises yield criterion with isotropic strain hardening was used to describe the constitutive behaviour of the reinforcement. The authors found a good agreement in the overall behaviour between the experimental and numerical specimens although the FE model had a higher stiffness than the experimental tests. Also, the strain values and distributions from the experimental observations showed a good agreement with those of the FE numerical predictions with few exceptions.

ATENA software:

Abdelwahed et al. (2005) investigated the behaviour of retrofitted beams (as parts of beam-column joints) using CFRP sheets with different lengths. The study consisted of experimental part and a parametric study using FE modelling with ATENA program. In this package, concrete could be modeled as either 4-node, 2-dimensional quadrilateral or 8-node, 3-dimensional solid elements having two or three degrees of freedom per node, respectively. Also, the internal reinforcement could be modeled using either a smeared layer approach or using 2-node linear truss elements having one degree of freedom per node, which are superimposed on the concrete elements at the required depth. A bi-linear stress-strain response taking into account the strain hardening phenomena is assigned for the reinforcement. Bond between the concrete and the internal reinforcement can also be modeled in the package using either the formulas defined in the CEB-FIB Model Code (CEB-FIB 1990) or user defined formulas. The authors found an excellent agreement between the experimental and the analytical location and type of flexural failure of all specimens considered with slight overestimations in the analytical values of approximately 10%.

SBETA software:

Baglin and Scott (2000) developed a numerical tool to supplement an existing experimental program to fully understand the behaviour of beam-column connections. Two-dimensional plane stress analysis was carried out using SBETA FE program. The whole model was built using first-order quadrilateral elements. SBETA generates concrete properties by default from a user-defined value for f'_c . However, a more accurate

definition of the compressive strain-softening curve was used. No tension stiffening effect was modeled. Bi-linear material definition was used for the steel bars. The authors found that numerical modeling, using the SBETA software package, offered considerable scope for complimenting the results from an ongoing experimental program. The stability of the numerical solution was found to be significantly better than some of the more complex packages available. Also, the load deflection characteristics were generally good, but modeling of the deformation due to crack growth and dislocation was inhibited by the smeared crack approach.

2.2.3 Factors Affecting the Behaviour of Steel-RC Beam-Column Joints

During the past four decades, significant amount of experimental research were carried out on different types of beam-column connections reinforced with steel. The effects of a number of factors on the joints behaviour have been evaluated. The structural performance of these joints, now, is well established.

In the following sections, a summary of the most important parameters that deemed to affect the behaviour of steel-reinforced beam-column joints subjected to earthquake loading is presented.

2.2.3.1 Flexural strength ratio

Flexural strength ratio of any beam-column joint can be defined as the ratio of the summation of the flexural capacities of the columns to that of the beams connected to the joint. The effect of this parameter was studied through both experimental testing (Ehsani and Wight 1985) and numerical modelling (Dooley and Bracci 2001).

Ehsani and Wight (1985) presented the experimental results of six exterior reinforced concrete beam-column joints subjected to reversal cyclic loading. All specimens were reinforced with adequate shear reinforcement in the beam and columns outside the joint to prevent shear failure. The parameters investigated included flexural strength ratio, joint reinforcement ratio and joint shear stresses. Reversal lateral quasi-static cyclic loads were applied directly at the beam tip simulating seismic loading. The authors concluded that the flexural strength ratio should not be less than 1.4 to achieve the strong-column-weak-beam concept. They added that larger flexural strength ratios are also improving the behaviour of the connection.

Dooley and Bracci (2001) investigated the influence of the flexural strength ratio on the behaviour of beam-column joints by performing inelastic time-history dynamic analyses on twenty-four building models. The authors concluded that using a minimum column-to-beam strength ratio of 2.0 results in a significantly high probability of preventing story mechanisms, under design-basis seismic loading, from occur.

2.2.3.2 Joint shear stresses

Joint shear stresses can be simply calculated by dividing the actual joint shear forces by the joint concrete area. Ehsani and Wight (1985), as described above, studied also the effect of this parameter and concluded that to reduce the excessive joint damage (column bar slippage and beam bar pullout chances), the maximum shear stress in exterior joints should be limited to $1.0\sqrt{f'_c}$. Moreover, to facilitate the construction process by reducing the amount of joint transverse reinforcement (less congestion) yet maintaining a

satisfactory performance, the joint shear stresses have to be more conservative than the limits of the draft code recommendations.

2.2.3.3 Concrete strength

Ehsani et al. (1987) and Ehsani and Alameddine (1991) studied experimentally the effect of using high-strength concrete instead of ordinary concrete on the behaviour of beam-column joints. The authors found that joints constructed with high strength concrete can exhibit ductile response similar to those constructed with normal strength concrete, if properly detailed. However, for high strength concrete joints, higher flexural strength ratio combined with lower joint shear stresses will have a favourable effect.

2.2.3.4 Type and rate of loading

Park (1989) discussed the procedures of testing structural assemblages under seismic loads. Three experimental methods for loading were discussed; shake table testing, pseudo-dynamic testing and quasi-static cyclic load testing.

Shake table testing: It is a realistic method to represent the seismic motion applied to a structure. Factors limiting the use of this method are the mass, size and strength of the tested specimens as well as the required equipments and instrumentations, which may not be available in many laboratories.

Pseudo-dynamic testing: In this method, measurements are recorded for the restoring forces of the structure at each step of testing. These measurements are then used to calculate the displacements, using non-linear computer analysis software, to be applied to the structure for the next step of testing.

Quasi-static cyclic load testing: In this method, specific number of displacement controlled loading cycles that are predetermined based on displacement ductility factors, are applied to the test specimens. Quasi-static loading usually gives a conservative estimate of the structural response as a result of eliminating the effect of the increasing strain rate due to the dynamic effect of the earthquake. The increased rate of strain yields an increase in the strength of the specimens. However, hysteresis loops obtained from a quasi-static loading are similar to those obtained using dynamic loading tests.

It is worth mentioning that quasi-static cyclic loading is the most commonly used test method by researchers (Hanson and Connor 1967; Abdel-Fattah and Wight 1987; Cheung et al. 1993; Filiatrault et al. 1995; LaFave and Wight 1999; Hakuto et al. 2000; Chutarat and Aboutaha 2003; Ghobarah and El-Amoury 2005; Chun et al. 2007; Solberg et al. 2008; Li and Tran 2009).

Chung and Shah (1989) investigated the effect of cyclic loading rate, shear span-to-depth ratio and stirrup spacing on the bond performance of exterior beam-column joints. Twelve anchorage-bond specimens were constructed and tested to study the effect of cyclic loading rate on a bar embedded in reinforced concrete. Each specimen represented a horizontal cantilever beam attached to a reinforced concrete block. Then the results of these tests were verified by testing three identical beam-column joints; the first specimen was tested under monotonic loading, the second specimen was tested under cyclic loading with a frequency of 0.0025 Hz (slow rate), while the third specimen was tested with a frequency of 1.0 Hz (fast rate).

The authors concluded that the faster loading rate is increasing the maximum load-carrying capacity. However, the failure occurred at a lower ductility ratio as a result

of early fracture of steel bars. This was induced by stress concentration caused by improved bond strength at faster rate. In addition, more widely-distributed cracks were observed in the beam at the slower rates of loading compared to fewer and wider cracks were at column face in case of faster loading rate.

2.2.3.5 Location of developed plastic hinges

Abdel-Fattah and Wight (1987) and Al-Haddad and Wight (1988) studied the factor of relocating the plastic hinge zone away from the column face. The authors found that relocating the beam-plastic hinges away from the column face will prevent beam bars yielding from penetrating into the joint; reducing slippage chance. In addition, relocating the hinging zone will achieve more joint confinement in case of using less transverse reinforcement ratio.

Furthermore, the authors found that no significant loss in the strength or the stiffness for the relocated hinging zones. Also, large increase in the rotational ductility of the relocated hinging zones is expected due to lower longitudinal reinforcement ratio and the low level of shear stresses.

2.2.3.6 Effect of anchorage length

Leon (1990) investigated the effect of the beam bars anchorage length on the behaviour of interior beam-column connections with respect to its hysteretic and shear performance. Four interior-half-scale beam-column connections were constructed and tested. All specimens had the same beam size and reinforcement, and the only variable was the

column depth which varied between 8, 10, 12 and 14 inches; corresponding to changing the beam bars anchorage length between 16, 20, 24 and 28 times the bar diameters.

The author found that an anchorage length of 28 times the bar diameter is required to ensure that the beam bars reach their ultimate strength and also to validate the design assumption that the joint is rigid.

2.2.3.7 Role of joint reinforcement

Hwang et al. (2005) studied the role of the joint hoops on the shear strength of exterior beam-column joints. The authors investigated whether the hoops transfer tensile force and necessitate a truss mechanism in the joint or the internal force will be transferred only by the diagonal concrete strut and the hoops are only for confining the concrete core. Another objective was to carry out a performance evaluation of the joints that conform to the softened strut-and-tie (SST) model. The experimental program included nine specimens. All specimens were designed according to the SST model.

It was found that the joint hoops should be considered as tension ties and crack control bars and not as concrete-confining reinforcement, which is not in agreement with the philosophy adopted by the ACI-ASCE 352 guideline. In addition, beam-column joints without any hoops, in the absence of the high column load, have satisfactory seismic behaviour as long as the joint is provided with adequate shear strength according to the SST model.

2.2.3.8 Effect of diagonal bars within the joint

Tosonos et al. (1992) investigated the improvement in the seismic behaviour of exterior RC beam-column joints as a result of using inclined bars inside the core of these joints. It was attempted to use these inclined bars to replace the vertical column side bars which were responsible to resist the vertical shear stresses developed in the joint. Twenty full-scale specimens were constructed and tested. The variable parameters covered in that study included the percentage of inclined reinforcing bars, the flexural strength ratio and the joint shear stresses. The authors found that the presence of the diagonal bars improved the bond condition within the joint which contributed to effectively maintaining the strength and stiffness of the overall assembly after reaching the maximum capacity. Also, a significant improvement was observed in the specimens that have high shear stresses and low flexural strength ratio in case of using the inclined reinforcement bars. Finally, the authors found that the presence of inclined bars within the joint core introduced an additional new mechanism of shear transfer.

Au et al. (2005) studied the effect of providing diagonal bars within the joint by replacing an equivalent amount of the joint shear transverse reinforcement (non-conventional reinforcing pattern). Six half-scale interior RC beam-column joints were constructed and tested. Two of these specimens did not have any transverse reinforcement in the joint zone. The other two specimens were reinforced with the conventional transverse hoops, while the last two specimens were reinforced with the inclined bars. The authors found that the empty joints were not suitable even under moderate seismicity. In addition, the presence of the diagonal bars improved the bond condition within the joint which in turn helped to control the development of the beam-

column interface cracks. Also, the proposed detailing of the beam-column joints with diagonal bars is suitable for joints that do not conform to the standards recommendations and also for joints of RC frame structures located in low to medium seismic regions.

Furthermore, Chalioris et al. (2008) investigated the efficiency of inclined bars as shear reinforcement in the joint area. Twenty exterior beam-column joint sub-assemblages were tested under cyclic loading. The main variables were the type of the joint shear reinforcement (stirrups, diagonal bars, vertical bars and combination of them), the joint steel reinforcement ratio and the joint shear stresses. The authors concluded that specimens with crossed inclined bars and joint stirrups showed enhanced hysteretic response and excellent performance capabilities. The combination of crossed-bars and stirrups within the joint is essential for the safety of the joint, since stirrups not only increasing the joint shear capacity but also restraining the deformations of the bent anchorage of the beam's bars from damaging concrete cover at the back of the joint area in the case of specimens without stirrups.

2.3 FRP COMPOSITE MATERIALS

Fibre Reinforced Polymer (FRP) materials were originally used in aerospace, automotive fields. The significant reduction in the materials and manufacturing costs helped the widespread of the FRP materials in civil engineering applications. FRP's are increasingly being used in civil infrastructure in several forms such as; reinforcing bars and tendons in new structures, wraps and laminates for strengthening of existing structures. To stay within the scope of this research, the following section will only focus on the FRP materials in the form of internal reinforcing bars.

2.3.1 Constituents

FRP products are composite materials consist of reinforcing fibres embedded in a matrix (resin) in addition to some fillers and additives. The fibres are responsible to provide the mechanical strength and stiffness to the composite, while the resins are responsible for protecting the fibres from mechanical abrasion, transfer stresses between the fibres, and prevent the fibres from buckling as well. Fibres are oriented in the longitudinal direction of the bars which is the direction of the primary loads. Also, strength, stiffness, durability and low cost are all properties should present in the fibres used for manufacturing the FRP composites. Three types of fibres are the most commonly used for FRP reinforcement products; aramid, carbon and glass (ACI 1996).

Aramid fibres are classified as highly crystalline aromatic polyamide fibres. Aramid fibres offer good mechanical properties; the highest tensile strength-to-weight ratio compared with the other types of fibres with the added advantage of toughness or impact resistance. In addition, aramid fibres have a negative coefficient of thermal expansion in the longitudinal direction and the fibres are resistant to organic solvents, fuels and lubricants. Aramid fibres are used in many marine and aerospace applications as well as in designing low thermal expansion composite panels. The major disadvantages of aramid fibres are their low compressive strengths and difficulty in cutting or machining.

Carbon fibres are manufactured from one of the three types of precursors (starting materials), namely, polyacrylonitrile (PAN) fibres, rayon fibres or pitch. Among the advantages of carbon fibres are their high tensile strength–weight ratios as well as tensile modulus–weight ratios, very low coefficient of linear thermal expansion, high fatigue strengths. However, among the disadvantages of these fibres are the difficulty of being

wet by resins, their low impact resistance and high electrical conductivity. The high cost of the carbon fibres has so far limited them from widespread commercial applications. They are used mostly in the aerospace industry, where weight saving is considered more critical than cost.

Glass fibres are the most common of all reinforcing fibres for polymeric matrix composites. Glass fibres are classified as fibre drawn from an inorganic product of fusion that has cooled without crystallizing. Among advantages of glass fibres are low cost, high tensile strength, high chemical resistance and excellent insulating properties. On the other hand, the disadvantages are relatively low tensile modulus, sensitivity to abrasion during handling and relatively low fatigue resistance. The types of glass fibres commonly used are E-glass, S-glass and C-glass. E-glass has the lowest cost of all commercially available reinforcing fibres, which is the reason for its widespread use in the FRP industry.

The final mechanical properties of the FRP product are significantly affected by the selection of the proper matrix (resin). There are two types of polymeric matrices widely used for FRP composites, namely, thermosetting and thermoplastic. Thermosetting polymers are low molecular-weight liquids joined together by chemical cross links. So, they form a rigid three dimensional structure that once set, cannot be reshaped again by neither heat nor pressure. Contrary, thermoplastic polymer are made from molecular in a linear structural form connected together by weak secondary bonds can be destroyed by heat or pressure. Thermosetting polymers are used more often than thermoplastic in FRP industry.

Polyesters, vinyl esters and epoxies are the commonly used thermosetting polymers. These materials have good chemical resistance and thermal stability and

undergo low creep and stress relaxation. On the other hand, the disadvantages are short shelf-life, low strain-to-failure, low impact strength and long manufacturing time.

Fillers and additives are not only to reduce the composite cost but also to improve the performance that might not be achieved by the fibres and resins ingredients. Fillers can improve mechanical properties by reducing organic content in composite laminates. In addition, filled resins have less shrinkage (dimension stability) and improved transfer of the load between fibres. Furthermore, the use of additives can perform number of critical functions; fire resistance, emission control, viscosity control and coloration.

2.3.2 Manufacturing

There are three common manufacturing processes for FRP materials; pultrusion, braiding and filament winding. Straight FRP bars are produced using the pultrusion technique. In this method the continuous strands of the fibres are pulled from a creel of fibres to be impregnated in a resin tank. Once they are saturated with resin, they are shaped through a heated die at which they can be cured as shown in Figure 2.5. Before the FRP bars are cut to the required lengths, the bars surface must be treated in the form of spirals or sand coating to ensure strong bond with concrete.

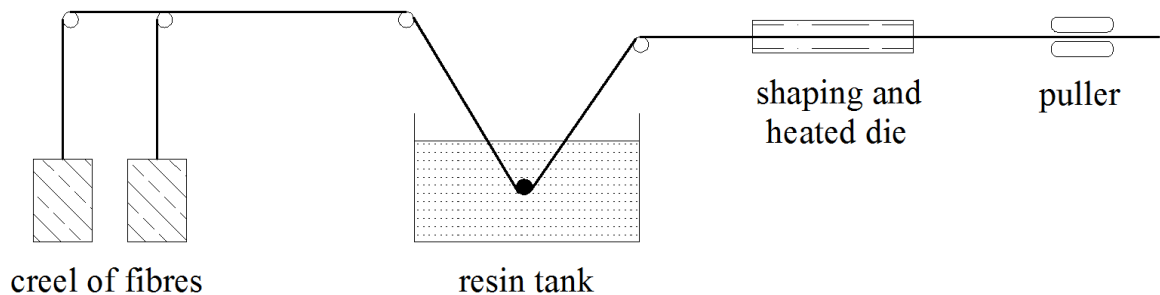


Figure 2.5: Pultrusion process (Reproduced from *ISIS Canada, 2007*)

2.3.3 Physical Properties

The main parameters defining the physical properties of any material are the coefficients of thermal expansion and the density. FRP bars have different thermal expansion in the longitudinal and transverse directions. The longitudinal coefficient of thermal expansion is governed by the type of fibre, while the transverse coefficient of thermal expansion is dominated by the type of resin (ACI 2006). Coefficients of thermal expansion for some FRP reinforcing bars are shown in Table 2.1.

Table 2.1: Typical coefficients of thermal expansion (Reproduced from ACI, 2006)

Direction	Coefficient of Thermal Expansion ($\times 10^{-6} / ^\circ\text{C}$)			
	Steel	GFRP	CFRP	AFRP
Longitudinal	11.7	6 to 10	-1 to 0	-6 to -2
Transverse	11.7	21 to 23	22 to 23	60 to 80

Furthermore, the density of FRP bars is considerably less than of the steel bars (i.e. one-sixth to one-fourth that of steel) as shown in Table 2.2.

Table 2.2: Typical densities of reinforcing bars (Reproduced from ACI, 2006)

	Steel	GFRP	CFRP	AFRP
Density (gm/cm^3)	7.9	1.25 to 2.10	1.5 to 1.6	1.25 to 1.40

2.3.4 Mechanical Properties

The unidirectional behaviour of the FRP bars is linear-elastic up to failure as shown in Figure 2.6. They do not exhibit yielding plateau as the conventional steel does. Generally, FRP bars have higher tensile strength than that of the conventional steel. However, less

and different values for the modulus of elasticity of the three FRP materials are observed. On the other hand, FRP bars have lower compressive strength than the steel due to buckling of fibres.

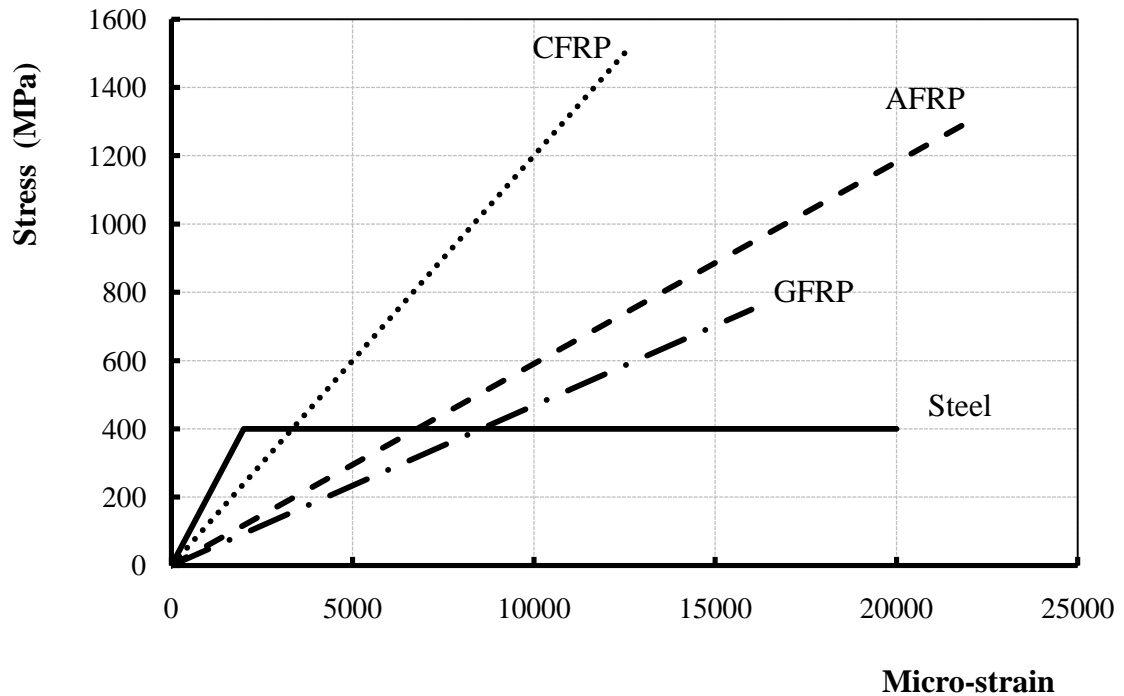


Figure 2.6: Stress-strain curve for different reinforcing materials

The mechanical properties of FRP bars depend mainly on number of factors such as the type and the volumetric ratio of fibres in the composite, the type of resin, and quality control during the manufacturing process. Even for the same product, the output mechanical properties differ between manufacturers. The mechanical properties of some commercially available FRP reinforcing bars are given in Table 2.3.

Table 2.3: Typical mechanical properties of FRP bars (reproduced from *ISIS Canada, 2007*)

	Trade Name	Tensile Strength (MPa)	Modulus of Elasticity (GPa)	Ultimate tensile Strain
Carbon Fibre	V-ROD	1596	120.0	0.013
	Aslan	2068	124.0	0.017
	Leadline	2250	147.0	0.015
	NEFMAC	1200	100.0	0.012
Glass Fibre	V-ROD	710	46.4	0.015
	Aslan	690	40.8	0.017
	NEFMAC	600	30.0	0.020

2.4 BEAM-COLUMN JOINTS REINFORCED WITH FRP

Significant amount of research were carried out on individual structural elements reinforced with FRP materials such as simply-supported beams, slabs and bridge decks. However, very few data is available for the framed structures, continuous beams, columns under axial and bending loads, and beam-column joints. More research is needed to help in establishing guidelines for the design and detailing of such elements.

In the following sections, a brief summary for an analytical research carried out on the FRP-reinforced concrete columns subjected to both axial and lateral loads is discussed. Also, the experimental tests that were carried out on beam-column joints reinforced with FRP materials are presented.

2.4.1 FRP-RC Columns under Combined Axial and Lateral Loads

Choo et al. (2006) explained that there are two undesirable modes of failure that need to be avoided in the process of strength analysis of any FRP-reinforced column:

- *Premature compression failure*; corresponding to the compression rupture of FRP bars in the compression zone prior to the concrete crushing
- *Brittle tension failure*; corresponding to tension failure of FRP in the tension zone prior to the concrete crushing

In both failure modes, the column will fail before the concrete utilizes its full capacity (strain in compression reach 0.003; the maximum usable strain according to ACI 318-02). Thus, the probability of getting the first mode of failure is lower than that of the second mode. The reason behind that is the concrete crushing strain in compression (0.003) is very small compared to the ultimate compressive strain in FRP bars. For instance, the ultimate compressive strain of the FRP bars may be assumed to be about 50% of the ultimate tensile strain (Deitz et al. 2003) and still larger than concrete crushing strain in compression (0.003). On the other hand, brittle tension failure is more likely to occur as the FRP tensile strain can easily exceed the ultimate tensile strain in the case of pure bending acting on a column with small reinforcement ratio.

Therefore, minimum amount of FRP reinforcement should be calculated, not considered 1% as for the steel-reinforced columns, in order to ensure avoiding the brittle tension failure mode. This ratio can be determined based on the analysis of the column by carrying pure bending moment (axial load = 0) and matching the strains in both concrete and reinforcement to the ultimate values. Then, choosing appropriate reinforcement ratio larger than this minimum ratio.

Finally, the authors recommended checking the column strength under the effect of both the axial compression force and the acting bending moment using axial load-moment (P - M) interaction diagram that can be investigated through the following steps:

- Assume a location of the neutral axis;
- Assume the concrete strain is equal to compressive strain 0.003 at the most outer concrete fibre in compression;
- From linear strain distribution, determine the strains at the centers of the concrete part in compression and the strains in all reinforcing bars;
- Calculate the corresponding forces in each reinforcing bar in the tension zone and forces in concrete in the compressive zone
- Determine the resultant axial load P and the bending moment M at the section mid-height;
- A new location of the neutral axis is selected and the procedure can be repeated;
- Finally, each pair values for both P and M can be drawn together to get the final P - M interaction diagram.

Sharbatdar (2003) carried out an experimental study on the behaviour of full-scale columns reinforced with CFRP bars and stirrups subjected to seismic loading. The author advised to follow the requirements of the CSA-S806-02 (Clause 12.7.1) to insure enough confinement for the columns. It was observed that columns that had 60% of the confinement reinforcement required by CSA-S806-02 showed increased deformability with lateral drift ratio up to 3.0% associated with approximately 23% strength degradation.

In addition, the author recommended using equation (2-23) to calculate the axial capacity of columns reinforced with FRP (P_{ro}):

$$P_{ro} = 0.85\phi_c f'_c (A_g - A_{frp}) + \phi_F \varepsilon_{frpc} E_{frpc} A_{frp} \quad (2 - 23)$$

Where ϕ_F is the material resistance factor for FRP reinforcement and A_{frp} is the longitudinal FRP reinforcement area. It was recommended to limit the value of the strain in FRP under concentric compression, ε_{frpc} , to 0.002 and assume the compressive modulus of elasticity, E_{frpc} , to be equal to 25% of the FRP tensile elastic modulus, E_{frp} .

2.4.2 Experimental Testing

2.4.2.1 Aramid FRP-reinforced joints

Fukuyama et al. (1995) studied the feasibility of using aramid-FRP bars as main and shear reinforcement in concrete frames and tried to establish a design philosophy for FRP reinforced frames and an evaluation method for this design. A half-scale two-bay two-story concrete frame reinforced totally with braided aramid fibre polymer reinforcing bars coated with silica sand had been tested in order to determine the structural performance and limit states of that frame. Both the ultimate limit state and the serviceability limit state were considered in this design to take the effect of normal loading and the earthquake loading.

At the end of the test, the authors concluded that using aramid FRP bars as flexural and shear reinforcement in concrete frames is feasible. They found that the frame behaviour remained elastic till the concrete crushing (rotation angle 0.02 rad). Therefore, they concluded that the rehabilitation processes of FRP-reinforced concrete framed-members are easier than those with steel.

2.4.2.2 Carbon FRP-reinforced joints

Sharbatdar et al. (2007) studied the behaviour of exterior beam-column joints totally reinforced with carbon FRP bars in the longitudinal direction and carbon FRP grids in the transverse direction (as stirrups). The test specimens were designed according to previous research work findings and available design codes (Sharbatdar 2003; CSA 2002). Three full scale exterior FRP-reinforced concrete beam-column joints were constructed and tested. The test parameters were the stirrups spacing within the joint and the arrangement of longitudinal reinforcement in beams and columns.

Under reversed cyclic loading, the capability of the CFRP-reinforced joints to resist lateral drift were found to exceed the 3% drift ratio required by codes, which means that CFRP-reinforced joints satisfy the strength and ductility (deformability) requirements of earthquake resistant structures. Also, the test data showed good agreement with the confinement provisions required by the CSA-S806-02 (CSA 2002) and indicated that CFRP-reinforced concrete joints can be confined to develop inelastic deformations. Moreover, the test results showed that CFRP bars are capable of adequately carrying tension and compression cycles.

2.4.2.3 Glass FRP-reinforced joints

Said and Nehdi (2004) investigated the performance of beam-column joints reinforced with GFRP grids under reversal quasi-static cyclic loading. Two specimens were tested in this research, one was totally reinforced with GFRP grids and the other specimen was reinforced with steel. Beams and columns cross section were similar and measured 250x400 mm. The GFRP-reinforced specimen was designed to have a similar flexural

capacity to that of the control steel-reinforced specimen, thus inducing a comparable level of joint shear input.

For the beam reinforcement, the longitudinal GFRP reinforcement was cut from NEFMAC G16 (201 mm² cross-sectional area) grids. The grids were cut into bars to have 5 nodes per meter outside the joint zone and were increased to 10 nodes per meter inside the joint. This was done to enhance the mechanical anchorage and to avoid premature slippage of the beam reinforcement in the joint. The same GFRP bars have been used in the column but with 5 nodes per meter along the whole length. For the transverse reinforcement, 3-branched grids (vertically and horizontally) G10 (77 mm² of cross-sectional area) spaced at 80 mm were used near the joint area in both beam and column. Away from the joint zone, the spacing was increased to 120 mm in the beam and 125 mm in the column.

At the end of the test, it was observed that the GFRP reinforced beam-column joints exhibited very low plasticity features under reversed cyclic loading. This resulted in lower energy dissipation compared to that of the conventional steel-reinforced beam-column joint. However, the GFRP-reinforced specimen showed a satisfactory drift capacity up to 6% drift ratio. In addition, the authors commented on the design code provisions for the seismic design of steel-RC structures as it needs to be re-evaluated for FRP-reinforced structures to address their low energy dissipation capacity.

Recently, Hasaballa (2009) studied the feasibility of using GFRP bars and stirrups as main reinforcement in exterior beam-column joints subjected to seismic loading focusing on beam reinforcement detailing. Four full-scale exterior beam-column joints were constructed and tested under reversed quasi-static cyclic loading (beams cross

section 350×450 mm and columns cross section 350×350 mm). The test parameters were the type of flexural and shear reinforcement and the beam reinforcement detailing. One specimen was reinforced with steel bars and the second specimen was reinforced with straight GFRP bars. The third specimen reinforced with bent GFRP bars while the fourth specimen reinforced with straight GFRP bars in addition to beam stub.

It was found that GFRP-reinforced joints can be designed to satisfy both strength and ductility (deformability) requirements of earthquake-resistant structures. In addition, GFRP-reinforced joints can safely reach 4.0% drift capacity under reversed cyclic loading. One of the tested specimens showed that 20 times bar diameter as embedment length for beam bars inside the joint were not enough to ensure avoiding free-end slippage of the GFRP straight bars subjected to cyclic loading. The use of bent bars or beam-stubs was good possible solution to avoid the slippage problem. More investigations about the adequate anchorage length are needed.

CHAPTER 3

EXPERIMENTAL PROGRAM

3.1 GENERAL

This chapter presents the details of the experimental study undertaken as part of this research work. A summary of the design strategy for the FRP-reinforced specimens is presented. Then, the details of the experimental phase are discussed through introducing the material properties, test specimens, instrumentations, test set-up, loading protocol and test procedure.

3.2 DESIGN STRATEGY OF FRP STRUCTURAL ELEMENTS

3.2.1 General

The beam, column and joint of each specimen in this research are designed according to the available design codes, design manuals and recommendations of previous research work, where applicable. Figure 3.1 shows the carefully-selected combination of these codes and guidelines used in this study.

For beams, the flexural design is performed according to CSA S806-02 (CSA 2002) and ISIS-07 (ISIS Canada 2007). However, for shear design, CSA S806-02 (2002) and CSA S6-09 (2009) are used for calculating the amount of stirrups while CSA A23.3-04 (2004) is utilized for calculating the stirrups spacing.

For columns, the axial compressive load capacity is determined according to the recommendations of Sharbatdar (2003) and Sharbatdar et al. (2007), while the load-moment interaction diagram is constructed according to the procedure introduced by Choo et al. (2006). However, for shear design, CSA S806-02 and CSA S6-09 are used for

calculating the amount of stirrups while CSA A23.3-04 is utilized for calculating the stirrups spacing. Finally, the joint shear capacity is checked according to CSA A23.3-04.

In the following sections, the details about the equations used for designing each structural element in the FRP-reinforced specimens are presented.

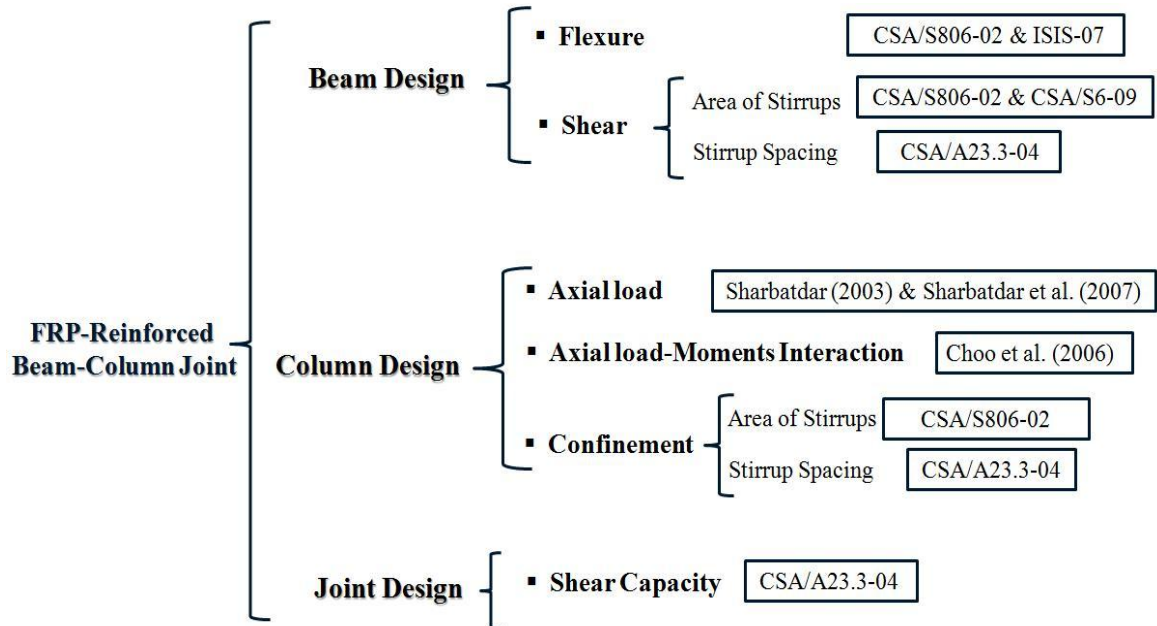


Figure 3.1: FRP-reinforced specimen design flowchart

3.2.2 Beam Design

3.2.2.1 Design for flexure

Following the provisions of CSA S806-02 - Clause 8.2.1, the FRP-reinforced section should be designed to fail in compression. In other words, the reinforcement ratio ρ_{frp} shall be greater than the balanced reinforcement ratio ρ_{frpb} , to avoid the brittle failure due to FRP bar rupture, and can be determined as:

$$\rho_{frp} = \frac{A_{frp}}{bd} > \rho_{frpb} = \alpha_1 \beta_1 \frac{\phi_c}{\phi_F} \frac{f'_c}{f_{frpu}} \left(\frac{\varepsilon_{cu}}{\varepsilon_{cu} + \varepsilon_{frpu}} \right) \quad (3-1)$$

Where b and d are the width and depth of the beam cross-section, respectively. α_1 and β_1 are the concrete rectangular stress block coefficients. f_{frpu} is the longitudinal FRP ultimate tensile strength. ε_{cu} and ε_{frpu} are the ultimate concrete compressive strain (crushing strain) and the ultimate tensile strain of the longitudinal FRP (rupture strain), respectively.

The developed tensile stresses in FRP bars in this case, f_{frp} , according to ISIS-07 - Clause 6.4.2) can be calculated as:

$$f_{frp} = 0.5 E_{frp} \varepsilon_{cu} \left[\left(1 + \frac{4 \alpha_1 \beta_1 \phi_c f'_c}{\rho_{frp} \phi_F E_{frp} \varepsilon_{cu}} \right)^{0.5} - 1 \right] \quad (3-2)$$

Where E_{frp} is the tensile modulus of elasticity of the FRP longitudinal reinforcement.

The beam nominal moment resistance, M_{nb} , can be calculated (ISIS-07, Clause 6.4.2) as:

$$M_{nb} = \phi_F f_{frp} A_{frp} \left(d - \frac{\beta_1 c}{2} \right) \quad (3-3)$$

Where c is the depth of the neutral axis.

3.2.2.2 Design for Shear

Since there are no seismic provisions available in FRP codes, the concepts provided by the steel design code CSA A23.3-04 (CSA 2004) were utilized. In CSA A23.3-04 - Clause 21.3.4.2, the contribution of concrete to shear strength of the beam is ignored at

the location of plastic hinges in order to accommodate the concrete deterioration due to cracking. In other words, the beam transverse reinforcement is responsible to carry the whole shear applied to the section. Following this concept, the shear reinforcement area is determined according to either CSA S806-02 (CSA 2002) for buildings or CSA S606-09 (CSA 2009) for bridges. Also, the spacing of shear reinforcement is determined according to confinement requirement; Clause 21.3.3.2 of CSA A23.3-04 (CSA 2004).

Based on CSA S806-02 code

According to CSA S806-02 - Clause 8.4.4.6, the required hoops' area, A_v , is given by:

$$V_F = \frac{0.4\phi_F A_v f_{fu,v} d}{s} \quad (3-4)$$

$$A_v \geq A_{v,min} = \frac{0.3\sqrt{f'_c} b s}{f_{uv,frp}} \quad (3-5)$$

Where V_F is the shear resisted by FRP hoops, $f_{fu,v}$ is the ultimate strength of the straight part in FRP hoop reinforcement, and $A_{v,min}$ is the minimum allowable shear hoops area. Also, $f_{uv,frp}$ is the hoop design strength; and taken the smaller of $0.004E_{f,v}$ or bend strength, where $E_{f,v}$ is the tensile modulus elasticity of FRP hoop reinforcement.

Based on CSA S6-09 code

According to CSA S6-09 - Clause 16.8.7, the required hoops area, A_v , can be calculated as:

$$V_F = \frac{\phi_F A_v \sigma_v d_v \cot \theta}{s} \quad (3-6)$$

$$A_v \geq A_{v,min} = 0.06\sqrt{f'_c} \frac{b \cdot s}{\sigma_v} \quad (3-7)$$

Where d_v is the effective shear depth; taken equal to $0.9d$, σ_v are the developed stresses in the shear hoops, and θ is inclination of the shear cracks. σ_v and θ can be determined according to:

$$\theta = (29 + 7000\varepsilon_x) \left(0.88 + \frac{S_{ze}}{2500} \right) \quad (3-8)$$

$$\sigma_v = \text{smaller of} \left\{ \begin{array}{l} \frac{\left[0.05 \frac{r_b}{d_b} + 0.3 \right] f_{fu,v}}{1.5} \\ 0.004 E_{f,v} \end{array} \right. \quad (3-9)$$

Where S_{ze} is the crack spacing parameter (will be taken equal to 300 in this research as the minimum transverse reinforcement will be used), r_b is the radius of the hoop bend and d_b is the diameter of the hoop. The longitudinal strain at the mid-depth of the cross section, ε_x , can be calculated as:

$$\varepsilon_x = \frac{\frac{M}{d_v} + V - V_p + 0.5N_f - A_p P_{po}}{2(E_{frrp} A_{frrp} + E_p A_p)} \leq 0.003 \quad (3-10)$$

Where M and V are the anticipated bending moment and the corresponding developed shear force, respectively, at the shear critical section. V_p is the component in the direction of the applied shear of all the effective prestressing forces crossing the critical section, N_f is the axial load normal to the cross-section occurring simultaneously with V_F including the effects of tension due to creep and shrinkage, and A_p is the area of steel tendons in the tension zone. P_{po} is the stress in tendons when the stress in the surrounding concrete is zero and E_p is the modulus of elasticity of steel tendons. In this study and since there is no prestressing, the terms $(V_p + 0.5N_f - A_p P_{po})$ and $(E_p A_p)$ will be taken equal to zero.

Finally, the maximum spacing of the shear hoops, s , according to CSA A23.3-04 - Clause 21.3.3.2, shall not exceed the smallest of:

- quarter of the section depth,
- eight times the diameter of the smallest longitudinal bars,
- 24 times the diameter of the hoop bars, or
- 300 mm

3.2.3 Column Design

3.2.3.1 Design for Axial Load-Moment Interaction

The column axial capacity can be calculated according to Sharbatdar (2003) [see Equation 2-21 in Section 2.4.2.2], while the interaction diagram of the column reinforced with FRP bars can be obtained according to Choo et al. (2006) [see Section 2.4.1]. Accordingly, the actual axial load acting on the specimen (percentage of the axial capacity P_{ro}) and the actual moment transferred to the column ($0.5M_{nb}$) can be checked and the nominal flexural strength of the column, M_{nc} , can be determined.

3.2.3.2 Design for Flexure

Flexural strength ratio in the exterior beam-column joints (M_R) can be calculated as:

$$M_R = \frac{2M_{nc}}{M_{nb}} \quad (3 - 11)$$

CSA A23.3-04 - Clause 21.4.2.2 (Equation 21-3) ensures the strong-column-weak beam behaviour in the joint performance by making $\Sigma M_{nc} \geq \Sigma M_{pb}$. Where ΣM_{nc} is the sum of nominal flexural strengths of columns framing into the joint and ΣM_{nb} is the sum of probable flexural strengths of beams framing into the joint; both evaluated at the face

of the joint. The term “probable” refers to the strength calculated considering the strain hardening phenomena in steel (multiplier $\alpha = 1.25$). Nevertheless, for FRP-reinforced elements, the probable and nominal flexural strengths are expected to be the same due to the linear-elastic behaviour of FRP reinforcement up to failure.

3.2.3.3 Design for Shear

The same methodology followed in the shear design of the beam is followed in the column. However, determining the required hoops area according to the lateral confinement is more critical for columns.

3.2.3.4 Design for Lateral Confinement

Based on CSA S806-02 code

Minimum transverse reinforcement for lateral confinement, A_{FH} according to CSA S806-02 - Clause 12.7.1, can be determined as:

$$A_{FH} = 14sh_c \frac{f'_c}{f_{FH}} \left(\frac{A_g}{A_{co}} - 1 \right) \frac{\delta}{\sqrt{K_c}} \frac{P_f}{P_{ro}} \quad (3 - 12)$$

$$\left(\frac{A_g}{A_c} - 1 \right) \geq 0.3 \quad \frac{P_f}{P_{ro}} \geq 0.2 \quad K_c = 0.15 \sqrt{\frac{h_c}{s} \frac{h_c}{s_1}}$$

Where h_c is the cross-sectional dimension of the column core, f_{FH} is equal to $0.004E_{f,v}$, and δ is the design lateral drift ratio; shall not be less than 3%. A_{co} is the core area of the column measured to the centerline of the hoops. Also, P_f is the actual applied axial load and s_1 is the spacing of the tie legs in the cross-sectional plane of the column.

Based on CSA S6-09 code

Due to lack of data, the only available provisions for confinement can be found in the steel reinforced columns section (CSA S6-09, Clause 4.7.4.2.5). In this case, replacement is needed for the yield strength of the steel hoops f_y with the hoop bend strength f_{fb} . The required hoop reinforcement A_{sh} shall not be less than the largest of the following:

$$A_{sh} = \text{larger of } \begin{cases} 0.30 sh_c \frac{f'_c}{f_y} \left[\frac{A_g}{A_c} - 1 \right] \\ 0.12 sh_c \frac{f'_c}{f_y} \left[0.5 + \frac{1.25 P_f}{\phi_c f'_c A_g} \right] \end{cases} \quad (3 - 13)$$

$$0.5 + \frac{1.25 P_f}{\phi_c f'_c A_g} \geq 1$$

Finally, according to CSA A23.3-04 - Clause 21.4.4.3, the spacing between the transverse stirrups of the column should not exceed the smallest of the following:

$$s = \text{smaller of } \begin{cases} \text{One - quarter of the minimum member dimension} \\ \text{six times the diameter of the smallest longitudinal bar} \end{cases}$$

3.2.4 Joint Design

According to CSA A23.3-04 - Clause 21.5.1.2, the shear forces acting on steel-reinforced joints shall be determined by assuming the tensile stresses in the longitudinal beam reinforcement equal to 1.25 times the yield stress ($1.25f_y$). However, FRP bars do not exhibit yielding behaviour and the developed strains are less than the ultimate tensile strain (compression failure). Hence, the transferred tensile forces from the longitudinal bars to the joint, T_b , can be calculated based on the actual developed tensile stresses corresponding to the beam nominal moment resistance as:

$$T_b = \varepsilon_{frp} E_{frp} A_{frp} \quad (3 - 14)$$

Where ε_{frp} is the actual developed tensile strain in the beam FRP bars. Shear force transferred by columns to the joint, V_{nc} can be calculated as:

$$V_{nc} = \frac{M_{col} = 0.5M_{nb}}{\text{column shear span}} \quad (3 - 15)$$

Finally, total shear force acting on the joint, V_j , can be calculated as:

$$V_j = T_b - V_{nc} \quad (3 - 16)$$

According to CSA A23.3-04 (Clause 21.5.4.1), the joint design shear force shall not exceed the following amount:

$$V_{jr} = 1.3\lambda\phi_c\sqrt{f'_c}A_j \quad (3 - 17)$$

Where V_{jr} is the maximum shear resistance of the unconfined exterior joint. CSA A23.3-04 (Clause 21.5.2.1) is also recommending that the transverse reinforcement provided for confinement at the end of columns, equation (3 – 12) or (3 – 13), shall be continued within the joints with the same spacing.

Appendix-A gives the design calculations of the test specimens reinforced with steel, CFRP and GFRP reinforcement.

3.3 MATERIAL PROPERTIES

3.3.1 Concrete

All test specimens were designed and constructed using normal weight, ready-mixed concrete with a targeted 28-day concrete compressive strength of 32 MPa with maximum aggregate size of 20 mm. All test prototypes were cast and wet-cured in the laboratory for 7 days. For ease of construction, all specimens were cast in a horizontal layout (on the

side). The actual concrete compressive and tensile strengths were determined based on the average value of compressive and tensile splitting tests carried out on standard cylinder specimens 100×200 mm and 150×300 mm, respectively. Table 3.1 shows the concrete compressive and tensile strengths at 7 days, 28 days and on the day of testing.

Table 3.1: Concrete material properties

Specimen Code *	7-day strength (MPa)		28-day strength (MPa)		Test-day strength (MPa)	
	compressive	Tensile	compressive	Tensile	compressive	Tensile
SS03-B06-J06	23.5	2.3	31.5	2.6	32.6	2.7
GG12-B11-J12	25	1.6	33.4	3.0	35.1	3.2
GG17-B11-J12	12.1	1.4	19.6	1.9	27.1	2.6
GG29-B11-J12	15.0	1.5	24.5	2.0	33.8	2.7
GS17-B11-J12	15.0	1.5	24.5	1.8	32.0	2.4
GG17-B07-J12	24.4	1.9	38.0	3.4	28.1**	2.1**
GG17-B11-J06	24.4	1.9	38.0	3.4	31.2**	2.3**
CG12-B11-J12	20.5	1.5	32.5	3.1	33.6	3.2

* Specimens' code explanation can be found on Page 66 of this thesis.

** These two specimens were tested before age of 28 days (14 and 18 days respectively).

3.3.2 Reinforcement

Three types of reinforcing bars were used in this study; CSA grade 400 deformed steel bars, sand-coated GFRP V-ROD™ and sand-coated CFRP V-ROD™ (Pultrall Inc. 2007). Two types of reinforcement stirrups were also used; CSA grade 400 deformed

steel stirrups and sand-coated GFRP C-shaped stirrups (Pultrall Inc. 2007). The mechanical properties of the used steel and FRP reinforcement which were used in the design process, as given by manufacturer, are shown in Tables 3.2 and 3.3. However, standard tests were performed on steel, GFRP and CFRP samples to confirm the manufacturers' values. The mechanical properties of these reinforcing bars were obtained from standard tests that were carried out according to CAN/CSA-S806-02 or ASTM A370-05, where appropriate. The obtained yield strength and yield strain of the used steel were 460 MPa and 0.0023, respectively. For GFRP reinforcement, the obtained properties were very close to those provided by the manufacturer. However, for CFRP bars, considerable inconsistency in the mechanical properties was found in the test results as will be explained later.

Table 3.2: Mechanical properties of the used steel bars and stirrups (Given by manufacturer)

Size	Diameter (mm)	Area (mm ²)	Modulus of Elasticity (GPa)	Yield Strength (MPa)	Ultimate Strain	Remarks
No. 10M	11.3	100	200	400	0.002	For the stirrups
No. 15M	15.9	200				Column main reinforcement
No. 20M	19.5	300				Beam main reinforcement

As shown in Table 3.3, GFRP No.10 and No.13 were used in form of C-shaped stirrups. Due to using a different manufacturing process to produce the FRP bent bars and stirrups; the tensile strength of the straight part of the FRP bent bar is less than its

pultruded counterpart. The manufacturer did not provide any information related to the tensile strength of the straight or the bend parts of these stirrups. However, these properties can be assumed based on the results of previous research (El-Sayed et al. 2007). The authors found that, for the same bar size, 75% of the typical tensile strength of the pultruded straight bars can be assumed for the straight part of the stirrups with reasonable accuracy. Accordingly, the tensile strengths of the straight part of the stirrups were considered equal to 642 and 590 MPa for GFRP stirrups No.10 and No.13, respectively.

In addition, considering the tensile strength of the straight parts, the tensile strength at the bend can be determined using ISIS Design Manual - Clause 10.3.2. Accordingly, the tensile strength of the bend part was found to be 50% of the tensile strength of the straight part of the stirrup. In this case, the tensile strength at the bend was calculated as 321 and 295 MPa for GFRP stirrups No.10 and No.13, respectively.

Table 3.3: Mechanical properties of the used FRP bars and stirrups (Given by manufacturer)

Size	Type	Diameter (mm)	Area (mm ²)	Tensile Modulus (GPa)	Tensile Strength (MPa)	Ultimate Strain	Remarks
No. 10	CFRP	9.5	71.3	124	1596	0.0140	main reinforcement
No. 10	GFRP	9.5	71.3	45.4	856	0.0189	For the stirrups
No. 13	GFRP	12.7	126.7	46.3	786	0.0170	For the stirrups
No. 16	GFRP	15.9	198	48.2	751	0.0156	main reinforcement
No. 19	GFRP	19.1	285	47.6	728	0.0153	main reinforcement

3.4 TEST SPECIMENS

Eight beam-column joint prototypes were constructed and tested to failure. Each prototype is simulating a beam-column connection taken from an exterior bay in a multi-bay, multi-story reinforced concrete moment-resisting plane frame. The span of the considered frame (bay length) is 4700 mm with a story height of 3650 mm. Each specimen represents a full-scale exterior connection between assumed contra flexural points in mid-height of the columns and mid-span of the beam. Figure 3.2 shows the overall dimensions of a typical test prototype where the beam is 2350 mm long with 350×450 mm in cross section and the column is 3650 mm high with cross section of 350×500 mm.

The variable parameters considered in this research are: type of longitudinal reinforcement bars, type of transverse reinforcement, beam longitudinal reinforcement ratio, beam transverse reinforcement ratio and joint reinforcement ratio and detailing, as shown in Table 3.4.

Three different materials; steel, GFRP and CFRP bars were used as longitudinal reinforcement. However, only steel and GFRP stirrups were used for the transverse reinforcement. Three reinforcement ratios, presented as multiples of the balanced reinforcement ratio, were tested; $1.20\rho_b$, $1.70\rho_b$ and $2.90\rho_b$. Furthermore, two different design standards; CSA S806-02 (CSA 2002) for building components and CSA S6-09 (CSA 2009) for bridge components were used for the shear design of the FRP-reinforced specimens, which resulted in two different beam transverse reinforcement ratios 1.10% and 0.70%, respectively. The effect of using inclined bars to replace some of the transverse stirrups within the joint was also tested. Accordingly, two different joint

reinforcement ratios were used; 0.60% and 1.20%. The corresponding reinforcement configuration for each specimen is shown in Table 3.5. Figure 3.3 shows the details of both steel and FRP reinforced specimens during construction.

The test prototypes were named based on the material of reinforcement as well as the reinforcement ratio in both longitudinal and transverse direction. The first two letters in the specimen name represents the reinforcement material of the longitudinal bars and the transverse stirrups, respectively; “G” for GFRP, “C” for CFRP and “S” for steel. The following 2-digit number represents the $\rho_{\text{actual}} / \rho_{\text{balance}}$ ratio for the beam flexural reinforcement. The letter “B” and the following 2-digit number represent the shear reinforcement ratio in the beam element. The last letter “J” and the following 2-digit number represent the shear reinforcement ratio in the joint area. For example, GS17-B06-J06 denotes a GFRP-reinforced specimen with steel stirrups, a beam flexural reinforcement ratio $\rho_{\text{actual}} / \rho_{\text{balance}} = 1.7$ and a shear reinforcement ratio of 0.6% for both beam and joint area.

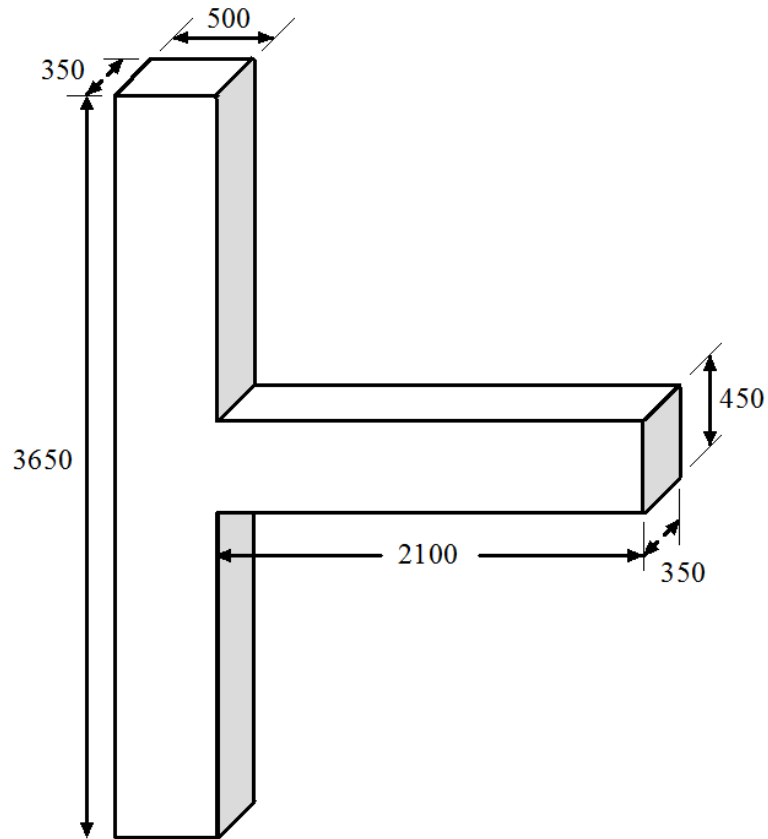


Figure 3.2: Geometry of beam-column joint specimens

Table 3.4: Specimens characteristics

Test Parameter Specimen Code	Longitudinal RFT Type	Type of Stirrups	Beam RFT ratio / Balanced Ratio	Beam Transverse Reinforcement Ratio	Joint RFT Ratio
SS03-B06-J06	Steel	Steel	0.30%	0.60%	0.60%
GG12-B11-J12	GFRP	GFRP	1.20%	1.10%	1.20%
GG17-B11-J12	GFRP	GFRP	1.70%	1.10%	1.20%
GG29-B11-J12	GFRP	GFRP	2.90%	1.10%	1.20%

GS17-B06-J06	GFRP	Steel	1.70%	0.60%	0.60%
GG17-B07-J12	GFRP	GFRP	1.70%	0.70%	1.20%
GG17-B11-J06	GFRP	GFRP	1.70%	1.10%	0.60%
CG12-B11-J12	CFRP	GFRP	1.20%	1.10%	1.20%

Table 3.5: Specimens reinforcement details

Specimen Code	Beam Reinforcement		Column Reinforcement	
	Bars (top & bottom)	Stirrups	Bars (distributed)	Stirrups
SS03-B06-J06	5 bars No.20M Steel	2-branche steel hoop No.10M@100 mm	8 bars No. 15M Steel	2-branche steel hoop No. 10M@90mm
GG12-B11-J12	5 bars No.16 GFRP	3-branche No.13 GFRP @100mm	8 bars No.16 GFRP	3-branche No.13 GFRP@90mm
GG17-B11-J12	5 bars No.19 GFRP	3-branche No.13 GFRP @100mm	8 bars No.19 GFRP	3-branche No.13 GFRP@90mm
GG29-B11-J12	8 bars No.19 GFRP	3-branche No.13 GFRP @100mm	12 bars No.19 GFRP	3-branche No.13 GFRP@90mm
GS17-B11-J12	5 bars No.19 GFRP	2-branche steel hoop No.10M@100 mm	8 bars No.19 GFRP	2-branche steel hoop No. 10M@90mm
GG17-B07-J12	5 bars No.19 GFRP	3-branche No.10 GFRP @85mm	8 bars No.19 GFRP	3-branche No.13 GFRP@90mm
GG17-B11-J06	5 bars No.19 GFRP	3-branche No.13 GFRP @100mm	8 bars No.19 GFRP	3-branche No.13 GFRP@180mm + 4 inclined bars No. 19 GFRP
CG12-B11-J12	7 bars No.10 CFRP	3-branche No.13 GFRP @100mm	12 bars No.10 CFRP	3-branche No.13 GFRP@90mm



SS03-B06-J06 reinforcement cage



GG12-B11-J12 reinforcement cage



GG17-B11-J12 beam reinforcement



GG17-B11-J12 column reinforcement



GG29-B11-J12 beam reinforcement



GG29-B11-J12 column reinforcement



GS17-B11-J12 beam reinforcement



GG17-B11-J06 joint detailing



Test prototype during curing



Test prototype after casting and curing

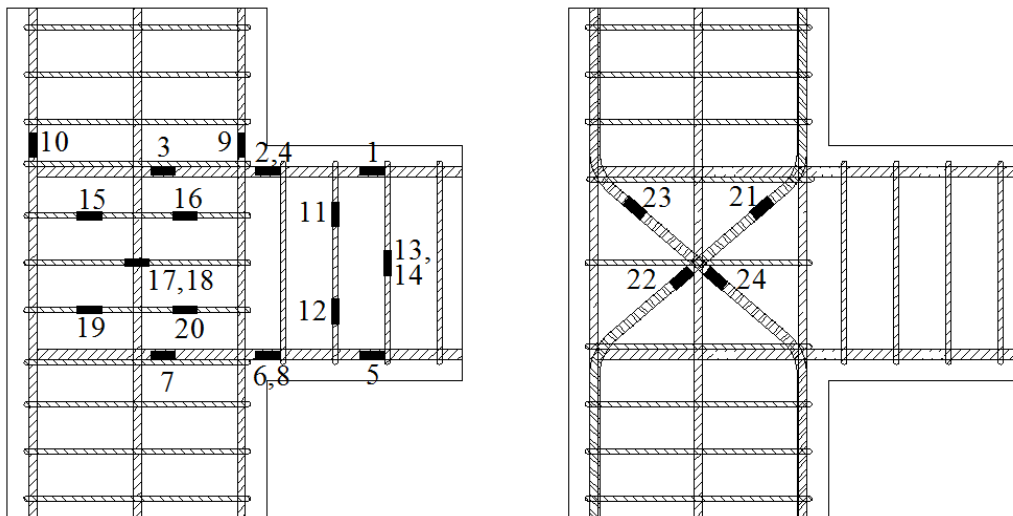
Figure 3.3: Construction details of beam-column joint test prototypes

3.5 INSTRUMENTATIONS

All specimens in this research were instrumented internally and externally with electrical resistance strain gauges and linear variable differential transformers (LVDTs), respectively. The instrumentations were installed at the critical locations shown in Figures 3.4 and 3.5 in order to measure the developed strains and displacements. Two longitudinal bars from each side of the beam were instrumented with strain gauges to measure the variation of strains along the length of the beam bars within the critical

region. Three strain gauges were attached to one of these bars; one strain gauge at the column face, one at a distance of 200 mm ($\approx d/2$) inside the joint and the third one at a distance of 200 mm away from the column face (inside the beam). The second beam bar was instrumented with one strain gauge as a replicate for the measurements at the column face. Also, two opposite bars at the column corners were instrumented with one strain gauge on each to measure the developed strains at the beam face.

In addition, three transverse reinforcement stirrups inside the joint were instrumented with two strain gauges on each. Two strain gauges were installed on each of the last two critical stirrups in the beam, as shown in Figure 3.4. Except for specimen GG17-B11-J06, a total of 20 strain gauges were installed in each specimen as shown in Figure 3.4-a. For specimen GG17-B11-J06, four additional strain gauges were attached to the inclined bars inside the joint to capture the strain profile along these bars as shown in Figure 3.4-b.



a- All tested specimens

b- extra strain gauges for specimen GG17-B11-J06

Figure 3.4: Position of strain gauges

During testing, each specimen was instrumented with eight LVDTs to measure the beams and columns rotations, and the joint distortion, as shown in Figure 3.5. The LVDTs were arranged in pairs at four locations in the vicinity of the joint. One pair was attached to the column at the boundaries of the joint (Figure 3.5a). Other two pairs were attached to the beam sides to measure the different types of beam rotations, as shown in Figure 3.5-b. The last pair was installed diagonally on the joint area (Figure 3.5c). The difference between the readings for any of the first three pairs of LVDTs divided by their spacing would give the rotation value in radian units. The joint distortion value (γ) can be calculated from the fourth pair of LVDTs' readings as shown in Figure 3.6 by substituting in the following equation:

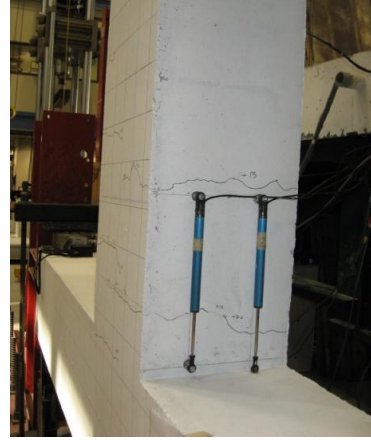
$$\gamma = \frac{\delta - \delta'}{2l} (\tan \alpha + \cot \alpha) \quad (3 - 18)$$

Where δ and δ' are the readings of LVDTs where elongations have positive sign, l is the initial distance between mounting rods, and α is the initial inclination of LVDTs to the horizontal or the vertical.

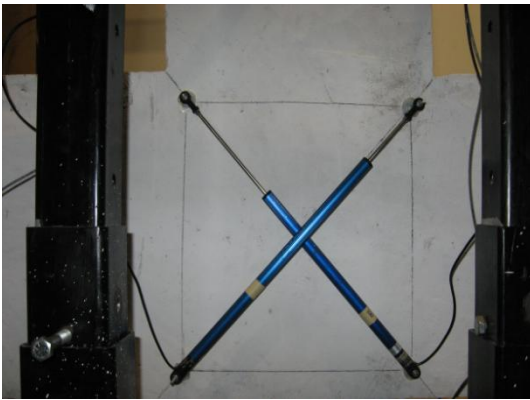
Also, two high-accuracy (± 0.001 mm) LVDTs were installed on each specimen. The first was at the location of first crack to measure crack width, while the second was at the end of one of the beam bars to measure slippage, if any, as shown in Figure 3.5-d and e respectively.



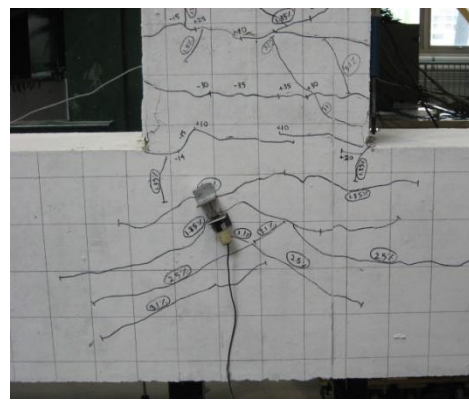
(a) Column rotation



(b) Beam rotations



(c) Joint distortion



(d) Crack width



(e) Bar slippage

Figure 3.5: Positions of LVDTs

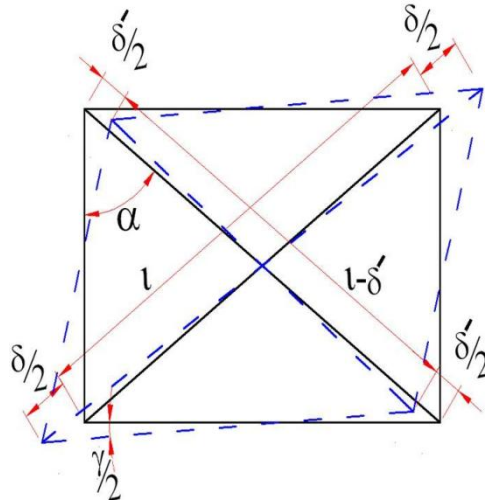


Figure 3.6: Estimation of joint shear distortion

Two load cells were used to monitor the column axial load and the vertical reaction at one of the column ends during the test, as shown in Figure 3.7. A data acquisition system, monitored by a computer, was programmed to record the readings of all strain gauges, LVDTs and the load cells.



a- Column axial load cell

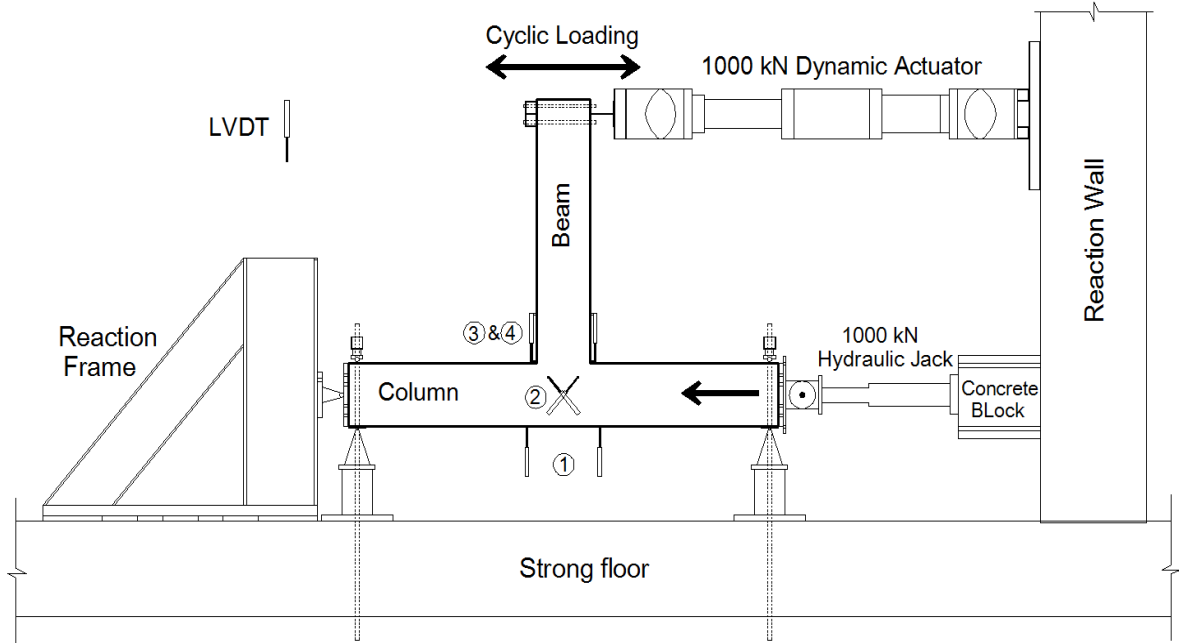


b- Column reaction load cell

Figure 3.7: Positions of load cells

3.6 TEST SET-UP AND PROCEDURE

All specimens were tested while the column was lying horizontally and the beam was standing vertically; 90-degree rotated position from the actual condition. The cyclic load was applied at the tip of the beam as shown in Figure 3.8. A fully-dynamic actuator, 1000 kN capacity and ± 250 mm stroke, was positioned horizontally against a strong reaction wall, as shown in Figure 3.9-a. The actuator was bolted to the tip of the beam to apply the seismic loading scheme, as shown in Figure 3.9-b.



(a) Schematic drawing - front view



(b) Photo of the set-up

Figure 3.8: Test setup



a- Actuator-to-wall connection



b- Actuator-to-specimen connection

Figure 3.9: Dynamic actuator photos

A 1000 kN-capacity hydraulic jack was positioned horizontally at one of the column ends at the centre of the column cross section to apply a constant axial compression force to the columns during testing, as shown in Figure 3.10. A heavy strong reaction steel frame was pre-stressed to the strong floor at the other end of the column to react the column load, as shown in Figure 3.11.



Figure 3.10: Hydraulic jack



Figure 3.11: Steel reaction frame

The two ends of the column were restrained against both vertical and horizontal displacements meanwhile their rotations were allowed (hinged boundary conditions). These boundary conditions were achieved through supporting the columns in the vertical direction over two roller supports, one at each end. Also, each end was tied down to the strong floor to prevent displacements, as shown in Figure 3.12.



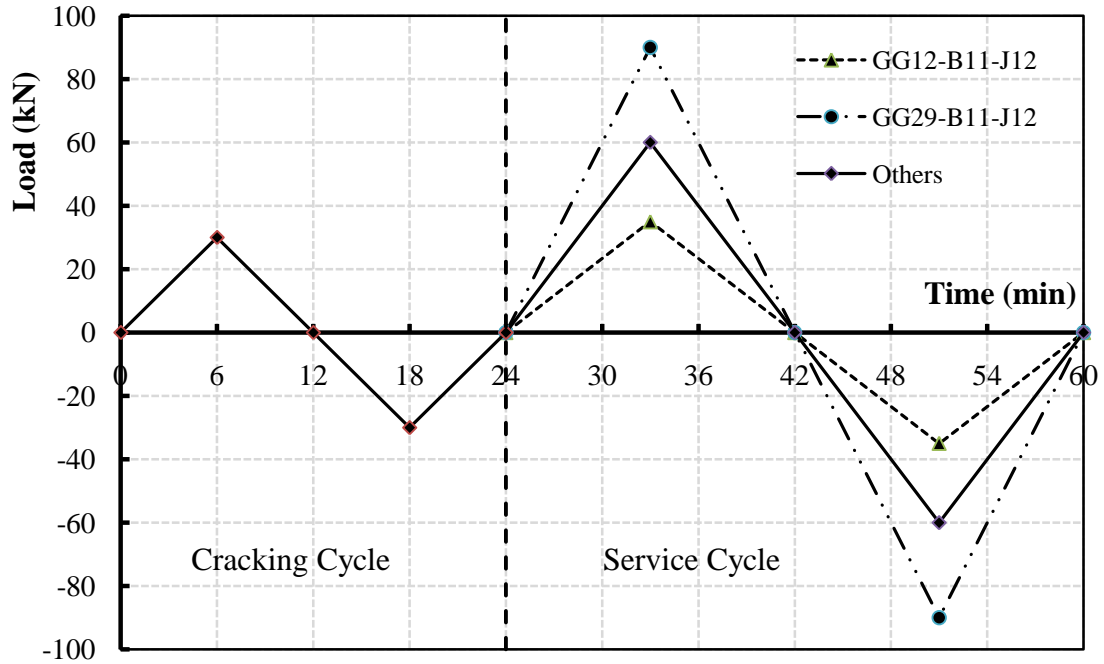
Figure 3.12: Column roller support

The loading procedure for all specimens consisted of two phases. It started with a load-controlled phase followed by a displacement-controlled one. During the load-controlled phase, two load cycles were applied; the first cycle was to determine the cracking load, while the second cycle was corresponding to the service limit state. The cracking load was calculated to be approximately 25 kN and therefore, one cycle with a peak load of 30 kN was applied to all specimens. The peak load of the second cycle was different for each specimen, based on code definitions. The service level for the steel-reinforced specimen (SS03-B06-J06) was considered at 60% of steel yielding strain (CSA 2004). However, for the FRP-reinforced specimens, it is corresponding to 25% and 60% of the ultimate tensile strength of GFRP and CFRP bars, respectively, according to CSA S6-09 - Clause 16.8.3 (CSA 2009). The specimens were loaded until reaching the calculated service strain levels as shown in Figure 3.13-a. It should be noted here that the steel-reinforced specimen, SS03-B06-J06, was tested first to obtain the beam yielding load, P_y , and its corresponding displacement Δ_y . Once the cracking and service loads

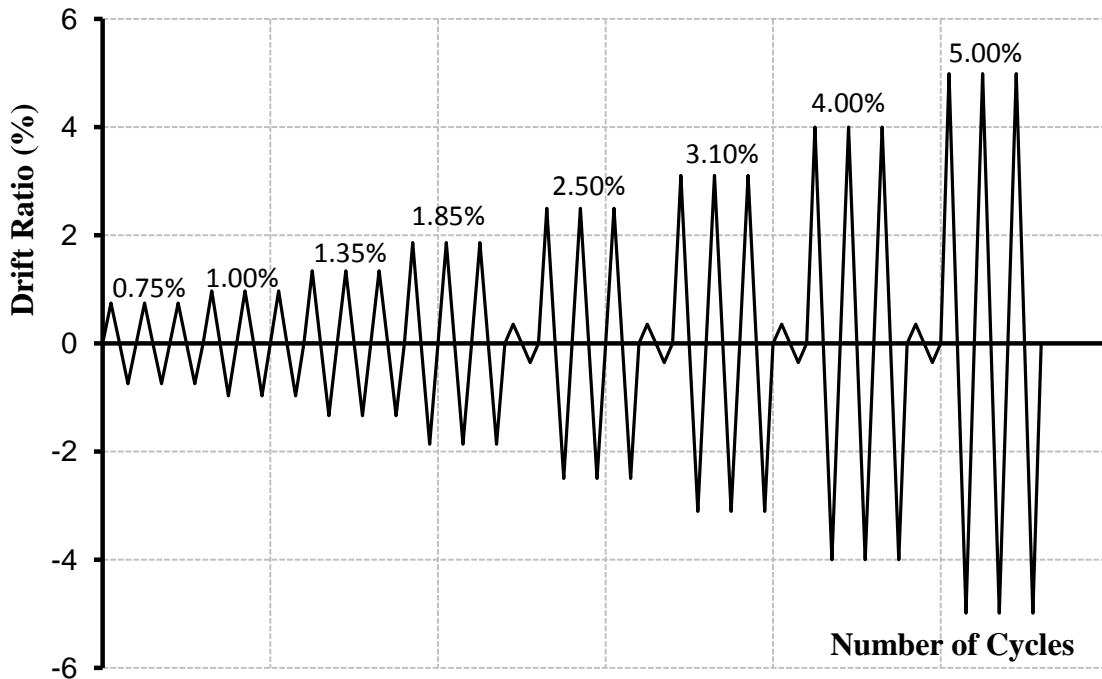
were obtained, the values of P_y and Δ_y were calculated considering linear behaviour of load-deflection graph up to yielding. Appendix-B gives the calculations for the cracking and service cycles for all specimens.

The second phase followed the recommendations of the ACI Committee 374 report on the acceptance criteria for moment frames based on structural testing (ACI 2005). This criteria has been adopted by many researchers (Hakuto et al. 2000; Ghobarah and El-Amoury 2005; Chun et al. 2007). In this second phase, the seismic loading was applied in several steps under displacement-control mode at a quasi-static rate of 0.01 Hz. Each loading step consisted of three identical displacement cycles applied to the beam end, following the history shown in Figure 3.13-b. In the first step, the displacement amplitude was equal to Δ_y . Then, the displacement amplitude of each subsequent step was a multiplier of Δ_y ; $1.3(\Delta_y)$, $1.8(\Delta_y)$, $2.5(\Delta_y)$, $3.35(\Delta_y)$, $4.17(\Delta_y)$, $5.37(\Delta_y)$ and $6.7(\Delta_y)$. The corresponding drift ratios for these displacements, calculated as the horizontal displacements of the beam end divided by the distance between the point of load application and the column centerline, are shown in Figure 3.13-b. After the completion of the fourth seismic loading step (drift ratio of 1.85%), one load-controlled cycle with a peak load equals to the service load was applied to evaluate the loss in stiffness due to load cycles, if any. Identical loading scheme, considering Δ_y , was applied to FRP-reinforced specimens. Appendix-C gives the detailed loading procedure for all specimens.

Following each loading step, the crack development and propagation was clearly marked on the concrete surface and several photos were taken to document the cracking patterns.



(a) Load-controlled phase (Phase 1)



(b) Displacement-controlled phase (Phase 2)

Figure 3.13: Loading history consequence

CHAPTER 4

EXPERIMENTAL RESULTS

4.1 GENERAL

The objective of this chapter is to summarize the experimental results for all tested specimens. The performance of the specimens is assessed and discussed in terms of cracking pattern and mode of failure, hysteretic behaviour, strain measurements, cumulative energy dissipation, rotation measurements and reinforcement behaviour under reversed-cyclic loading. The cracking pattern, mode of failure and hysteretic response are discussed individually for each specimen. However, for better understanding, other result aspects are presented in a comparison approach.

4.2 TEST RESULTS AND OBSERVATIONS

4.2.1 Cracking Pattern and Mode of Failure

4.2.1.1 Specimen SS03-B06-J06

Figure 4.1 shows the cracking patterns at different loading stages for specimen SS03-B06-J06. In the first two loading steps (0.75% and 1.00%), the cracks were distributed along half the length of the beam (Figure 4.1-a). Starting at 1.85% drift level, the intensity of cracks was increased in the plastic hinge zone (the zone extended from the column face to a distance equal to the beam depth), which in turn resulted in causing a permanent damage in this zone at 2.50% drift level. The width of these permanent cracks kept increasing in the higher loading steps (3.10% and 4.00%) as shown in Figure 4.1-b and c. No significant cracks appeared in the column or in the joint area. The observed mode of failure for that specimen was a concrete crushing at 5.00% drift ratio due to

excessive deformation in the beam (buckling of steel bars in compression), as shown in Figure 4.1-d.

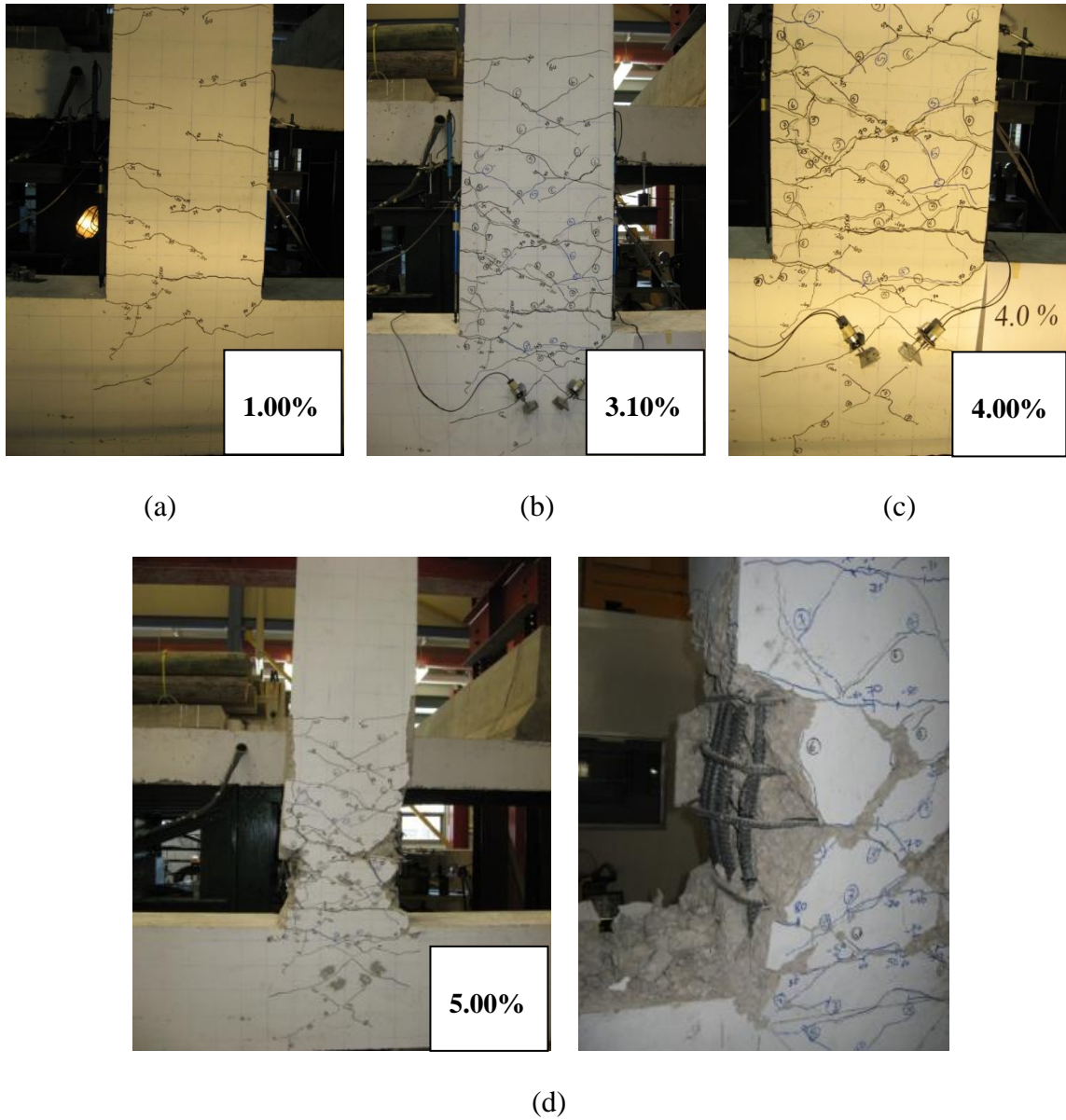
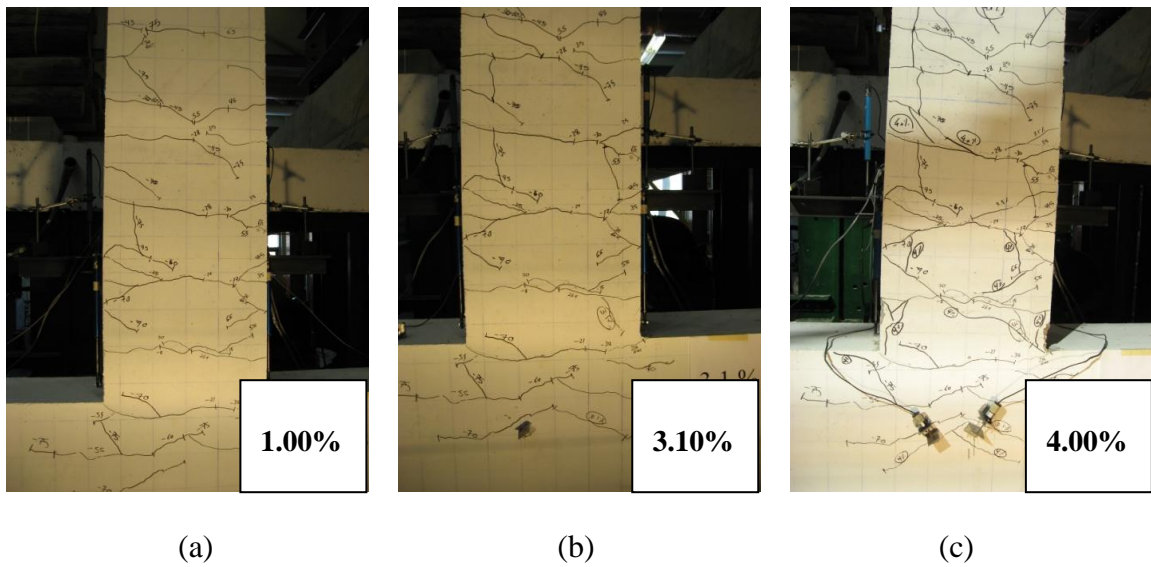
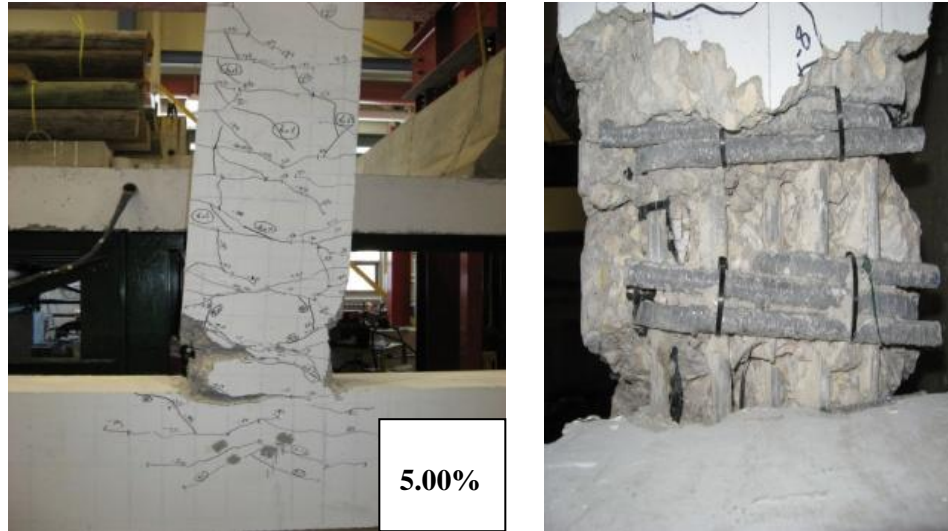


Figure 4.1: Cracking sequence of specimen SS03-B06-J06

4.2.1.2 Specimen GG12-B11-J12

Figure 4.2 shows the cracking patterns at different loading stages for specimen GG12-B11-J12. Uniform cracks distribution was observed along the whole beam length till the end of the test. The intensity of cracks did not increase in the virtual plastic hinge zone (near the column face) till the end of the 4.00% drift level (Figure 4.2-a, b and c). Also, no significant cracks (only hair cracks) appeared in the column or in the joint till the end of the test. The observed mode of failure for this specimen was a concrete crushing immediately followed by rupture of the beam GFRP bars at 5.00% drift ratio, as shown in Figure 4.2.d. This may be due to the low ratio of $\rho_{FRP} / \rho_b = 1.2$.





(d)

Figure 4.2: Cracking sequence of specimen GG12-B11-J12

4.2.1.3 Specimen GG17-B11-J12

Figure 4.3 shows the cracking patterns at different loading stages for specimen GG17-B11-J12. Similar to GG12-B11-J12, uniform cracks distribution was observed along the whole beam length till the end of the test. The intensity of cracks did not increase in the virtual plastic hinge zone (near the column face) till the end of 3.10% drift level (Figure 4.2-a and b). Also, no significant cracks (only hair cracks) appeared in the column or in the joint till the end of the test. Compared to specimen GG12-B11-J12, the failure of specimen GG17-B11-J12 was quite gradual starting with a concrete crushing at 4.00% drift ratio followed by a rupture of the beam bars at 5.00% drift level, as shown in Figure 4.3.c and d. This may be due to the higher ratio of $\rho_{FRP} / \rho_b = 1.7$ for specimen GG17-B11-J12.

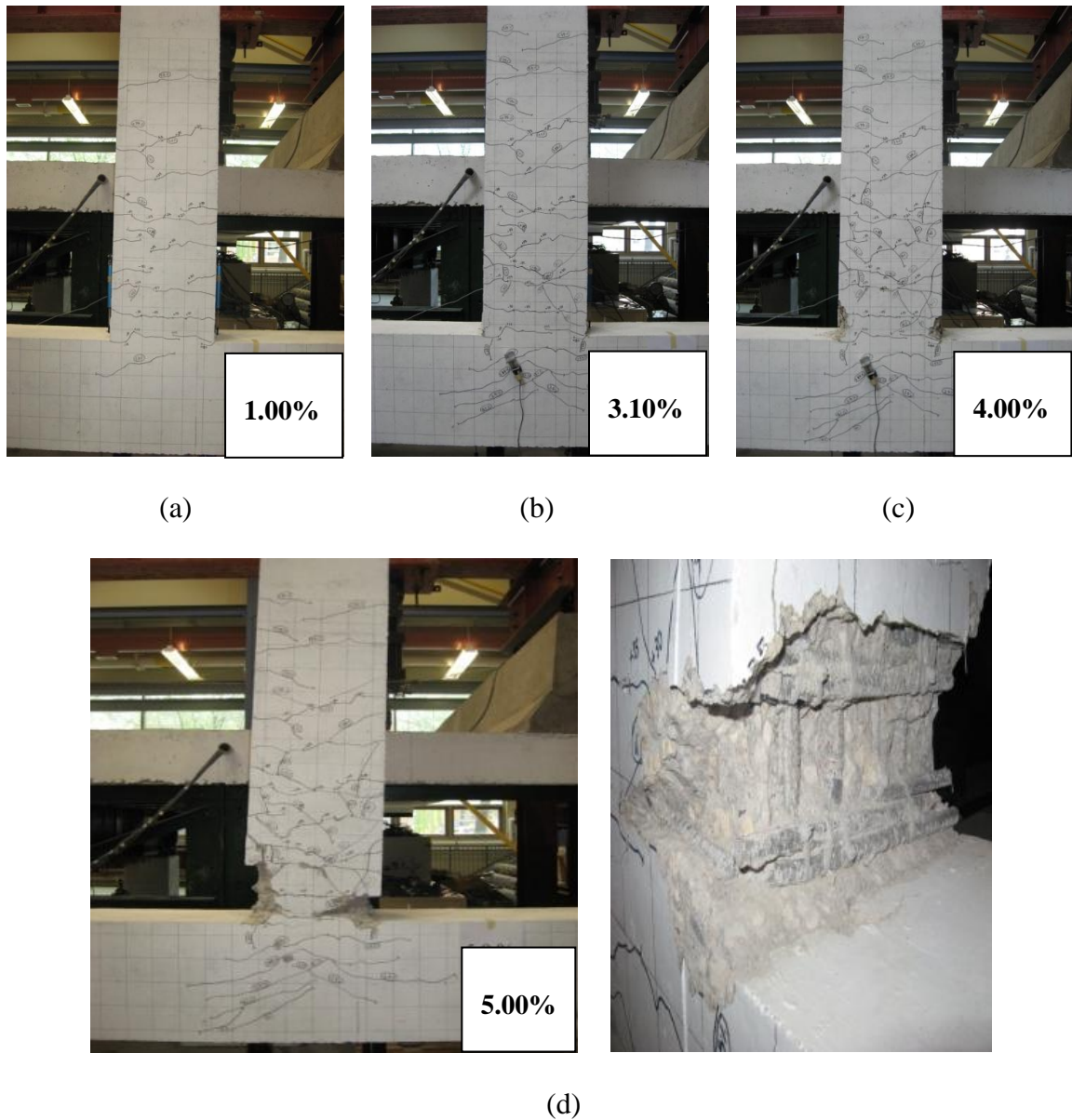


Figure 4.3: Cracking sequence of specimen GG17-B11-J12

4.2.1.4 Specimen GG29-B11-J12

Figure 4.4 shows the cracking patterns at different loading stages for specimen GG29-B11-J12. Uniform cracks distribution was observed along the whole beam length till 1.85% drift level. Starting at 2.50% drift ratio, large number of diagonal shear cracks appeared in the joint area and the penetration of these cracks was increasing till 3.10%

drift level (Figure 4.4- b). At 4.00% drift ratio, the cracks became wider and started to propagate toward the far edge of the column accompanied with concrete cover spalling from the beam (Figure 4.4- c). Finally, specimen GG29-B11-J12 failed in the joint area at 5.00% drift ratio (test stopped), as shown in Figure 4.4-d.

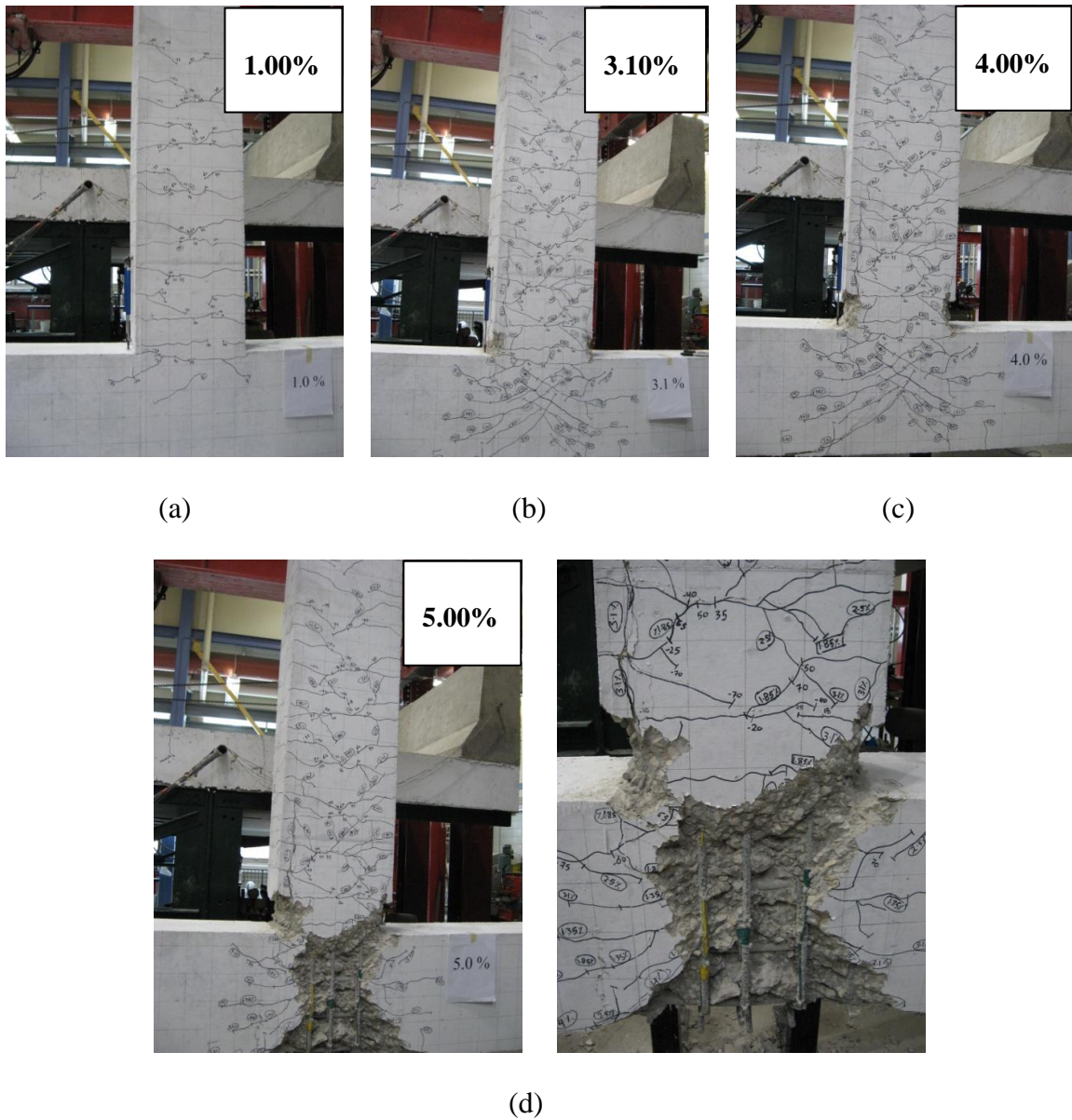
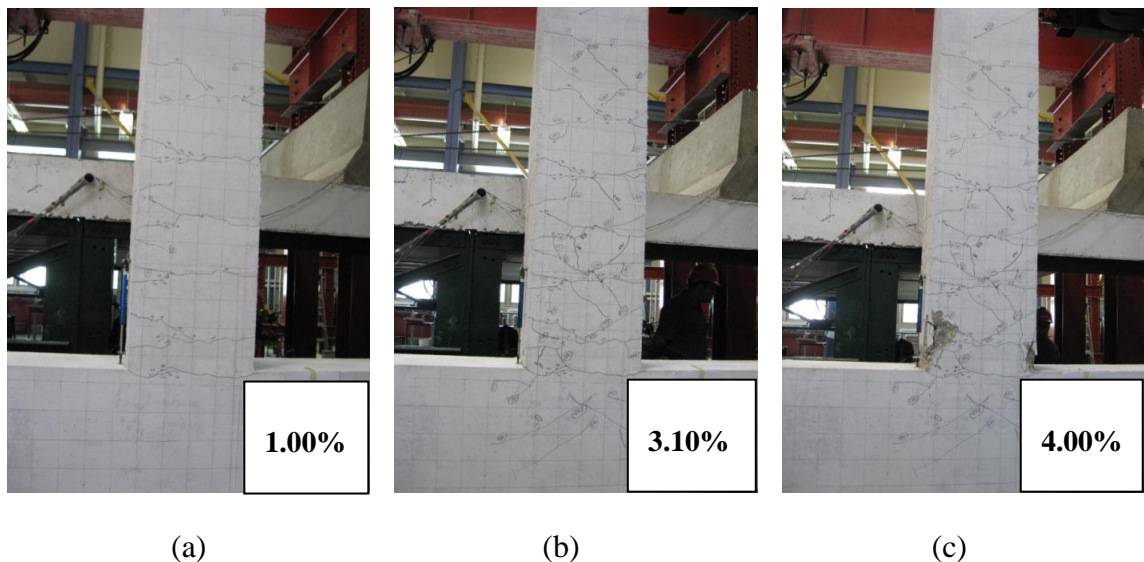


Figure 4.4: Cracking sequence of specimen GG29-B11-J12

4.2.1.5 Specimen GS17-B11-J12

Figure 4.5 shows the cracking patterns at different loading stages for specimen GS17-B11-J12. Uniform cracks distribution was observed along the whole beam length till the end of the test. The intensity of cracks did not increase in the virtual plastic hinge zone (near the column face) till the end of 3.10% drift level (Figure 4.5-a and b). Also, no significant cracks (only hair cracks) appeared in the column or in the joint till the end of the test. The failure occurred gradually starting by spalling of concrete cover at 4.00% drift ratio (Figure 4.5-c), followed by complete concrete crushing combined with partial rupture for one GFRP bar at 5.00% drift ratio. The first bar was completely ruptured (test stopped) after completing the first cycle of the 6.50% drift ratio, as shown in Figure 4-5-d.



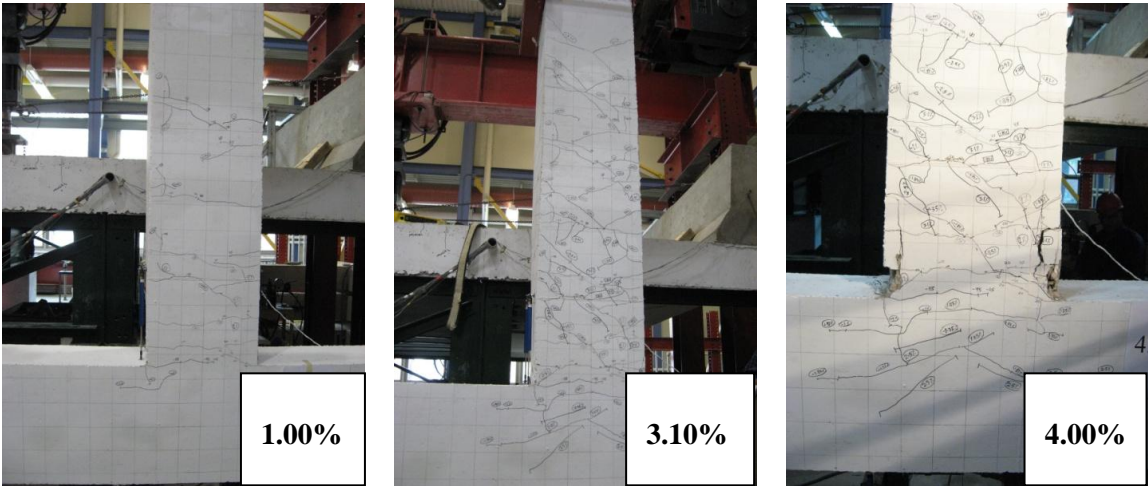


(d)

Figure 4.5: Cracking sequence of specimen GS17-B11-J12

4.2.1.6 Specimen GG17-B07-J12 and Specimen GG17-B11-J06

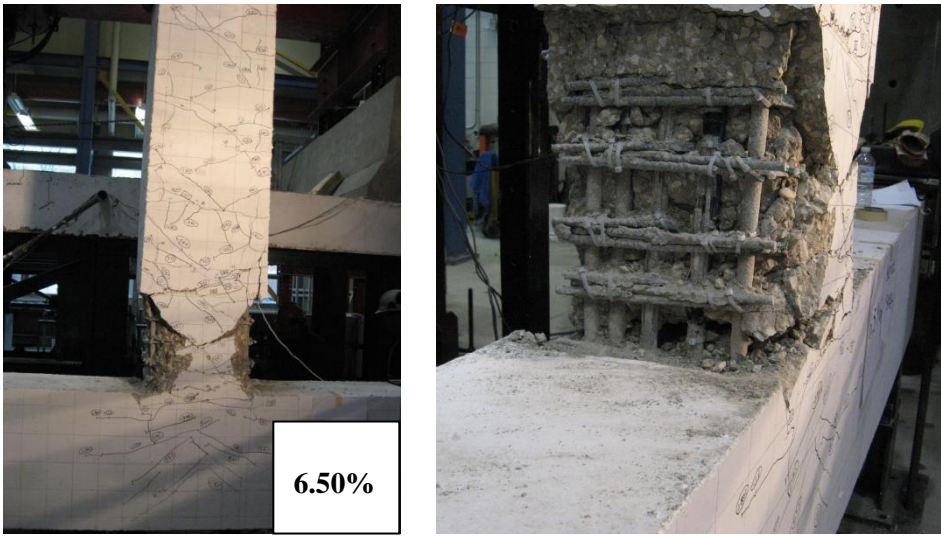
Similar behaviour was observed for both specimens, GG17-B07-J12 and GG17-B11-J06. Figures 4.6 and 4.7 show the cracking patterns at different loading stages for both specimens, respectively. Uniform crack distribution was observed along the whole beam length till the end of the test. The intensity of cracks did not increase in the virtual plastic hinge zone (near the column face) till the end of 3.10% drift level (Figure 4.5-a and b and Figure 4.6-a and b). Also, no significant cracks (only hair cracks) appeared in the column or in the joint till the end of the test. The failure occurred gradually starting by spalling of concrete cover at 4.00% drift ratio (Figure 4.6-c and Figure 4.7-c), followed by concrete crushing at 5.00% drift ratio. The beam bars started to rupture at the first cycle of the 6.50% drift ratio loading step for both specimens GG17-B07-J12 and GG17-B11-J06, as shown in Figures 4.6-d and 4.7-d, respectively.



(a)

(b)

(c)



(d)

Figure 4.6: Cracking sequence of specimen GG17-B07-J12

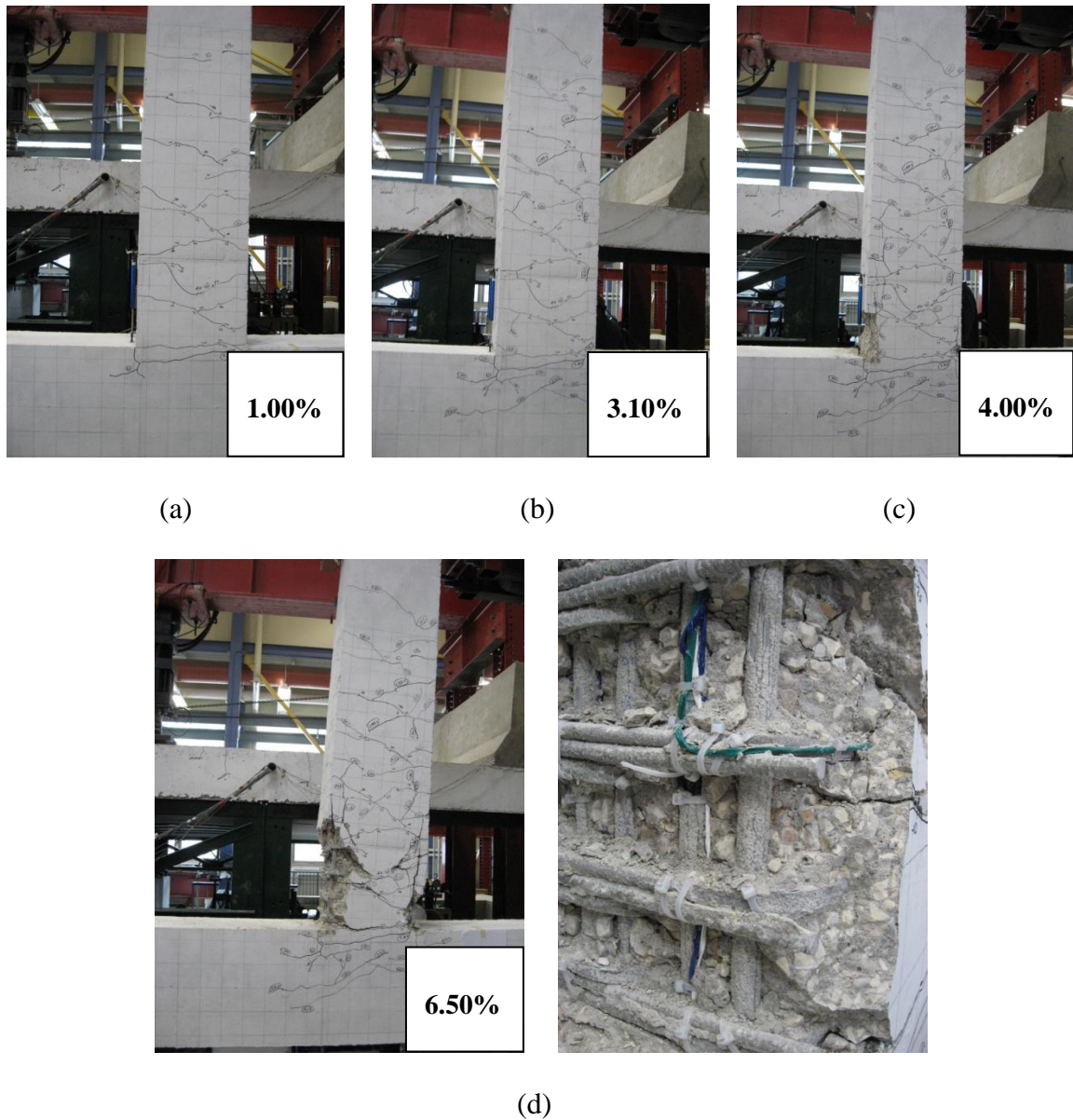


Figure 4.7: Cracking sequence of specimen GG17-B11-J06

4.2.1.7 Specimen CG12-B11-J12

For specimen CG12-B11-J12, a premature failure occurred at early stages (1.85% drift) due to slippage of the beam bars followed by bars rupture in dowel action, as shown in Figure 4.8. Following this unexpected behaviour, pullout and tensile tests were carried out on CFRP bars in order to evaluate the bond stress and the tensile characteristics of

these bars. The average bond stress obtained for five carbon segments cut from one bar was 7.5 MPa, as shown in Figure 4.9. This obtained bond strength is much less than that given by the manufacturer (16.5 MPa). Furthermore, the results obtained from the tensile tests carried on five carbon segments cut from one bar were not consistent, as shown in Figure 4.10. These inconsistent and low characteristics of the CFRP bars well-explain the observed behaviour of specimen CG12-B11-J12. Accordingly, it was decided not to include the results of this specimen in further analysis or discussion.

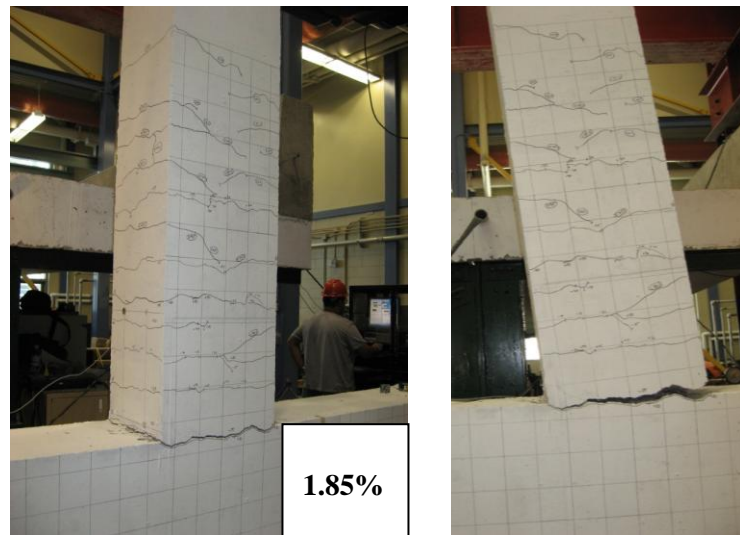


Figure 4.8: Mode of failure of specimen CG12-B11-J12

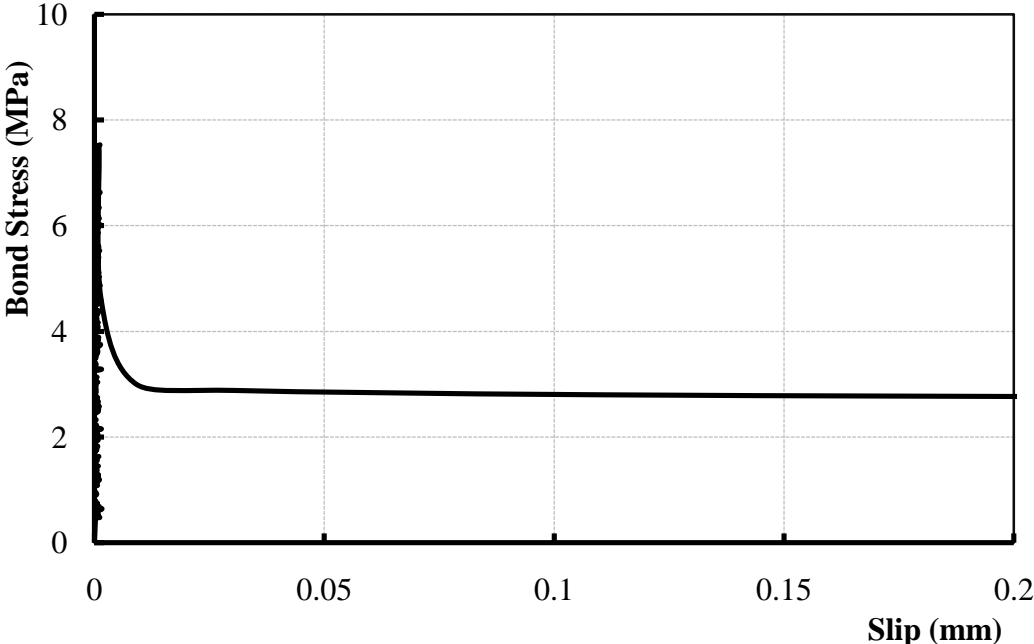


Figure 4.9: Bond stress-slip relationship for CFRP bars

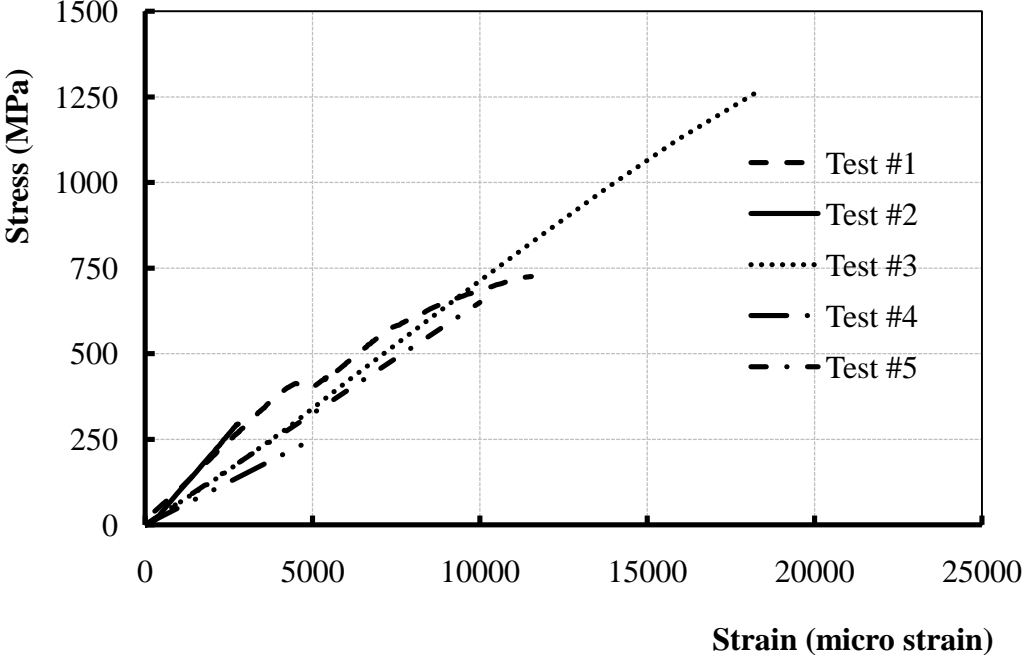


Figure 4.10: Stress-strain relationship for CFRP bars

Table 4.1 shows a comparison between the theoretical and experimental values for the cracking, service and ultimate capacity for each specimen in addition to the corresponding mode of failure as well.

Table 4.1: Summary of test results

Specimen	Cracking Load (kN)		Service load (kN)		Ultimate capacity (kN)		Mode of failure
	Theo.	Exp.	Theo.	Exp.	Theo.	Exp.	
SS03-B06-J06	25	25	64	60	137	178	Excessive deformation due to beam bars yielding
GG12-B11-J12	21	25	35	35	120	131	Balanced failure (concrete crushing / bar rupture)
GG17-B11-J12	21	22	49	57	136	150	Concrete crushing followed by bar rupture
GG29-B11-J12	21	18	71	89	152	173	Joint degradation
GS17-B11-J12	21	20	49	58	136	150	Concrete crushing followed by bar rupture
GG17-B07-J12	21	21	49	57	136	167	Concrete crushing followed by bar rupture
GG17-B11-J06	21	17	49	60	136	178	Concrete crushing followed by bar rupture
CG12-B11-J12	21	19	98	72	136	74	Bond slippage followed by bars rupture

In general, compared to specimen SS03-B06-J06, more uniform cracks were observed along the full beam length for all GFRP-reinforced specimens as shown in Figure 4.1 to Figure 4.7. Also, it was observed that, between loading steps (no load), these cracks would almost close without significant residual deformations. This was

expected due to the elastic behaviour and the bond characteristics of the used sand-coated GFRP bars.

Furthermore, based on the results of a previous study by the authors (Mady et al. 2010), it was found that an embedment length of 20 times bar diameter was not enough to prevent the GFRP beam bars from slippage under reversal loading. Therefore, the actual embedment length used in this study was 24 times bar diameter for all GFRP-reinforced specimens, except for specimen GG12-B11-J12; the embedment length was 30 times bar diameter. According to the LVDT readings, no slippage of the beam bars was observed before failure for all GFRP-reinforced specimens. This indicates that embedment length of 24 times bar diameter ($24d_b$) seems to be adequate to transfer the beam bars forces to the joint under cyclic loading. Further investigations are required regarding the bond behaviour of the GFRP bars subjected to cyclic loading.

4.2.2 Hysteretic Behaviour

Figure 4.11 through Figure 4.17 show the load on the beam end at each seismic loading step versus lateral drift. Except for the last loading step, the first two cycles in each loading step were eliminated from the graphs for clarity.

4.2.2.1 Specimen SS03-B06-J06

For the steel-reinforced specimen, SS03-B06-J06, the load-drift relationship indicates that the steel-reinforced specimen reached the maximum lateral load carrying capacity (178 kN) at the first cycle of the 5.0% drift ratio loading step, and then this capacity started to decrease. It is worth mentioning that the experimentally obtained capacity is higher than the design capacity (137 kN) due to strain hardening phenomenon and higher

yield strength of steel reinforcement than that given by manufacturer (used in design). Considering the experimentally obtained yielding stress for the used steel bars, the corresponding ultimate capacity would be 156 kN. In addition, up to 1.0% drift level, neither significant pinching length nor stiffness loss was observed. However; starting at 1.35% drift level up to the maximum reached drift level of 5.0%, pinching length was increasing gradually, which indicates the capability of the specimen to dissipate energy, in addition to a gradual decrease in the overall stiffness as shown in Figure 4.11.

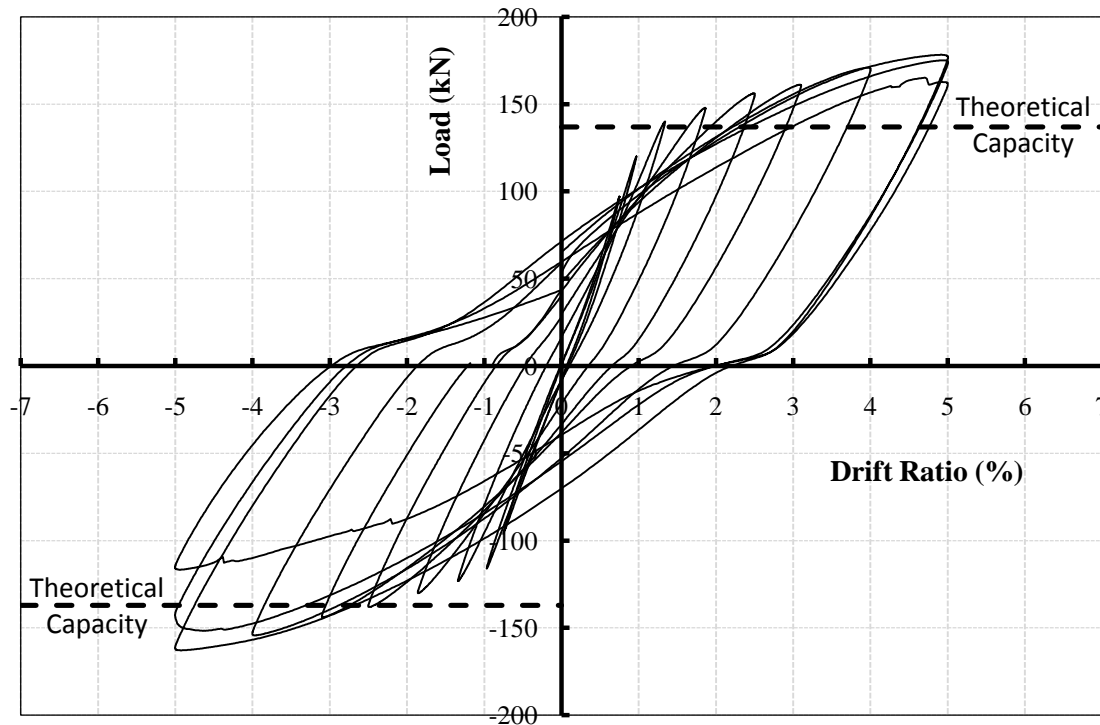


Figure 4.11: Hysteretic load-drift ratio relationship of specimen SS03-B06-J06

4.2.2.2 Specimen GG12-B11-J12

For specimen GG12-B11-J12, the lateral load capacity continued to increase up to failure at 131 kN and 5.0% drift ratio. This obtained capacity was higher than the design

capacity by approximately 8%. In addition, no significant pinching length appeared through the whole test and the behaviour of the specimen was linear-elastic without any significant stiffness degradation observed up to failure as shown in Figure 4.12.

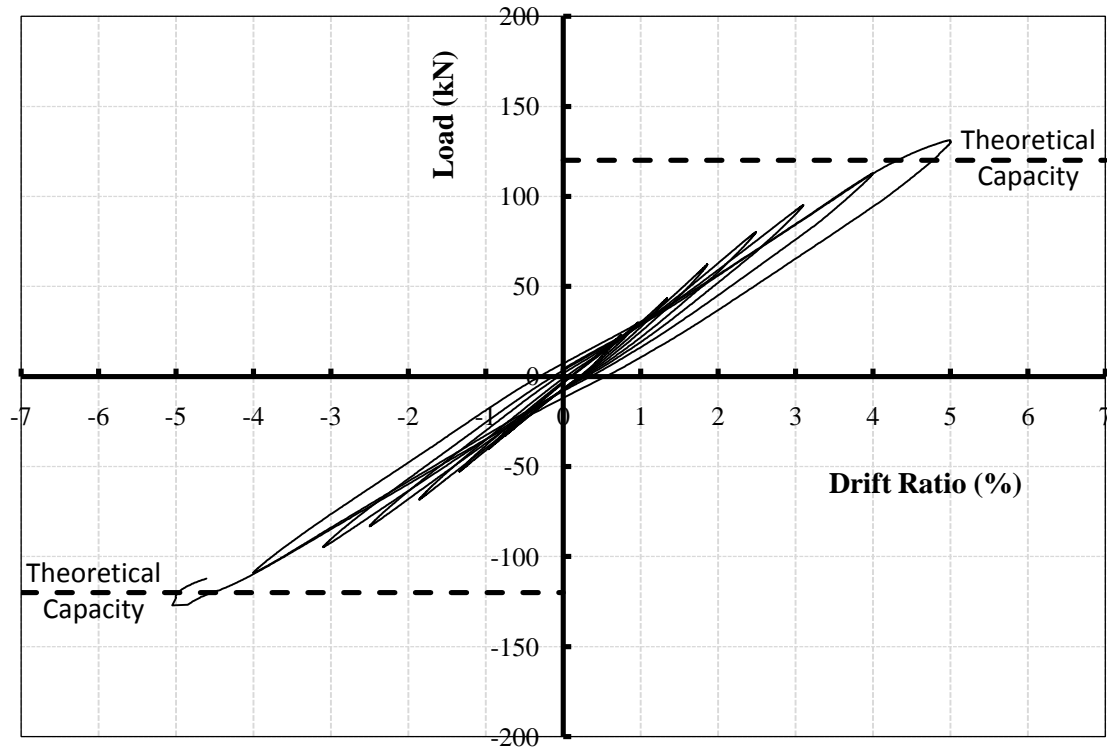


Figure 4.12: Hysteretic load-drift ratio relationship of specimen GG12-B11-J12

4.2.2.3 Specimen GG17-B11-J12

For specimen GG17-B11-J12, the load-drift relationship indicates that the specimen started to fail at a drift level of 4.0%, where the lateral load capacity started to decrease. The maximum measured capacity was 150 kN, which is approximately 9% higher than the design capacity. The behaviour of the specimen remained linear-elastic without significant pinching length up to the 3.1% drift level. Differently from specimen GG12-

B11-J12, a gradual decrease in the overall stiffness combined with an increase in pinching length was observed up to failure, as shown in Figure 4.13.

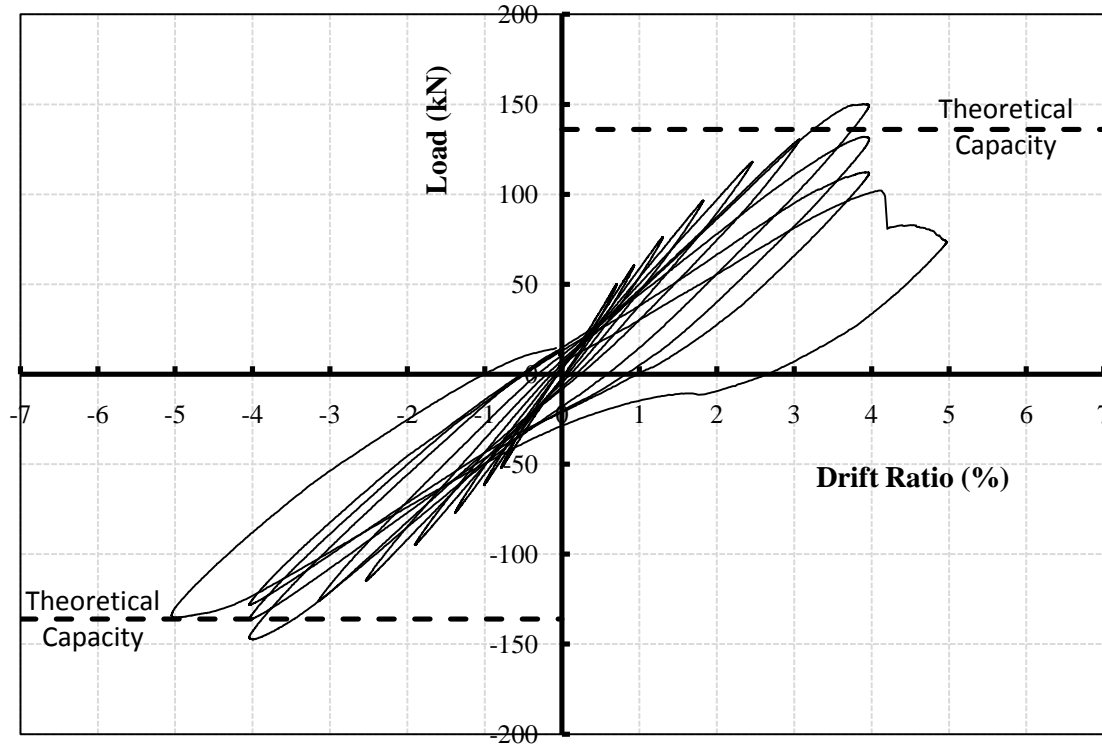


Figure 4.13: Hysteretic load-drift ratio relationship of specimen GG17-B11-J12

4.2.2.4 Specimen GG29-B11-J12

For specimen GG29-B11-J12, the load-drift relationship indicates that the specimen reached the maximum lateral load carrying capacity (173 kN) at the first cycle of the 4.0% drift ratio loading step, and then this capacity started to decrease. This obtained capacity was higher than the design capacity by approximately 12%. In addition, no significant pinching length appeared up to 3.1% drift level, as shown in Figure 4.14.

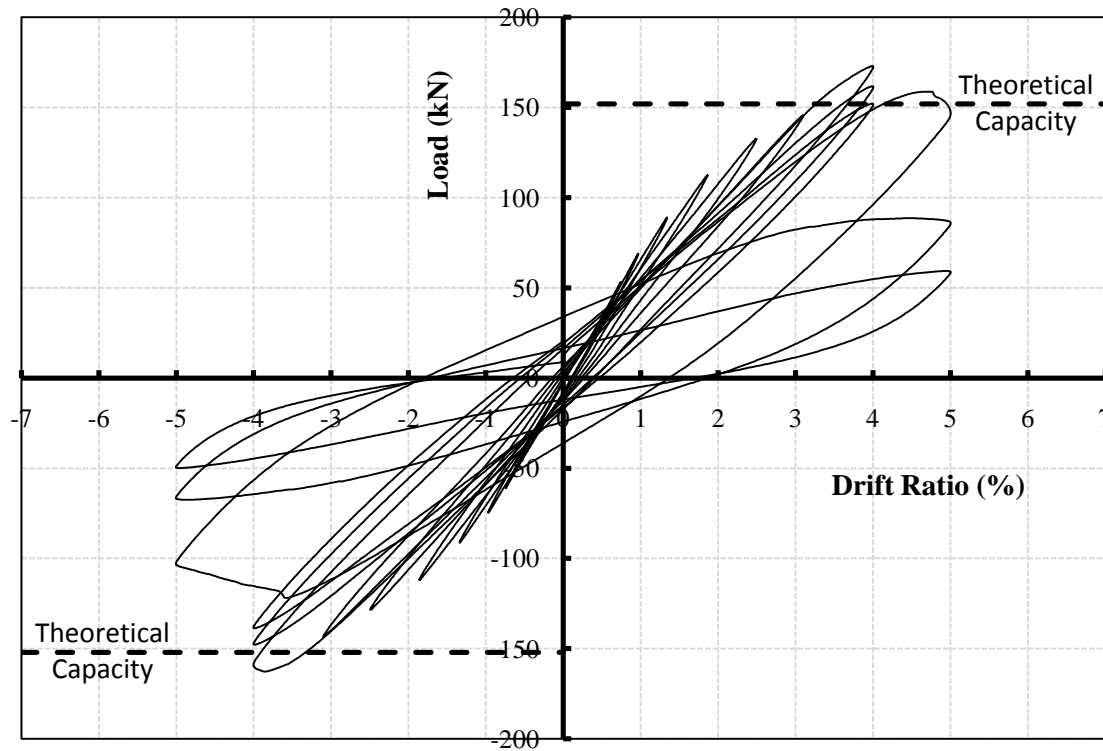


Figure 4.14: Hysteretic load-drift ratio relationship of specimen GG29-B11-J12

4.2.2.5 Specimen GS17-B11-J12

For specimen GS17-B11-J12, the load-drift relationship indicates that the specimen reached the maximum lateral load carrying capacity (150 kN) at the first cycle of the 5.0% drift ratio loading step, and then this capacity started to decrease. Similar to specimen GG17-B11-J12, the obtained capacity was approximately 9% higher than the design capacity. In addition, no significant pinching length appeared until failure started as shown in Figure 4.15.

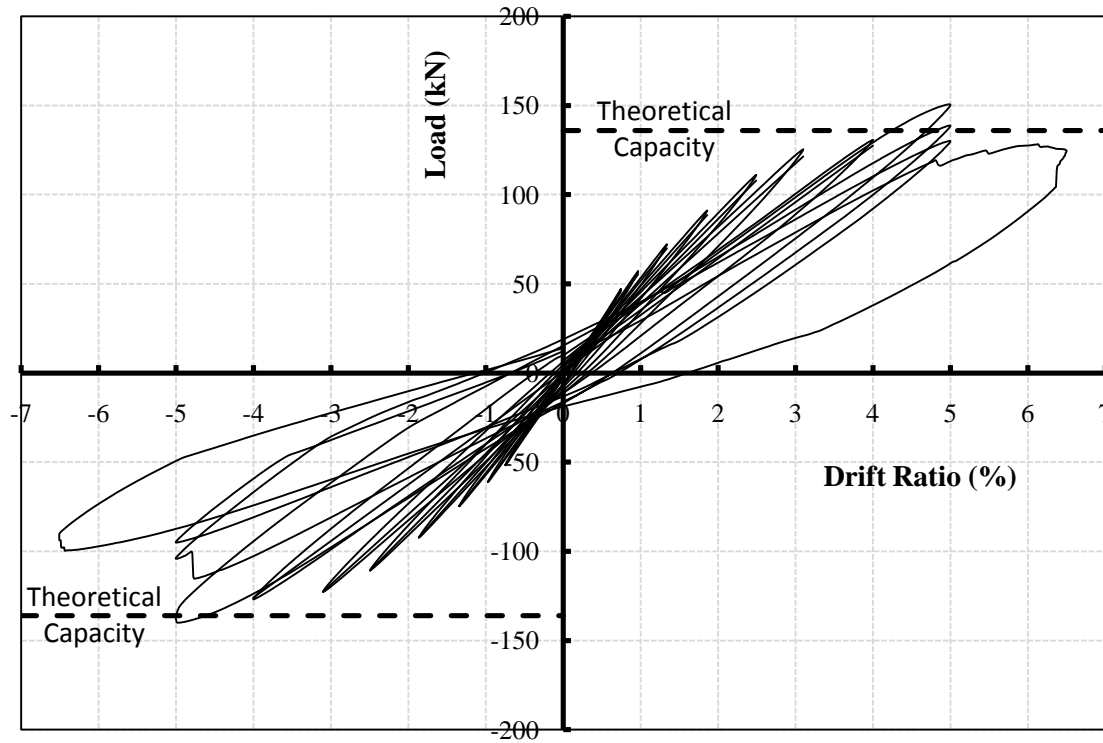


Figure 4.15: Hysteretic load-drift ratio relationship of specimen GS17-B11-J12

4.2.2.6 Specimen GG17-B07-J12 and Specimen GG17-B11-J06

For specimen GG17-B07-J12, better behaviour was observed as the load-drift relationship indicates that the specimen reached the maximum lateral load carrying capacity (167 kN) at the first cycle of the 5.0% drift ratio loading step, and then this capacity started to decrease. This obtained capacity was approximately 22% higher than the design capacity. In addition, no significant pinching appeared until failure started as shown in Figure 4.16. The behaviour of specimen GG17-B11-J06 was similar to that of specimen GG17-B07-J12. However, the lateral load carrying capacity of specimen GG17-B11-J06 was 178 kN as shown in Figure 4.17. This obtained capacity was approximately 30% higher than the design capacity. This may be due to the enhancement of the flexural strength ratio for this specimen as the used inclined bars contributed in

increasing the column reinforcement ratio close to the joint zone or may be attributed to differences in the used material strengths.

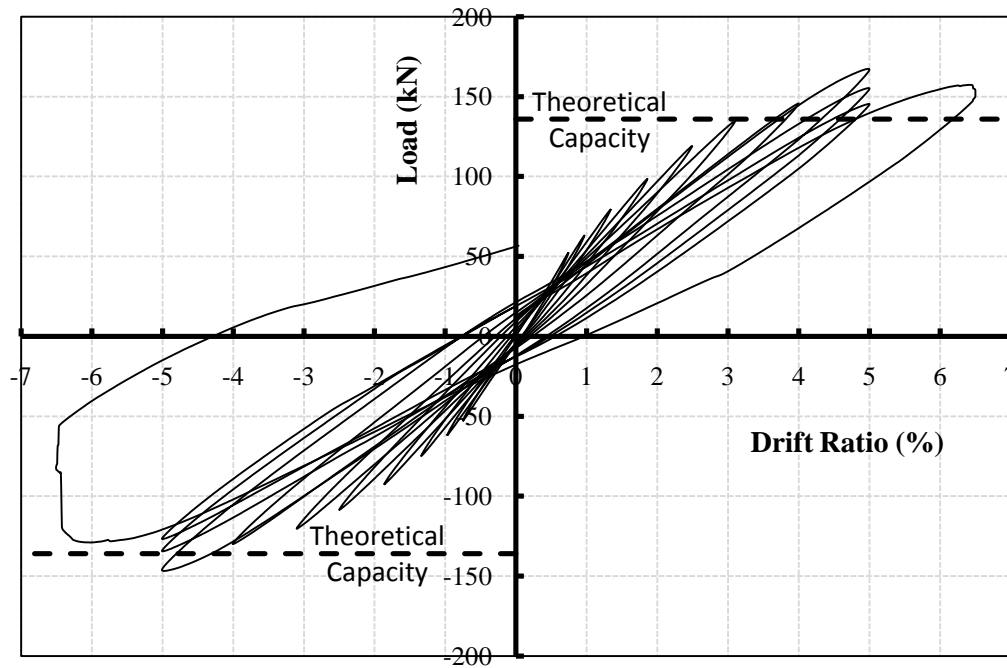


Figure 4.16: Hysteretic load-drift ratio relationship of specimen GG17-B07-J12

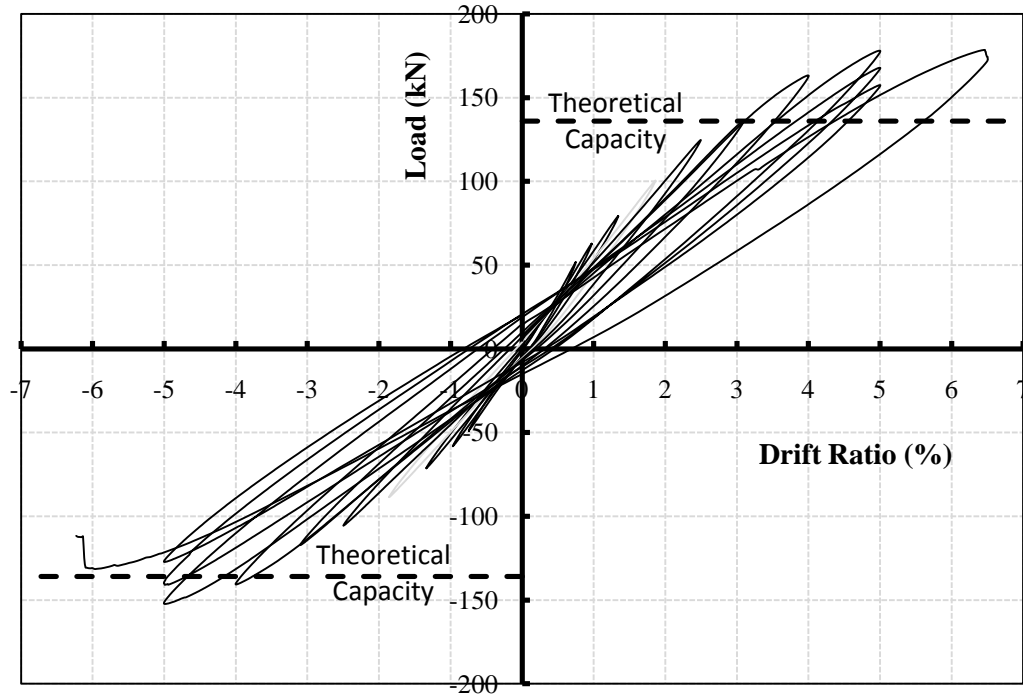


Figure 4.17: Hysteretic load-drift ratio relationship of specimen GG17-B11-J06

The observed loss in stiffness, based on Figure 4.11 through Figure 4.17, was also confirmed by the service cycles that were performed after each seismic loading step. Figure 4.18 shows the stiffness-drift ratio relationship, in which the stiffness of the specimen is calculated as the slope of the line connecting the positive and negative peaks of load-lateral deflection relationship. At 4.0% drift level, approximately 65% loss in the tangent stiffness was observed (compared to the initial stiffness) for the steel reinforced specimen, SS03-B06-J06. However, for the GFRP-reinforced specimen, GG12-B11-J12, only 22% stiffness losses was recorded up to failure. For specimens GG17-B11-J12, GG29-B11-J12, GS17-B11-J12, GG17-B07-J12 and GG17-B11-J06 the recorded losses in stiffness (prior to failure) were about 62, 48, 55, 54 and 46%, respectively. It is worth

mentioning that for the GFRP-reinforced specimens, the behaviour remained basically linear-elastic until failure initiated.

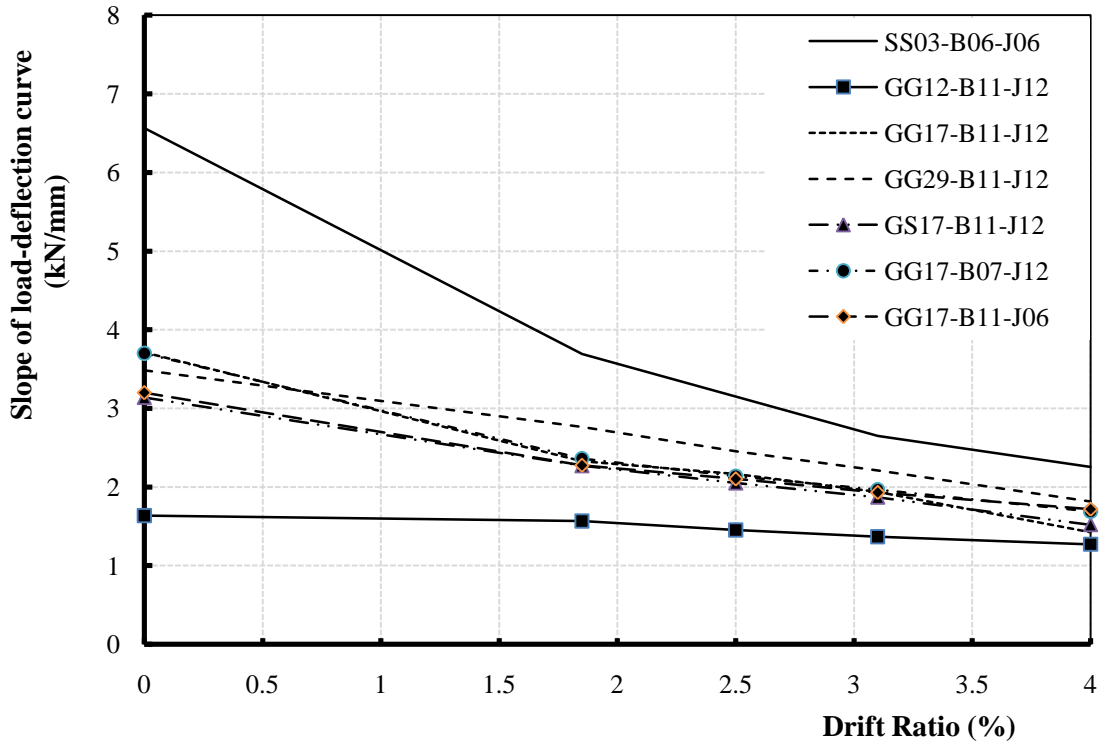


Figure 4.18: Stiffness-drift ratio relationship

In addition, it appears that the low modulus of elasticity for the GFRP reinforcement led to reducing the overall stiffness of the specimen, which may be considered an advantage on the overall structural behaviour. It is true that the lower stiffness for the GFRP-reinforced frame will result in higher displacements; however, in the meantime it will result in higher natural period, which is inversely proportioned to the design spectral acceleration. This means that the total base shear of the structure with lower stiffness is expected to be less. Further investigation is required to evaluate the overall seismic behaviour of FRP-reinforced concrete frames.

It is worth mentioning that the ACI acceptance criteria (ACI 2005) requires that the joint should be able to retain its structural integrity and at least three-quarter of its ultimate capacity through peak displacements equal to or exceed a story drift ratios of $\pm 3.5\%$. While, the corresponding drift ratio required by the National Building Code of Canada (NBCC 2005) for earthquake resistant columns is only 2.5% . All tested specimens were successfully able to sustain drift ratios higher than the values required by both ACI and NBCC.

4.2.3 Strain Measurements

Figure 4.19 shows the measured strains in the beam longitudinal reinforcing bars at the column face for the tested specimens. For the steel-reinforced specimen, SS03-B06-J06, the measured strains in the beam bars remained elastic up to 1.0% drift ratio. Then, the maximum measured strains ($13,400$ micro-strains; approximately 5.8 times the yielding strain) in the beam bars were reached at 1.85% drift level. Afterwards, they decreased to approximately 5300 micro-strain and stayed constant till the end of the test. This can be due to the yield penetration into the joint since the measured strains on beam bars inside the joint exceeded the yield strain at 1.85% drift level. Accordingly, the local slippage from the joint reduced the strain values for the beam bars at the column face (plastic hinge zone).

For all the GFRP-reinforced specimens, the GFRP beam bars remained, as expected, linear-elastic up to failure with maximum measured strains of approximately 14400 , 13350 , 9950 , 17700 , 15610 and 16830 micro-strain for specimens, GG12-B11-J12, GG17-B11-J12, GG29-B11-J12, GS17-B11-J12, GG17-B07-J12 and GG17-B11-J06, respectively. These strain values show that GFRP bars exhibited deformations in the

same order as steel at failure of specimens, which indicates the validity of replacing yielding of steel with large elastic deformations of GFRP reinforcement. It should be noted here that, for all test specimens except GS17-B11-J12, GG17-B07-J12 and GG17-B11-J06, all strain gauges on longitudinal reinforcing beam bars were malfunctioned after the 4.0% drift loading step. For GS17-B11-J12, GG17-B07-J12 and GG17-B11-J06 specimens, the strain gauges were properly functioning till the 5.0% drift ratio as shown in Figure 4.19.

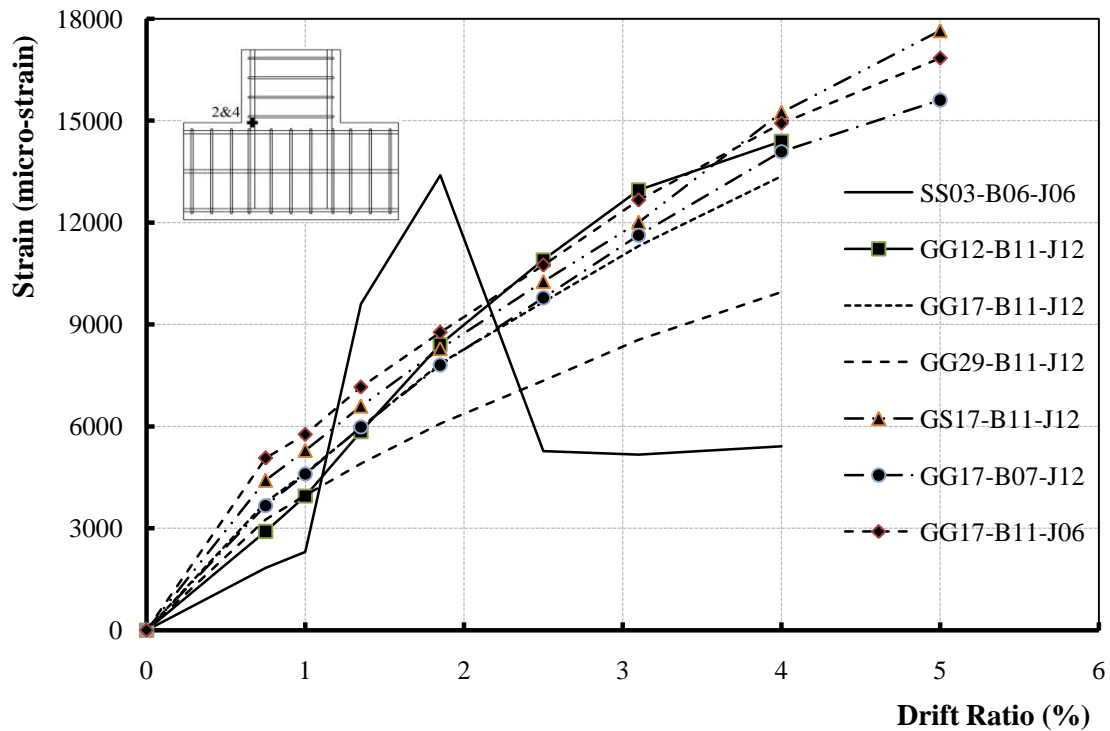


Figure 4.19: Maximum strain in beam longitudinal bars-drift ratio relationship

Figure 4.20 shows the measured strains in the longitudinal column reinforcement of the tested specimens. For all specimens, the strains in the column bars remained elastic up to failure. For specimen GG29-B11-J12, the maximum strain developed in the column

bars was approximately 5900 micro-strain (3.5 times the steel-reinforced specimen), but still much less than the rupture strain of the FRP material (15,300 micro strains). This indicates the applicability of the column design approach followed in this study.

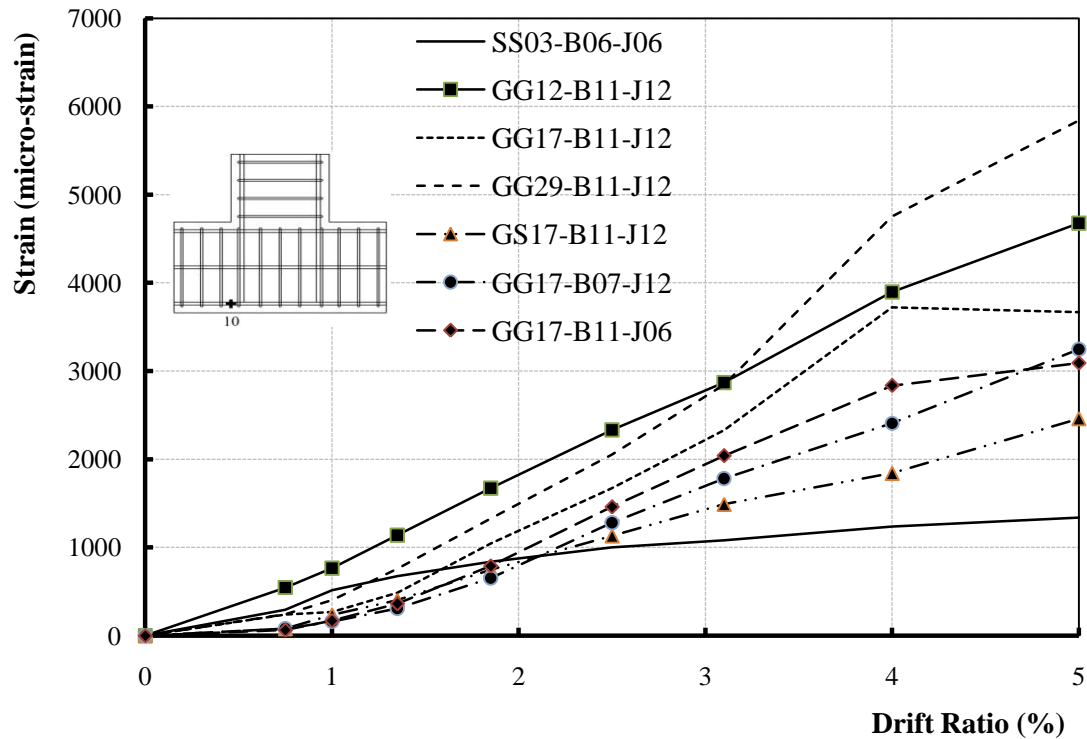


Figure 4.20: Maximum strain in column longitudinal bars-drift ratio relationship

For the beam transverse reinforcement, the maximum strains developed in the beam stirrups at failure were approximately 1900, 3650, 3600, 4200, 1500, 2640 and 4114 micro-strain for specimens SS03-B06-J06, GG12-B11-J12, GG17-B11-J12, GG29-B11-J12, GS17-B11-J12, GG17-B07-J12 and GG17-B11-J06, respectively, as shown in Figure 4.21. However, at 2.50% (NBCC limit) the maximum observed strain was 2750 and 3320 micro-strain for specimen GG29-B11-J12 and GG17-B11-J06, respectively, which is less than 4000 micro-strain; the CSA-S806-02 limit. It is worth mentioning,

although that the specimen GG17-B07-J12 had a beam shear reinforcement ratio less than that of GG17-B11-J12, but the smaller stirrups spacing in specimen GG17-B07-J12 helped in reducing the developed shear strain values in the same location by approximately 30%.

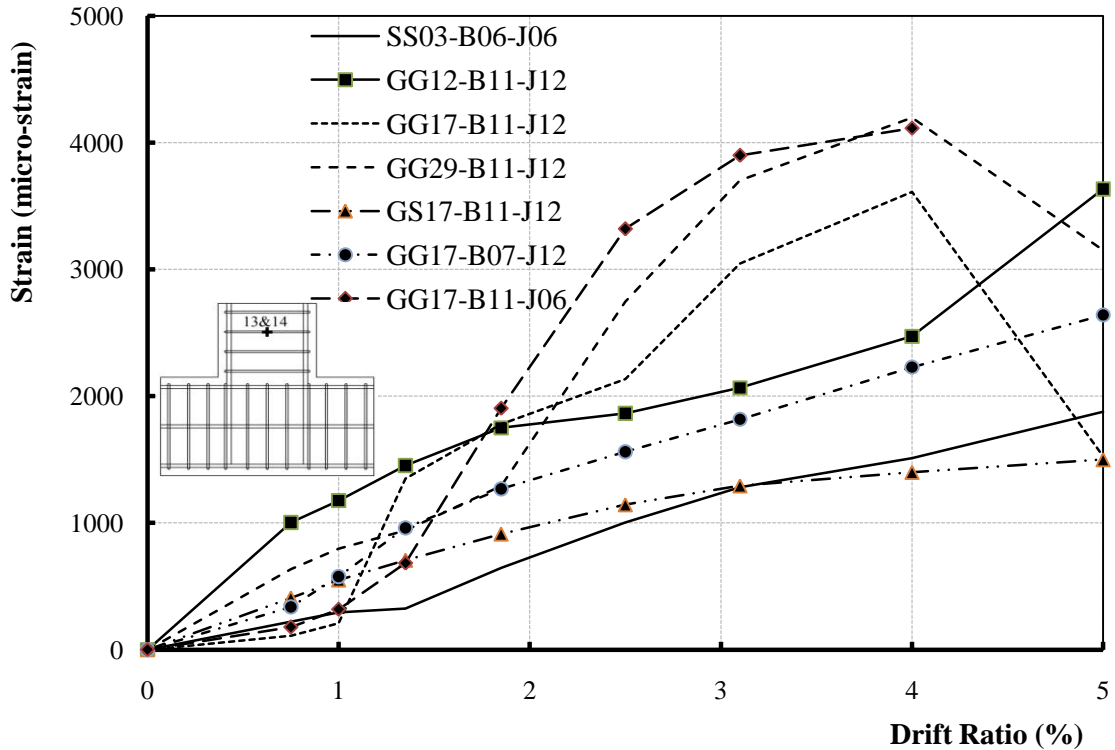
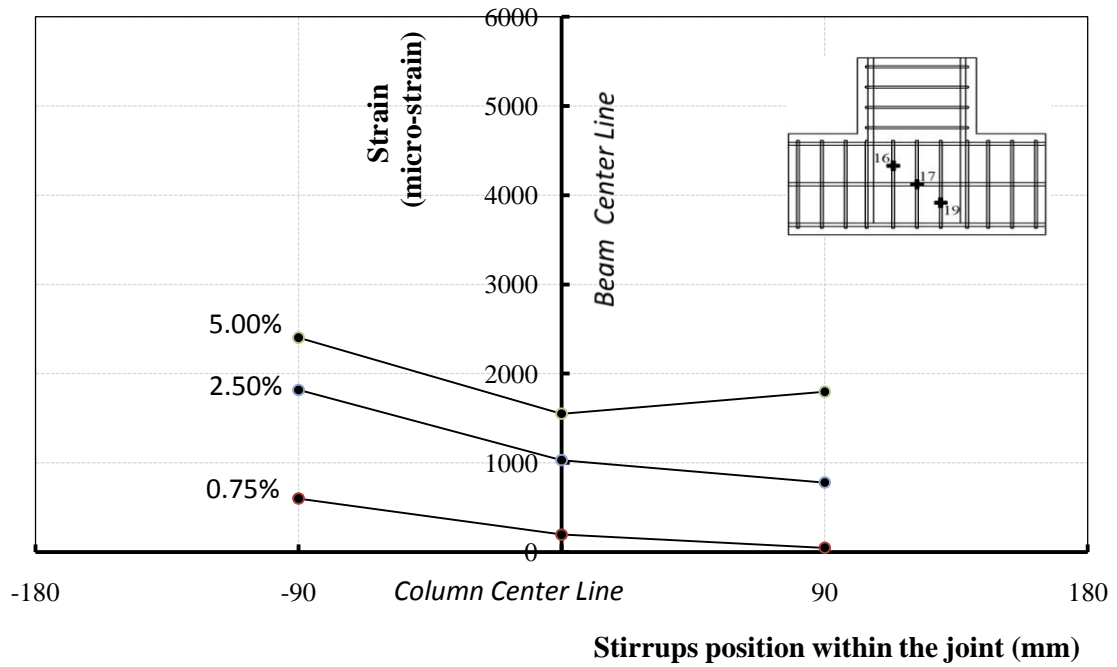


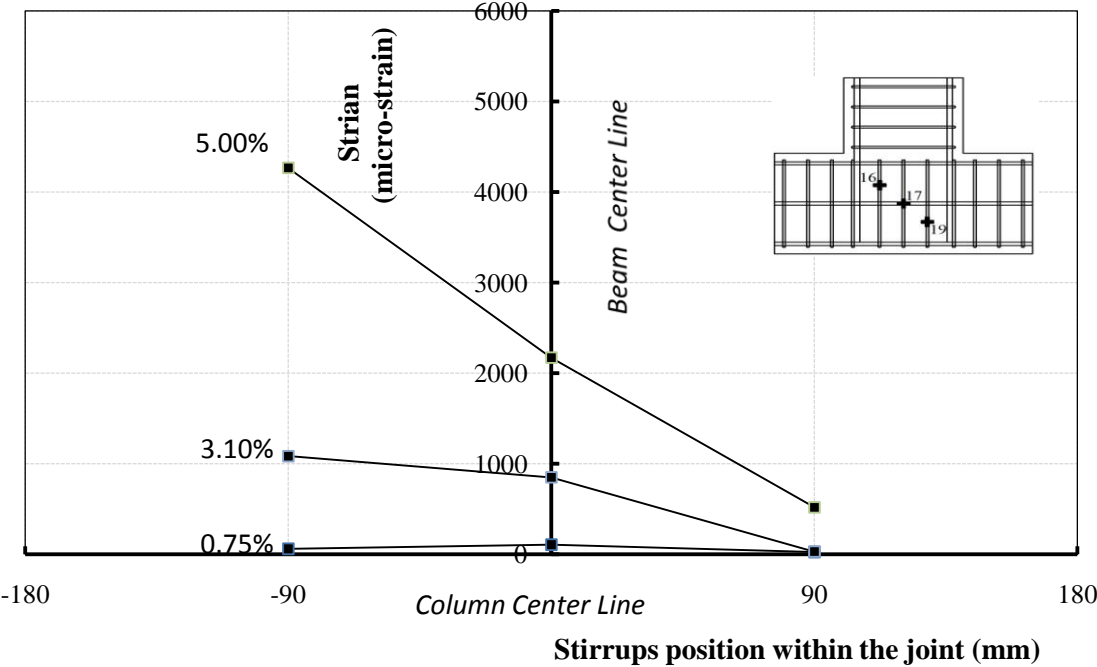
Figure 4.21: Maximum strain in beam stirrups-drift ratio relationship

Furthermore, the maximum measured strain in the transverse reinforcement inside the joint for the specimens SS03-B06-J06, GG12-B11-J12, GG17-B11-J12, GG29-B11-J12, GS17-B11-J12, GG17-B07-J12 and GG17-B11-J06 were 2400, 4250, 3400, 9400, 1950, 4600 and 3300 micro-strains, respectively, as shown in the stirrups strain profile across the joint (Figure 4.22). However, at 2.50% (NBCC limit) the maximum observed strain for any of the specimens did not exceed 4000 micro-strain. It is worth mentioning

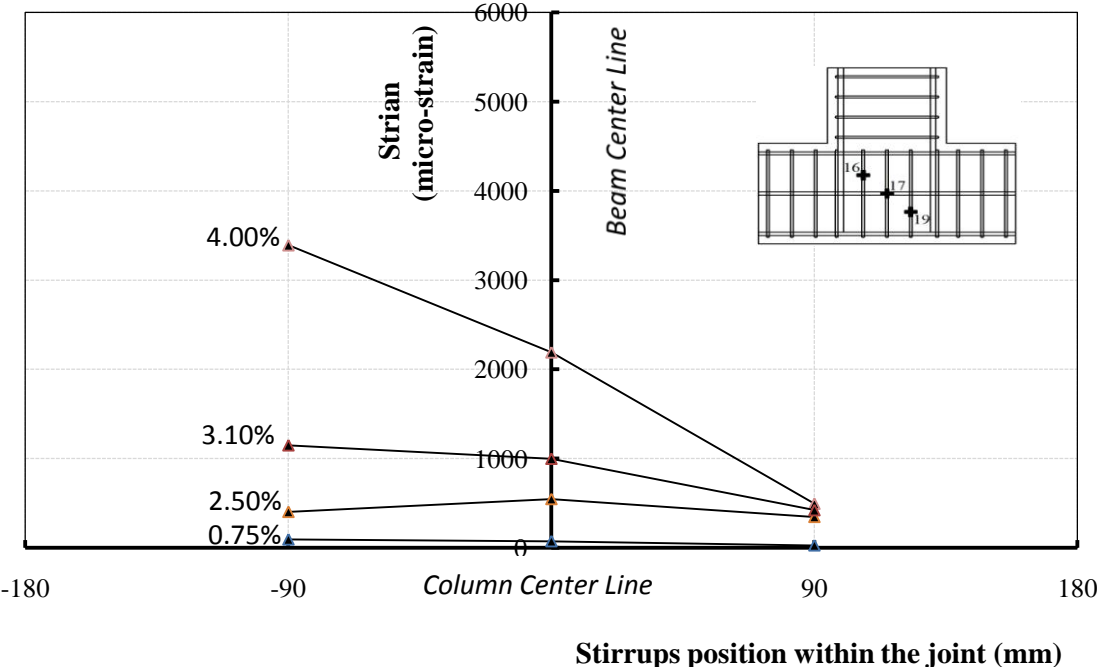
that both types of shear reinforcement (GFRP and steel) provided adequate confinement for the beams and columns to exceed the permitted drift ratio by CSA standards.



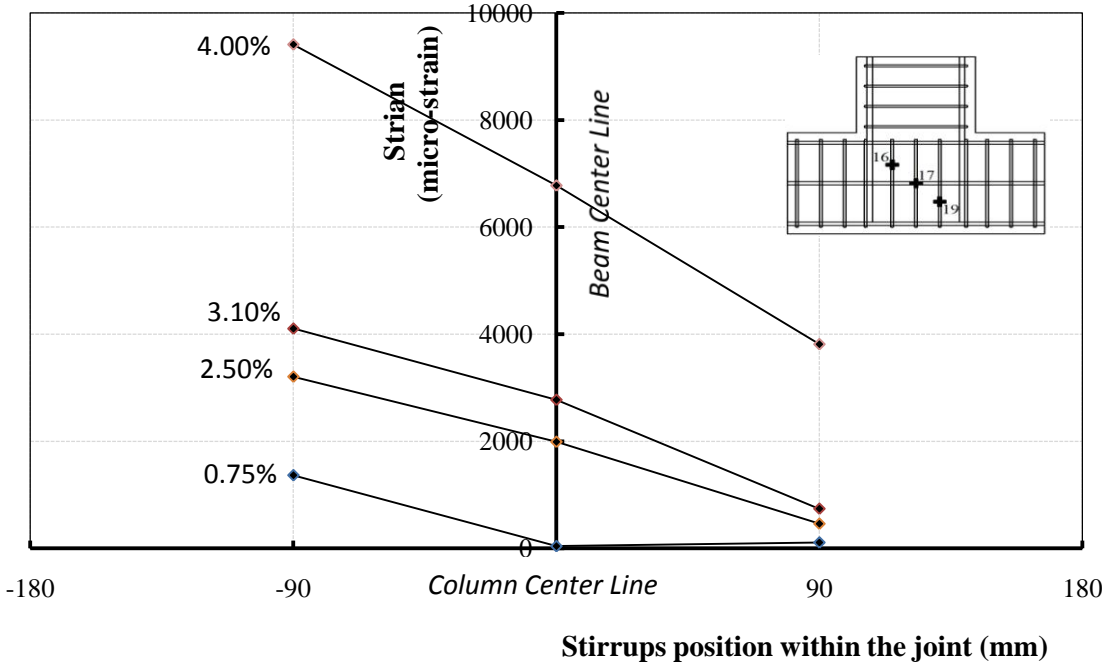
(a) Specimen SS03-B06-J06



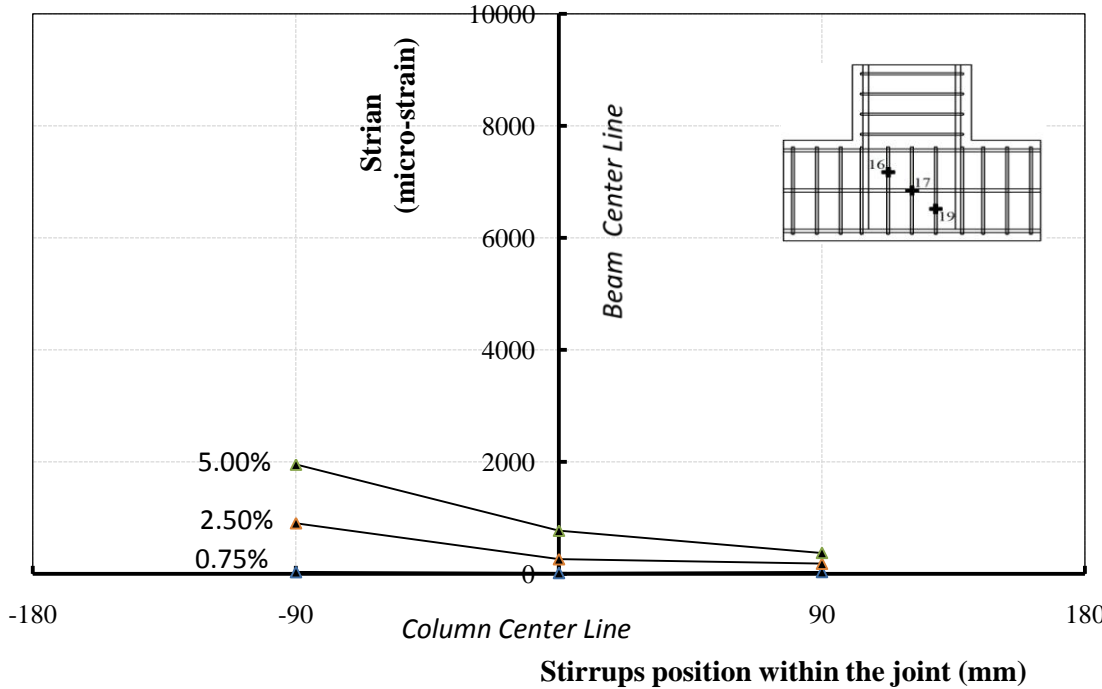
(b) Specimen GG12-B11-J12



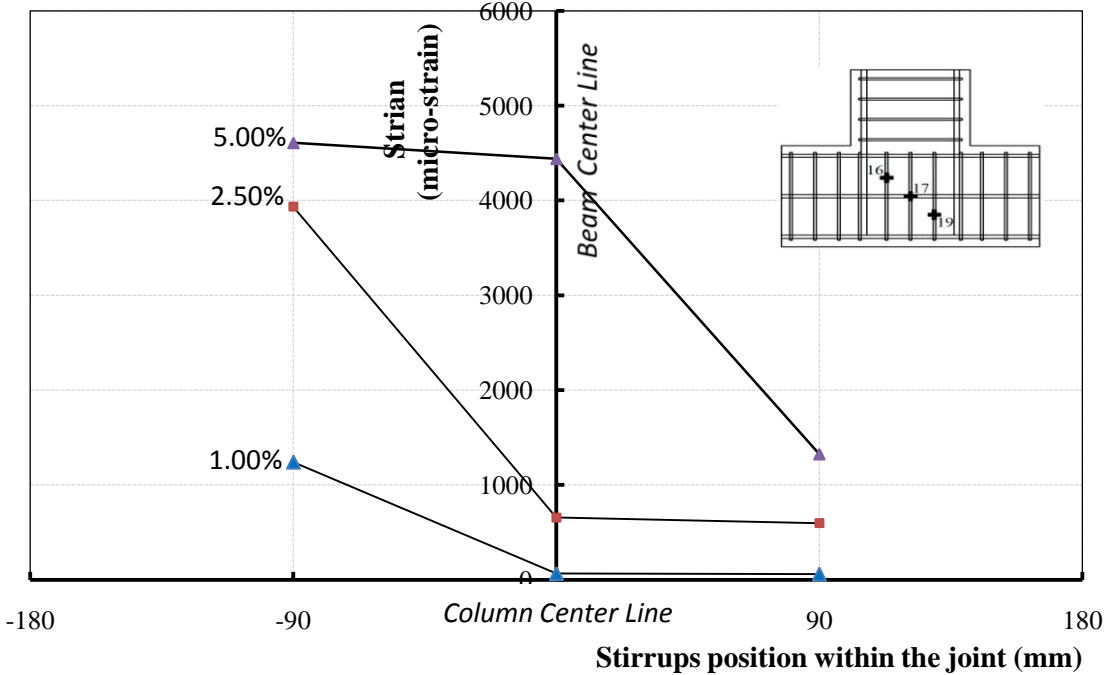
(c) Specimen GG17-B11-J12



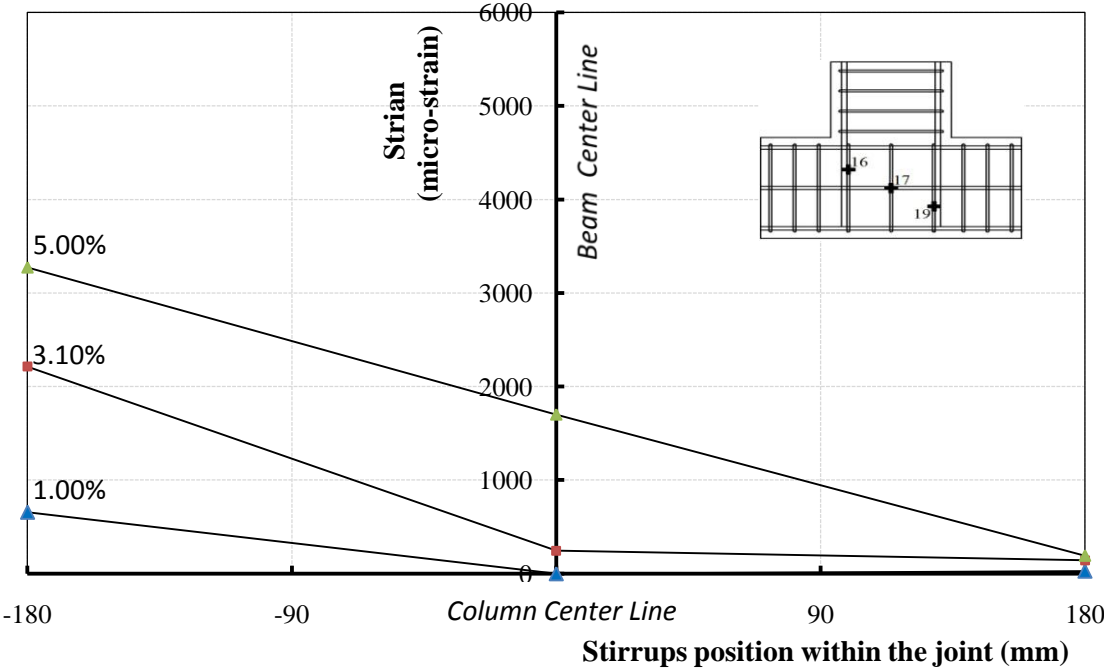
(d) Specimen GG29-B11-J12



(e) Specimen GS17-B11-J12



(f) Specimen GG17-B07-J12



(g) Specimen GG17-B11-J06

Figure 4.22: Stirrups strain profile across the joint

For specimen GG29-B11-J12, the developed strains in the joint stirrups were 9300 micro-strain; much higher than the allowable limit of 4000 micro-strain (CSA-S806-02), which resulted in the development of wider cracks. In other words, no more confinement was provided for the joint, which in turn led to the joint failure. From section analysis, as the outer layer of beam reinforcement reached strain level of 9950 micro-strain, the developed strains in the inner layer of the beam reinforcement were calculated to be 8850 micro strain. Such strains induce a shear stress of approximately 5.3 MPa on the joint, which is in good agreement with the joint capacity of 5.6 MPa predicted by both ACI-318-08 (ACI 2008) and CSA-A23.3-04 (CSA 2004).

For specimen GG17-B11-J06, it was clear that the use of diagonal bars within the joint and reducing the congested stirrups by doubling the spacing within the joint core had improved the hysteretic performance of the connection compared to specimen GG17-B11-J12. Though the ultimate capacity of specimen GG17-B11-J06 increased by approximately 18% and the corresponding drift ratio at failure was 6.50% instead of 5.00% compared to specimen GG17-B11-J12, meanwhile, the developed strains in the joint shear reinforcement (stirrups) were exactly equal to those developed in specimen GG17-B11-J12. Figure 4.23 shows the strain profile along the inclined bars inside the joint area assuming zero strain value at the free end of the inclined portion. It can be noticed that the trend of the strain distribution started to change at 1.85% drift level, and the strain at the middle of the diagonal length started to increase to reach a maximum value of 4300 micro-strain at 5.0% drift ratio. This observation is in agreement with the cracking development during the test, where the diagonal cracks inside the joint started to appear after 1.85% drift ratio.

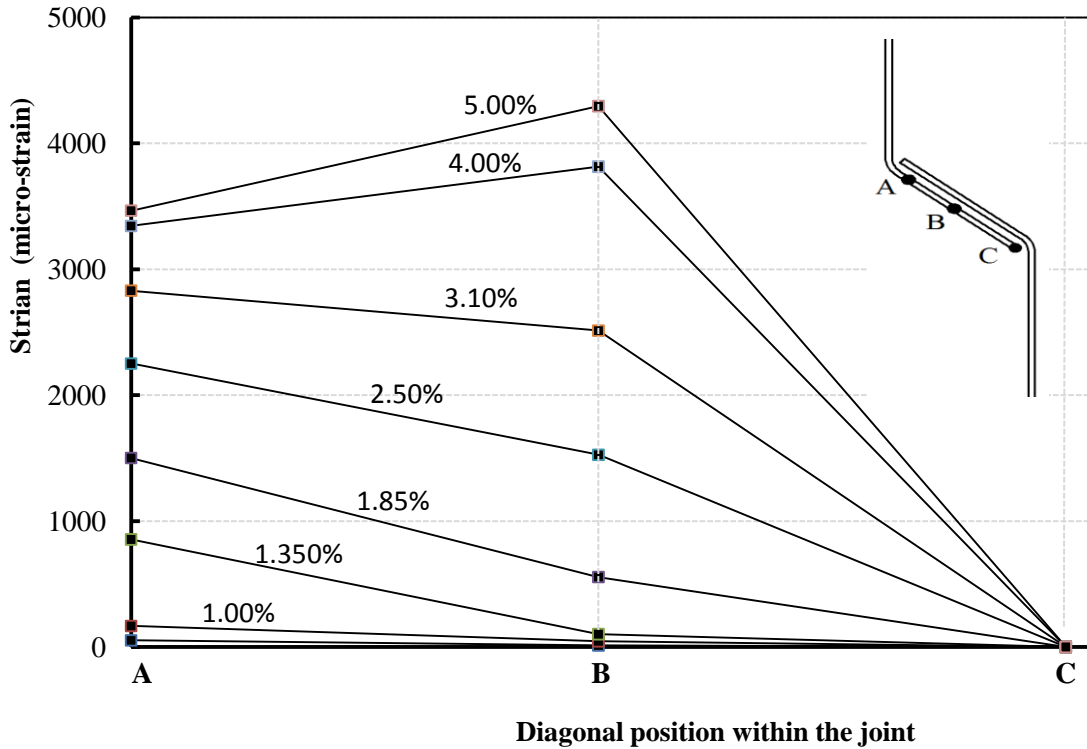


Figure 4.23: Strain profile across the diagonal bars inside the joint GG17-B11-J06

4.2.4 Cumulative Energy Dissipation

Figure 4.24 shows the cumulative energy dissipated by test specimens during reversed cyclic loading with respect to drift ratio. The cumulative energy dissipation; or cumulative energy absorbed, was calculated by summing up the dissipated energy in successive load-displacement cycles. Throughout the test, it was obvious that the absorbed energy of the steel-reinforced specimen is much higher than the GFRP-reinforced specimens. For example, at 2.50% drift level the cumulative absorbed energy for specimen SS03-B06-J06 was 23 kN.m; while, for the GG17-B11-J12 specimen it was only 7.5 kN.m (approximately 1/3). However, it was observed that increasing the beam reinforcement ratio, which resulted in changing the mode of failure of the beam section to concrete crushing (specimen GG17-B11-J12) instead of the balanced failure mode

(specimen GG12-B11-J12), led to enhance the ability of the joint to dissipate the seismic energy through utilizing the inelastic behaviour of concrete.

It should be noted here that increasing the beam reinforcement ratio would increase the shear forces transmitted to the joint and may result in joint failure (specimen GG29-B11-J12). Therefore, the beam reinforcement ratio should be limited to the available shear capacity of the joint (Equation 3-17, Chapter 3). Although this lower energy dissipation for the GFRP-reinforced specimens is considered a disadvantage, the joint will regain its original shape after removing the loads, thus requiring minimum amount of repair. On the other hand, specimen GG17-B11-J12 with GFRP stirrups showed 20% more cumulative energy dissipation compared to specimen GS17-B11-J12 with steel stirrups. This indicates the validity of using GFRP stirrups in such connections subjected to reversal cyclic loading.

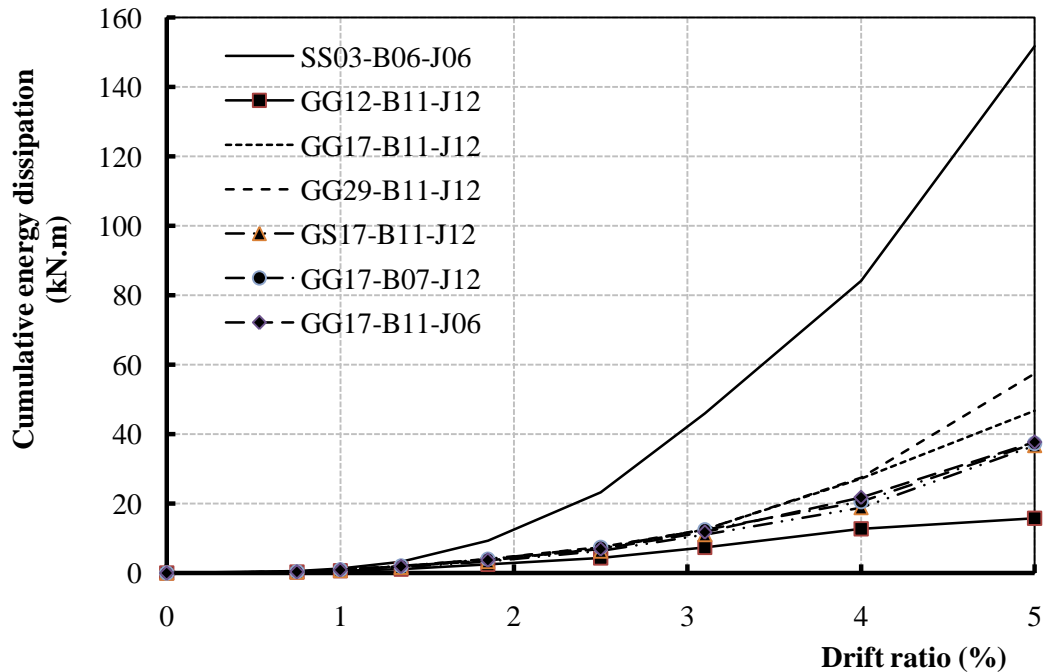


Figure 4.24: Cumulative energy dissipation- drift ratio relationship

4.2.5 Rotation Measurements

The measured drift values can be divided into four main components as shown in Figure 4.25. These components are: (1) rotation in the anticipated beam plastic hinge zone (for steel-reinforced joint); (2) rotation due to local slippage and large strains developed in the beam bars within the joint; (3) rotation due to overall column rotation; and (4) joint distortion. Each pair of LVDTs was installed to measure the rotation due to one of the main drift components (Chapter 3 – Figure 3.5). Hence, the percentage contribution of each rotation component can be determined by dividing each component by the total beam drift angle (drift ratio). It should be noted here that, in FRP-reinforced joints, the plastic hinge zone is presented by the large elastic deformation exhibited by the GFRP bars; could be called “virtual plastic hinge”.

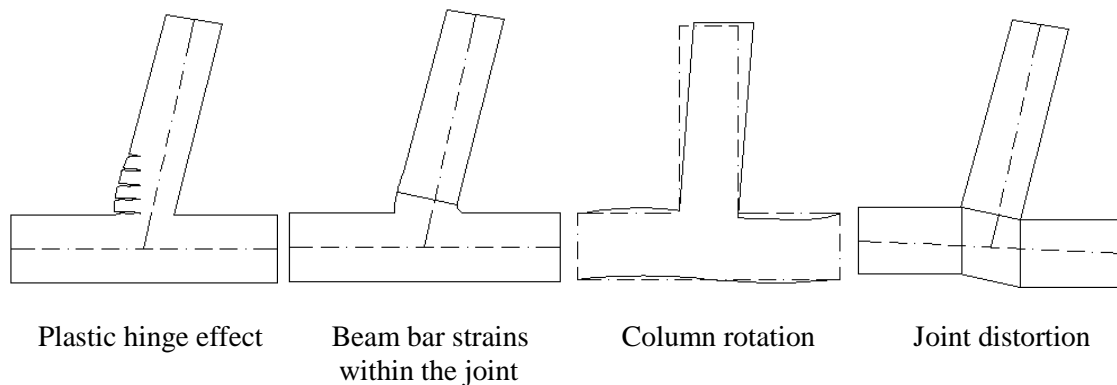
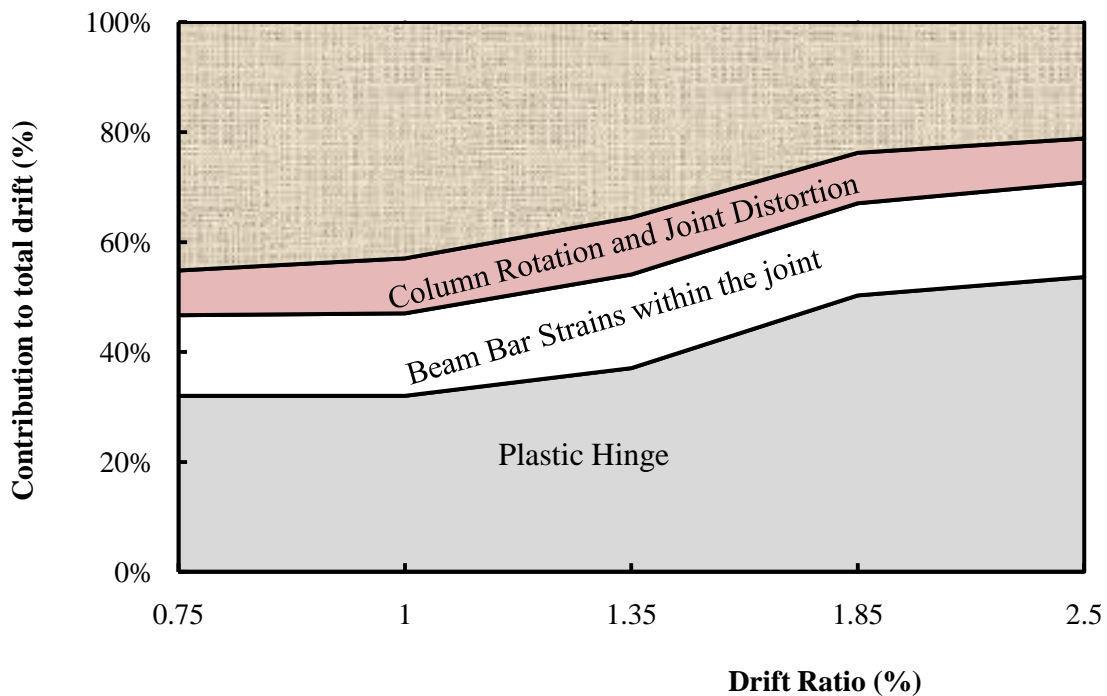


Figure 4.25: Main components to total beam drift angle

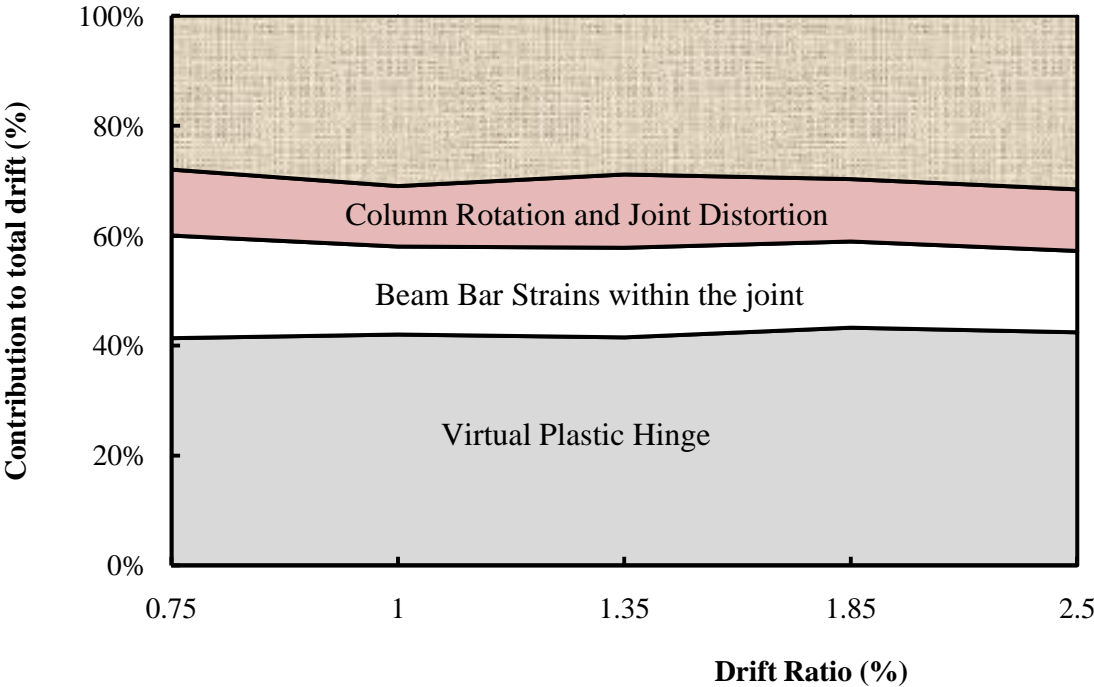
As shown in Figure 4.26, rotation due to beam bar strains in the virtual plastic hinge zone contributed most to the total drift angle for all tested joints. Up to 2.50% drift ratio (NBCC limit), the contribution of the virtual plastic hinge rotation was approximately 35 to 40% of the total drift angle. However, rotation due to beam bar

slippage and large strains in the joint was approximately 20 to 30% of the total drift angle while, the column rotation combined with the joint distortion effect was not more than 12% of the total drift angle.

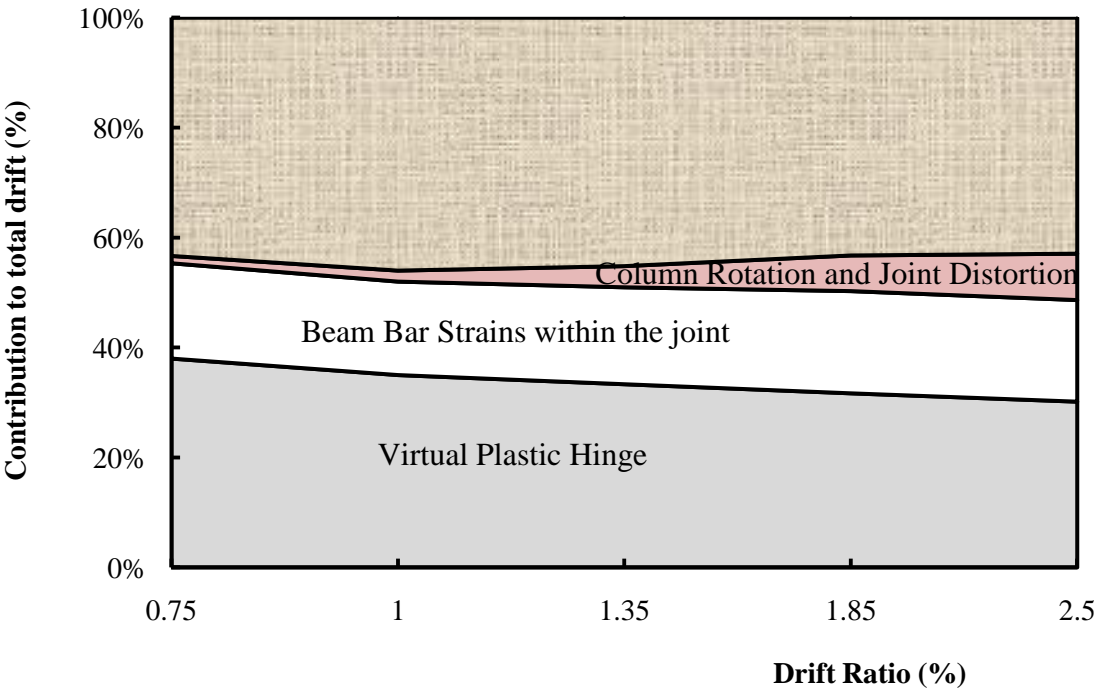
These obtained ratios are in agreement with the observed damage on the tested specimens up to the code limit (no significant damage was observed in the column or the in joint area). All remaining rotations from the total beam drift in Figure 4.26 are probably due to unmeasured factors; i.e. beam cracks outside the anticipated plastic hinge zone and elastic beam displacement.



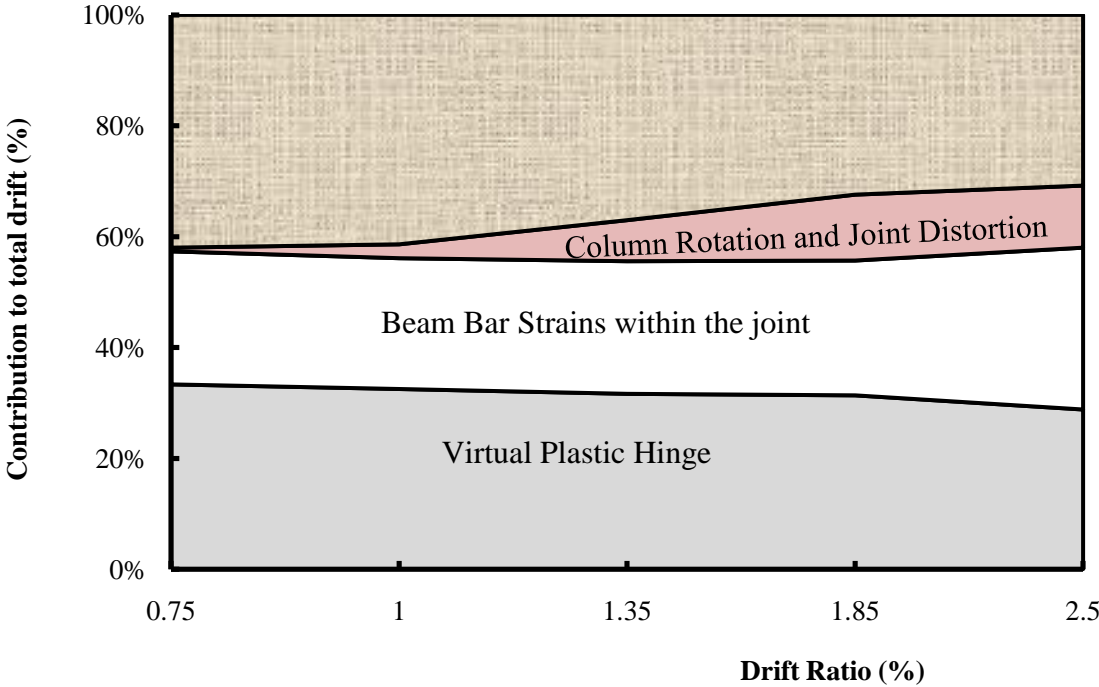
(a) Specimen SS03-B06-J06



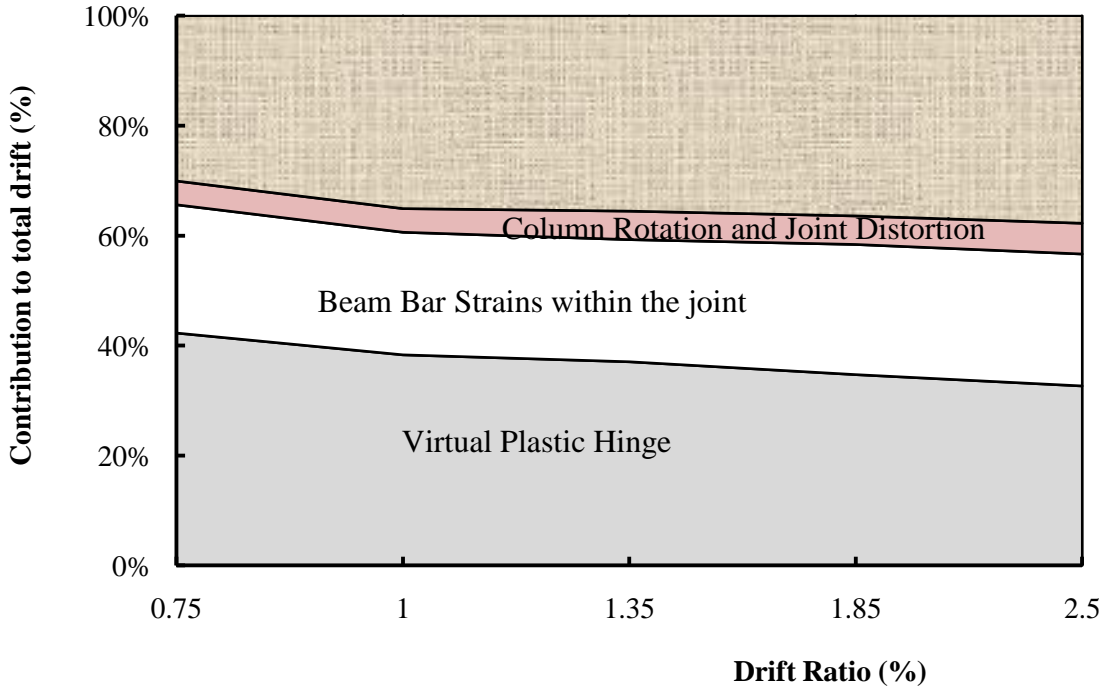
(b) Specimen GG12-B11-J12



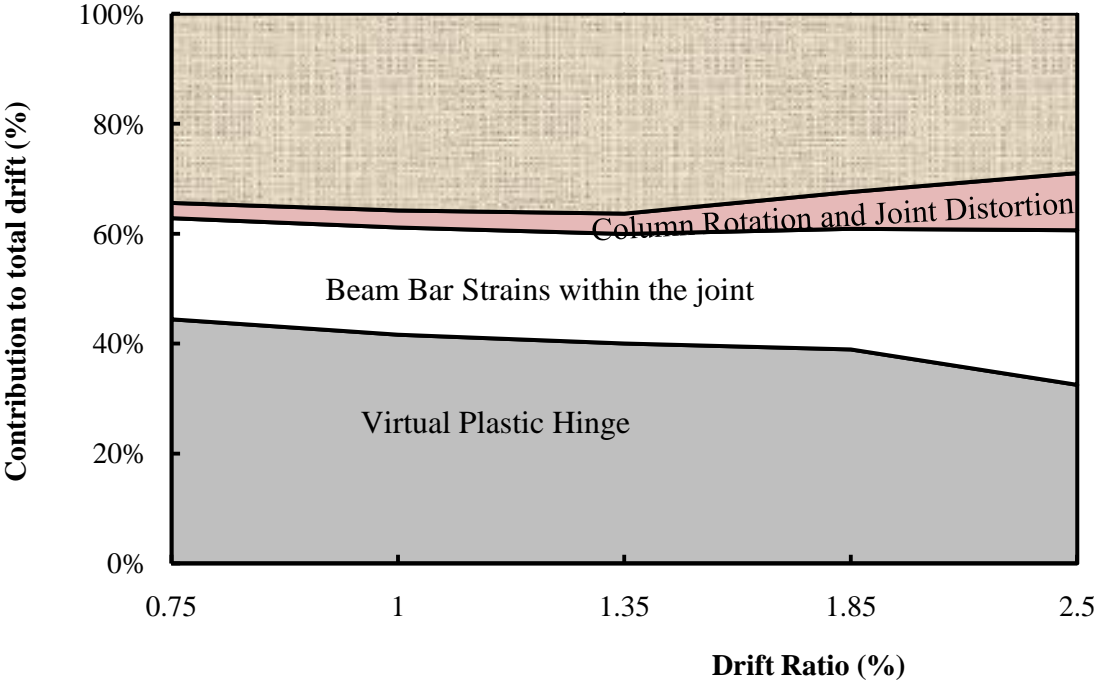
(c) Specimen GG17-B11-J12



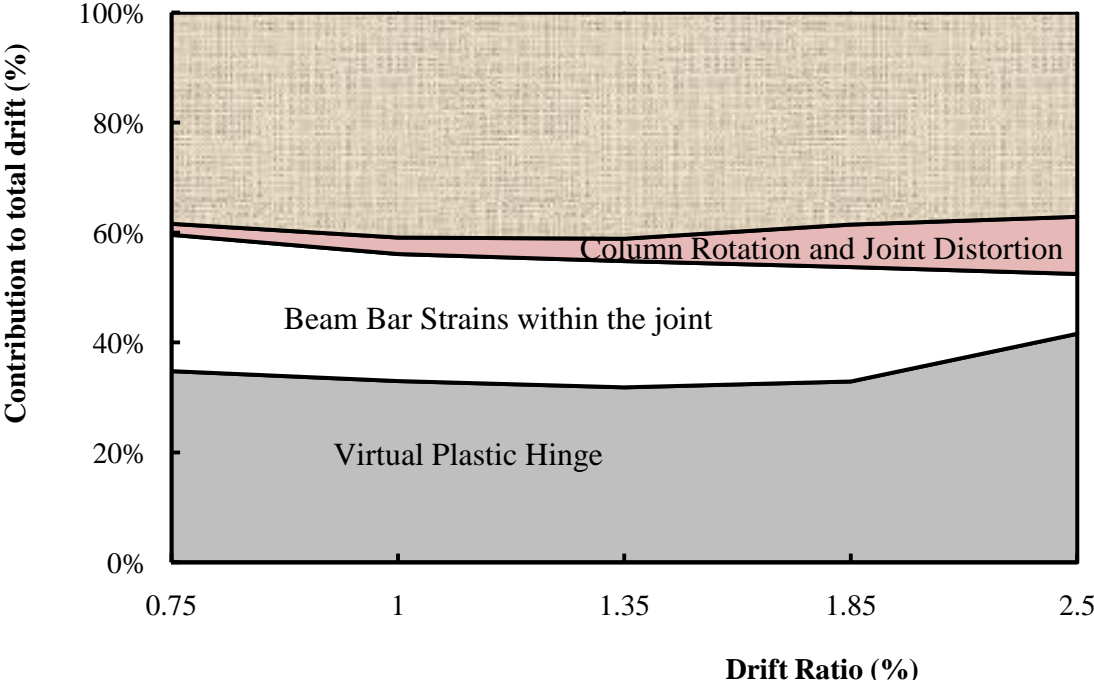
(d) Specimen GG29-B11-J12



(e) Specimen GS17-B11-J12



(f) Specimen GG17-B07-J12



(g) Specimen GG17-B11-J06

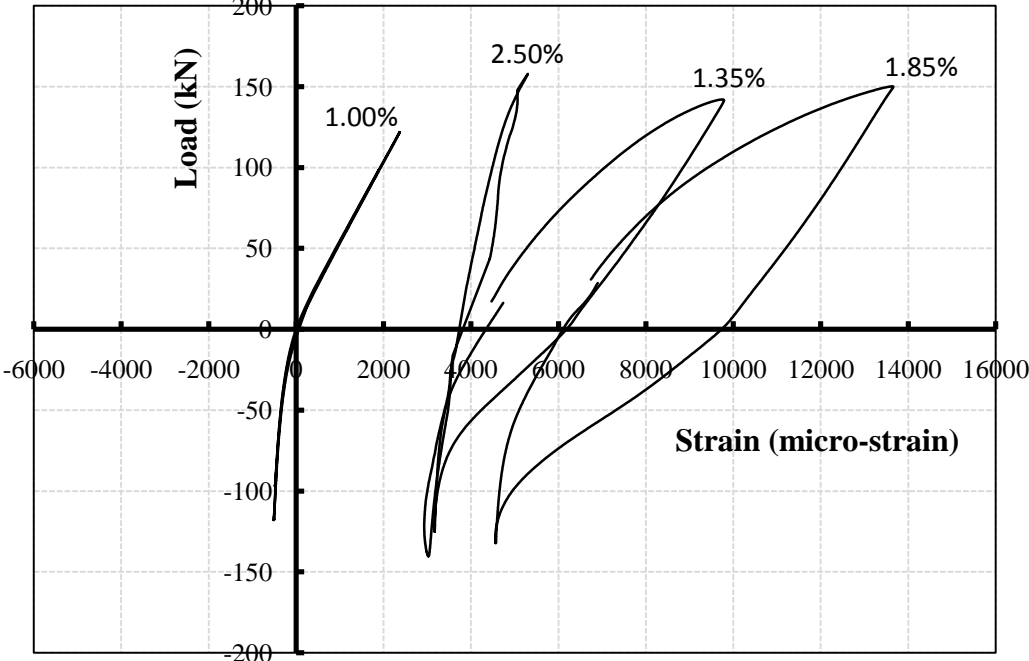
Figure 4.26: Percentage of contribution to total drift angle before failure

4.2.6 GFRP Bars under Reversed-Cyclic Loading

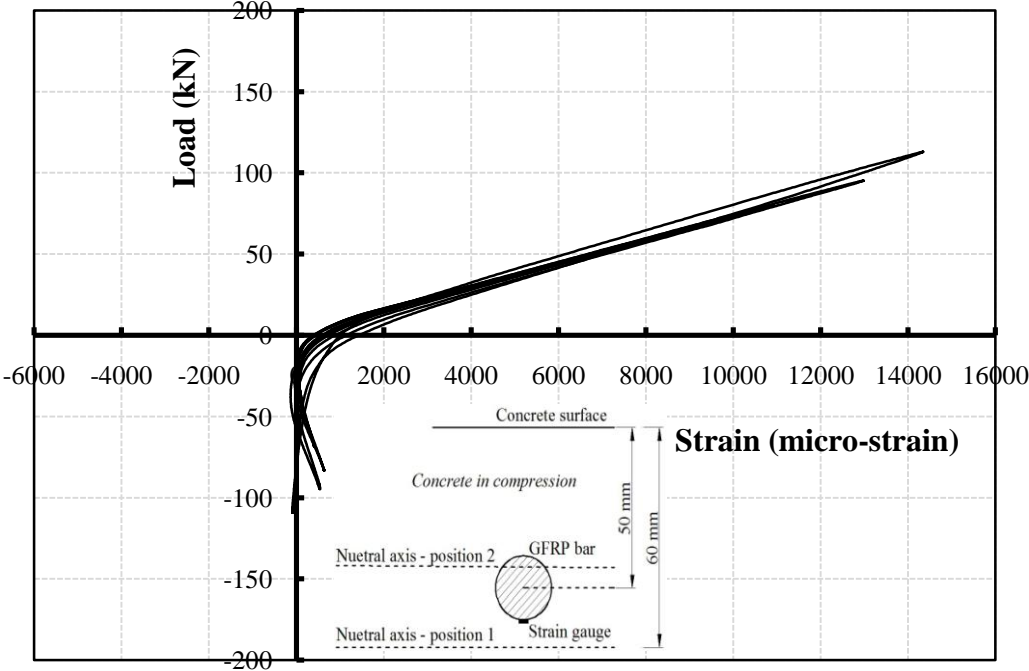
Figure 4.27 and 4.28 show the load-strain relationship for the beam and column longitudinal bars under reversed-cyclic loading for all tested specimens, respectively. It is clear that the GFRP bars behaved linearly-elastic with minimum residual strains as expected. On the other hand, the steel bars suffered from large residual strains after exceeding the yield strain. This indicates that, surviving an earthquake event, GFRP-reinforced joints will remain functional with minimum repair requirements, if any.

Regarding the compressive behaviour of the GFRP bars, Figure 4.27 showed that for specimens GG12-B11-J12, GG17-B11-J12 and GG17-B07-J12, the beam GFRP bars in the compression side did not contribute in carrying the load, except in the first few cycles, till the concrete started to crush. In the first few cycles, the depth of the neutral axis from elastic analysis was 60 and 70 mm for GFRP reinforcement ratios 1.20 and 1.70 times the balanced reinforcement ratio, respectively (position 1). GFRP bars tended to carry compression loads at that stage. With the centerline of the GFRP bars had a concrete cover of 50 mm, the strain gauges (at bottom surface of the bars) is too close to the neutral axis position as shown in Figure 4.27. Once loading started to increase, the neutral axis shifted up slightly (to be approximately within the concrete cover) so that even the FRP bars in the compression side located in the cracked concrete zone (strain gauge beneath the neutral axis - position 2). Accordingly, the strain gauges started to read tension forces. After concrete crushed, these bars became responsible to carry all the compression loads, which increased the measured compressive strains. For instance, this phenomenon did not appear in specimen GG29-B11-J12 due to deeper neutral axis depth resulted from higher reinforcement ratio used. The GFRP bars in compression for this

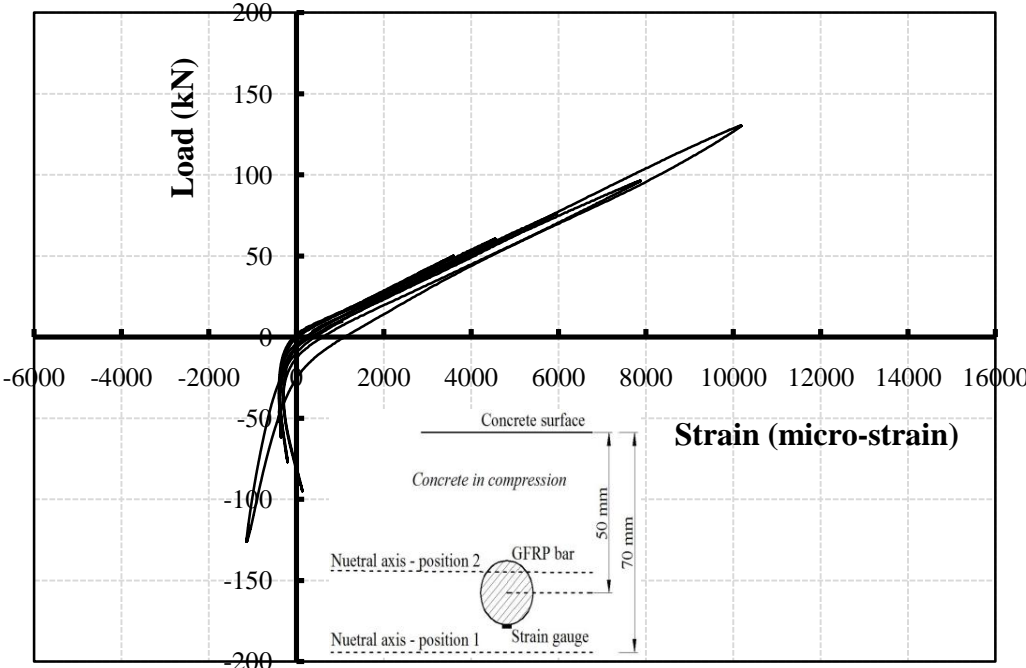
specimen carried compressive strains from the beginning of the test with a maximum value did not exceed 4360 micro-strain.



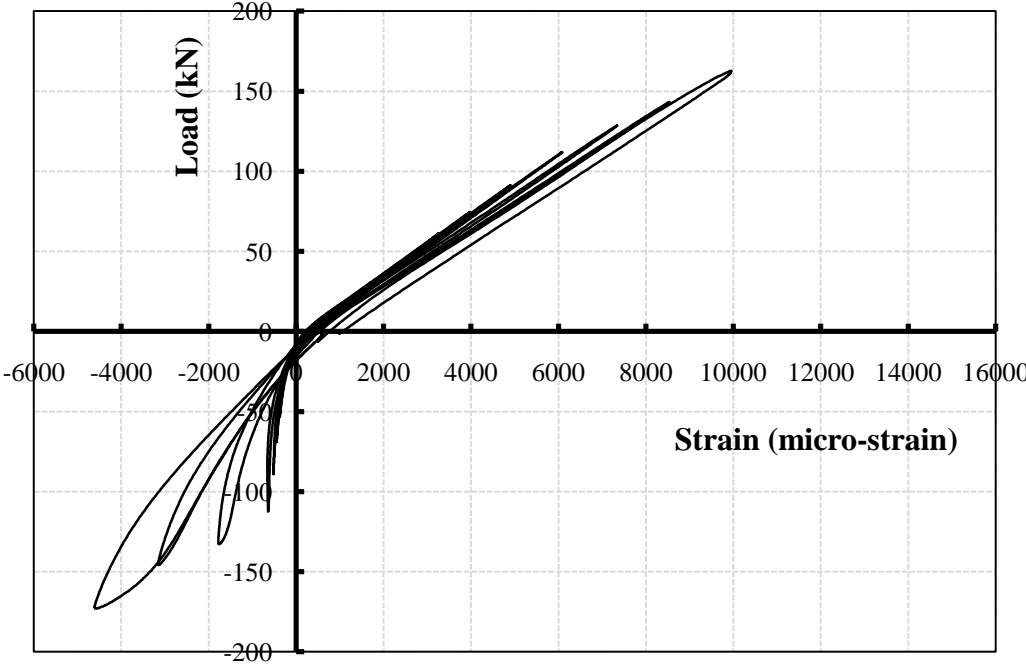
(a) Specimen SS03-B06-J06



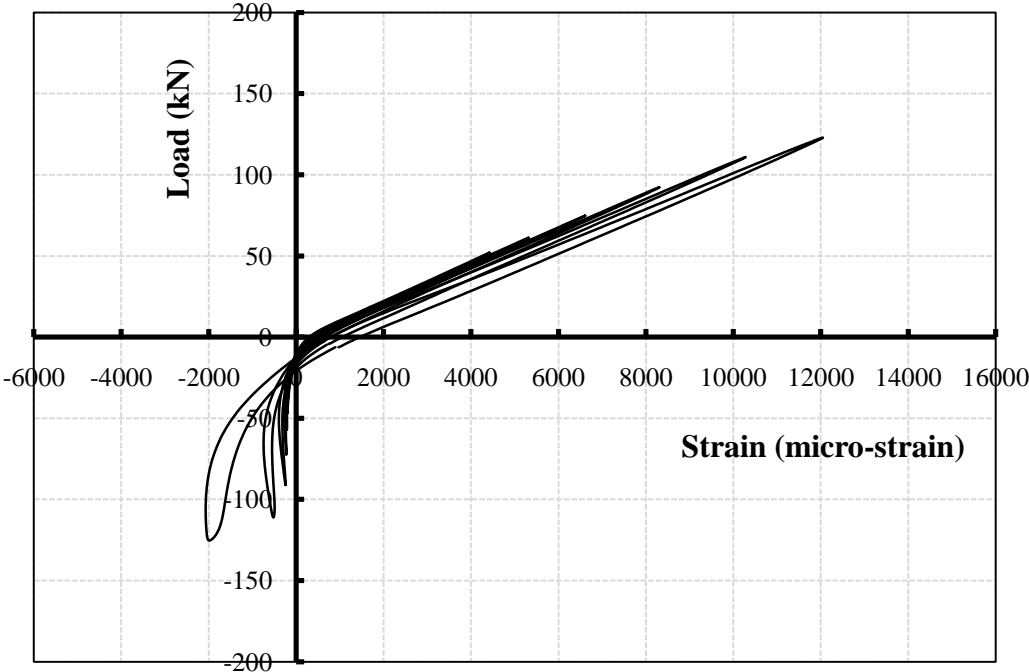
(b) Specimen GG12-B11-J12



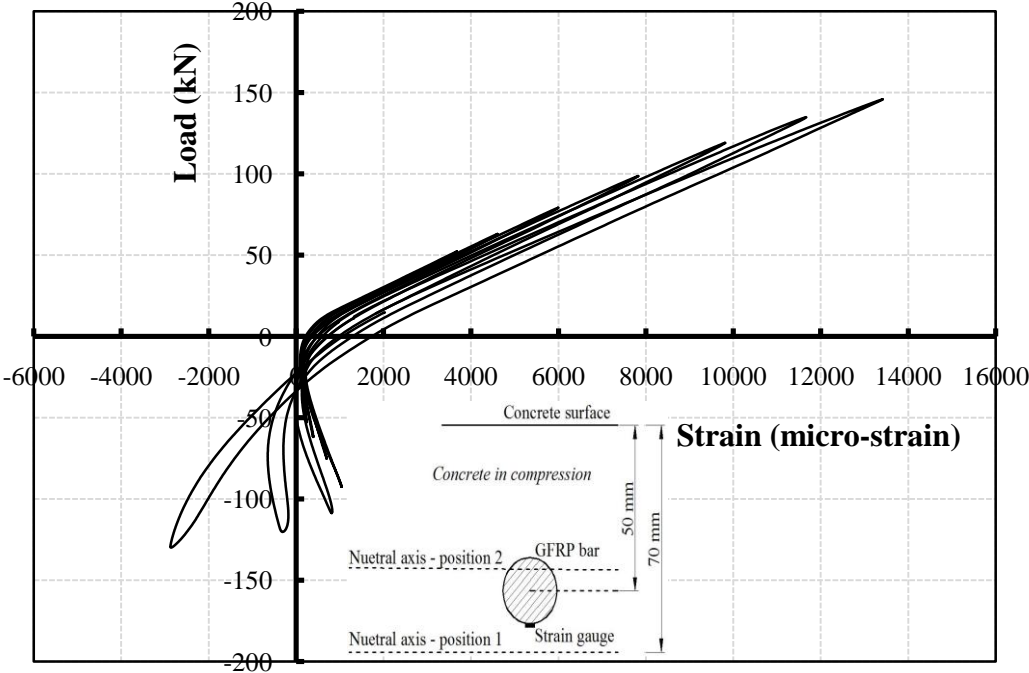
(c) Specimen GG17-B11-J12



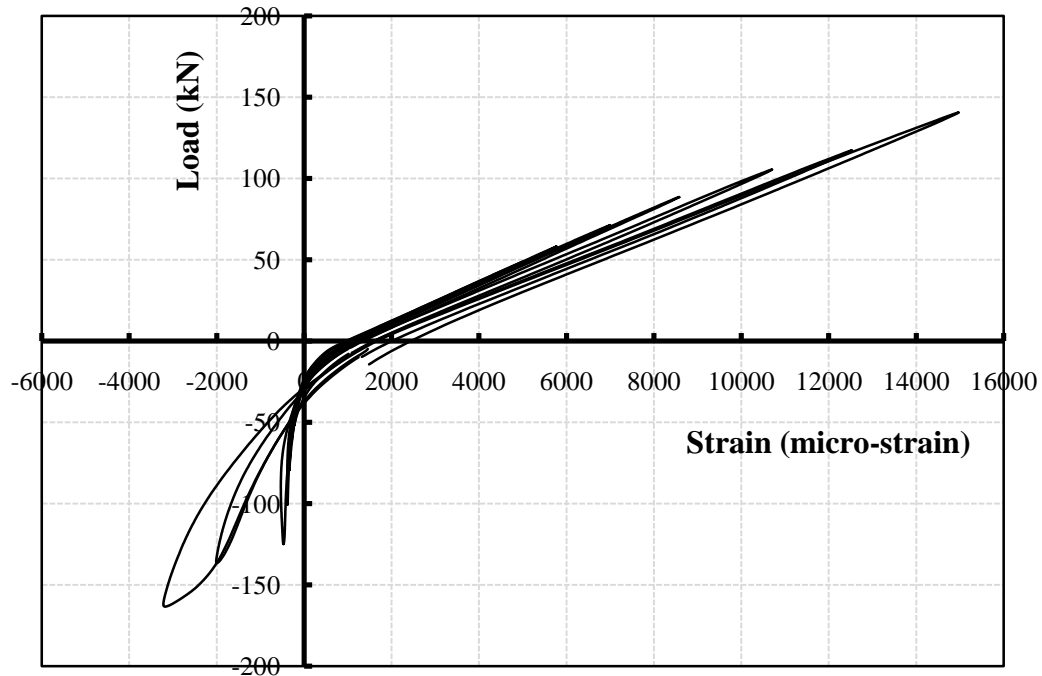
(d) Specimen GG29-B11-J12



(e) Specimen GS17-B11-J12



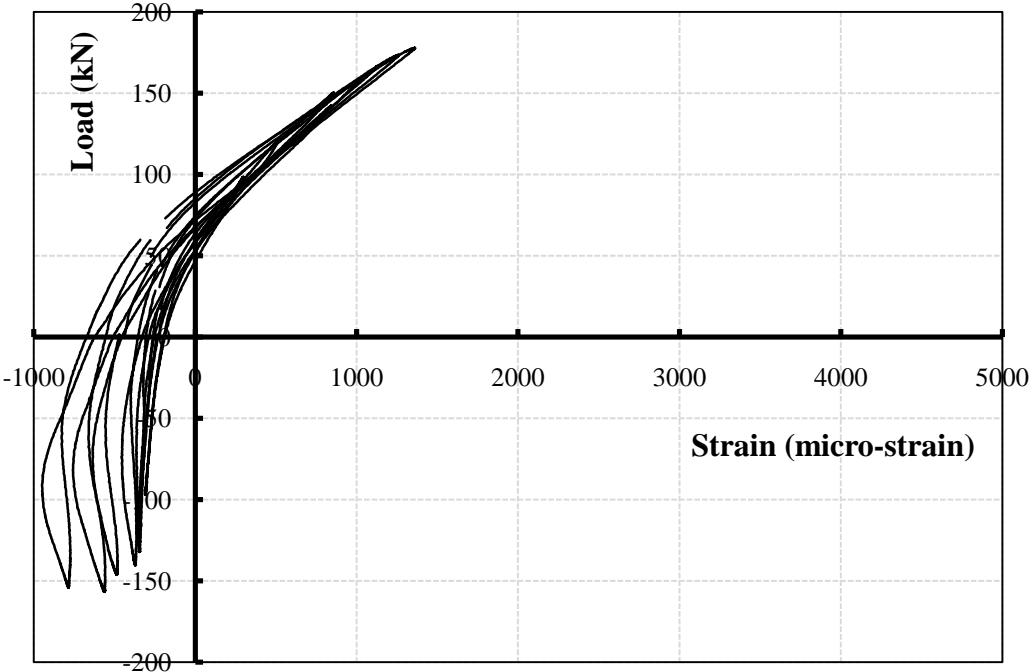
(f) Specimen GG17-B07-J12



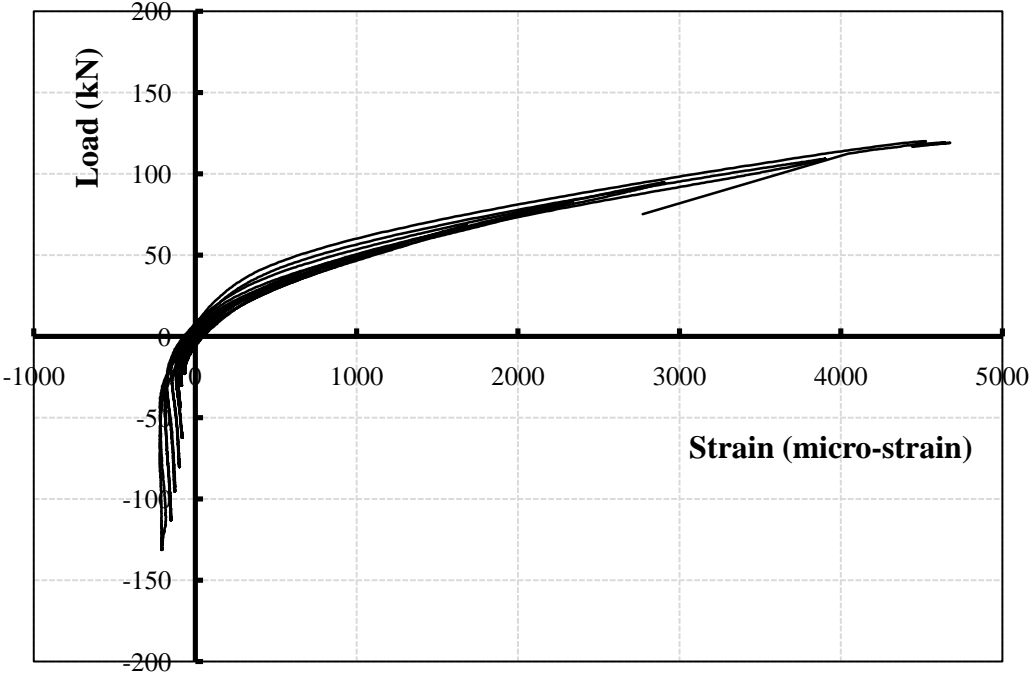
(g) Specimen GG17-B11-J06

Figure 4.27: Behaviour of Steel and GFRP beam bars under reversed loading

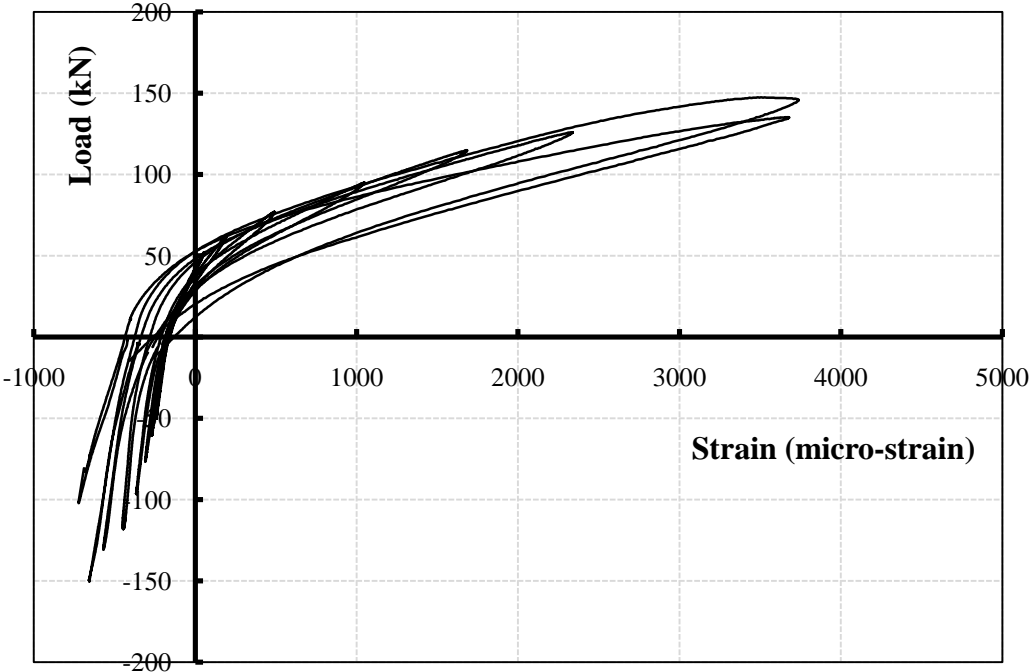
Contrary, Figure 4.28 showed that the column GFRP bars contributed in compression from the beginning until the end of the test. This validates the design assumptions regarding ignoring the FRP bars compression behaviour in beam design while considering it in column. More research is needed to investigate the compressive behaviour of the GFRP reinforcement.



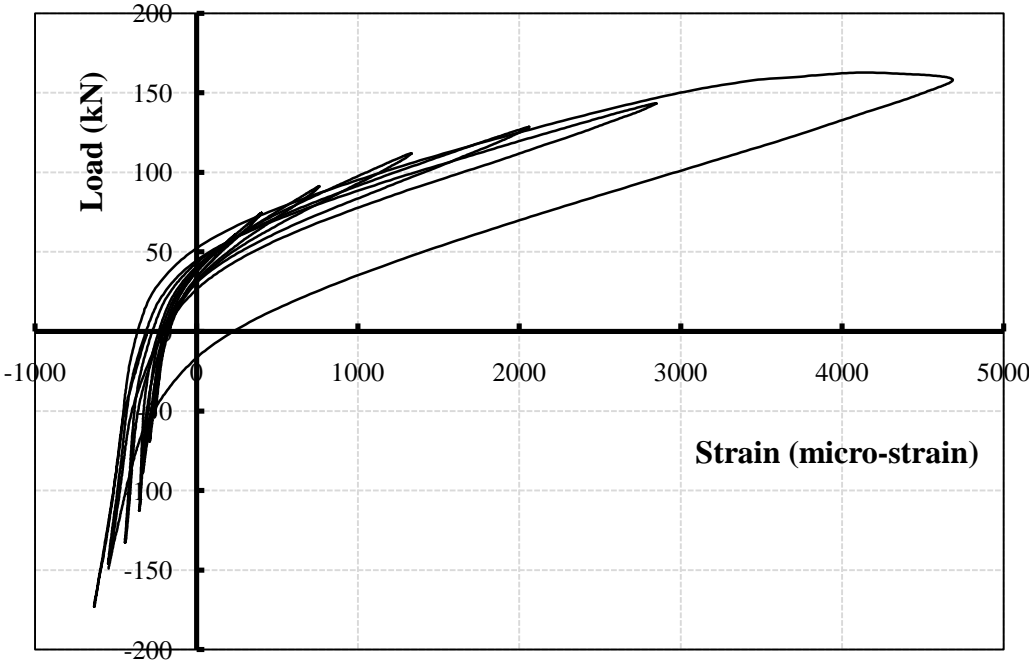
(a) Specimen SS03-B06-J06



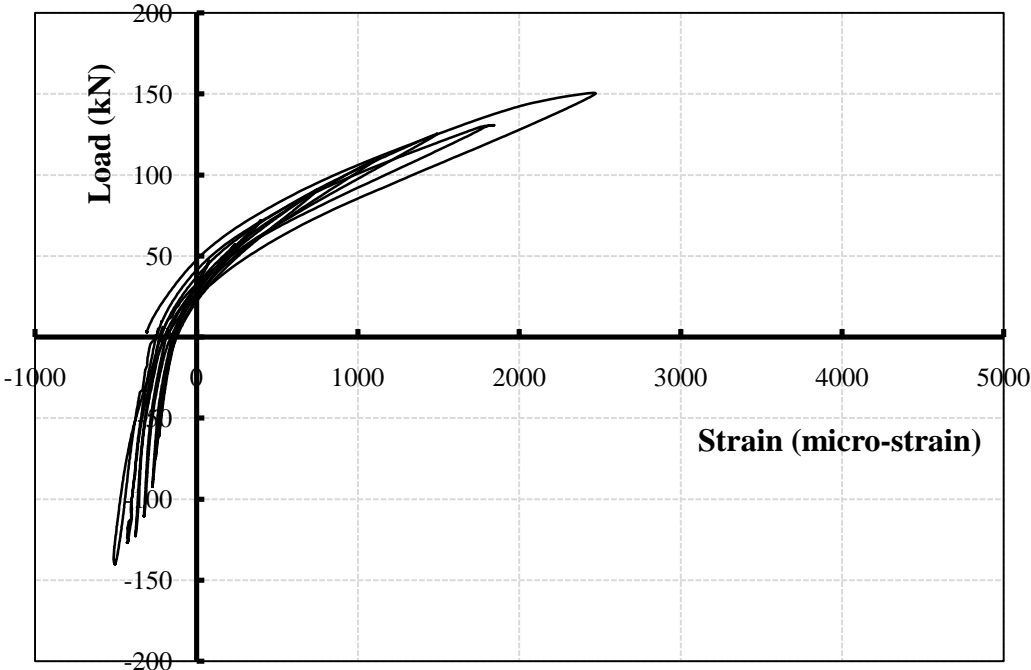
(b) Specimen GG12-B11-J12



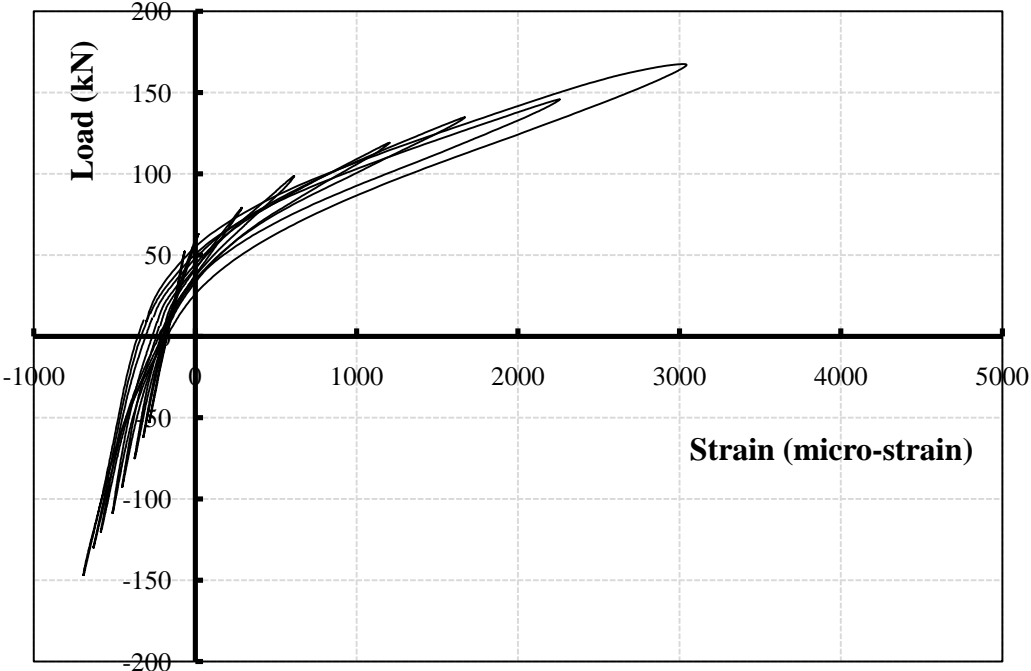
(c) Specimen GG17-B11-J12



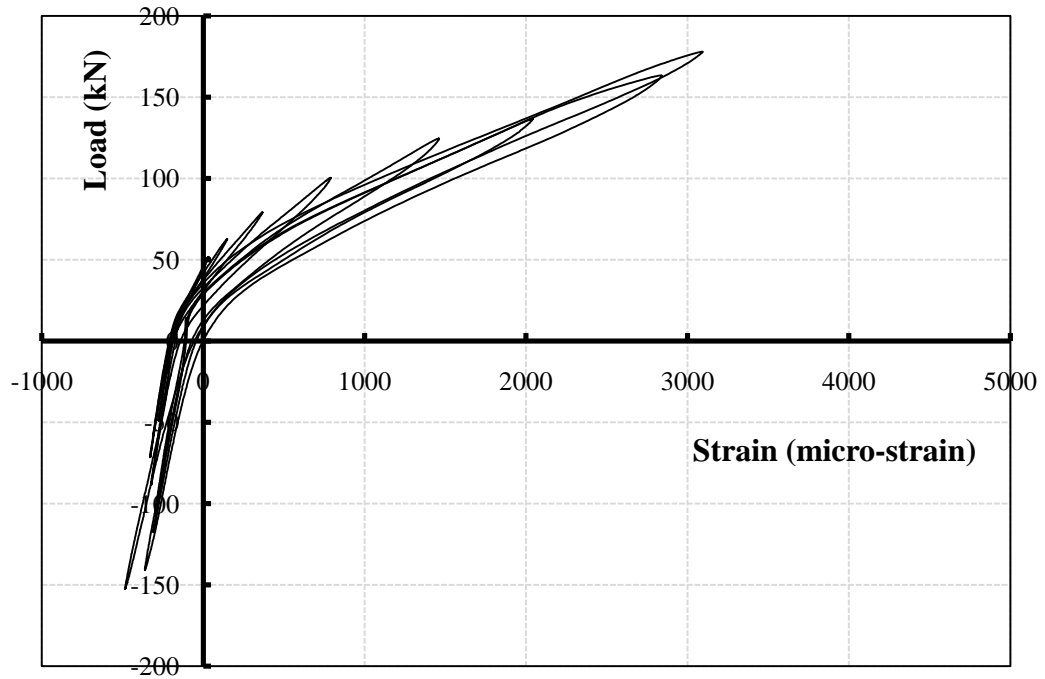
(d) Specimen GG29-B11-J12



(e) Specimen GS17-B11-J12



(f) Specimen GG17-B07-J12



(g) Specimen GG17-B11-J06

Figure 4.28: Behaviour of Steel and GFRP column bars under reversed loading

CHAPTER 5

NUMERICAL MODELLING

5.1 GENERAL

The numerical analysis in this thesis includes the construction of non-linear finite element model to simulate the seismic behaviour of beam-column joints totally reinforced with FRP. The available finite element software package, ANSYS program (ANSYS, Release 11 2007), was used for this purpose. The finite element analysis considered both geometrical and material non-linearity. The experimental results presented in Chapter 4 were used to calibrate the created finite element model. The calibrated model is then used to run a parametric study as shown in Chapter 6.

In the following sections, all the necessary steps to create the finite element (FE) model are explained in details. This includes the elements used to model the different materials, constitutive models for concrete, steel and FRP, meshing, boundary conditions and the solution method used. Finally, the FE model was verified against the experimental results obtained in Chapter 4.

5.2 ANSYS FINITE ELEMENT MODEL

5.2.1 Material Properties

5.2.1.1 Concrete material

An eight-node solid element, SOLID65, is used for the three-dimensional modeling of concrete. The most important aspect of this element is the treatment of nonlinear material properties. This element has the capability of cracking (in three orthogonal directions), crushing, plastic deformation and creep (if needed). The cracks in concrete are treated as

smearred bands, rather than discrete cracks, at the element integration points when the principal stress exceeds the concrete tensile strength and the material properties are adjusted accordingly. This shows the capability to model the softening behaviour of concrete as a result of sliding at individual cracks. The element is defined by eight nodes having three translational degrees of freedom at each node in the nodal x, y and z directions, as shown in Figure 5.1.

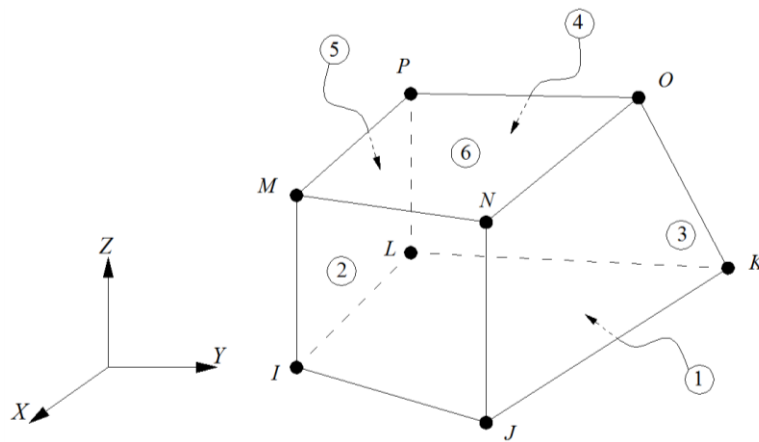


Figure 5.1: SOLID65 3-D concrete solid element (Reproduced from *ANSYS manual-Release 11, 2007*)

The SOLID65 element requires linear isotropic and multi-linear isotropic material properties to properly model concrete. The multi-linear isotropic material uses the Von-Mises failure criterion along with the Willam and Warnke model to define the failure of the concrete (ANSYS, Release 11 2007).

The modulus of elasticity of the concrete (E_c) and the Poisson's ratio (ν) are mandatory information for the material definition. The modulus was calculated based on Equation 5-1 with a value of f'_c equal to 32 MPa. Poisson's ratio was assumed to be 0.2.

$$E_c = 4500\sqrt{f'_c} \quad (5 - 1)$$

For normal strength concrete, a typical stress-strain model consists of two parts; ascending branch and descending branch, as shown in Figure 5.2. However, in the ANSYS software, the use of this ideal stress-strain curve with the descending part leads to convergence problems. In this study, the negative slope was ignored and the stress-strain relationship, shown in Figure 5.3, was used for the concrete material model in ANSYS as recommended by many researchers (Kachlakev et al. 2001; Wolanski 2004; Perera 2005; Gorji 2009; Ibrahim and Mahmood 2009; Büyükkaragöz 2010).

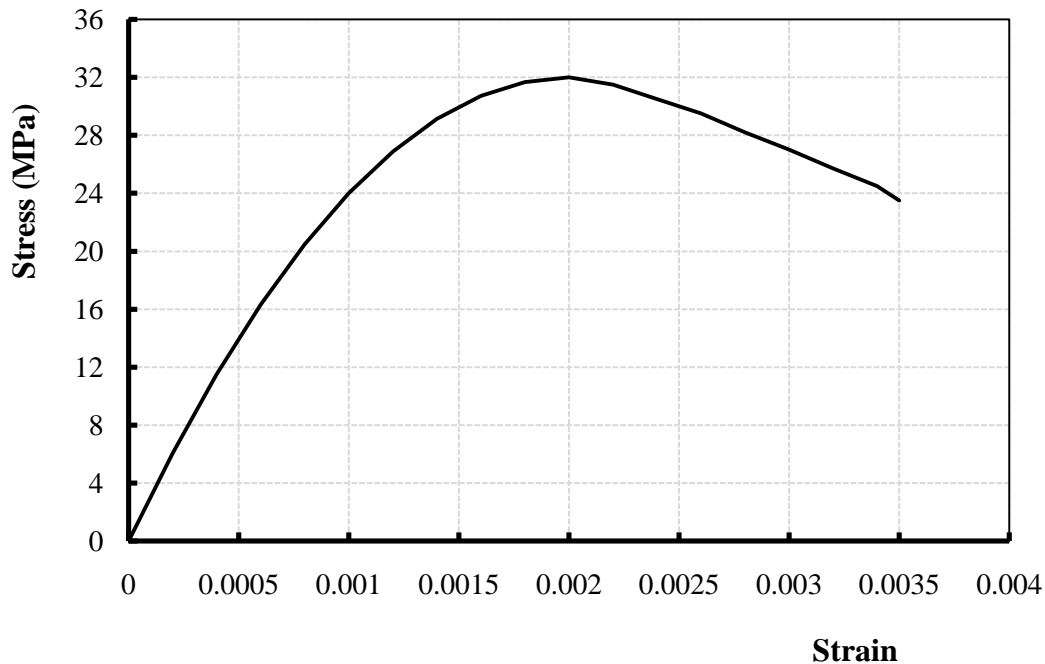


Figure 5.2: Standard stress-strain curve for 32 MPa concrete

The ascending branch for the concrete model followed the numerical expression in Equation 5-2 (Kent and Park 1971). Five points were adequate to well define the

parabolic curve. It is worth mentioning that the first point defined on the used stress-strain curve for concrete must satisfy Hook's Law considering the pre-defined Young's Modulus. The first point on the curve in Figure 5.3 represents the linear behaviour of concrete up to 40% of the ultimate compressive strength.

$$f_c = f'_c \cdot \left[\frac{2\varepsilon_c}{\varepsilon_0} - \left(\frac{\varepsilon_c}{\varepsilon_0} \right)^2 \right] \quad (5 - 2)$$

Where f_c and ε_c are the concrete stress and corresponding strain at any arbitrary point on the curve, and ε_0 is the concrete strain at the ultimate compressive strength f'_c .

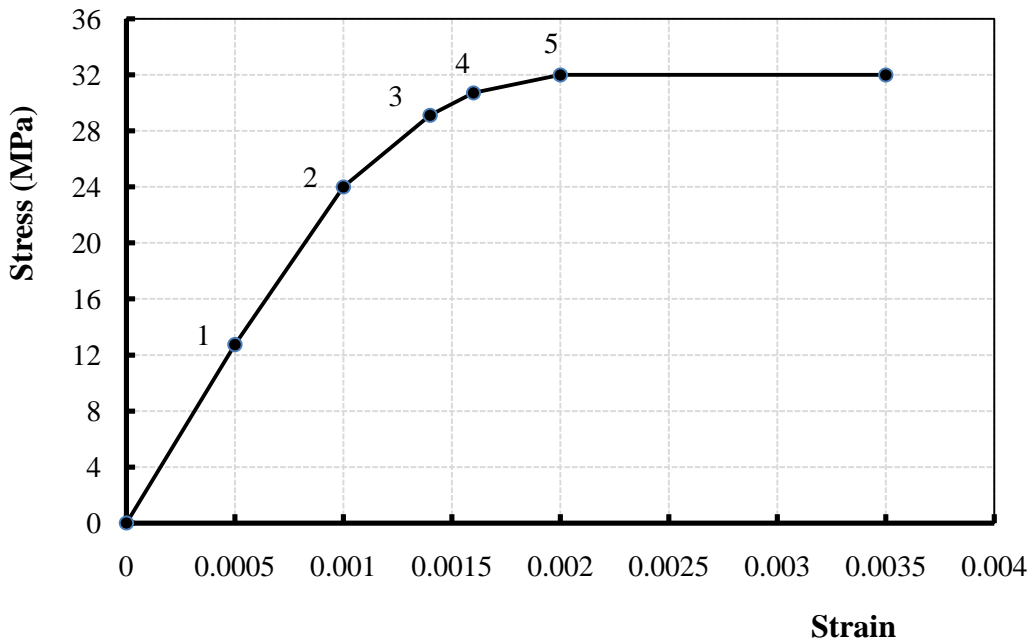


Figure 5.3: Simplified stress-strain curve for concrete used in FE model

For concrete, ANSYS requires four mandatory input data for material properties to be defined; open shear transfer coefficient, closed shear transfer coefficient, uni-axial cracking stress and uni-axial crushing stress. The shear transfer coefficients for open and

closed cracks represent the conditions at the crack face while it is open (loaded) or closed (reversed load), respectively. The value of these coefficients ranges from 0.0 to 1.0, with 0.0 representing a smooth crack (complete loss of shear transfer) and 1.0 representing a rough crack (no loss of shear transfer) (ANSYS, Release 11 2007). A shear transfer coefficient of 0.2 and 0.9 has been used for the open and closed situations, respectively. In addition, a value of 3.0 MPa, the average of all experimentally-obtained concrete tensile strengths for all tested specimens (Table 3.1 - Chapter 3), was used for the uniaxial cracking stress of concrete.

The geometry of the beam-column connection has a significant influence on the model. The existence of corners at the interface between beam and column is resulting in stress concentration which in turn leads not only to convergence problems but also to a pre-mature failure for the finite element model. Therefore, in this study, the concrete crushing capability was turned off to avoid such problems as recommended by many researchers (Kachlakev et al. 2001; Wolanski 2004; Mostofinejad and Talaeitaba 2006; Chansawat et al. 2009; Gorji 2009; Büyükkaragöz 2010).

5.2.1.2 Reinforcement materials

The reinforcement material was modeled using LINK8 element. The LINK8 element is a truss element that has one node at each end. Each node has three degrees of freedom; translations in the nodal x, y and z directions. The element is also capable of simulating plastic deformations. Figure 5.4 shows the geometry and node locations for this element type. This element was used to model the steel and FRP reinforcements (bars and stirrups).

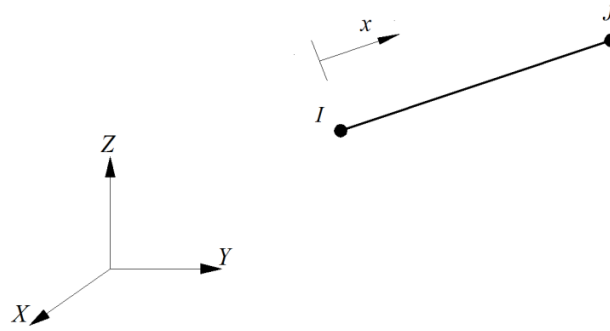


Figure 5.4: LINK8 3-D spar elements (Reproduced from *ANSYS manual-Release 11, 2007*)

The LINK8 element requires linear isotropic and bi-linear isotropic material properties to properly model steel reinforcement. For the FRP reinforcement modelling, linear-elastic material properties are used instead. Poisson's ratios of 0.3 and 0.2 were assumed for the steel and the FRP reinforcements, respectively. The used Young's Modulus were those obtained experimentally (Section 3.3.2 – Chapter 3). However, a tangent modulus of 5000 was assumed for the steel reinforcement to take the strain hardening effect into consideration. Figure 5.5 and Figure 5.6 show the stress-strain relationships for the steel and FRP reinforcement, respectively, used in this study.

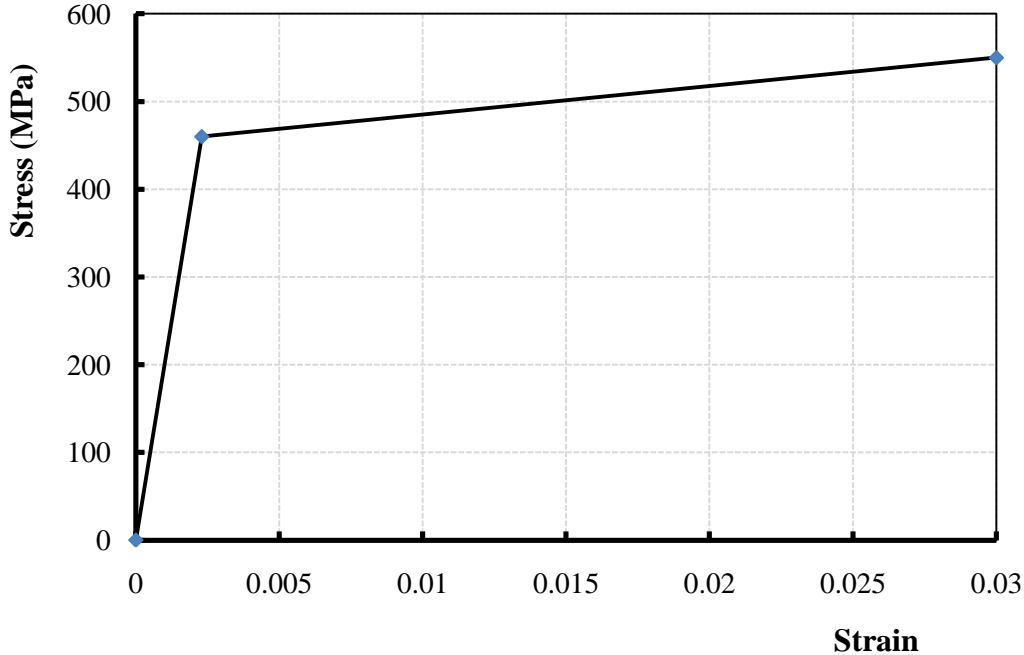


Figure 5.5: Stress-strain curve for steel reinforcement used in FE model

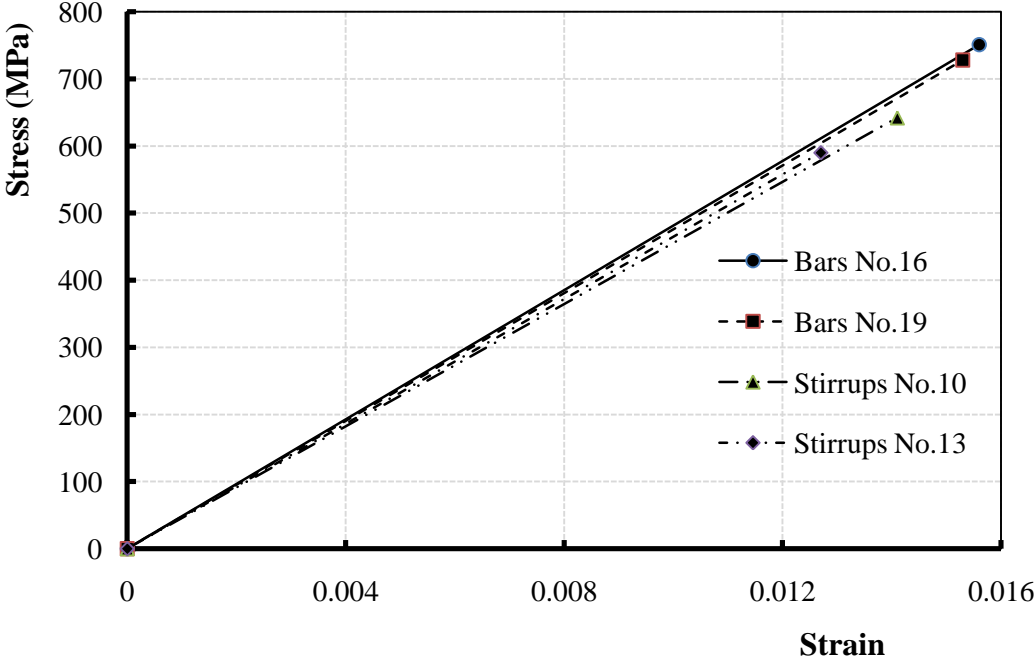


Figure 5.6: Stress-strain curve for GFRP reinforcement used in FE model

5.2.1.3 Loading and bearing plates

The steel plates that have been used at the support and loading locations were also modelled. Commonly, SOLID45 element is selected for this purpose. The SOLID45 element is an eight-node element having three degrees of freedom at each node; translations in the nodal x, y and z directions, as shown in Figure 5.7. This element has plasticity, creep, swelling, stress stiffening, large deflection and large strain capabilities.

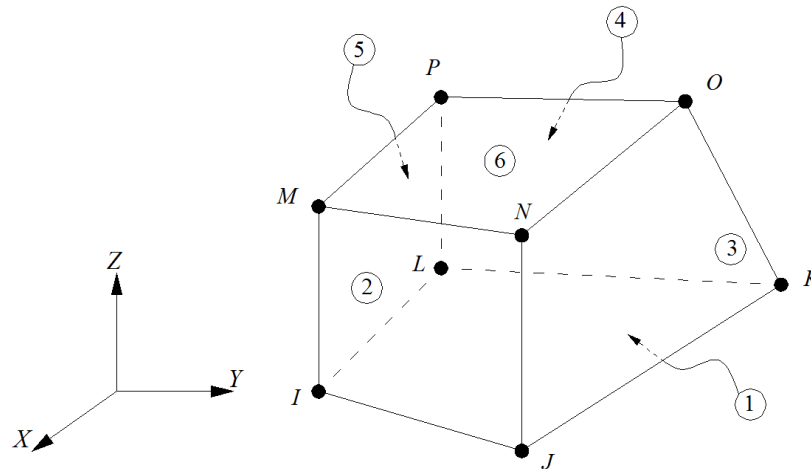


Figure 5.7: SOLID45 3-D solid element (Reproduced from *ANSYS manual-Release 11, 2007*)

The steel plates under the loading and support points have been modelled as a linear-elastic material with strain hardening ignored. Values of modulus of elasticity and Poisson's ratio used for the steel plates were similar to the steel reinforcement; 200 GPa and 0.3, respectively.

5.2.1.4 Concrete-reinforcement interface

Number of methods is available to model reinforced concrete elements. The two most common techniques are smeared modelling or discrete modelling. The smeared model assumes that reinforcement is uniformly distributed throughout the concrete elements in a defined region of the finite element mesh, as shown in Figure 5.8-a. This approach is preferable to be used only where the reinforcement location does not significantly contribute to the overall structure response. In the discrete model, the reinforcement elements have to be connected to the concrete mesh nodes. Therefore, the concrete and the reinforcement mesh share the same nodes, as shown in Figure 5.8-b. In this research, the discrete model concept was used.

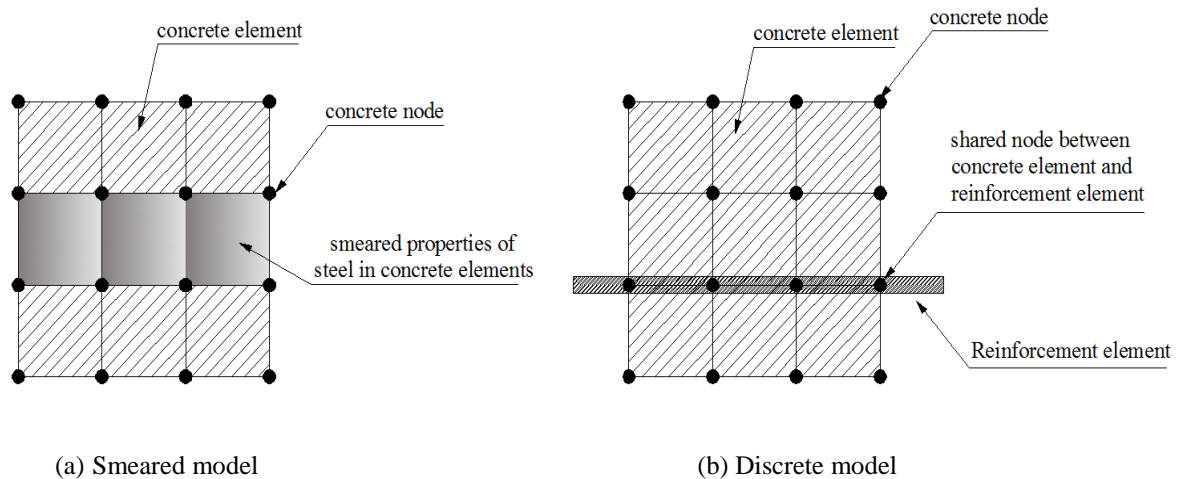


Figure 5.8: Models for reinforced concrete element (Reproduced from *Wolanski, 2004*)

Furthermore, there are two ways to simulate the bond between reinforcement and concrete elements. The first approach is to assume full contact between the concrete element nodes and reinforcement element nodes. In this case, both reinforcement and

concrete elements have to share the same node location and the same node numbering. This method can be adopted if no slippage is expected (perfect bond).

The second approach is to take the bond-slip relationship between the reinforcement bars and surrounding concrete into consideration. Thus, both reinforcement and concrete elements have to share the same node location, but different numbering should be assigned for each material nodes. In this case, non-linear spring elements are needed to represent the ability of the reinforcement nodes to slip from concrete nodes according to the bond-slip curve under consideration. The most common used spring element in modelling reinforced concrete structures is COMBIN39 element. The COMBIN39 is a unidirectional element with nonlinear generalized force-deflection capability that can be used in any analysis. The element has large displacement capability for which there can be two or three degrees of freedom at each node (ANSYS, Release 11 2007).

In this research, COMBIN39 was used to model the bond-slip effect between reinforcement and concrete. Two different bond-slip relationships were used in this study; one for steel and one for FRP bars. For the steel bars, the bond-slip model introduced by the CEB-FIP Model Code (CEB-FIP 1990) for unconfined concrete was used. The bond-slip model consists of ascending curve followed by descending and steady-constant lines as shown in Figure 5.9. The ascending portion of the model follows the numerical expression in Equation 5-3 (CEB-FIP 1990).

$$\tau = \tau_{max} \left(\frac{s_l}{0.6} \right)^{0.4} \quad (5 - 3)$$

Where τ and s_l are the bond stress and the corresponding slippage respectively. τ_{max} is the maximum bond strength for the steel bars embedded in concrete and can be

calculated according to Equation 5-4. Six points were enough to adequately define this curve. The descending portion of the model is linearly decreasing to the level of $0.15 \tau_{max}$. Finally, the third portion is a horizontal (constant) line as recommended by the CEB-FIP Model Code (CEB-FIP 1990) and shown in Figure 5.9.

$$\tau_{max} = 2.0 \sqrt{f'_c} \quad (5 - 4)$$

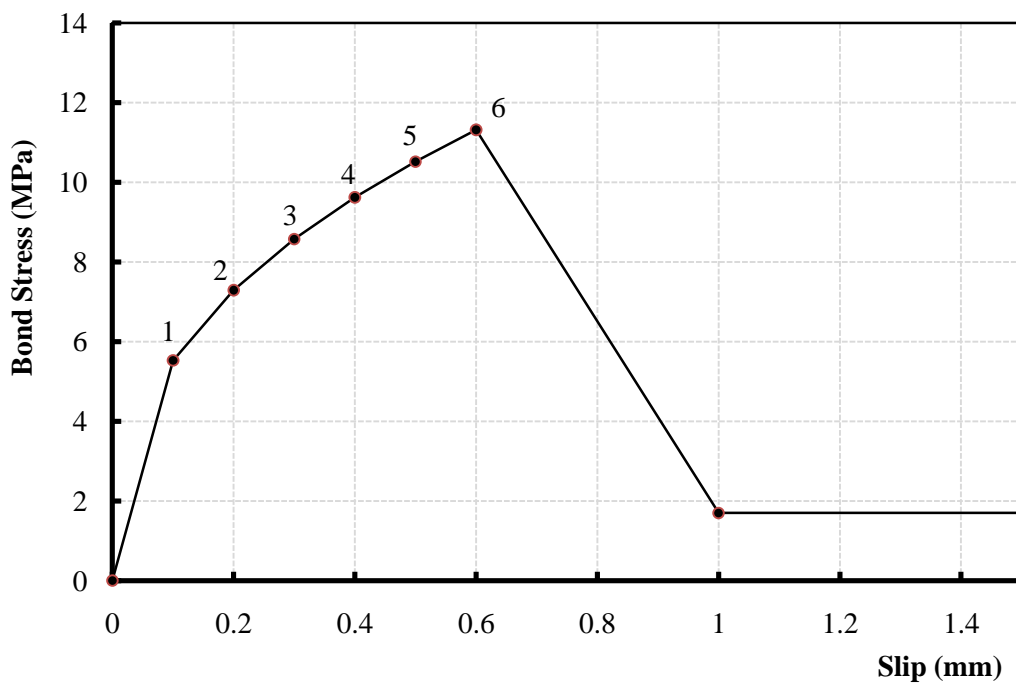


Figure 5.9: Bond-slip curve for ripped steel bars embedded in concrete

(Reproduced from CEB-FIP Model Code, 1990)

For the GFRP bars, the used bond-slip relationship was based on a recent work conducted at the University of Manitoba using the same GFRP bar (Alves et al. 2011). The obtained average bond-slip relationship from this research is shown in Figure 5.10.

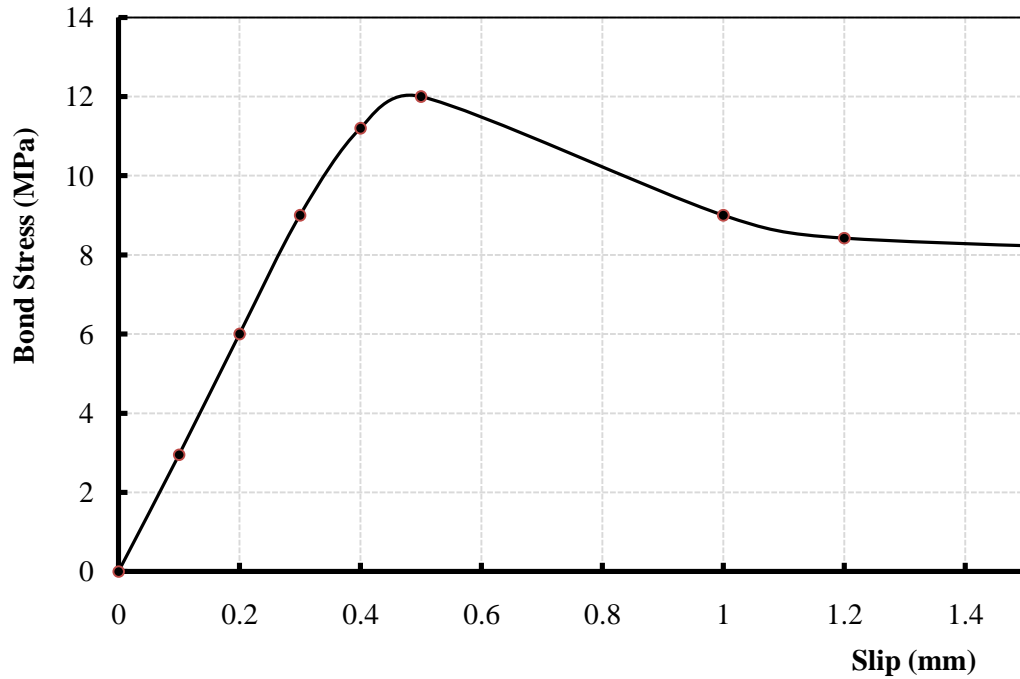
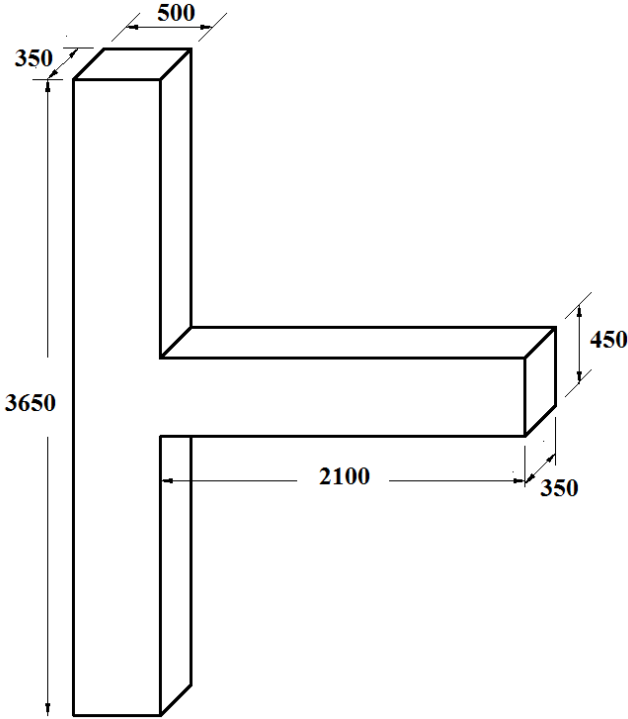


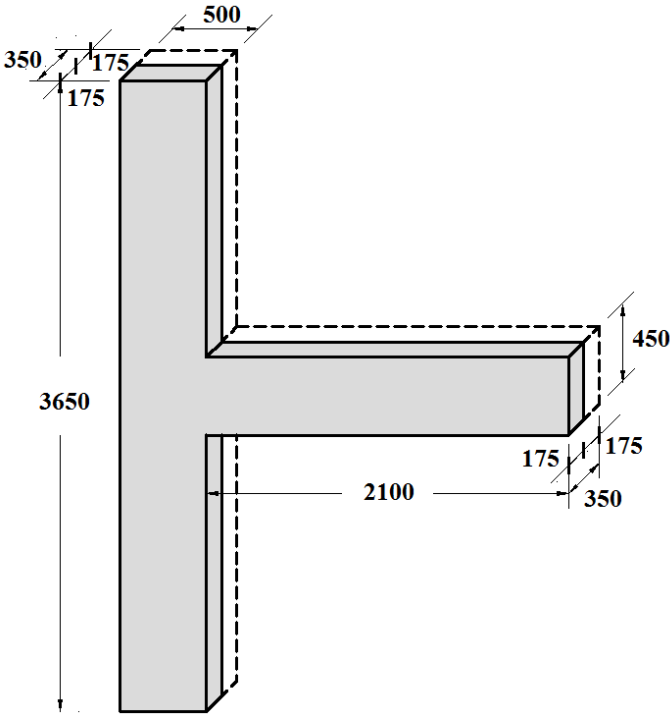
Figure 5.10: Bond-slip curve for GFRP bars embedded in concrete (*Reproduced from Alves et al., 2011*)

5.2.2 Geometry and Boundary Conditions

All test specimens were modelled in ANSYS taking the advantage of symmetry across the width of the beams and columns, as shown in Figure 5.11. This plane of symmetry was represented using relevant constrains in the finite element node points. This approach reduced computational time and computer disk space requirements significantly.



(a) Test connection



(b) Half symmetry model for the connection

Figure 5.11: Finite element model dimensions

All models were created to have the beam and column lengths in x-y plane; however, the width is located in the z-direction. To simulate the test conditions, column ends were restrained to simulate hinge supports at the left side and roller support at the right side, as shown in Figure 5.12. All nodes at the symmetry plane were prevented from the movement in z-direction to satisfy the symmetry requirements, as shown in Figure 5.13. A complete view of the finite element model and the internal reinforcement cage are shown in Figure 5.14 and Figure 5.15, respectively.

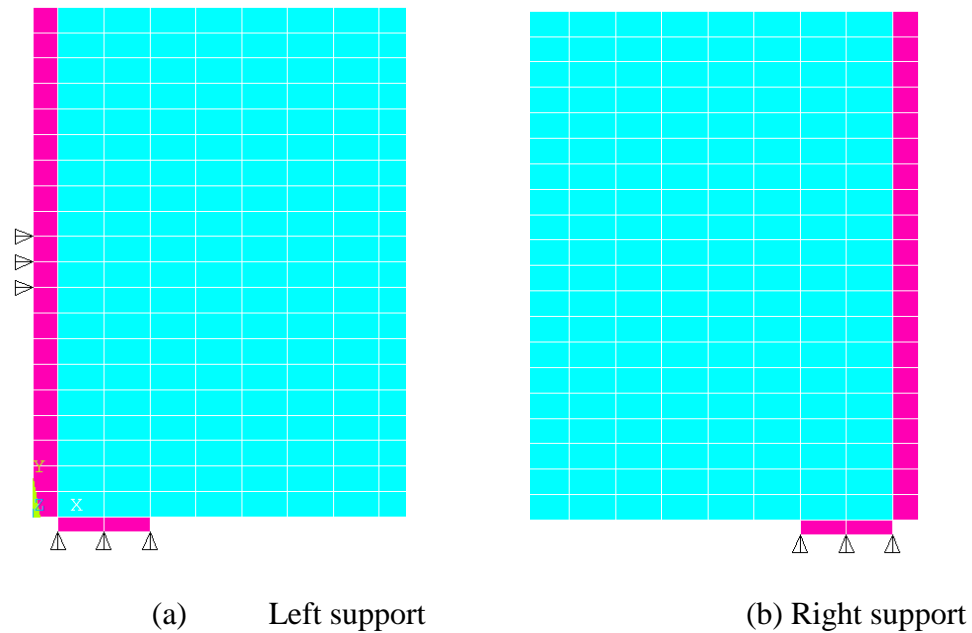


Figure 5.12: Boundary conditions for supports

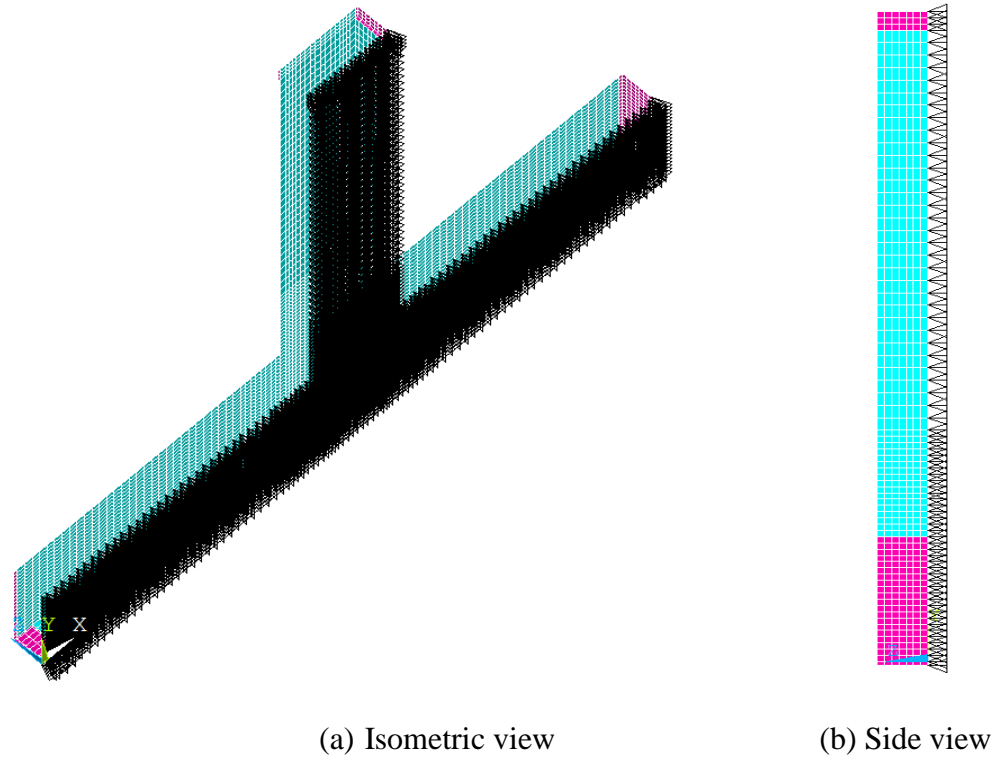


Figure 5.13: Boundary conditions for plane of symmetry

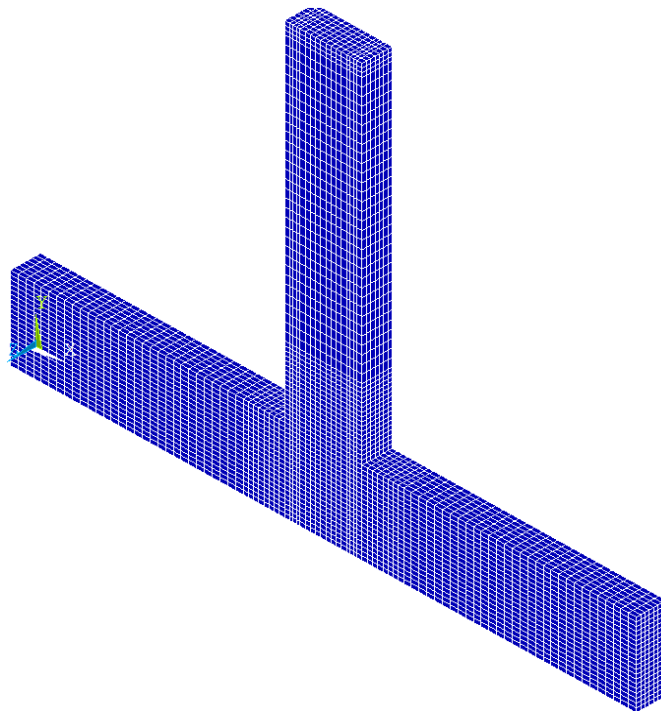


Figure 5.14: Full view for the finite element ANSYS model

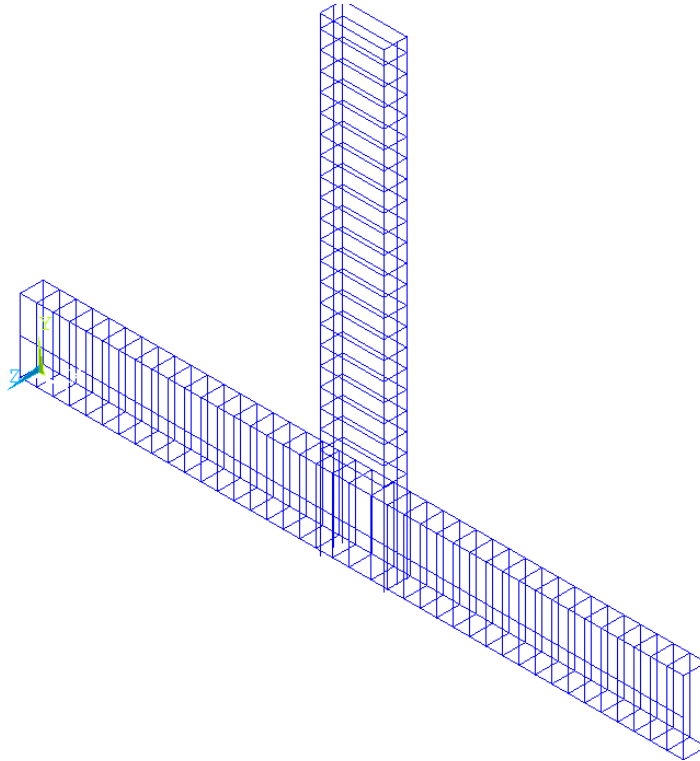


Figure 5.15: Full view for the internal reinforcement cage

5.2.3 ANSYS Solution Control

The ANSYS software gives the option to perform a geometric non-linear solution for the model under consideration. This option was selected in the current study. In non-linear FE analysis, the total load applied to a structure is divided into a series of load increments. Each load increment is assigned a specific amount of load in the specified direction. To ensure accurate results and faster convergence, each load increment would be divided into a number of equal steps. At the completion of each load increment, the stiffness matrix of the model is adjusted to reflect the non-linear changes in structural stiffness before proceeding to the next load increment. Newton-Raphson equilibrium iterations technique was selected for updating the model stiffness.

Newton-Raphson equilibrium iterations provide convergence at the end of each load increment within tolerance limits. Prior to each solution, the Newton-Raphson approach assesses the out-of-balance load vector, which is the difference between the restoring forces (the loads corresponding to the element stresses) and the applied loads, and checks for convergence. If convergence criteria are not satisfied, the out-of-balance load vector is re-evaluated, the stiffness matrix is updated, and a new solution is attained. This iterative procedure continues until the problem converges (ANSYS, Release 11 2007).

5.3 MODEL VERIFICATION

In this section, the output of the finite element model was verified against the experimental results presented in Chapter 4. Three specimens were selected for the verification process including SS03-B06-J06, GG17-B11-J12 and GG29-B11-J12. These specimens were selected to show the validity of the FE model for modelling both steel and FRP-reinforced joints, and also to prove that the model is capable of capturing the change in behaviour associated with different FRP reinforcement ratios. The comparison was performed with respect to the hysteretic behaviour and the strain measurements in the beam and column longitudinal bars.

5.3.1 Specimen SS03-B06-J06

Figure 5.16 shows the hysteretic behaviour for the steel-reinforced specimen SS03-B06-J06; both experimentally and analytically. The FE model was able to show a similar trend for the fat-hysteretic/cyclic behaviour for the steel-reinforced specimen, however, the stiffness of the modelled specimen in the negative loading direction was higher than the

experimental one. The hysteretic diagram shows that the model reached the same drift ratio that was observed in the experimental test (5.00% drift ratio) with corresponding load capacity of 188 kN. This capacity was higher than the experimental one by approximately 5%. The mode of failure of the model was a concrete crushing in the beam sections near the column face matching with the experimental observations.

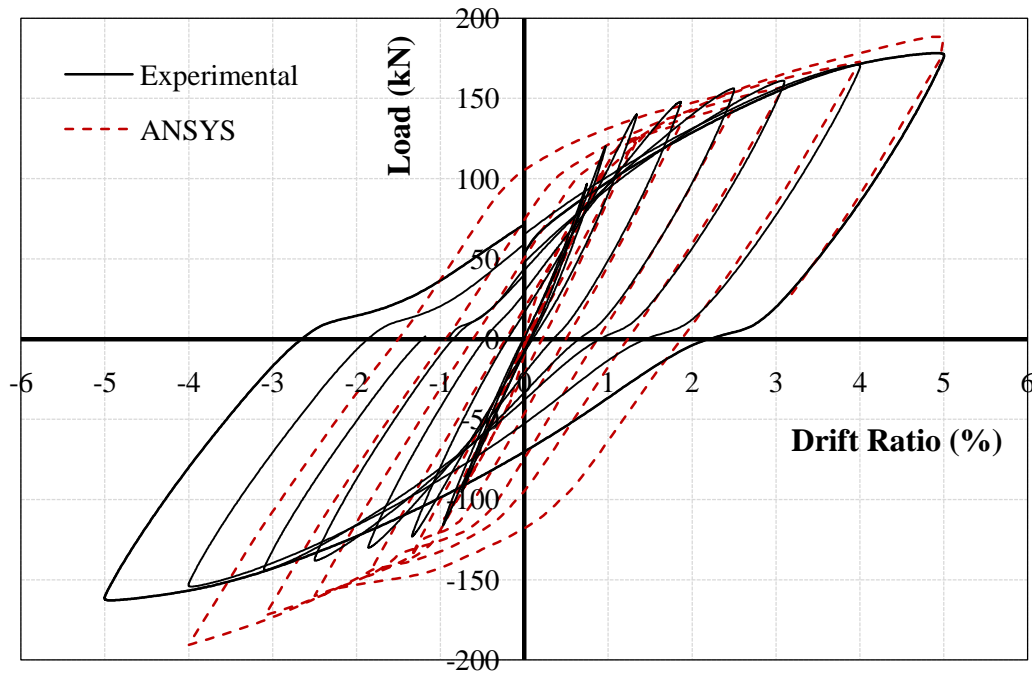


Figure 5.16: Hysteretic behaviour comparison for specimen SS03-B06-J06

For better understanding the hysteretic behaviour, the load-lateral drift envelope for all cycles was shown in Figure 5.17. The FE model was able to capture the same stiffness as the experimental test till 1.00% drift ratio; however, the stiffness of the model after yielding occurred was higher than the experimental test especially in the negative loading direction. The maximum capacities observed were at 5% and 4% drift ratios for the positive and negative loading directions, respectively. The reason behind this that

after completing the 4% drift ratio-seismic step, the model failed at 5% drift ratio in the positive direction. The program stopped immediately without completing the cycle of the 5% drift ratio. Also, the FE model was able to capture the same yielding point as the experimental test. This observation was confirmed by the maximum measured strains on the beam longitudinal bars from Figure 5.18. Figure 5.18 shows that the strains calculated by ANSYS agree well with those from the experimental results for the beam longitudinal bars up to 1.85% drift ratio with maximum differences not exceeding 6%. Then, the strains from the FE model kept increasing till the failure of the model. Also, Figure 5.19 shows that the strains calculated by ANSYS are exactly equal to those from the experimental results for the column longitudinal bars up to 2.50% drift ratio. All these observations prove the applicability of the bond-slip model from CEB-FIP model code (1990), for steel reinforcement, for the FE analysis in this study.

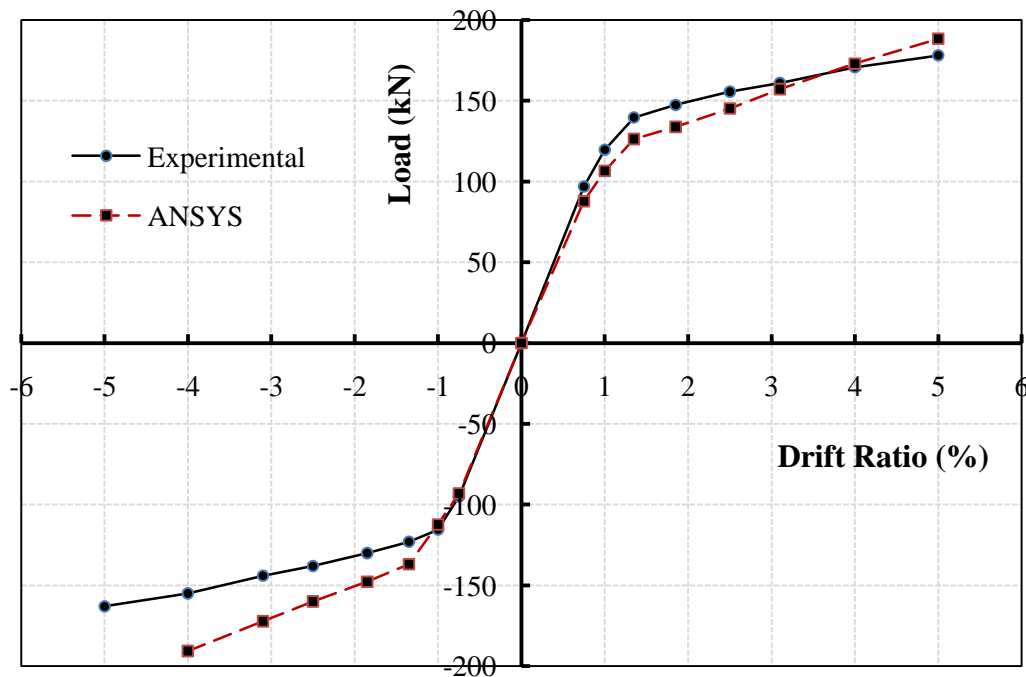


Figure 5.17: Load-drift relationship envelopes for specimen SS03-B06-J06

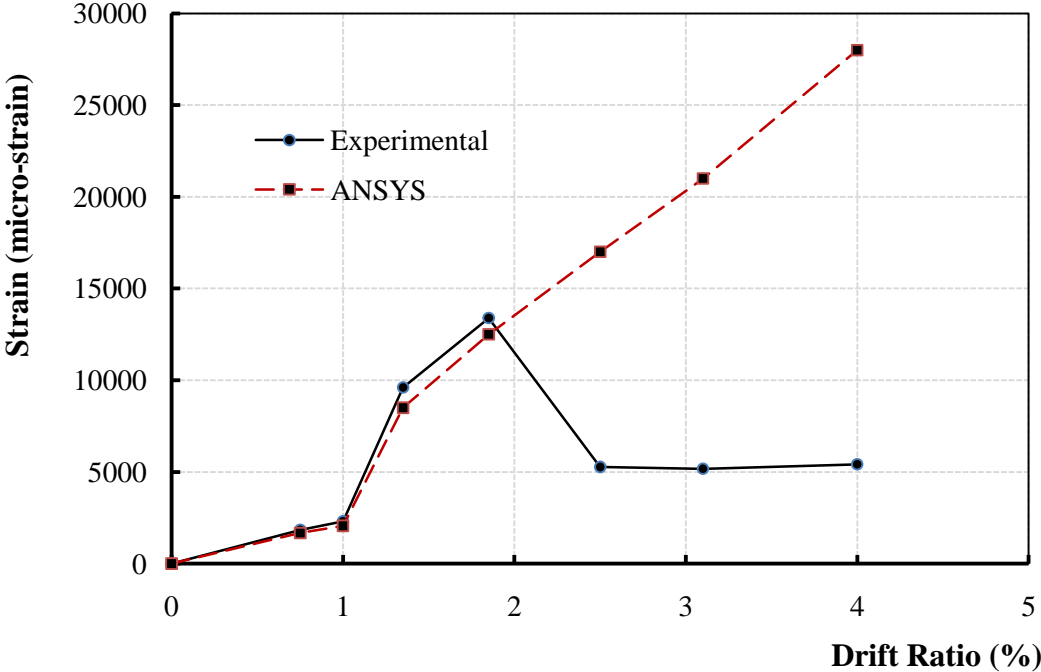


Figure 5.18: Strain comparison of beam longitudinal bars for specimen SS03-B06-J06

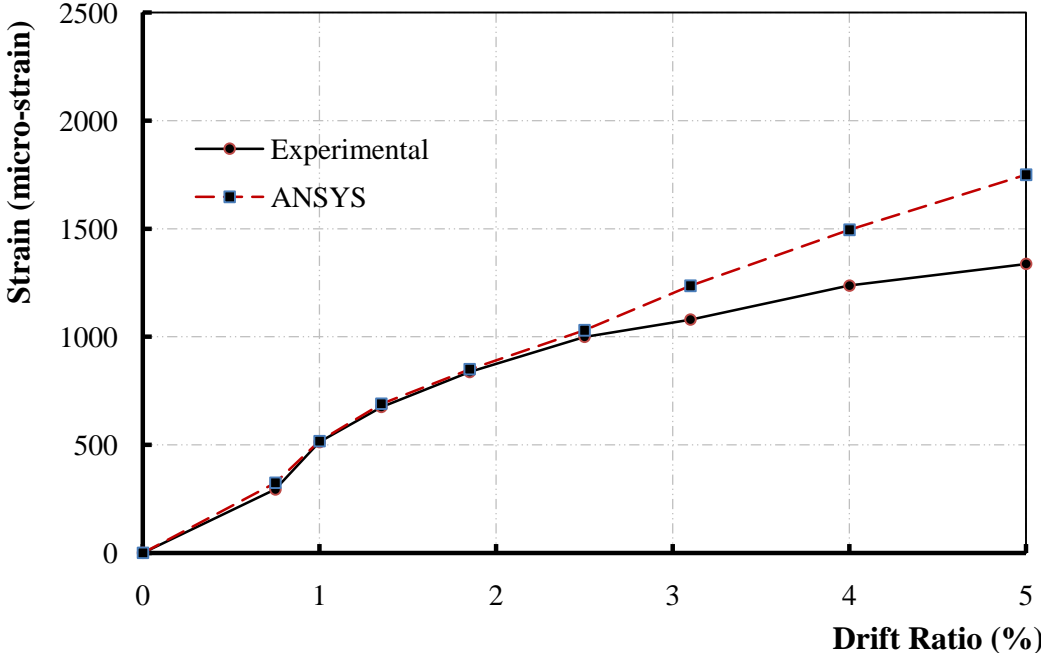


Figure 5.19: Strain comparison of column longitudinal bars for specimen SS03-B06-J06

5.3.2 Specimen GG17-B11-J12

Figure 5.20 shows the hysteretic behaviour for specimen GG17-B11-J12; both experimentally and analytically. The FE model was able to show a similar trend for the hysteretic/cyclic behaviour for the FRP-reinforced specimen. The model showed linear-elastic behaviour till failure occurred. The hysteretic diagram shows that the model kept carrying capacity till failure started at the same drift ratio that was observed in the experimental test (4.00% drift ratio) with corresponding load capacity of 156 kN. This capacity was higher than the experimental one by only 4%. The model failure was a concrete crushing in the beam section close to the column face matching with the experimental observations.

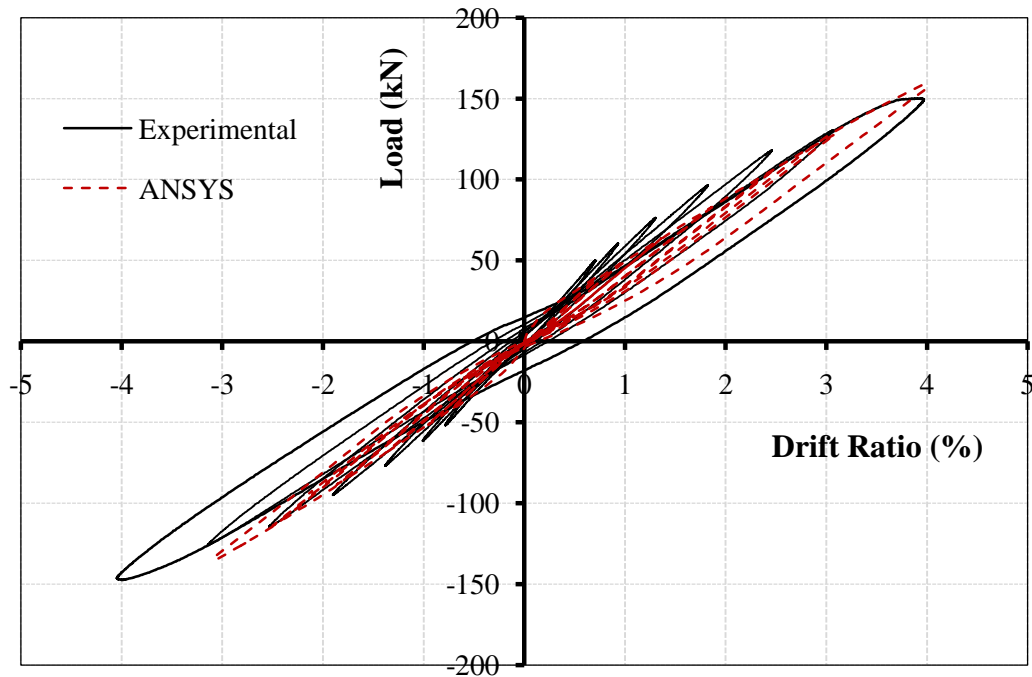


Figure 5.20: Hysteretic behaviour comparison for specimen GG17-B11-J12

Figure 5.21 shows the load-lateral drift envelope comparison for the specimen GG17-B11-J12. The average stiffness of the FE model was higher than the experimental one by approximately 7%. The bond-slip model used for the GFRP reinforcement seems to be sufficient to describe the interaction between concrete elements and the FRP reinforcement. This observation can be also proved through the maximum measured strains on the beam and column longitudinal bars from Figures 5.22 and 5.23, respectively. Figure 5.22 shows that the model captured exactly the same experimentally measured strain at failure. Before failure, the model was able to follow the same trend as the experimental one with maximum differences did not exceed 15%. Also, Figure 5.23 shows that not only the model was able to follow the same trend as the experimental one but also captured the same column longitudinal bars strain values as the experimental ones at the majority of the points with maximum differences did not exceed 10%.

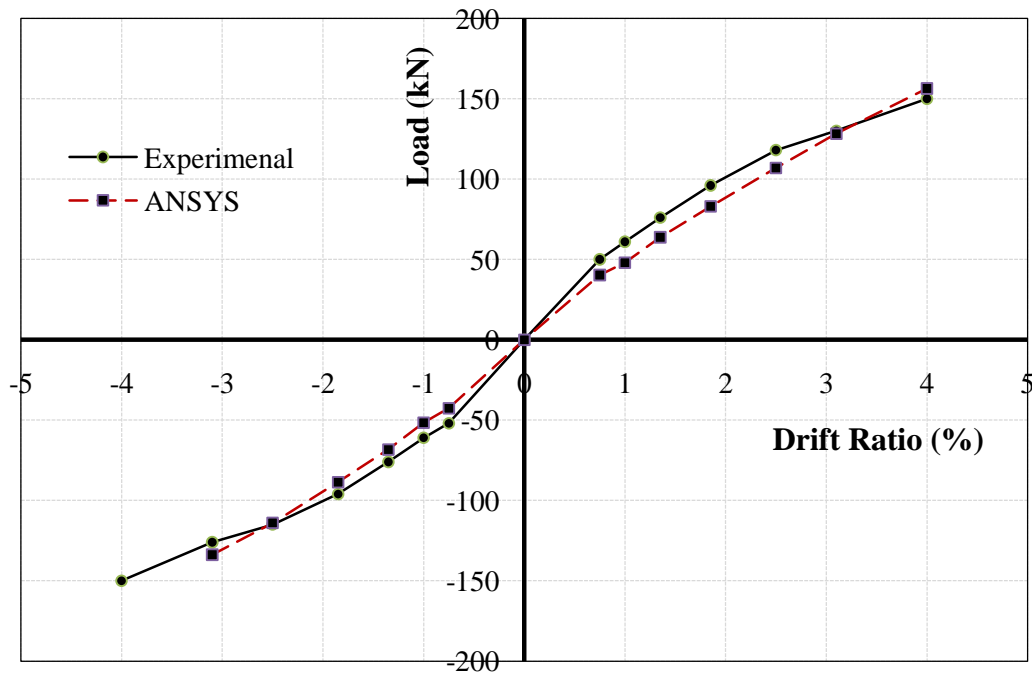


Figure 5.21: Load-drift relationship envelopes for specimen GG17-B11-J12

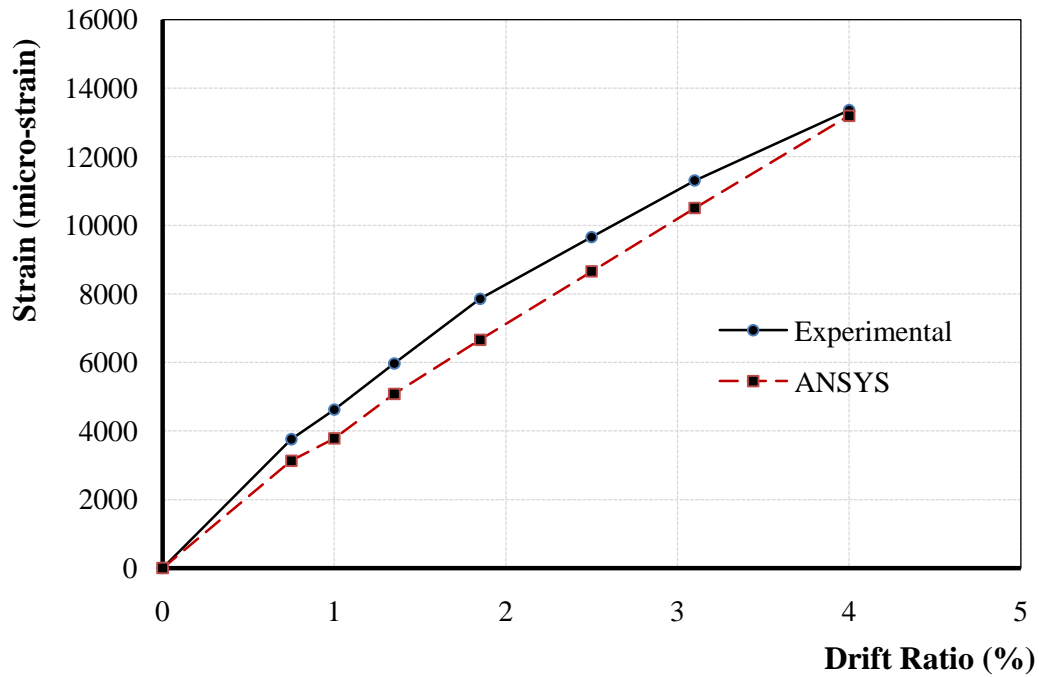


Figure 5.22: Strain comparison of beam longitudinal bars for specimen GG17-B11-J12

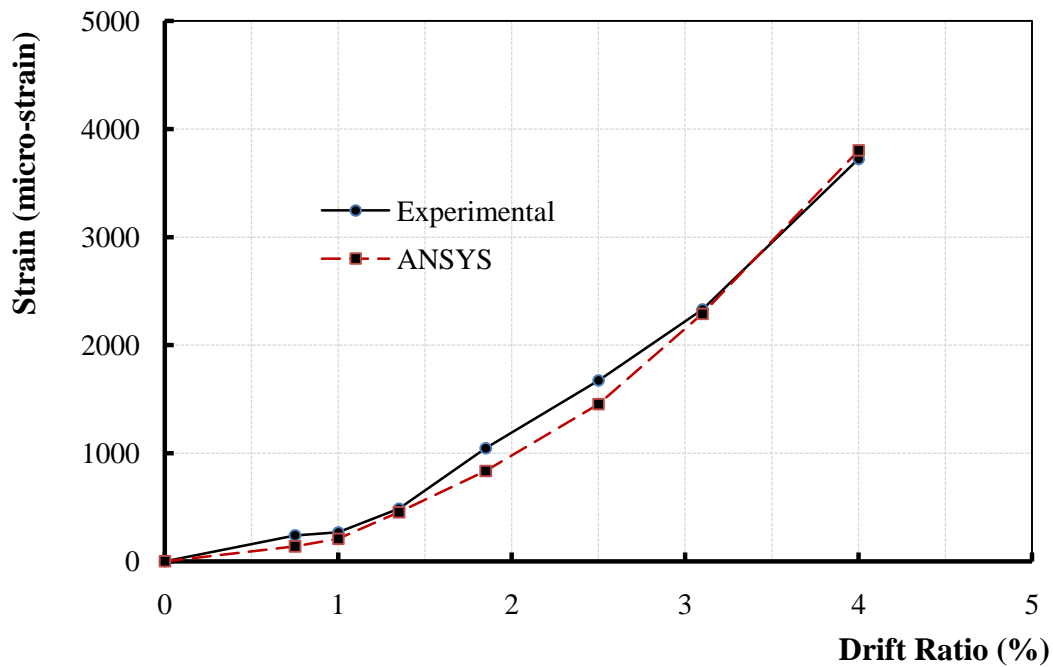


Figure 5.23: Strain comparison of column longitudinal bars for specimen GG17-B11-J12

5.3.3 Specimen GG29-B11-J12

Figure 5.24 shows the hysteretic behaviour for specimen GG29-B11-J12; both experimentally and analytically. Again, the FE model was able to show a similar trend for the hysteretic/cyclic behaviour for the FRP-reinforced specimen. The model showed linear-elastic behaviour till failure occurred. The hysteretic diagram shows that the model kept carrying capacity till failure started at the same drift ratio that was observed in the experimental test (4.00% drift ratio) with corresponding load capacity of 184 kN. This capacity was higher than the experimental one by approximately 7%. The failure mode of the FE model was a concrete crushing at the beam sections close to the column face, which is matching with the experimental observations at 4.00% drift ratio.

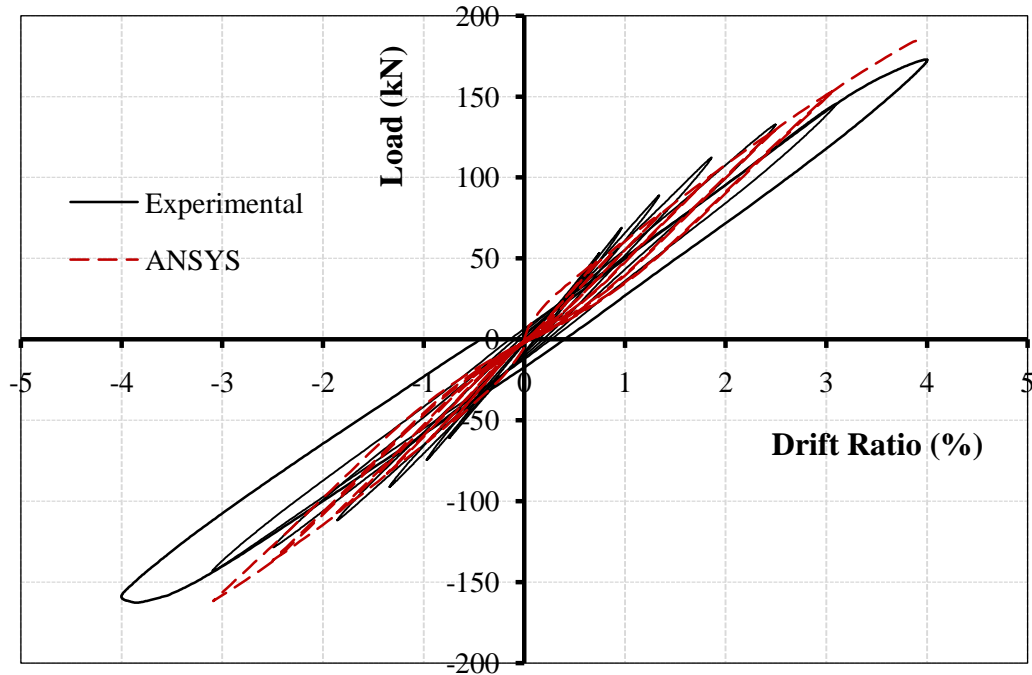


Figure 5.24: Hysteretic behaviour comparison for specimen GG29-B11-J12

Figure 5.25 shows the load-lateral drift envelope comparison for the specimen GG29-B11-J12. Again, the FE model proved its capability to accurately predict the experimental behaviour. The average stiffness of the FE model was lower than the experimental one by approximately 6%. The bond-slip model used for the GFRP reinforcement also proved to be sufficient to describe the interaction between concrete elements and the FRP reinforcement. The maximum measured strains on the beam longitudinal bars from Figure 5.26 seem to agree well with the experimentally measured ones with maximum differences did not exceed 10%. Also, Figure 5.27 shows that the column longitudinal bars' strains from the FE model agree well with the experimentally observed ones till 3.10% drift level with maximum differences did not exceed 10%.

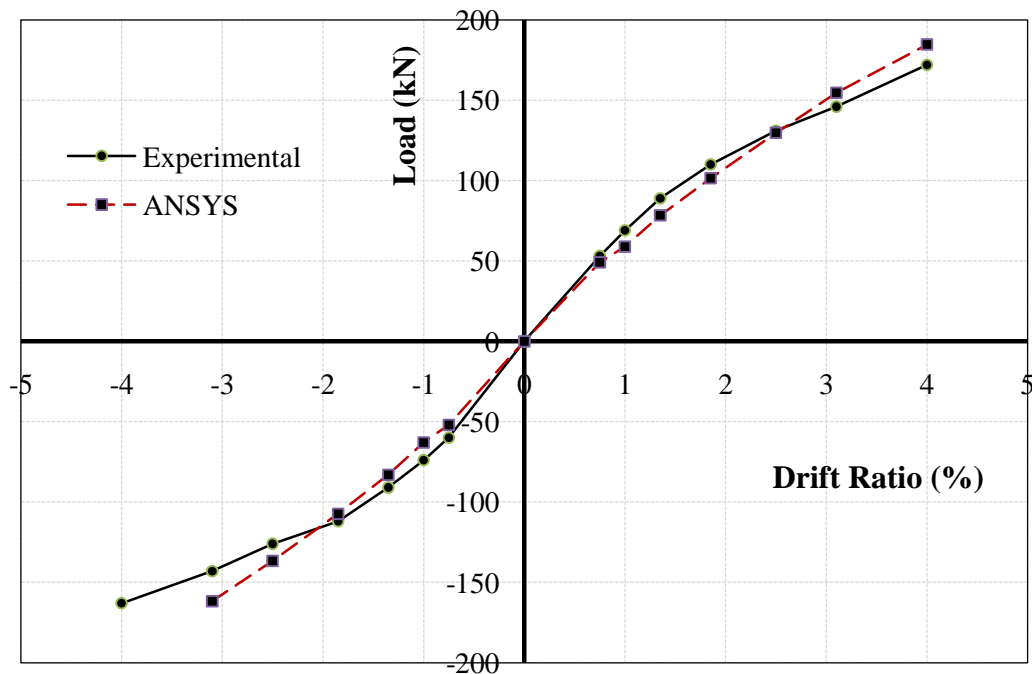


Figure 5.25: Load-drift relationship envelopes for specimen GG29-B11-J12

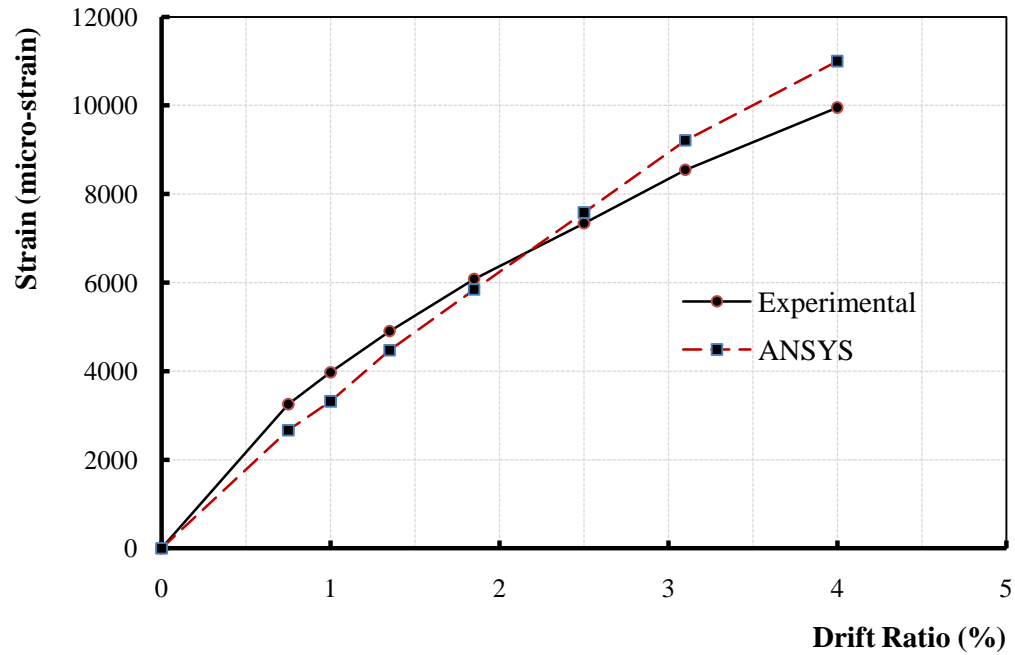


Figure 5.26: Strain comparison of beam longitudinal bars for specimen GG29-B11-J12

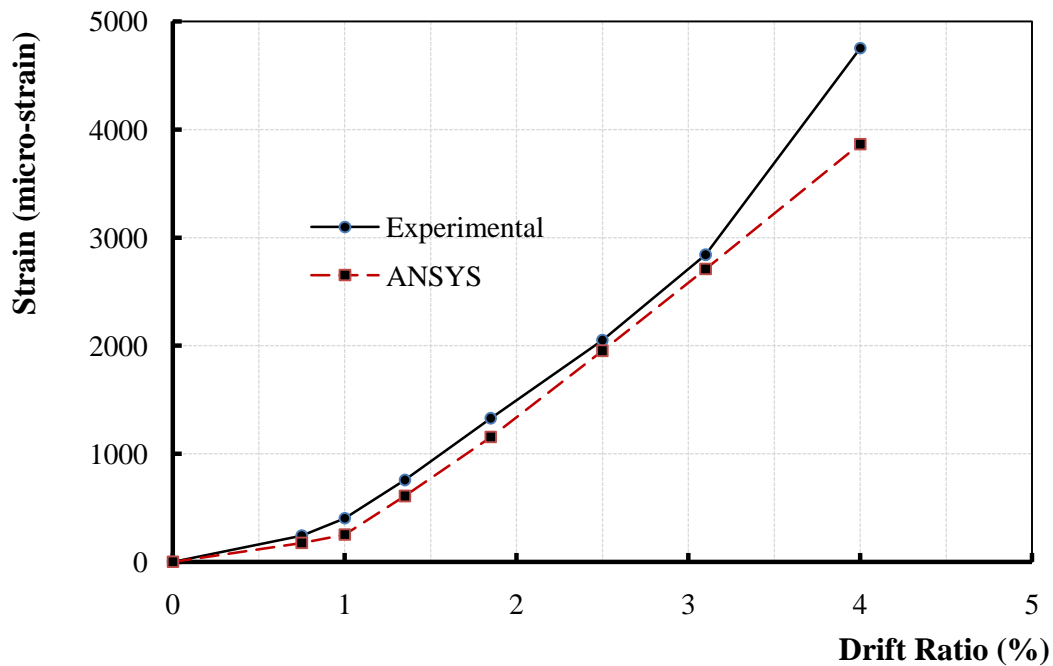


Figure 5.27: Strain comparison of column longitudinal bars for specimen GG29-B11-J12

5.4 REMARKS

The results from the finite element model were able to accurately predict the hysteretic behaviour and the developed strains in both beam and column longitudinal reinforcement for all FRP-reinforced specimens. However, the program was not able to predict post-failure behaviour of concrete, where the program solution is showing difficulties in convergence once failure started.

Accordingly, the FE model can be used to perform a parametric study to investigate the influence of key parameters on the behaviour of FRP-reinforced beam-column joints. The results of this parametric study are shown in Chapter 6.

CHAPTER 6

PARAMETRIC STUDY

6.1 GENERAL

The finite element model (FEM) for FRP-RC beam-column connections constructed in this study was used to investigate some of the parameters known to affect the performance of such joints. The parameters studied included the column axial load, the concrete compressive strength, the flexural strength ratio and the joint transverse reinforcement.

Finite element models with identical geometry and reinforcement details as discussed in Chapter 5 were used to carry out the parametric study. The FEM of the reference specimen, GG17-B11-J12, was selected for the majority of the tested parameters, unless otherwise mentioned, as it represents the control specimen for the experimentally-tested GFRP-reinforced connections (Chapter 3). The following sections present the details of the FEM and the studied parameters.

6.2 STUDIED PARAMETERS

6.2.1 Column Axial Load

The selected FEM (specimen GG17-B11-J12) considered a range from zero to 70% ($N = 0$ to $0.7 N_{\max}$) of the column axial capacity with 5% increments for each run. The results of these runs were compared in terms of the envelope of the hysteric behaviour and the corresponding mode of failure, and the developed strains in the beam and column longitudinal reinforcement.

Figure 6.1 shows envelopes of the load-drift relationships for selected axial load ratios for clarity. The connection without axial load showed the lowest capacity in both positive (pushing) and negative (pulling) direction of loading. The failure for this connection occurred in the joint core at 3.1% drift ratio due to the absence of confinement. Also, the connection with axial load equals 5% of the column capacity ($N = 0.05 N_{\max}$) failed in the joint area; however, at higher drift ratio of 4%. Starting at axial load level equals to 10% of the column axial capacity, no joint failure was observed. All investigated connections, except the one with 70% axial load level ($N = 0.7 N_{\max}$), failed due to concrete crushing in the beam sections. Figure 6.2 summarizes the mode of failure and the corresponding drift capacity for each axial load ratio.

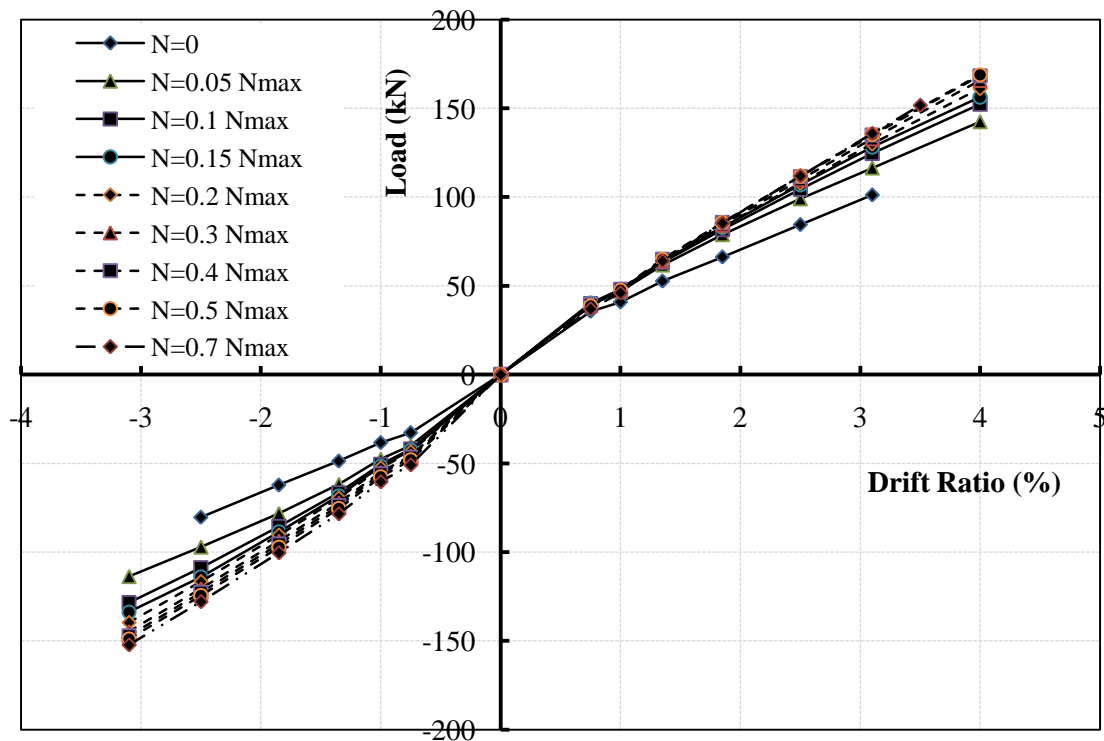


Figure 6.1: Load-drift relationship envelopes under various column axial loads for specimen GG17-B11-J12

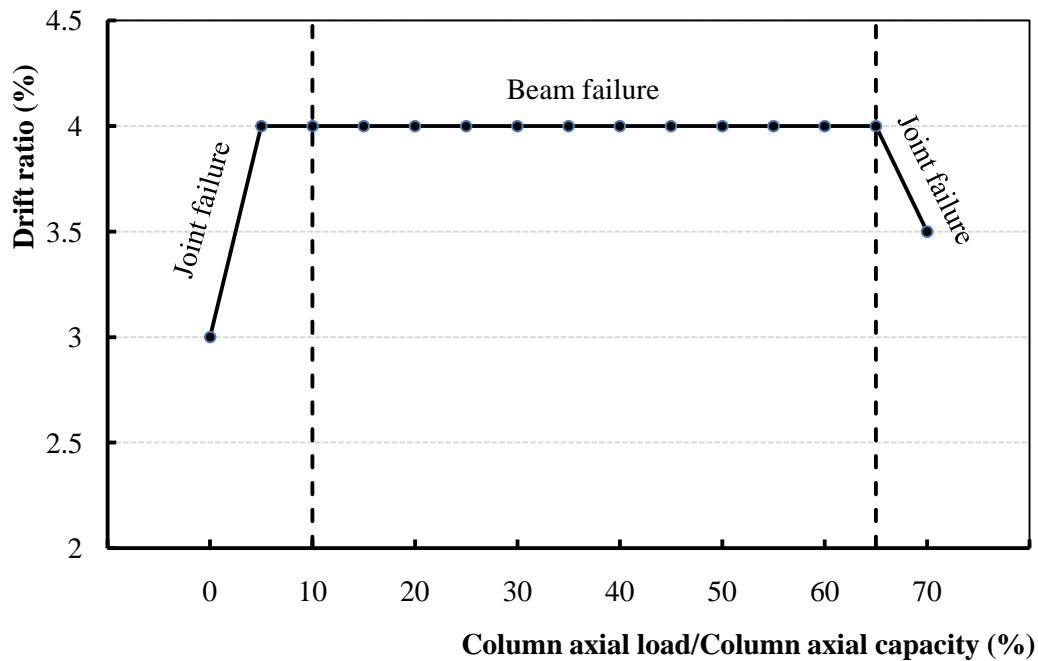


Figure 6.2: The mode of failure and the corresponding drift capacity for each column axial load ratio

Also, it was observed from Figure 6.1 that increasing the axial load provided more confinement for the connection, which in turn resulted in an increase in the lateral load capacity. At the same drift ratio of 4%, increasing the column axial load from 5% to 30% resulted in increasing the lateral load capacity by approximately 22% and 33% in the positive and negative directions, respectively.

However, in the range of 35 to 65% of the column axial capacity, no significant increase in the lateral load capacity was observed. All connections failed at 4% drift ratio. At axial load level of 70% of the column capacity, the lateral load capacity started to decrease as the connection failed in the joint core at 3.5% drift ratio. This was due to the higher compressive stresses developed in the joint core as a result of the high level of column axial force.

Figures 6.3 and 6.4 show the beam and column longitudinal bars' strains-drift relationships, respectively. Similar observations can be made through the strain measurements. Figure 6.3 shows that, at the same drift ratio of 4%, increasing the column axial load from 5 to 30% ($N = 0.05$ to $0.3 N_{\max}$) resulted in increasing the developed strains in the beam longitudinal bars by approximately 20%.

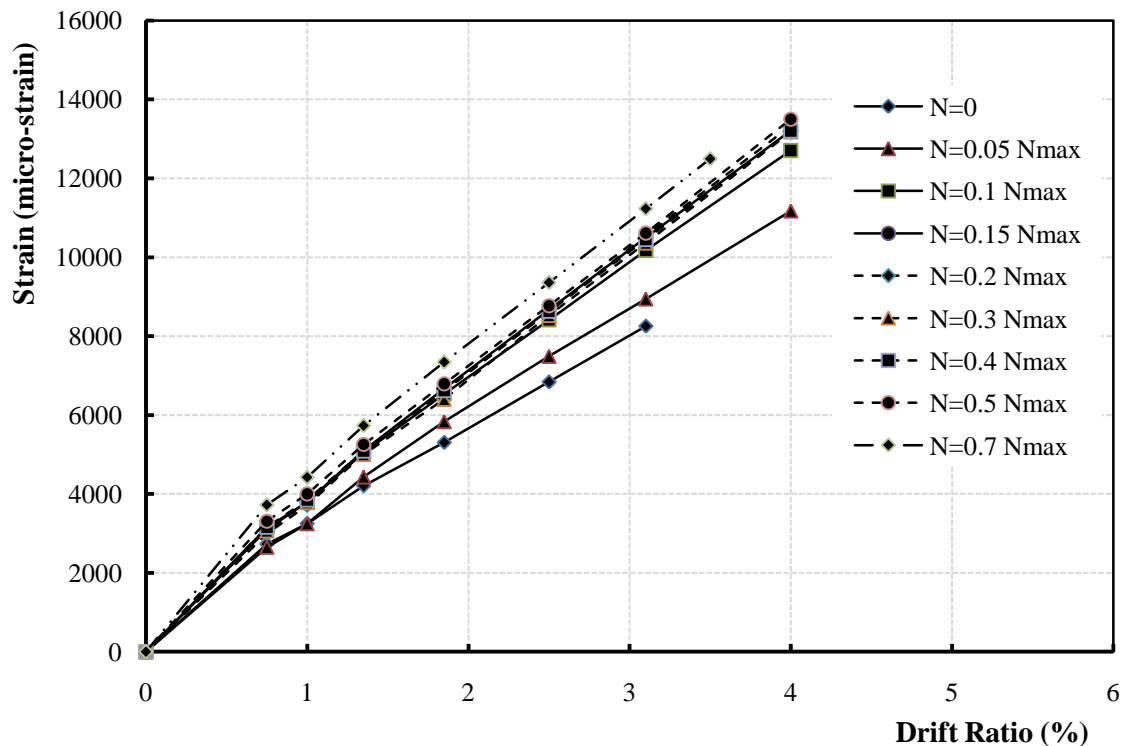


Figure 6.3: Strain comparison of beam longitudinal bars under various column axial loads for specimen GG17-B11-J12

Figure 6.4 shows that increasing the column axial load resulted in decreasing the tensile strains and increasing the compressive strains in the column longitudinal bars. At 40% column axial load level ($N = 0.4 N_{\max}$), no tensile strains at all were detected in the column cross sections.

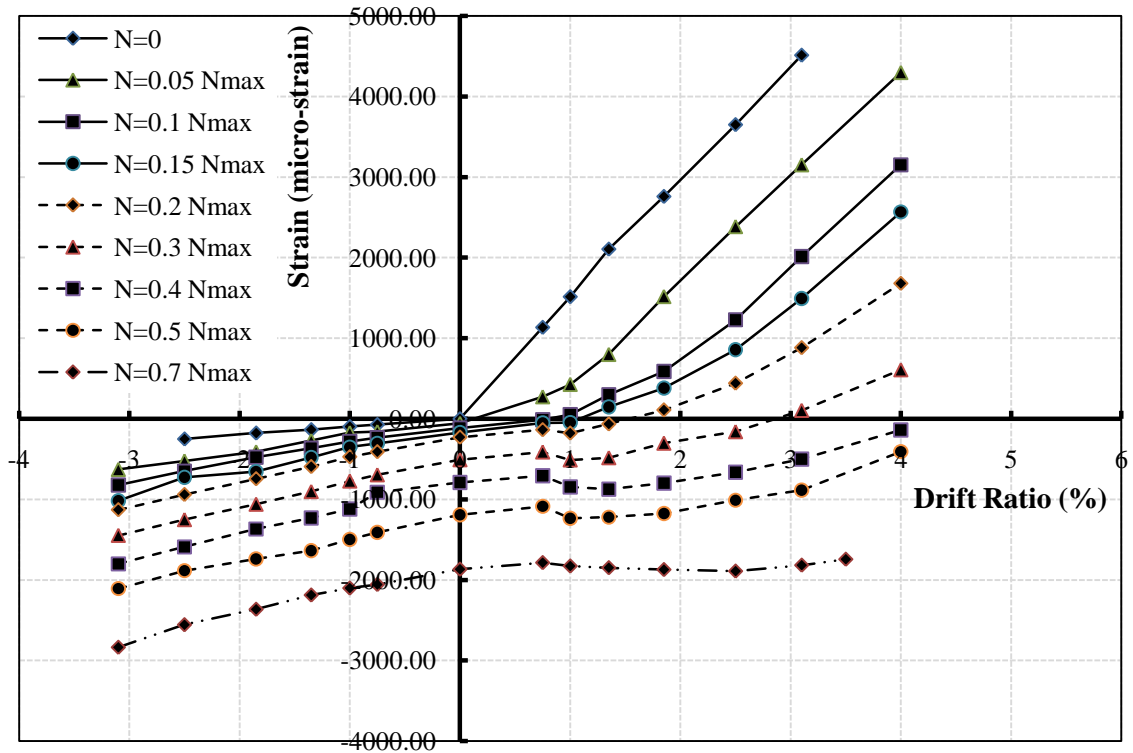


Figure 6.4: Strain comparison of column longitudinal bars under various column axial loads for specimen GG17-B11-J12

6.2.2 Concrete Compressive Strength

To investigate the effect of the concrete compressive strength on the performance of the FRP-RC beam-column connections, the FEM of specimen GG29-B11-J12 was selected. The FEM considered a range of concrete compressive strength from 20 to 70 MPa with 10 MPa increments for each run. The reason behind selecting this specimen is the high beam longitudinal reinforcement ratio, which allows a compression mode of failure for the investigated range of concrete strength. The results of these runs were compared in terms of the envelope of the hysteric behaviour and the corresponding mode of failure, and the developed strains in the beam and column longitudinal reinforcement.

Figure 6.5 shows envelopes for the load-drift relationships for different concrete compressive strengths, f_c' . The connection with $f_c' = 20$ MPa showed the lowest capacity and the lowest drift ratio in both positive and negative direction of loading. It was observed from Figure 6.5 that increasing the concrete compressive strength enhanced the lateral load capacity and the corresponding drift level. At the same drift ratio of 4%, increasing the concrete compressive strength from 30 to 70 MPa resulted in increasing the lateral load capacity by approximately 32%.

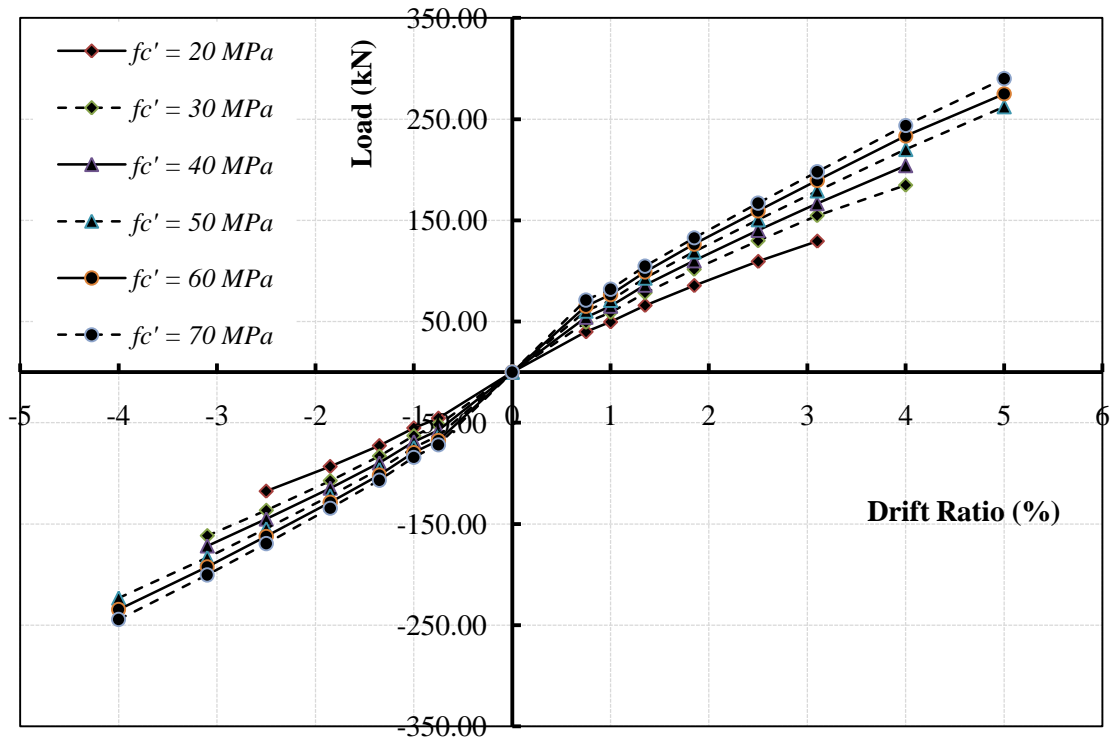


Figure 6.5: Load-drift relationship envelopes under various concrete compressive strengths for specimen GG29-B11-J12

Figure 6.6 summarizes the mode of failure and the corresponding drift capacity for each concrete compressive strength. All specimens failed in compression (concrete

crushing) at the beam sections in the vicinity of the column. It was also observed that increasing the concrete compressive strength resulted in increasing the drift capacity of the connection.

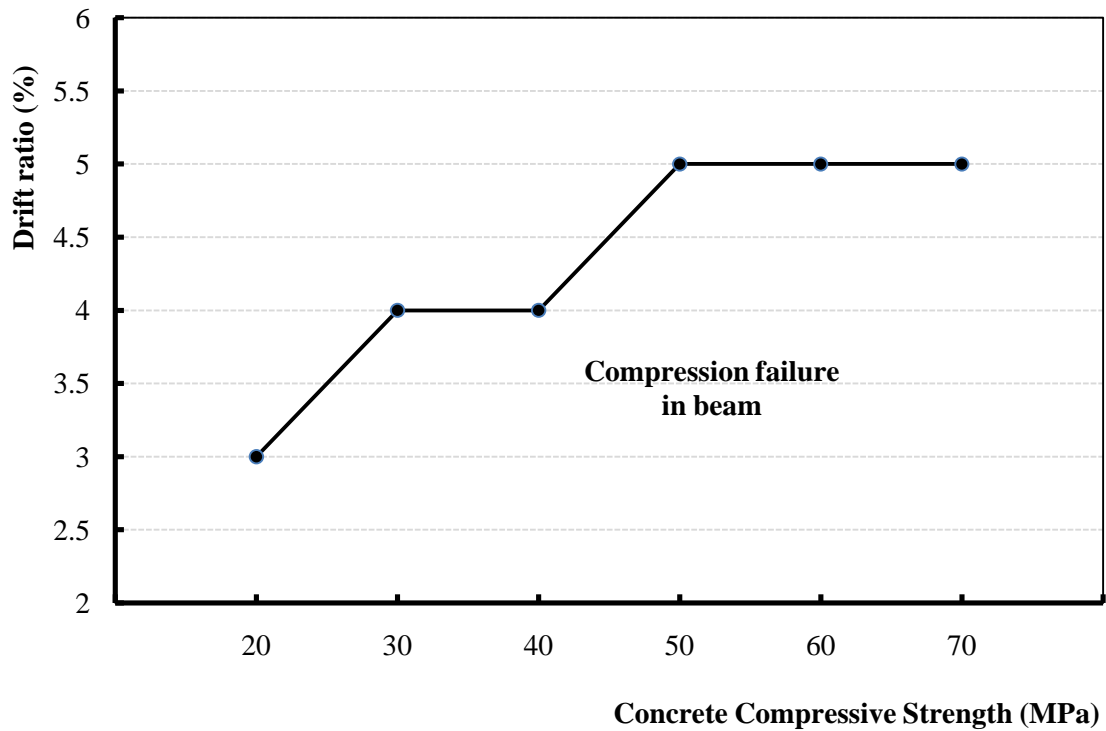


Figure 6.6: The mode of failure and the corresponding drift capacity for each concrete compressive strength

Figures 6.7 and 6.8 show the beam and column longitudinal bars' strains-drift relationships, respectively. Similar observations can be made through the strain measurements. Figure 6.7 shows that, at the same drift ratio of 4%, increasing the concrete compressive strength from 30 to 70 MPa resulted in increasing the developed strains in the beam longitudinal bars by approximately 17%.

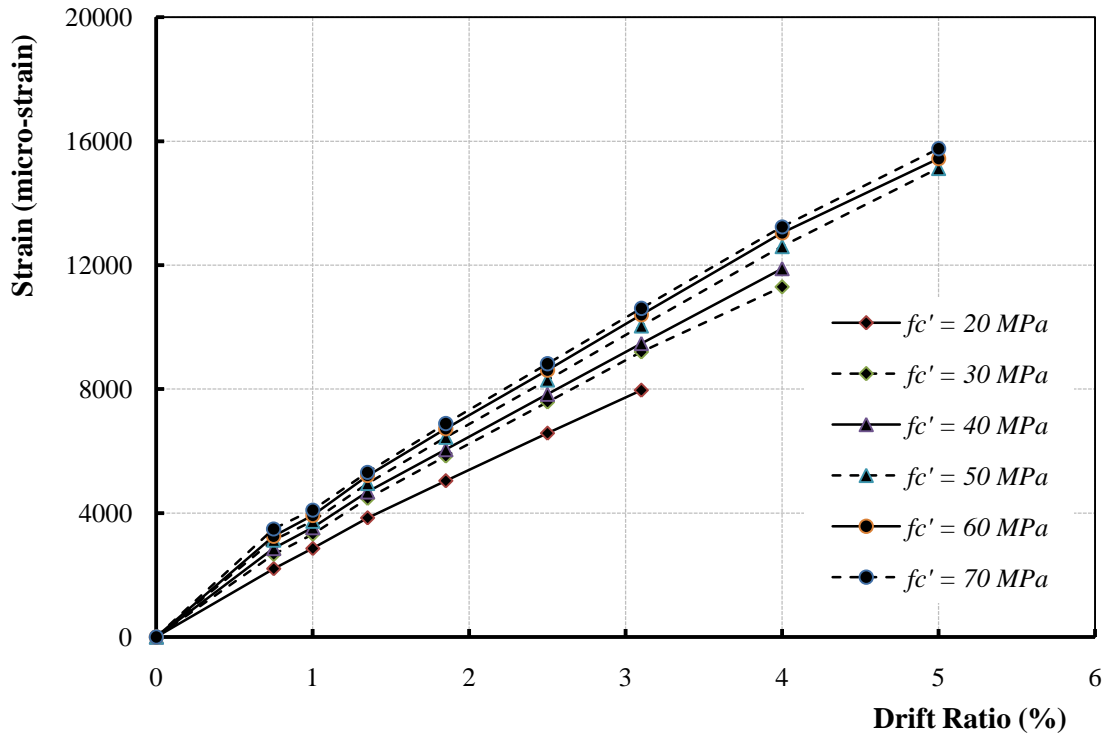


Figure 6.7: Strain comparison of beam longitudinal bars under various concrete compressive strengths for specimen GG29-B11-J12

Within low drift ratio levels (up to 1.85%), Figure 6.8 did not show any significant change in the developed tensile strains in column longitudinal bars. Afterwards, increasing the concrete compressive strength from 30 to 70 MPa increased the developed tensile strains in the column longitudinal bars by approximately 32% at 4% drift ratio. On the other hand, increasing the concrete compressive strength resulted in decreasing the developed compressive strains in the column longitudinal bars. This might be attributed to the fact that the depth of the neutral axis decreases as the compressive strength of the concrete increases. Therefore, the compressive strains at the longitudinal bars located at the compression zone also decreases. At the same drift ratio of 3.1%,

increasing the concrete compressive strength from 30 to 70 MPa resulted in decreasing the compressive strains in the column longitudinal bars by approximately 40%.

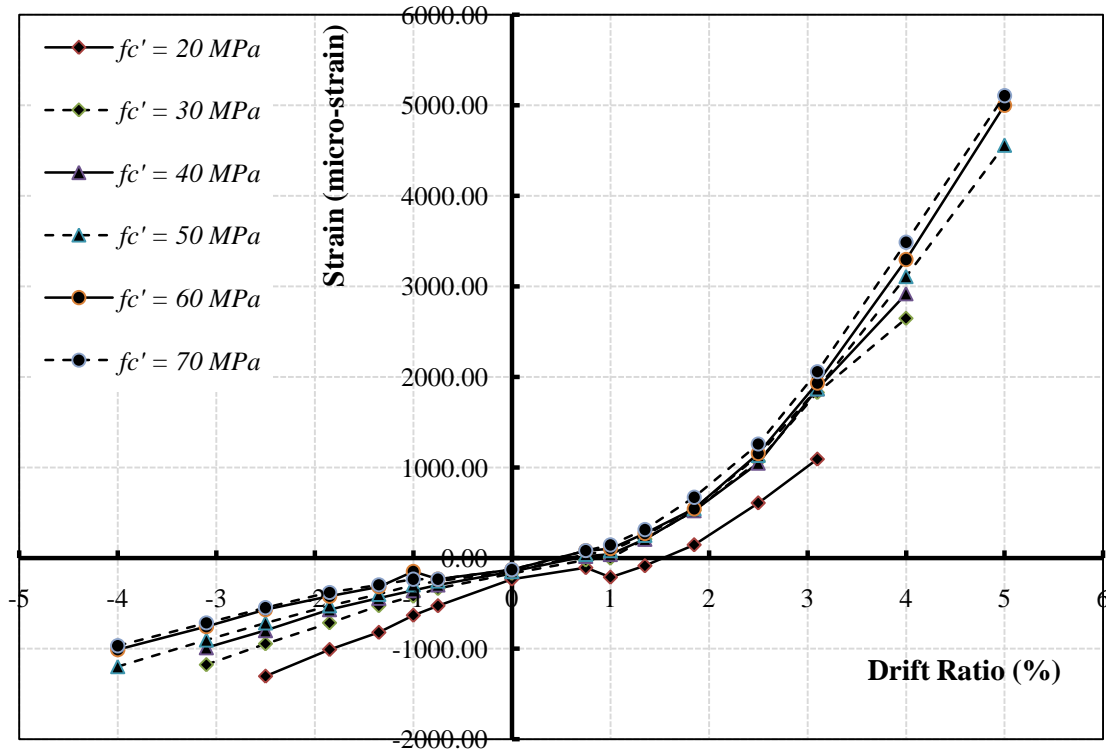


Figure 6.8: Strain comparison of column longitudinal bars under various concrete compressive strengths for specimen GG29-B11-J12

6.2.3 Flexural Strength Ratio

In this parameter, the FEM of specimen GG17-B11-J12 was selected to run eight different flexural strength ratios; MR = 0.80, 1.00, 1.25, 1.50, 2.00, 2.50, 4.00 and 6.00. These MR ratios were obtained by maintaining the beam reinforcement ratio while changing the reinforcement ratio of the column longitudinal bars. This approach enabled the comparison of different connections having the same beam capacity. The results of these runs were compared in terms of the envelope of the hysteric behaviour and the

corresponding mode of failure, and the developed strains in the beam and column longitudinal bars.

Figure 6.9 shows envelopes for the load-drift relationships for the selected flexural strength ratios. The connection with flexural strength ratio, MR, of 0.80 showed the lowest capacity in both positive and negative direction of loading. It was observed from Figure 6.9 that increasing the flexural strength ratio increased the lateral load capacity. This was due to pushing the failure location more toward the beam with increasing the flexural strength ratio. At the same drift ratio of 4%, increasing the flexural strength ratio from 0.80 to 6.00 resulted in increasing the lateral load capacity by approximately 33%. However, no significant change in the lateral load capacity (only 4%), was observed in the range of MR = 2.00 to 4.00. In addition, it was observed that at the highest flexural strength ratio (MR = 6.00), the connection was capable of reaching 5% drift ratio at failure; higher than other connections with lower flexural strength ratios.

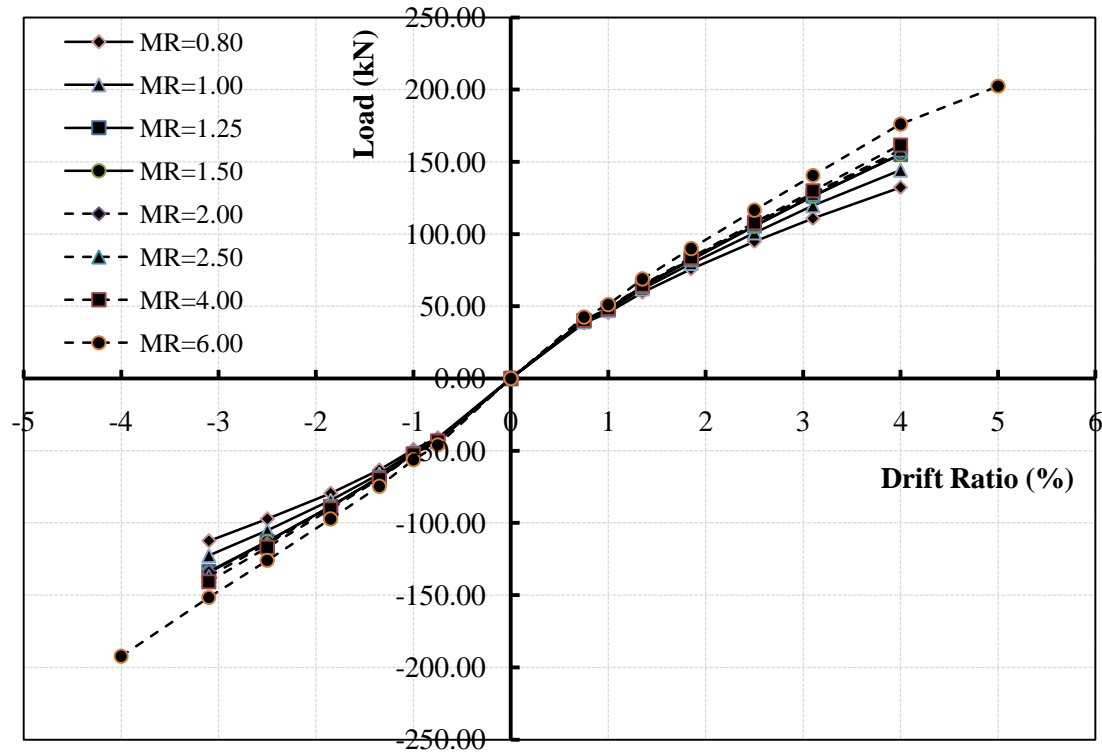


Figure 6.9: Load-drift relationship envelopes under various flexural strength ratios for specimen GG17-B11-J12

Figure 6.10 summarizes the mode of failure and the corresponding drift capacity for each flexural strength ratio. All specimens failed at 4.00% drift ratio except the connection with $MR = 6.00$, which failed at 5.00% drift ratio. The specimens with $MR = 1.25$ or less suffered from failure in the column zone. However, increasing the flexure strength ratio to be equal or greater than 1.50 changed the failure location to be in the beam rather than in the column.

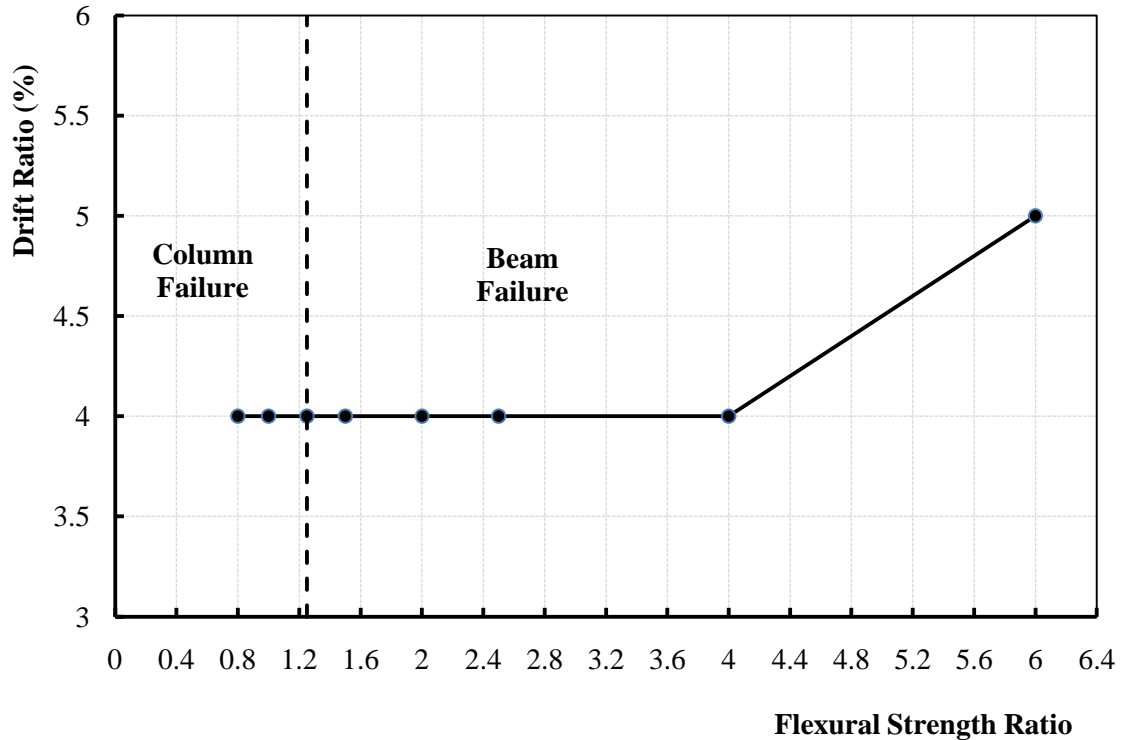


Figure 6.10: The mode of failure and the corresponding drift capacity for each flexural strength ratio

Figures 6.11 and 6.12 show the beam and column longitudinal bars' strains-drift relationships, respectively. It can be seen from Figure 6.11 that, at the same drift ratio of 4%, increasing MR from 0.80 to 6.00 resulted in increasing the developed strains in the beam longitudinal bars by approximately 26%. Also, increasing MR from 2.00 to 4.00 did not result in any significant change in the developed strains.

Increasing the column reinforcement ratio resulted in decreasing the developed tensile and compressive strains in the longitudinal bars. It was observed that the tensile and compressive strains decreased by approximately 93 and 77%, respectively, as shown in Figure 6.12.

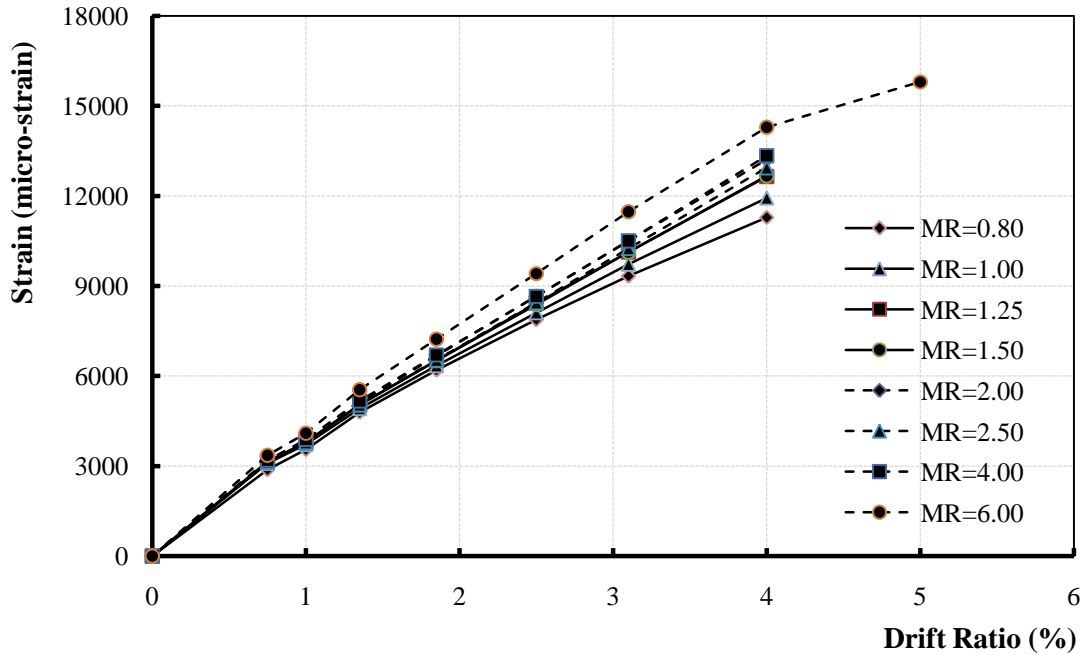


Figure 6.11: Strain comparison of beam longitudinal bars under various flexural strength ratios for specimen GG17-B11-J12

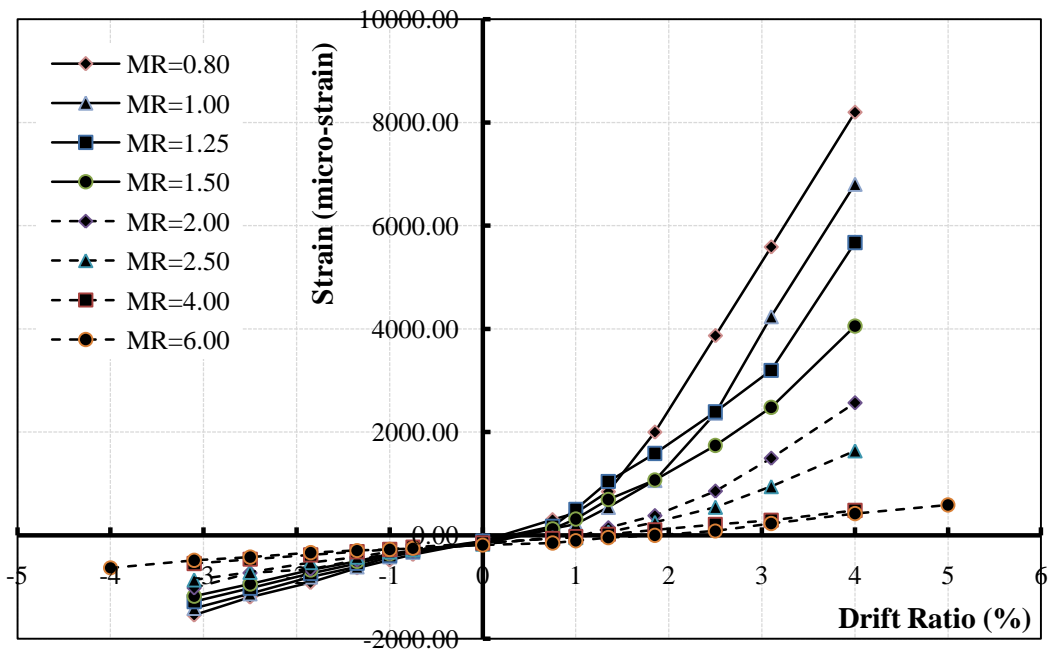


Figure 6.12: Strain comparison of column longitudinal bars under various flexural strength ratios for specimen GG17-B11-J12

6.2.4 Joint Transverse Reinforcement

To investigate this parameter, the FEM of specimen GG17-B11-J12 was selected to run seven different joint reinforcement ratios; 0%, 0.10%, 0.15%, 0.30%, 0.40%, 0.60% and 1.20%. These ratios were obtained by using three different shear reinforcement spacing within the joint area; 270, 180 and 90 mm, as well as two different stirrup diameters; 8 and 13 mm. The results of these runs were compared in terms of the envelope of the hysteric behaviour and the corresponding mode of failure, the developed strains in the beam and column longitudinal reinforcement, and the shear stress distribution across the joint at failure.

In Figures 6.13 to 6.17, the beam-column connections were named based on the joint reinforcement ratio as well as the stirrups spacing. The first letter “J” and the following percentage represent the joint reinforcement ratio in the connection. The second letter “s” and the following number represent the stirrups spacing within the joint in mm. For example, J0.40%-s270 denotes a specimen with joint reinforcement ratio of 0.40% and stirrups spacing of 270 mm.

Figure 6.13 shows envelopes for the load-drift relationships for different joint reinforcement ratios. It is clear that changing the joint reinforcement ratio has no effect on the stiffness of the connections. However, the joint reinforcement ratio affected the failure load and the corresponding drift ratio. Generally, it was observed that increasing the joint reinforcement ratio increased the failure load/drift ratio of the connection. However, unexpectedly, the connection with joint reinforcement ratio of 0.40% failed at lower load and drift capacity than those of the connection with 0.30% reinforcement ratio (Figure 6.14). This was due to the larger stirrups spacing of 270 mm used in the former

connection compared to 90 mm spacing used in the latter one. This indicates that the stirrup spacing rather than size has greater influence on the joint capacity.

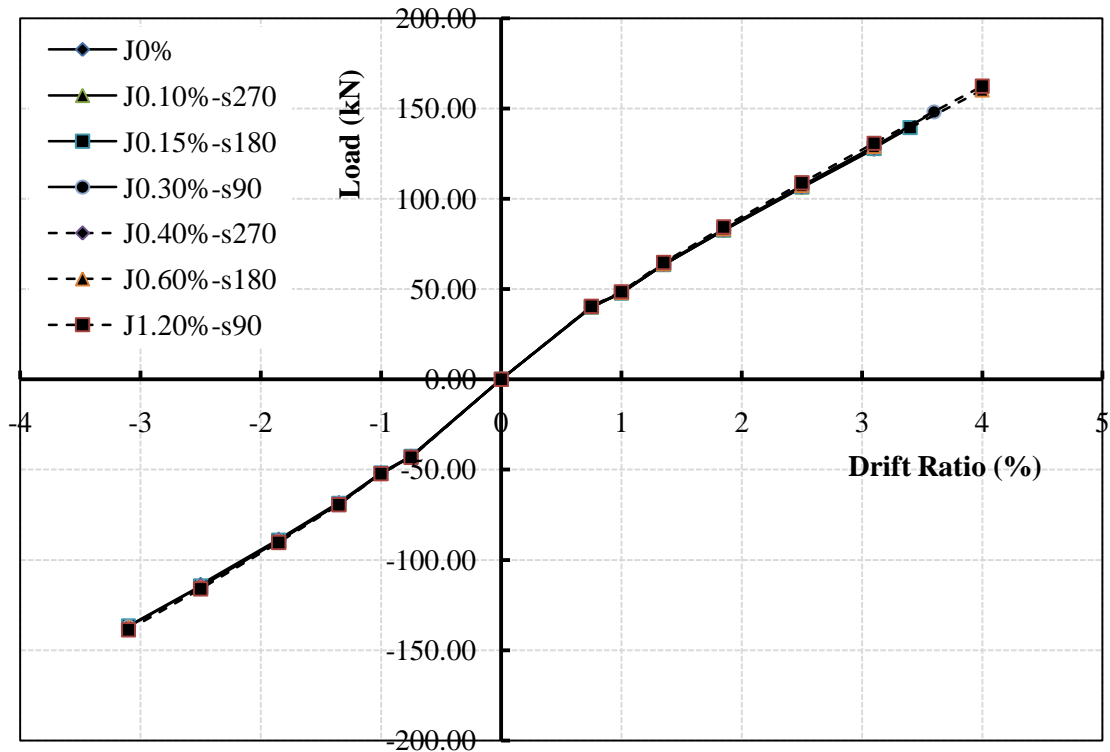


Figure 6.13: Load-drift relationship envelopes under various joint reinforcement ratios for specimen GG17-B11-J12

Figure 6.14 summarizes the mode of failure and the corresponding drift capacity for each joint reinforcement ratio. In this figure, the letter “s” and the following number represent the stirrups spacing within the joint in mm. All specimens with joint reinforcement ratio less than 0.60% suffered from joint failure. A minimum joint reinforcement ratio of 0.60% allowed the failure to occur in the beam section rather than the joint. For stirrup spacing 270 mm, using either 8 mm or 13 mm stirrup diameter did not show any enhancement in the connection performance. While, for stirrup spacing 180

mm and 90 mm, increasing the stirrup diameter from 8 to 13 mm increased the corresponding drift capacity at failure by approximately 14%. Also, it was observed that, for the same stirrup diameter, decreasing the stirrups spacing improved the behaviour by increasing the drift capacity and the corresponding load at failure.

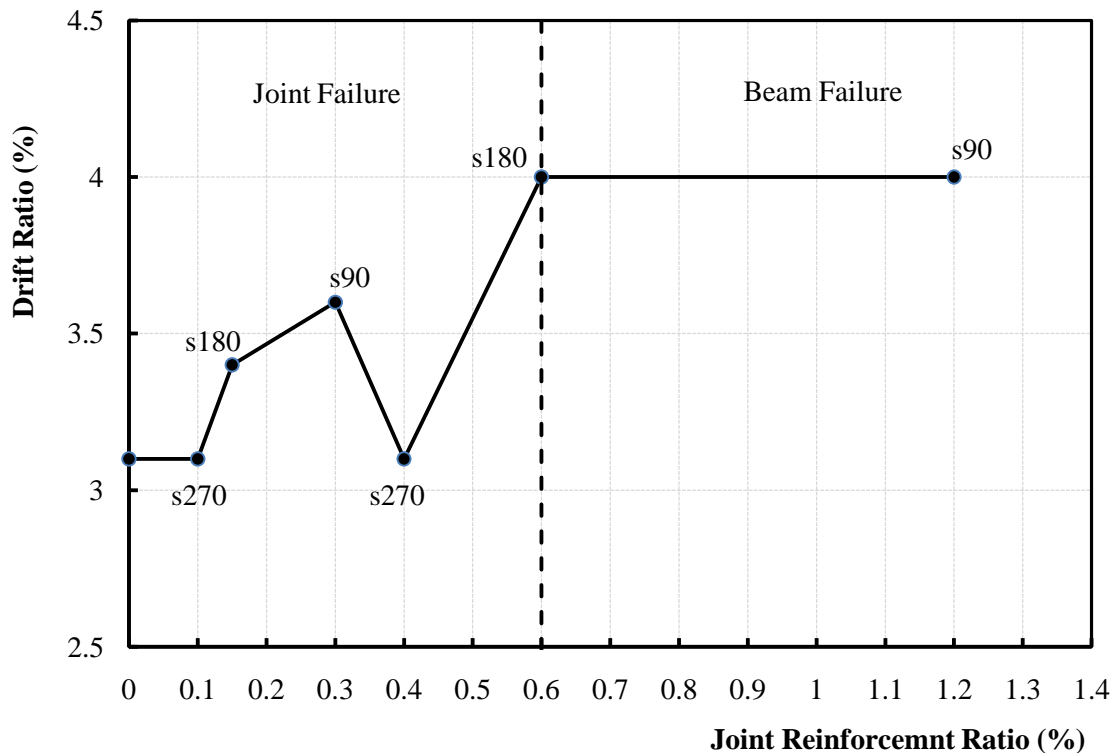


Figure 6.14: The mode of failure and the corresponding drift capacity for each joint reinforcement ratio

Figures 6.15 and 6.16 show the beam and column longitudinal bars' strains-drift relationships, respectively. At the same drift ratio, no significant difference in the strain measurements was noticed. However, it was observed that increasing the joint reinforcement ratio increased the observed tensile and compressive strains at failure.

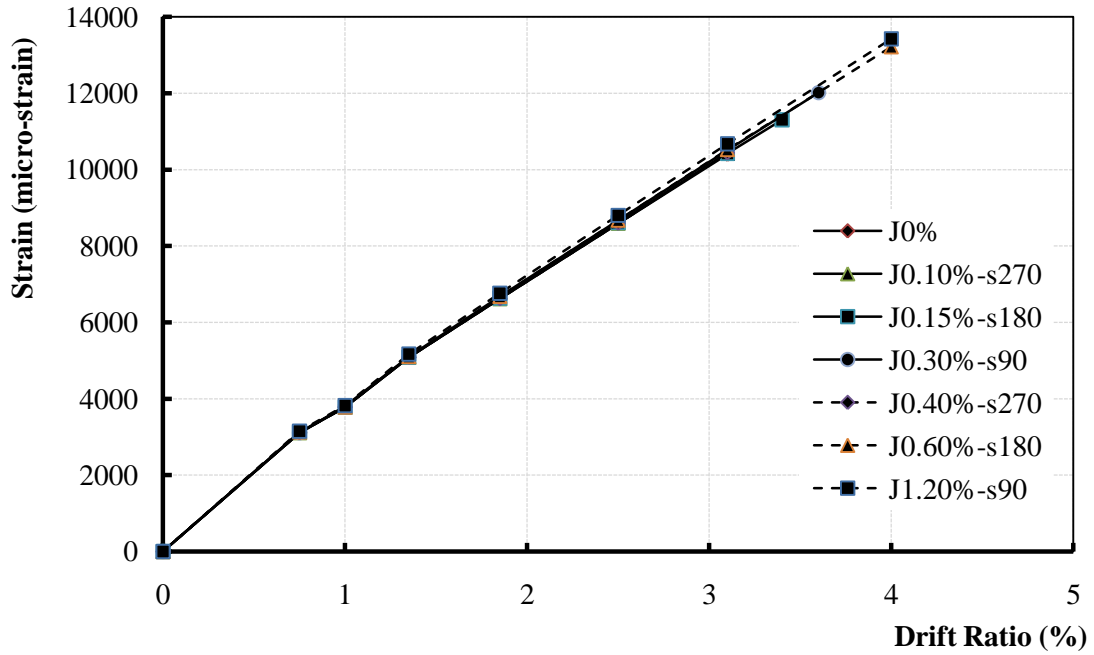


Figure 6.15: Strain comparison of beam longitudinal bars under various joint reinforcement ratios for specimen GG17-B11-J12

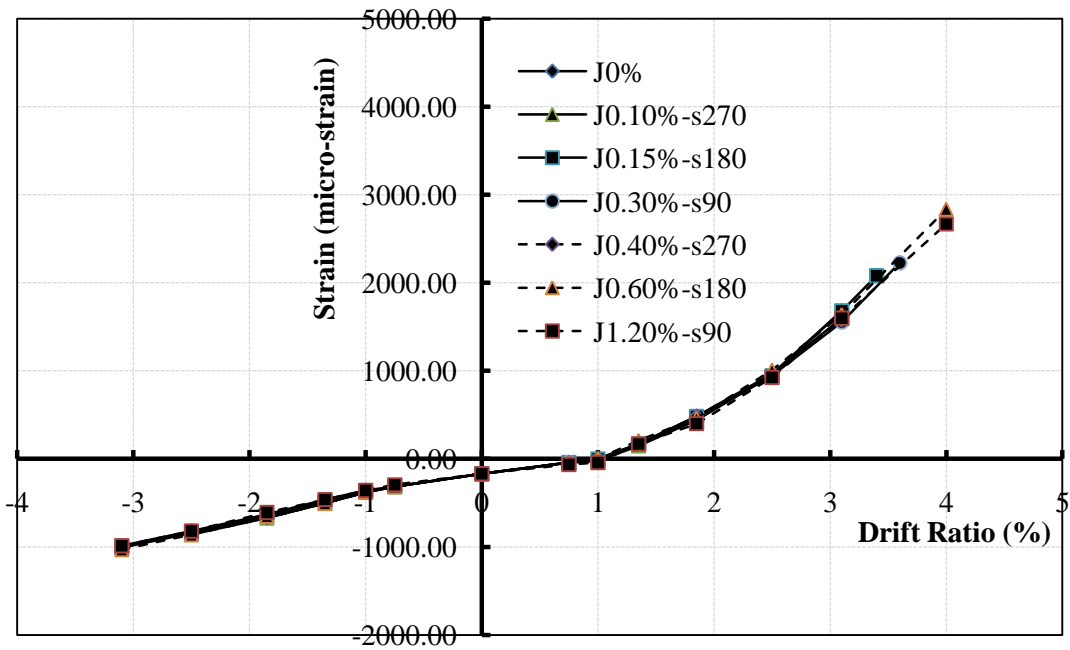
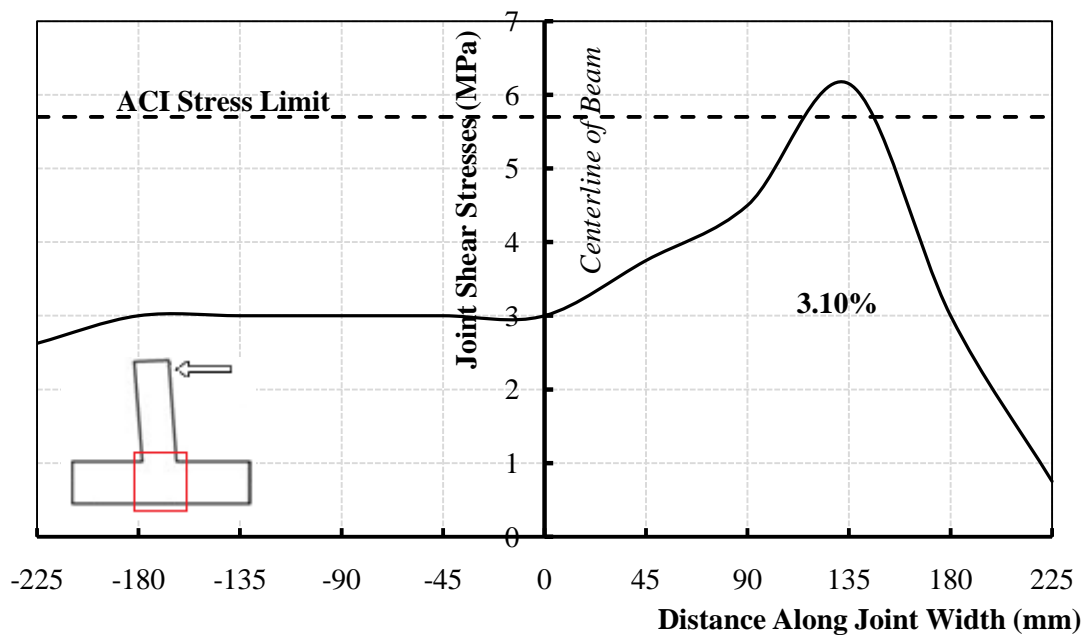
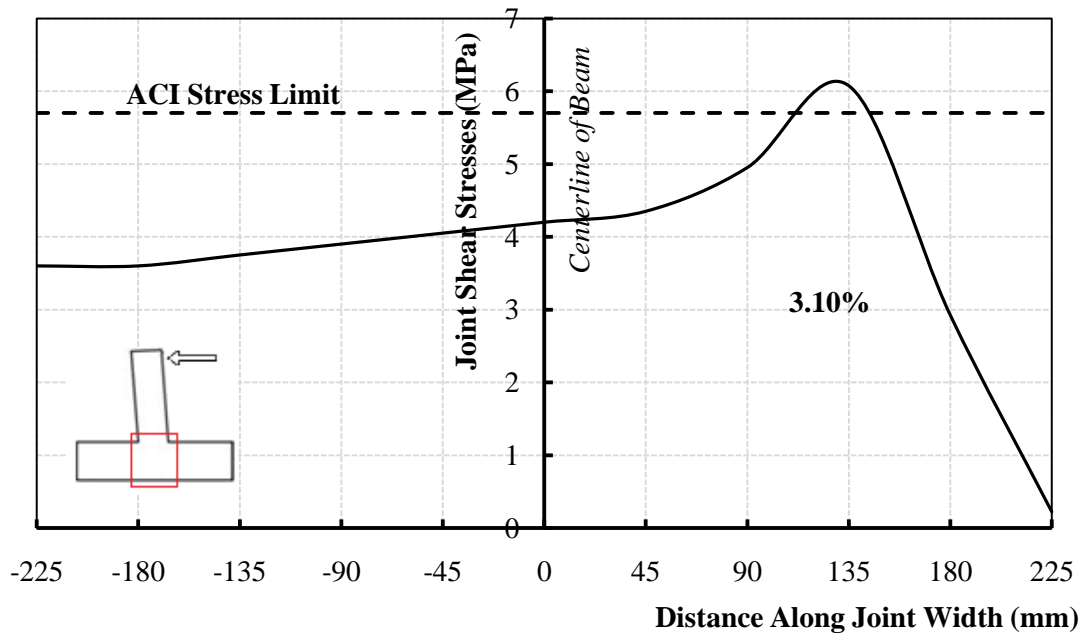


Figure 6.16: Strain comparison of column longitudinal bars under various joint reinforcement ratios for specimen GG17-B11-J12

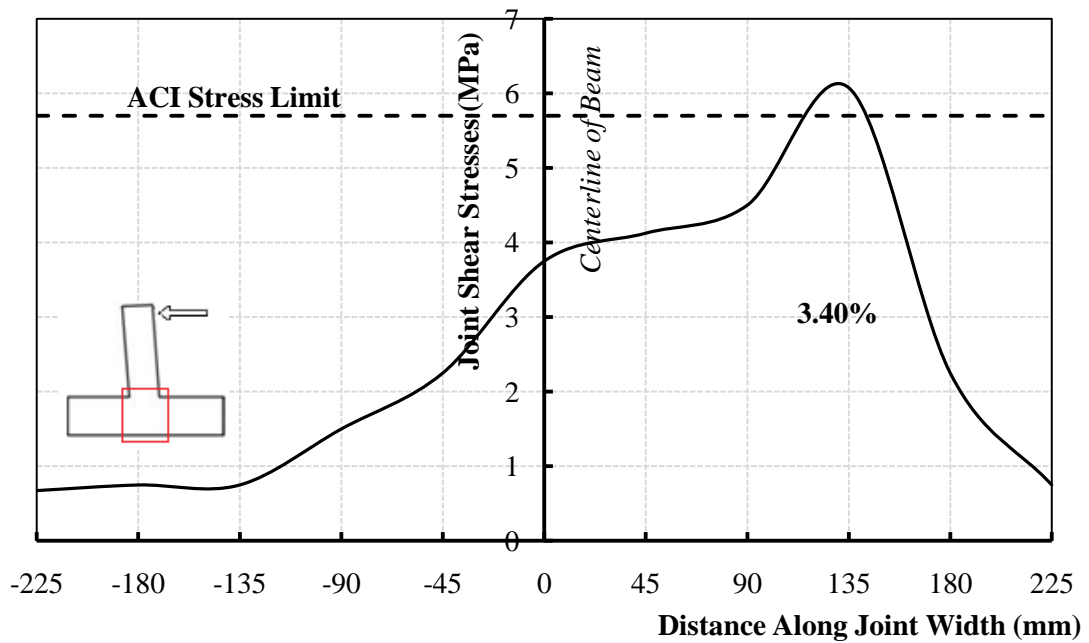
To better understand and explain the reason behind the failure for each connection, the shear stress distribution across the joint for each joint reinforcement ratio at failure was plotted in Figure 6.17. It is clear that increasing the joint reinforcement ratio decreased the developed shear stresses across the joint. Furthermore, the mode of failure for each connection is in good agreement with the joint shear capacity level predicted by both ACI-318-08 (ACI 2008) and CSA-A23.3-04 (CSA 2004); $1.0 \sqrt{f'_c}$. The shear stresses in the specimen with joint reinforcement ratio of 0.60% barely reached the joint shear capacity level at 4.00% drift ratio, however, the concrete crushing in the beam zone dominated the mode of failure for this specimen. Finally, the shear stresses in the connection with joint reinforcement ratio of 1.20% reached approximately 90% of the joint shear capacity level at 4% drift ratio. Accordingly, the mode of failure for this connection was a concrete crushing in the beam zone away from the joint.



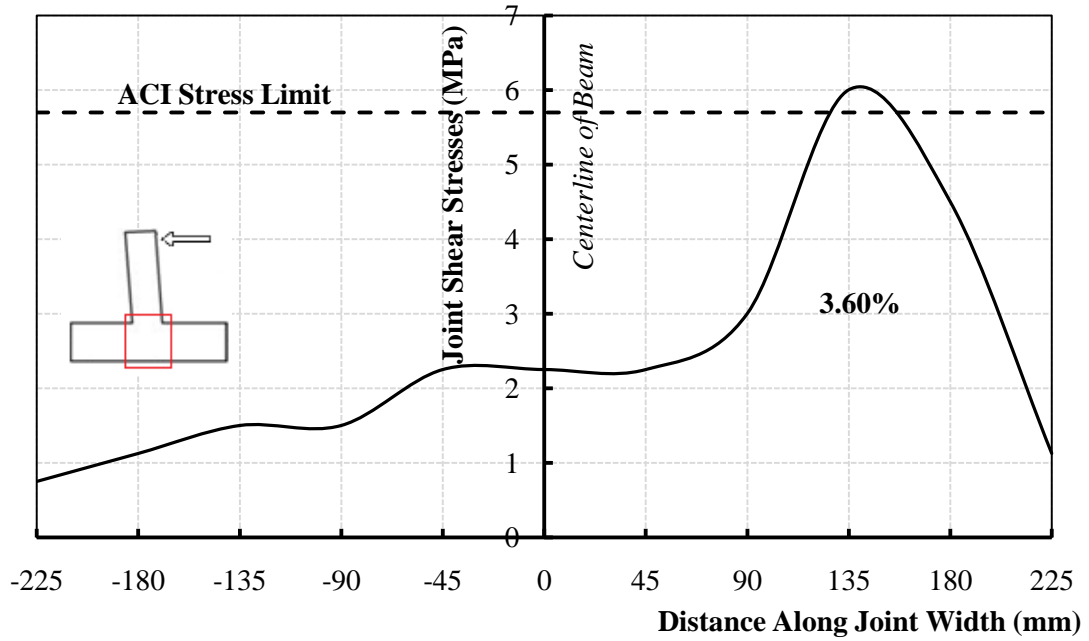
(a) Specimen J0%



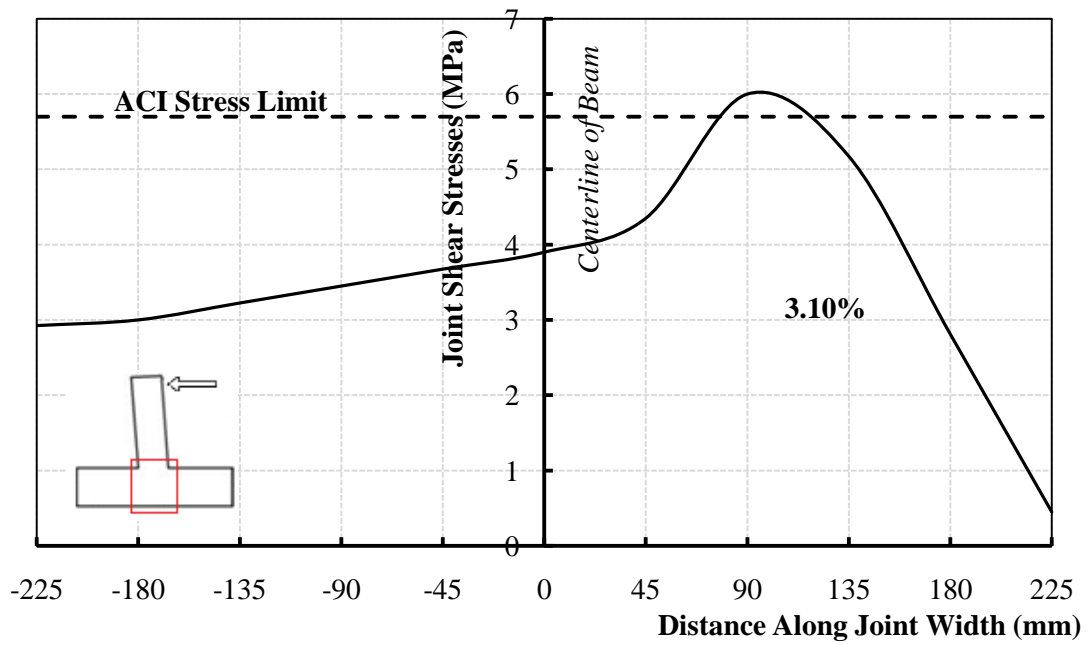
(b) Specimen J0.10%-s270



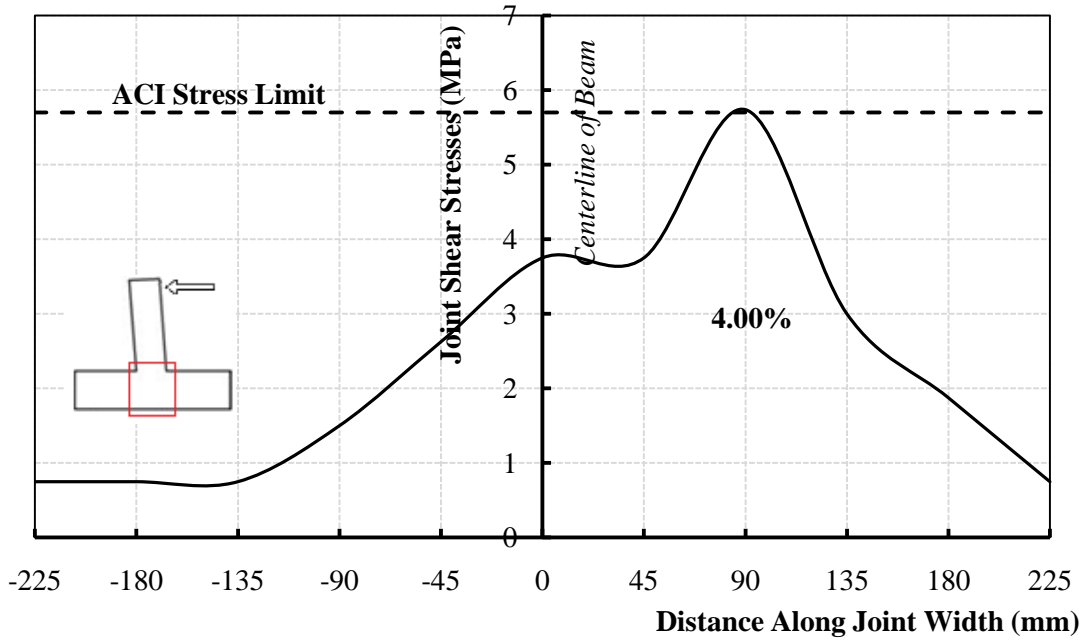
(c) Specimen J0.15%-s180



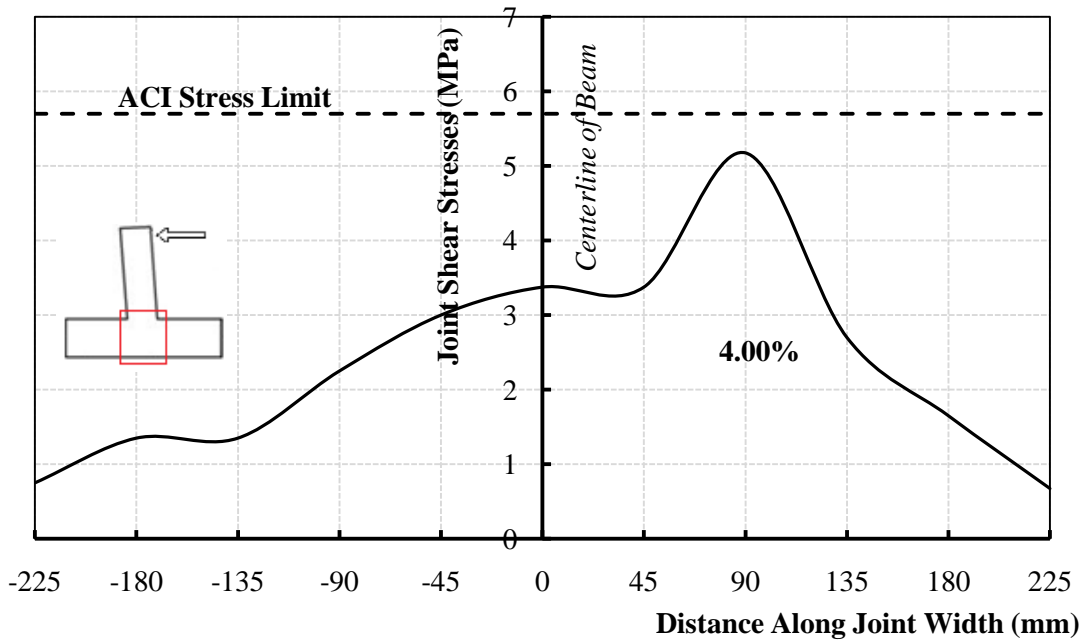
(d) Specimen J0.30%-s90



(e) Specimen J0.40%-s270



(f) Specimen J0.60%-s180



(g) Specimen J1.20%-s90

Figure 6.17: Shear stresses distribution across the joint at failure

CHAPTER 7

SUMMARY AND CONCLUSIONS

7.1 SUMMARY

The current study has investigated the influence of using FRP bars and stirrups as main reinforcement on the performance of exterior beam-column joints subjected to simulated-seismic loading. The study included two phases, experimental and analytical investigations. These investigations resulted in proposing a design strategy for the FRP-reinforced beam-column connections, in addition to number of findings on the effect of different parameters including reinforcement detailing on the performance of these joints.

The experimental phase included the construction and testing of eight full-scale exterior beam-column joint prototypes (T-shaped). Each prototype represents an exterior joint isolated from an end bay of a multi-storey structure between the assumed points of contra-flexure located at the mid-height and mid-span of the column and the beam, respectively. Reversal lateral quasi-static cyclic loads are applied directly at the beam tip to simulate seismic loading. The test variables were the type of longitudinal reinforcement bars (steel, GFRP and CFRP), the type of transverse reinforcement (steel and GFRP), the beam longitudinal reinforcement ratio, the beam transverse reinforcement ratio and the joint reinforcement ratio.

The analytical phase included constructing a finite element model (FEM) for the beam-column joints using ANSYS software. The FEM was validated against the experimental results. Afterwards, the verified model was used to conduct a parametric study on number of variable parameters including column axial load, concrete compressive strength, flexural strength ratio and joint transverse reinforcement.

7.2 CONCLUSIONS

The findings of the current study are summarized in the following sections.

7.2.1 Conclusions from the Experimental Tests

Based on the test results of the eight beam-column joints tested in the experimental phase, the following conclusions can be drawn:

1. GFRP bars and stirrups can be used as reinforcement in beam-column joints subjected to seismic loading conditions. The GFRP bars were capable of resisting reversal tension-compression cycles with no problems.
2. The design approach followed in this study; utilizing design concepts from CSA-A23.3-04 (CSA 2004) for steel-reinforced concrete structures and available provisions from CSA-S806-02 (CSA 2002) and CSA-S6-09 (CSA 2009) for FRP-reinforced concrete structures along with recommendations from previous research work, is yielding good results.
3. The GFRP-reinforced joints can be designed to satisfy both strength and deformability requirements. The tested GFRP-reinforced concrete beam-column joints reached 4.0% drift capacity safely with insignificant damage. The obtained drift capacities are more than the 2.5% required by the National Building Code of Canada (NBCC 2005) and the 3.5% required by the ACI (ACI 374.1 2005).
4. For the steel-reinforced joint, the plastic hinge was developed in the beam at the face of the column. However, for the GFRP-reinforced joints and due to large elastic deformation, a virtual plastic hinge was developed away from the column face, which was spread over the whole length of the beam. In other words, the

local yielding of steel reinforcement was partially substituted with the large-elastic deformations exhibited by GFRP bars.

5. Following the 4.0% drift cycle, the measured residual strains in the GFRP longitudinal beam reinforcement were negligible. However, at the same drift level, the steel-reinforced joint exhibited much larger residual strains. This indicates that, surviving an earthquake event, GFRP-reinforced joints would remain functional with a minimum required amount of repair, if any.
6. The low modulus of elasticity for the GFRP reinforcement led to reducing the stiffness of the tested specimens, which resulted in attracting lower forces from the acting drifts. Considering the overall behavior of an FRP-reinforced frame, even though the lower stiffness will require higher displacement demand it is expected to reduce the base shear forces.
7. According to the used design concepts, the GFRP stirrups were adequate to provide the required confinement for both beams and columns. Specimen GG17-B11-J12 with GFRP stirrups obtained cumulative dissipation energy higher than that obtained from the identical specimen, GS17-B11-J12, with steel stirrups by approximately 20%.
8. For the GFRP-reinforced joints, as long as the joint is safe under the applied shear stresses, increasing the beam over-reinforcement ratio (from 1.2 to 1.7%) led to enhance the ability of the connection to dissipate the seismic energy through utilizing the inelastic behaviour of concrete.
9. In specimen GG17-B07-J12, the amount of shear reinforcement (approximately 0.7%) required for the beam, according to CSA-S6-09 (CSA 2009), was adequate

to avoid beam shear failure. However, the smaller stirrup spacing (85 mm compared to 100 mm) rather than size played more important role in improving the behaviour of that specimen.

10. Reducing the amount of shear reinforcement within the joint area by replacing it with equivalent diagonal bars not only facilitated the construction process but also enhanced the overall performance. This kind of detailing presents a better alternative for the FRP-reinforced joints to reduce the congestion of these joints during construction.
11. For all GFRP-reinforced specimens, no slippage of the beam bars was observed before failure. In other words, an embedment length of 24 times beam bar diameter ($24d_b$) was adequate to transfer the forces in the straight beam bars to the joint under cyclic loading.
12. No reliable conclusions can be made from the CFRP-reinforced joint CG12-B11-J12 due to the premature failure. This unexpected failure occurred as a result of bad bond quality and the non-homogenous characteristics for the tensile properties of the used CFRP bars.

7.2.2 Conclusions from the Numerical Modelling

Based on the results of the finite element model constructed in the analytical phase, the following conclusions can be drawn:

13. The finite element modeling using ANSYS software was able to predict the hysteretic behaviour and the developed strains in both beam and column longitudinal reinforcement for all FRP-reinforced specimens within a reasonable accuracy. However, the program was not able to predict post-failure behaviour of

concrete, where the program solution is showing difficulties in convergence once failure started.

14. For moment-resisting frames subjected to seismic loading, it is recommended to limit the applied axial loads on the column to 70% of the column axial load capacity in order to avoid the joint failure that may occur due to high compressive stresses developed in the joint core.
15. Increasing the column axial load level from 5 to 30% of the column axial capacity resulted in increasing the average lateral load capacity by approximately 27% and the developed tensile strains in the beam longitudinal bars by approximately 20%. However, in the range of 35 to 65% of the column axial capacity, no significant change in the overall behaviour was observed.
16. Increasing the concrete compressive strength is not only increasing the lateral load capacity of the connection, but also contributing to reaching higher drift ratio levels before failure.
17. Increasing the concrete compressive strength from 30 to 70 MPa resulted in increasing the developed tensile strains in the beam and column longitudinal bars by approximately 17 and 32%, respectively. In the mean time, it also resulted in decreasing the developed compressive strains in the column longitudinal bars by approximately 40%. This might be attributed to the decrease in the depth of the neutral axis resulted from increasing the concrete compressive strength.
18. A minimum flexural strength ratio of 1.50 is recommended to ensure the strong-column weak-beam mechanism. Joints with flexural strength ratio 1.25 or less suffered from failure in the column zone.

19. Using very high flexural strength ratios (6.00 or more) is not only increasing the expected lateral load capacity of the connection, but also contributing to reaching higher drift ratio levels before failure. It was observed that increasing the flexural strength ratio from 0.80 to 6.00 resulted in increasing the lateral load capacity by approximately 33% and the developed strains in the beam longitudinal bars by approximately 26%. However, within the range of flexural strength ratios of 2.00 to 4.00, no significant change in the overall behavior was observed.
20. Changing the joint reinforcement ratio has no effect on the stiffness of the beam-column connection. However, increasing the joint reinforcement ratio; especially by reducing the stirrups spacing, helped in increasing the failure load and the corresponding drift ratio of the connection.
21. Increasing the transverse joint reinforcement ratio did not affect the measured strains in the longitudinal reinforcement, neither in the beam nor in the column, while compared at the same drift ratio.
22. Increasing the joint reinforcement ratio decreases the developed shear stresses across the joint. In addition, the mode of failure for each connection was in good agreement with the joint shear capacity level predicted by both ACI-318-08 (ACI 2008) and CSA-A23.3-04 (CSA 2004); $1.0 \sqrt{f'_c}$.
23. Accordingly, a minimum joint reinforcement ratio of 0.60% is recommended to insure that the failure will not occur in the joint zone.

7.3 FUTURE WORK

This research work not only provides a guide for future studies in this area but also the research findings were extremely useful to the knowledge in this field and could be helpful in the development of the Canadian and international codes addressing this subject. Based on the findings and conclusions of the current study, the following recommendations are made for future research:

1. More research is needed to study the bond characteristics of the GFRP bars subjected to cyclic loading.
2. Research is needed to investigate the effect of the transverse slabs and beams on the behaviour of FRP-reinforced beam-column connections.
3. Additional experiments investigating the behaviour of FRP bars under compression loading should be conducted.
4. The behaviour of different types of GFRP bars (sand coated vs. ribbed bars) need to be investigated.
5. The obtained results are encouraging to extend the scope of testing to include various design parameters, which will result in developing design formulas and guidelines for such structural elements.
6. Full-scale tests on GFRP-reinforced concrete moment-resisting frames are needed to assess the overall behaviour of the entire frame under seismic loading.

REFERENCES

- Abdel-Fatah, B. A. and Wight, J. K. (1987). "Study of Moving Beam Plastic Hinging Zones for Earthquake-Resistant Design of R/C Buildings," *ACI Structural Journal*, V. 84, No. 1, pp. 31-39.
- Abdel-Wahed, O. H., Elnesr, O. M., EL-Ghandour, A. A. and Saad Eldin, W. A. (2005). "Behaviour of Retrofitted Beam-Column Joint with FRP," *11th International Colloquium on Structural and Geotechnical Engineering*, 17-19 May, Cairo, Egypt., ID: E05RC38, 15 p.
- ACI-ASCE Committee 352. (1976). "Recommendations for Design of Beam-Column Joints in Monolithic Reinforced Concrete Structures," ACI 352R-76, *American Concrete Institute*, Detroit, 19 p.
- ACI-ASCE Committee 352. (1985). "Recommendations for Design of Beam-Column Joints in Monolithic Reinforced Concrete Structures," ACI 352R-85, *American Concrete Institute*, Detroit, 19 p.
- ACI-ASCE Committee 352. (2002). "Recommendations for Design of Beam-Column Connections in Monolithic Reinforced Concrete Structures," ACI 352R-02, *American Concrete Institute*, Farmington Hills, Mich., 37 p.
- ACI Committee 318. (1971). "Building Code Requirements for Reinforced Concrete," ACI 318-71, *American Concrete Institute*, Detroit, 78 p.
- ACI Committee 318. (2002). "Building Code Requirements for Structural Concrete and Commentary," ACI 318-02, *American Concrete Institute*, Farmington Hills, Mich., 443 p.

- ACI Committee 318. (2008). "Building Code Requirements for Structural Concrete and Commentary," ACI 318-08, *American Concrete Institute*, Detroit, 467 p.
- ACI Committee 374. (2005). "Acceptance Criteria for Moment Frames Based on Structural Testing and Commentary," ACI 374.1-05, *American Concrete Institute*, Farmington Hills, Mich., 9 p.
- ACI Committee 440. (1996). "State-of-the-Art Report on Fibre Reinforced Plastic (FRP) Reinforcement for Concrete Structures," ACI 440R-96, *American Concrete Institute*, Farmington Hills, Mich., 65 p.
- ACI Committee 440. (2006). "Guide for the Design and Construction of Concrete Reinforced with FRP Bars," ACI 440.1R-06, *American Concrete Institute*, Farmington Hills, Mich., 44 p.
- Al-Haddad, M. S. and Wight, J. K. (1988). "Relocating Beam Plastic Hinging Zones for Earthquake Resistant Design of Reinforced Concrete Buildings," *ACI Structural Journal*, V. 85, No. 2, pp. 123-133.
- Alves, J., El-Ragaby, A. and El-Salakawy, E. (2011). "Durability of GFRP Bars Bond to Concrete under Different Loading and Environmental Conditions," *Journal of Composites for Construction, ASCE*, V. 15, No. 3, pp. 249-262.
- ANSYS User's Manual, Release 11. (2007). ANSYS, Inc., Canonsburg, Pennsylvania.
- Au, F. T. K., Huang, K. and Pam, H. J. (2005). "Diagonally-Reinforced Beam-Column Joints Reinforced under Cyclic Loading," *Proceedings of the Institution of Civil Engineers Structures and Buildings 158*, Issue SB1, pp. 21-40.
- Baglin, P. S. and Scott, R. H. (2000). "Finite Element Modeling of Reinforced Concrete Beam-Column Connections," *ACI Structural Journal*, V. 97, No. 6, pp. 886-894.

- Bindhu, K. R. and Jaya, K. P. (2008). "Performance of Exterior Beam Column Joints with Cross-Inclined Bars under Seismic Type Loading," *Journal of Engineering and Applied Sciences*, V. 3, No. 7, pp. 591-597.
- Bindhu, K. R. and Jaya, K. P. (2010). "Strength and Behaviour of Exterior Beam-Column Joints with Diagonal Cross Bracing Bars," *Asian Journal of Civil Engineering (Building and Housing)*, V. 11, No. 3, pp. 397-410.
- Büyükkaragöz, A. (2010). "Finite Element Analysis of the Beam Strengthened with Prefabricated Reinforced Concrete Plate," *Scientific Research and Essays*, V. 5, No. 6, pp. 533-544.
- Canadian Standards Association. (2002). "Design and Construction of Building Components with Fibre-Reinforced Polymers," CAN/CSA S806-02, *Canadian Standards Association*, Rexdale, Ontario, 177 p.
- Canadian Standards Association. (2004). "Design of Concrete Structures," CAN/CSA A23.3-04, *Canadian Standards Association*, Rexdale, Ontario, 214 p.
- Canadian Standards Association. (2009). "Canadian Highway Bridge Design Code," CAN/CSA S6-09, *Canadian Standards Association, Addendum*, Rexdale, Ontario.
- CEB-FIB Model code. (1990). "Model Code for Concrete Structures," *Euro-International Committee for Concrete*, Thomas Telford, London, United Kingdom, 437 p.
- Chalioris, C. E., Favvata, M. J. and Karayannis, C. G. (2008). "Reinforced concrete beam-column joints with crossed inclined bars under cyclic deformations," *Earthquake Engineering and Structural Dynamics*, V. 37, No. 6, pp. 881-897.

- Chansawat, K., Potisuk, T., Miller, T. H., Yim, S. C. and Kachlakev, D. I. (2009). "FE Models of GFRP and CFRP Strengthening of Reinforced Concrete Beams," *Advances in Civil Engineering*, DOI:10.1155/2009/152196, V. 2009, ID. 152196, 13 p.
- Cheung, P. C., Paulay, T. and Park, R. (1993). "Behaviour of Beam-Column Joints in Seismically Loaded RC Frames," *The Structural Engineer*, V. 71, No. 8, pp. 129-138.
- Choo, C. C., Harik, I. E. and Gesund, H. (2006). "Strength of Rectangular Concrete Columns Reinforced with Fibre-Reinforced Polymer Bars," *ACI Structural Journal*, V. 103, No. 3, pp. 452-459.
- Chun, S. C., Lee, S. H., Kang, T. H., Oh, B. and Wallace, J. W. (2007). "Mechanical Anchorage in Exterior Beam-Column Joints Subjected to Cyclic Loading," *ACI Structural Journal*, V. 104, No. 1, pp. 102-112.
- Chung, L. and Shah, S. P. (1989). "Effect of Loading Rate on Anchorage Bond and Beam-Column Joints," *ACI Structural Journal*, V. 86, No. 2, pp. 132-142.
- Chutarat, N. and Aboutaha, R. S. (2003). "Cyclic Response of Exterior Reinforced Concrete Beam-Column Joints Reinforced with Headed Bars- Experimental Investigation," *ACI Structural Journal*, V. 100, No. 2, pp. 259-264.
- Danesh, F., Esmaeeli, E. and Alam, M. F. (2008). "Shear Strengthening of 3D RC Beam-Column Connection using GFRP: FEM Study," *Asian Journal of Applied Sciences*, V. 1, No. 3, pp. 217-227.

- Deitz, D. H., Harik, I. E. and Gesund, H. (2003). "Physical Properties of Glass Fibre Reinforced Polymer Rebars in Compression," *Journal of Composites in Construction*, V. 7, No. 4, pp. 363-366.
- Dooley, K. L. and Bracci, J. M. (2001). "Seismic Evaluation of Column-to-Beam Strength Ratios in Reinforced Concrete Frames," *ACI Structural Journal*, V. 98, No. 6, pp. 843-851.
- Ehsani, M. R. and Wight, J. K. (1985). "Exterior Reinforced Concrete Beam-to-Column Connections Subjected to Earthquake Type Loading," *ACI Journal, Proceedings*, V. 82, No. 3, pp. 492-499.
- Ehsani, M. R., Moussa, A. E. and Vallenilla, C. R. (1987). "Comparison of Inelastic Behaviour of Reinforced Ordinary- and High-Strength Concrete Frames," *ACI Structural Journal*, V. 84, No. 2, pp. 161-169.
- Ehsani, M. R. and Alameddine, J. (1991). "Design Recommendations for Type 2 High-Strength Reinforced Concrete Connections," *ACI Structural Journal*, V. 88, No. 3, pp. 277-291.
- Eligehausen, R., Genesio, G., Özbolt, J. and Pampanin, S. (2008). "3D Analysis of Seismic Response of RC Beam-Column Exterior Joints Before and After Retrofit," *2nd International Conference on Concrete Repair, Rehabilitation and Retrofitting*, 24-26 November, Rondebosch, South Africa., pp. 1141-1147.
- El-Sayed, A. K., El-Salakawy, E., Benmokrane, B. (2007). "Mechanical and Structural Characterization of New Carbon FRP Stirrups for Concrete Members," *Journal of Composites for Constructions*, V. 11, No. 4, pp. 352-362.

- Filiatrault, A., Pineau, S. and Houde, J. (1995). "Seismic Behavior of Steel Fiber Reinforced Concrete Interior Beam-Column Joints," *ACI Structural Journal*, V. 92, No. 5, pp. 1-10.
- Fukuyama, H., Masuda, Y., Sonobe, Y. and Tanigaki, M. (1995). "Structural Performances of Concrete Frame Reinforced with FRP Reinforcement," Non-Metallic (FRP) Reinforcement for Concrete Structures, Proceeding of the Second International RILEM Symposium (FRPRCS-2), E&FN Spon, London, pp. 275-286.
- Ghobarah, A. and El-Amoury T. (2005). "Seismic Rehabilitation of Deficient Exterior Concrete Frame Joints," *Journal of Composites for Construction, ASCE*, V. 9, No. 5, pp. 408-416.
- Gorji, M. S. (2009). "Analysis of FRP Strengthened Reinforced Concrete Beams using Energy Variation Method," *World Applied Sciences Journal*, V. 6, No. 1, pp. 105-111.
- Hakuto, S., Park, R. and Tanaka, H. (2000). "Seismic Load Tests on Interior and Exterior Beam-Column Joints with Substandard Reinforcing Details," *ACI Structural Journal*, V. 97, No. 1, pp. 11-25.
- Hanson, N. W. and Connor, H. W. (1967). "Seismic Resistance of Reinforced Concrete Beam-Column Joint," *Journal of the Structural Division, ASCE*, V. 93, ST5, pp. 533-560.
- Hasaballa, M. H. (2009). "Seismic Behaviour of Exterior GFRP Reinforced Concrete Beam-Column Joints," M.Sc. Thesis, University of Manitoba, Winnipeg, Manitoba, Canada.

- Hwang, S. J. and Lee, H. J. (1999). "Analytical Model for Predicting Shear Strengths of Exterior Reinforced Concrete Beam-Column Joints for Seismic Resistance," *ACI Structural Journal*, V. 96, No. 5, pp. 846-858.
- Hwang, S. J., Lee, H. J., Liao, T. F., Wang, K. C. and Tsai, H. H. (2005). "Role of Hoops on Shear Strength of Reinforced Concrete Beam-Column Joint," *ACI Structural Journal*, V. 102, No. 3, pp. 445-453.
- Ibrahim, A. M. and Mahmood, M. Sh. (2009). "Finite Element Modeling of Reinforced Concrete Beams Strengthened with FRP Laminates," *European Journal of Scientific Research*, V. 30, No. 4, pp. 526-541.
- ISIS Canada. (2007). "Reinforcing Concrete Structures with Fibre Reinforced Polymers," ISIS-M03-07, *The Canadian Network for Centers of Excellence on Intelligent Sensing for Innovative Structures*, ISIS Canada, Winnipeg, Manitoba, Canada.
- Kachlakev, D., Miller, T., Yim, S., Chansawat, K. and Potisuk, T. (2001). "Finite Element Modeling of Reinforced Concrete Structures strengthened with FRP Laminates," *Final Report SPR-316*, Oregon Department of Transportation, Salem, Oregon.
- Kent, D. C. and Park, R. (1971). "Flexural members with confined concrete," *Journal of the Structural Division, ASCE*, V. 97, pp. 1969-1990.
- Kulkarni, S. A. and Li, B. (2009). "Seismic Behaviour of Reinforced Concrete Interior Wide-Beam Column Joints," *Journal of Earthquake Engineering*, V. 13, pp. 80-99.
- LaFave J. M. and Wight, J. K. (1999). "Reinforced Concrete Exterior Wide Beam-Column-Slab Connections Subjected to Lateral Earthquake Loading," *ACI Structural Journal*, V. 96, No. 4, pp. 577-587.

- Leon, R.T. (1990). "Shear Strength and Hysteretic Behaviour of Interior Beam-Column Joints," *ACI Structural Journal*, V. 87, No. 1, pp. 3-11.
- Li, B. and Tran, C. T. N. (2009). "Seismic Behavior of Reinforced Concrete Beam-Column Joints with Vertically Distributed Reinforcement," *ACI Structural Journal*, V. 106, No. 6, pp. 790-799.
- Mady, M., Hasaballa, M., El-Ragaby, A. and El-Salakawy, E. (2010). "Effect of Reinforcement Detailing on the Behavior of GFRP-RC Beam-Column Joints," *The 5th International Conference on FRP Composites in Civil Engineering, CICE-2010*, September 27-29, Beijing, China, ID: 170-14, 9 p.
- Mostofinejad, D. and Talaeitaba, S. B. (2006). "Finite Element Modeling of RC Connections Strengthened with FRP Laminates," *Iranian Journal of Science & Technology*, V. 30, No. B1, pp. 21-30.
- NBCC. (2005). "National Building Code of Canada," *National Research Council of Canada*, Ottawa, Ontario, 1167 p.
- Parvin, A. and Granata, P. (2000). "Investigation on the effects of fibre composites at concrete joints," *Journal of Composites: Part B*, V. 31, pp. 499-509.
- Paulay, T., Park, R. and Priestley, M. J. N. (1978). "Reinforced Concrete Beam-Column Joints under Seismic Actions," *ACI Journal, Proceedings*, V. 75, No. 11, pp. 585-593.
- Park, R. (1989). "Evaluation of Ductility of Structures and Structural Assemblages from Laboratory Testing," *Bulletin of the New Zealand National Society for Earthquake Engineering*, V. 22, No. 3, pp. 155-166.

- Perera, U. (2005). "Seismic Performance of Concrete Beam-Slab-Column Systems Constructed with a Re-Useable Sheet Metal Formwork System," M.Sc. Thesis, University of Melbourne, Victoria, Australia.
- Pultrall Inc. V-RODTM. (2007). "Technical Data Sheet," *ADS Composites Group Inc.* <http://www.pultrall.com>, Thetford Mines, Quebec, Canada, 9 p.
- Saatcioglu, M. (2001). "Cracking in Concrete Structures during the August 17, 1999 Earthquake in Turkey," ACISP-20, *American Concrete Institute*, pp. 261-277.
- Sagbas, G. (2007). "Nonlinear Finite Element Analysis of Beam-Column Subassemblies," M.Sc. Thesis, University of Toronto, Ontario, Canada.
- Said, A. M. and Nehdi, M. L. (2004). "Use of FRP for RC Frames in Seismic Zones: Part II. Performance of Steel-Free GFRP-Reinforced Beam-Column Joints," *Applied Composite Materials*, V. 11, pp. 227-245.
- Sharbatdar, M. K. (2003). "Concrete Columns and Beams Reinforced with FRP Bars and Grids under Monotonic and Reversed Cyclic Loading," Ph.D. Thesis, University of Ottawa, Ottawa, Canada.
- Sharbatdar, M. K., Saatcioglu, M., Benmokrane, B. and El-Salakawy, E. (2007). "Behaviour of FRP Reinforced Concrete Beam-Column Joints under Cyclic Loading," *3rd International Conference on Durability & Field Applications of Fibre Reinforced Polymer (FRP) Composites for Construction*, (CDCC-07), Quebec City, Quebec, Canada, pp. 541-548.
- Solberg, K., Dhakal, R. P., Bradley, B., Mander, J. B. and Li, L. (2008). "Seismic Performance of Damage-Protected Beam-Column Joints," *ACI Structural Journal*, V. 105, No. 2, pp. 205-214.

-
- Sritharan, S., Priestley, M. J. N. and Seible, F. (2000). "Nonlinear Finite Element Analyses of Concrete Bridge Joint Systems Subjected to Seismic Actions," *Finite Elements in Analysis and Design*, V. 36, pp. 215-233
- Supaviriyakit, T., Pimanmas, A. and Warnitchai, P. (2008). "Nonlinear Finite Element Analysis of Non-Seismically Detailed Interior Reinforced concrete Beam-Column Connection under Reversed Cyclic Load," *Journal of Science Asia*, V. 34, pp. 49-58.
- Tajima, K., Mishimia, T., Shairai, N. (2004). "3-D Finite Element Cyclic Analysis of RC Beam-Column Joint using Special Bond Model," *13th World Conference on Earthquake Engineering*, August 1-6, Vancouver, B.C., Canada., ID: 446, 15p.
- Tosonos, A. G., Tegos, I. A. and Penelis, G. Gr. (1992). "Seismic Resistance of Type2 Exterior Beam-Column Joints Reinforced with Inclined Bars," *ACI Journal, Proceedings*, V. 89, No. 1, pp. 3-12.
- Wolanski, A. J. (2004). "Flexural Behavior of Reinforced and Prestressed Concrete Beams using Finite Element Analysis," M.Sc. Thesis, Marquette University, Milwaukee, Wisconsin.
- Yunovich, M. and Thompson, N. (2003). "Corrosion of Highway Bridges: Economic Impact and Control Methodologies," *ACI Concrete International*, V. 25, No. 1, pp. 52-57.

APPENDICES

APPENDIX-A

SPECIMENS DESIGN PROCEDURES

Design Procedures for Specimen SS03-B06-J06

Beam Design

Design for flexural

$$\text{Depth } (d) = 450 - 40 - \frac{19.5}{2} = 400 \text{ mm}$$

According to CSA A23.3-04 (Clause 10.1.7):

$$\alpha_1 = 0.85 - 0.0015 f'_c \geq 0.67$$

$$\alpha_1 = 0.85 - 0.0015(32) = 0.802$$

$$\beta_1 = 0.97 - 0.0025 f'_c \geq 0.67$$

$$\beta_1 = 0.97 - 0.0025(32) = 0.89$$

Assume using **5 bars 20M** steel top and bottom

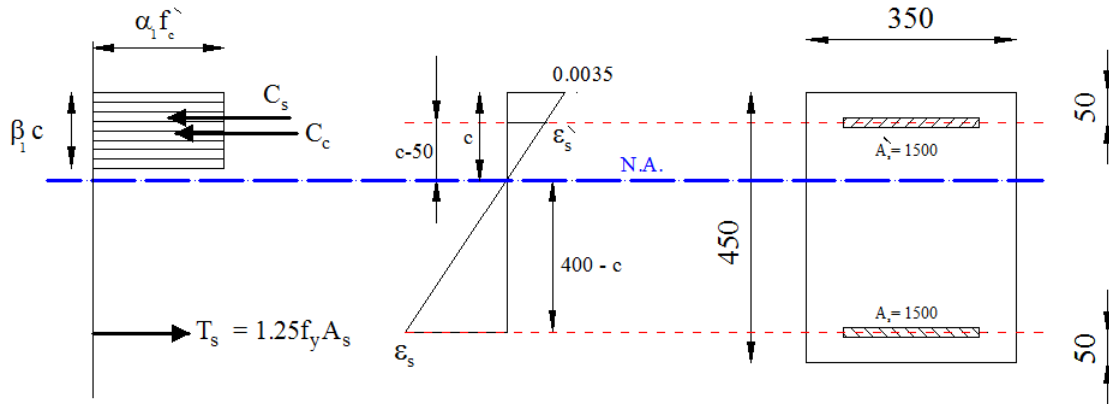
$$A_s = 5 \times 300 = 1500 \text{ mm}^2$$

According to CSA A23.3-04 (Clause 21.3.2.1):

$$A_{s,min} = \frac{1.4 bd}{f_y} = \frac{1.4 \times 350 \times 400}{400} = 490 \leq 1500 \quad \text{ok}$$

$$\rho_b = \alpha_1 \beta_1 \frac{f'_c}{f_y} \left(\frac{700}{700 + f_y} \right) = 0.802 \times 0.89 \times \frac{32}{400} \times \left(\frac{700}{700 + 400} \right) = 0.03634$$

$$\rho_{bactual} = \frac{A_s}{bd} = \frac{1500}{350 \times 400} = 0.0107 \approx 0.29 \rho_{frpb}$$



From compatibility:

$$\varepsilon_s = \left(\frac{400 - c}{c} \right) \times 0.0035$$

$$\varepsilon'_s = \left(\frac{c - 50}{c} \right) \times 0.0035$$

$$T_s = 1.25f_y A_s = 1.25 \times 400 \times 1500 = 750000$$

$$C_c = \alpha_1 \beta_1 f'_c b c = 0.802 \times 0.89 \times 32 \times 350 \times c = 7994.34c$$

$$C_s \text{ (assume no yielding)} = \varepsilon'_s E_s A'_s = \left(\frac{c - 50}{c} \right) \times 0.0035 \times 200 \times 10^3 \times 1500$$

$$C_s = 1050000 \left(\frac{c - 50}{c} \right)$$

From Equilibrium:

$$T_s = C_c + C_s$$

$$750000 = 7994.34c + 1050000 \left(\frac{c - 50}{c} \right)$$

$$c \approx 64.4 \text{ mm}$$

$$\varepsilon'_s = \left(\frac{64.4 - 50}{64.4} \right) \times 0.0035 = 0.00078 < 0.002 \quad \text{ok}$$

$$\varepsilon_s = \left(\frac{400 - 64.4}{64.4} \right) \times 0.0035 = 0.0182 > 0.002 \quad \text{ok}$$

According to CSA A23.3-04 (Clause 10.5.2)

$$\frac{c}{d} = \frac{64.4}{400} = \mathbf{0.161} \leq \frac{700}{700 + f_y} = \frac{700}{700 + 400} = \mathbf{0.64} \quad \text{Tension failure mode}$$

$$\text{Probable Moment } (M_{pb}) = T_s \left(d - \frac{\beta_1 c}{2} \right) + C_s \left(\frac{\beta_1 c}{2} - d' \right)$$

$$\begin{aligned} M_{pb} &= 750000 \times \left(400 - \frac{0.89 \times 64.4}{2} \right) + 1050000 \times \left(\frac{64.4 - 50}{64.4} \right) \\ &\quad \times \left(\frac{0.89 \times 64.4}{2} - 50 \right) = \mathbf{274 \text{ kN.m}} \end{aligned}$$

Design for shear

According to CSA A23.3-04 (Clause 21.3.3.2):

The stirrups spacing can be determined as the smallest of:

- Quarter of the section depth
- Eight times the diameter of the smallest longitudinal bars
- 300 mm

$$s = \text{smaller of } \left\{ \begin{array}{l} \frac{400}{4} = 100 \text{ mm} \\ 8 \times 19.5 = 156 \text{ mm} \\ 300 \text{ mm} \end{array} \right.$$

$$\mathbf{s = 100 \text{ mm}}$$

Maximum acting shear, V , can be calculated from the probable moment of the beam:

$$V = \frac{M_{pb}}{\text{Shear span}} = \frac{274}{2.00} = 137 \text{ kN}$$

$$\text{Effective depth } d_v = \text{larger of } \left\{ \begin{array}{l} 0.9d = 0.9 \times 400 = 360 \\ 0.72h = 0.72 \times 450 = 324 \end{array} \right.$$

$$\mathbf{d_v = 360 \text{ mm}}$$

According to CSA A23.3-04, Clause 21.3.4.2: (within the plastic hinge region)

Concrete contribution to shear (V_c) = zero and $\theta = 45^\circ$

Steel contribution to shear (V_s) = $\frac{\phi_s A_v f_y d_v \cot \theta}{s}$

$$137 \times 10^3 = \frac{1 \times A_v \times 400 \times 360 \times \cot 45}{100}$$

$$A_v = 95 \text{ mm}^2$$

Use 2-leg steel hoop 10M

According to CSA A23.3-04, Clause 11.2.8.2: (Outside the plastic hinge region):

Using the minimum stirrups:

$$A_{v,min} = 0.06 \sqrt{f'_c} \frac{bs}{f_y} = 0.06 \times \sqrt{32} \times \frac{350 \times 100}{400} = 30 \text{ mm}^2$$

Use 2-leg steel hoop 10M

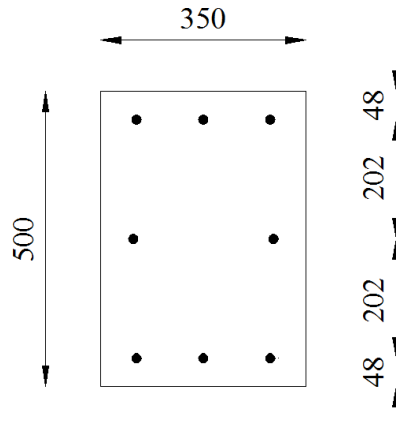
Column Design

Flexural calculations

$$\text{Depth } (d_c) = 500 - 40 - \frac{15.9}{2} = 452 \text{ mm}$$

The actual M_R will be determined after satisfying the minimum detailing requirements and check, using the interaction diagram, the capacity of this cross section against the acting loads.

Using 8-15M steel bars distributed around the section as shown:



Axial load calculations

According to CSA A23.3-04, Clause 10.10.4:

$$P_{ro} = \alpha_1 \phi_c f'_c (A_g - A_s) + \phi_s f_y A_s$$

$$P_{ro} = 0.802 \times 1 \times 32 \times [(350 \times 500) - (8 \times 200)] +$$

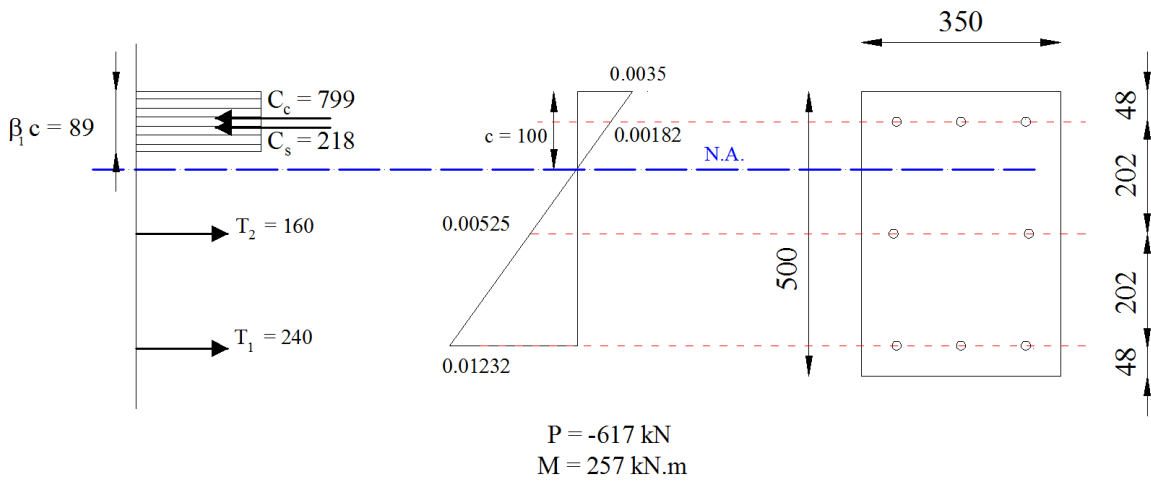
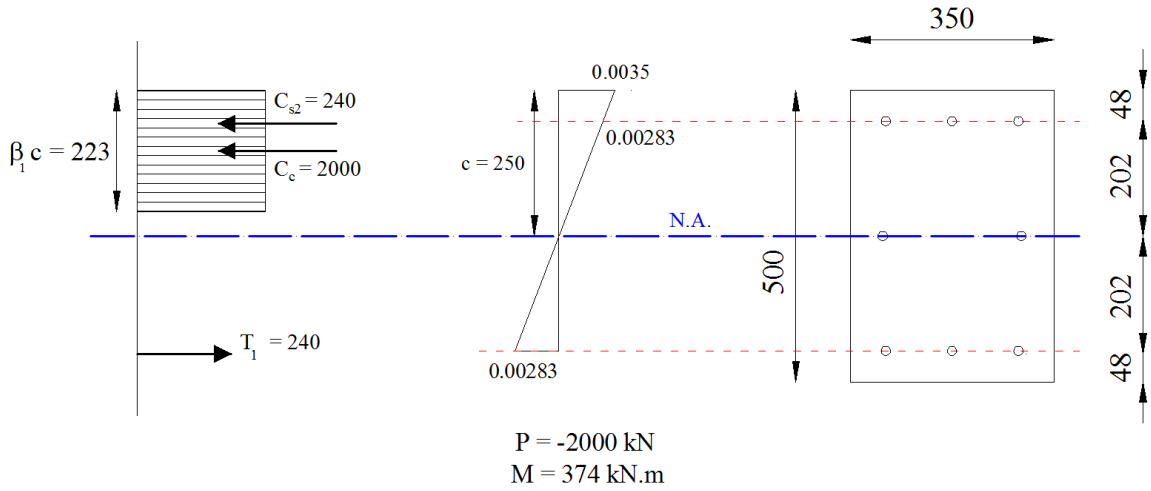
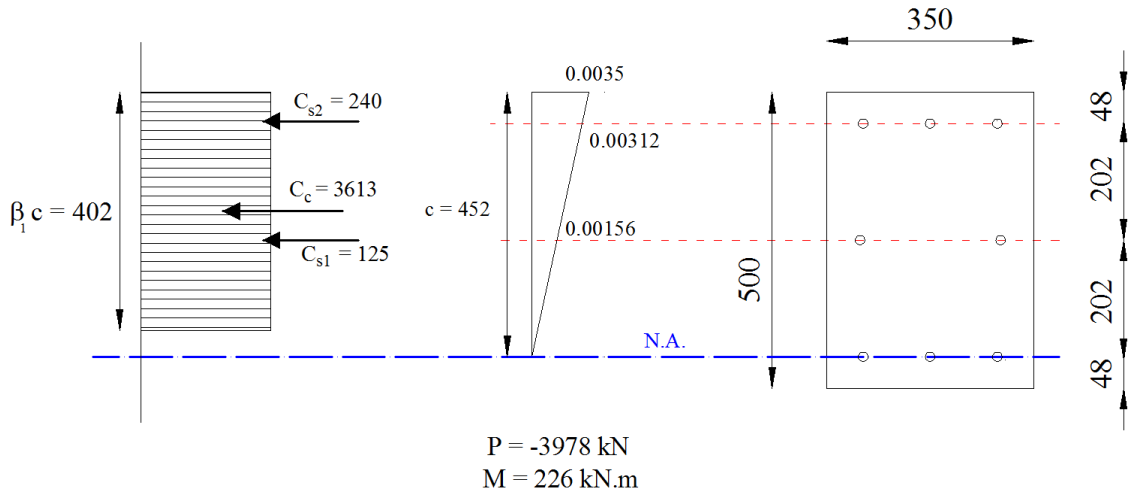
$$1 \times 400 \times (8 \times 200)$$

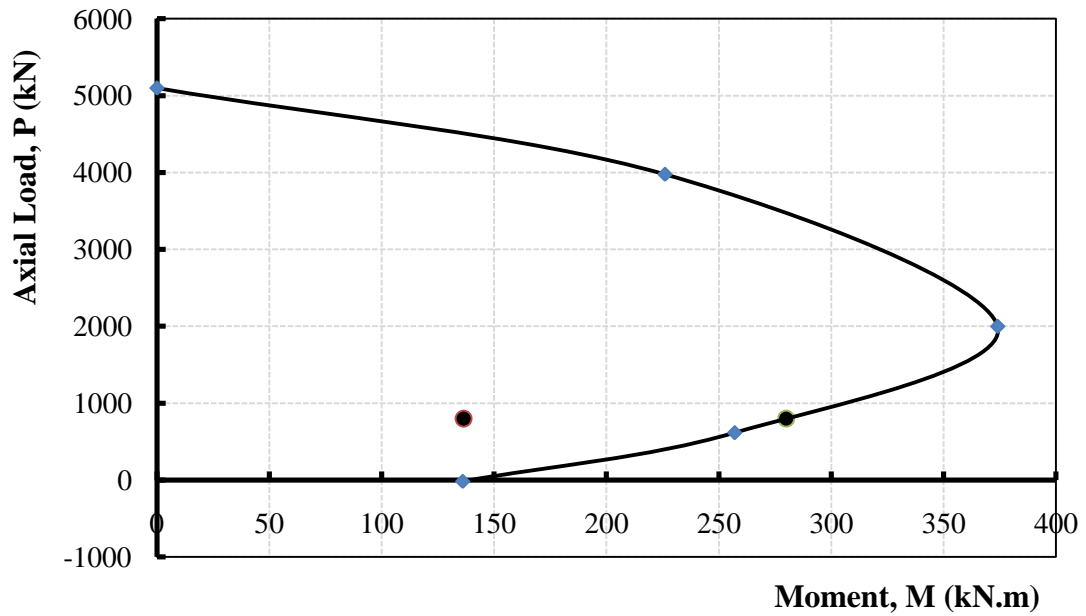
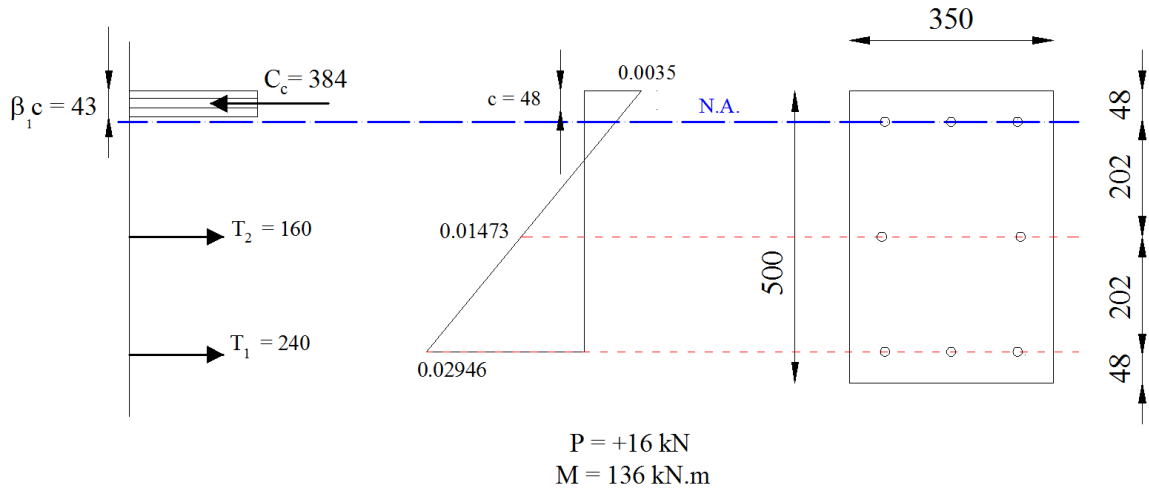
$$P_{ro} \approx 5100 \text{ kN}$$

The reduction factor $[0.8 \times P_{ro}]$ was neglected due to the absence of any possible eccentricity in loading the tied columns in the laboratory. Under sustained load, creep and shrinkage of concrete tend to transfer load from concrete to reinforcement, the matter that will increase the stresses in the reinforcement, especially with lower reinforcement ratios. So, strength reduction factor $[0.5(1 + \rho_t/0.01)]$ for reinforcement ratios lower than 0.01 should be introduced into calculations. However, this factor was also neglected as the specimen will be loaded and the load will increased up to failure and there is no creep expected within this short testing period (3 – 5 hours).

$$P_{actual} = 15\% P_{ro} = 765 \text{ kN}$$

Axial load-moment interaction diagram





Checking the location on the interaction diagram:

$$(P \approx 800 \text{ kN}, \quad M = 137 \text{ kN.m})$$

Safe

Actual column nominal moment

$$M_{nc} \approx 280 \text{ kN.m}$$

Actual flexural strength ratio

$$M_R = \frac{2M_{nc}}{M_{pb}}$$

$$M_R = \frac{2 \times 280}{274} = 2.04 \geq 1.00 \quad \text{ok}$$

Shear calculations

According to CSA A23.3-04, Clause 21.4.4.3:

stirrups spacing

$$= \text{smaller of } \begin{cases} \text{One - quarter of the minimum member dimension} \\ \text{six times the diameter of the smallest longitudinal bar} \end{cases}$$

$$s = \text{smaller of } \begin{cases} 0.25 \times 350 = 87.5 \text{ mm} \\ 6 \times 15.9 = 95.4 \text{ mm} \end{cases}$$

$$s = 90 \text{ mm}$$

Maximum acting shear, V_{col} can be calculated from the actual probable moment of the beam:

$$\text{Column design shear force } (V) = \frac{0.5 \times M_{pb}}{\text{Column shear span}} = \frac{0.5 \times 274}{1.500} \approx 91.3 \text{ kN}$$

Following the same procedure of the shear design of the beam:

Use the minimum: 2-leg steel hoop 10M

Lateral confinement calculations

According to CSA A23.3-04 (Clause 21.4.4.2), rectangular columns should be laterally confined with adequate hoop reinforcement area, A_{sh} , that should not be less than the largest of the following:

$$A_{sh1} = 0.2K_nK_p \frac{A_g}{A_c} \frac{f'_c}{f_{yh}} Sh_c$$

$$A_{sh2} = 0.09 \frac{f'_c}{f_{yh}} Sh_c$$

Where:

$$K_n = \frac{n_l}{n_l - 2} = \frac{6}{6 - 2} = 1.5$$

n_l = number of bars in the column cross-section that are tied by the corner of hoops or by hooks of seismic cross-ties.

$$K_p = \frac{P_f}{P_o} \approx 0.15$$

Column core dimensions are $\approx (431 \times 281)$

$$A_{sh1} = 0.2 \times 1.5 \times 0.15 \times \frac{350 \times 500}{281 \times 431} \times \frac{32}{400} \times 90 \times 281 = 132$$

$$A_{sh2} = 0.09 \times \frac{32}{400} \times 90 \times 281 = 182$$

So: $A_{sh} = \text{larger of } \begin{cases} A_{sh1} \\ A_{sh2} \end{cases} = 182 \text{ mm}^2$

Use 2-legs steel hoop 10M @ 90mm

Joint Design

According to CSA A23.3-04, Clauses 21.5.1.2 and 21.5.4.1:

$$T_b = 1.25F_y A_s$$

$$T_b = 1.25 \times 400 \times 1500 = 750 \text{ kN}$$

$$V_{nc} = \frac{0.5M_{pb}}{\text{column shear span}}$$

$$V_{nc} = \frac{0.5 \times 274 \times 10^6}{1500} = 91.3 \text{ kN}$$

$$V_j = T_b - V_{nc}$$

$$V_j = 750 - 91.3 = 658.7 \text{ kN}$$

$$V_{jr} = 1.3\lambda\phi_c\sqrt{f'_c}A_j$$

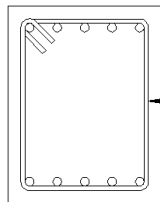
$$V_{jr} = 1.3 \times 1 \times 1 \times \sqrt{32} \times (350 \times 500) = 1287 \text{ kN}$$

$$V_{jr} \geq V_j \quad \text{safe}$$

The hoops of the column shall be continue within the joint with the same spacing

Final Details of the Joint SS03-B06-J06

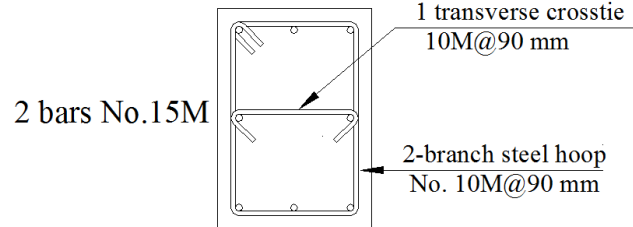
5 bars No. 20M



5 bars No. 20M

Beam cross- section

3 bars No.15M



3 bars No.15M

Column cross section

Design Procedures for Specimen GG17-B11-J12

Beam Design

Design for flexural

$$\text{Depth } (d) = 450 - 40 - \frac{19}{2} = 400 \text{ mm}$$

$$\alpha_1 = 0.85 - 0.0015 f'_c \geq 0.67$$

$$\alpha_1 = 0.85 - 0.0015(32) = 0.802$$

$$\beta_1 = 0.97 - 0.0025 f'_c \geq 0.67$$

$$\beta_1 = 0.97 - 0.0025(32) = 0.89$$

$$\rho_{frpb} = \alpha_1 \beta_1 \frac{\phi_c}{\phi_F} \frac{f'_c}{f_{frpu}} \left(\frac{\varepsilon_{cu}}{\varepsilon_{cu} + \varepsilon_{frpu}} \right)$$

$$\rho_{frpb} = \frac{A_{frpb}}{bd} = 0.802 \times 0.89 \times \frac{1}{1} \times \frac{32}{728} \times \left(\frac{0.0035}{0.0035 + 0.0153} \right) = 0.00584$$

$$A_{frpb} = 0.00584 \times 350 \times 400 = 818 \text{ mm}^2$$

$$\text{Number of bars} = \frac{818}{285} = 2.9$$

Use **5 bars No. 13** GFRP top and bottom to ensure the concrete crushing failure mode

$$A_{frp} = 5 \times 285 = 1425 \text{ mm}^2$$

$$\rho_{frp} = \frac{A_{frp}}{b \cdot d} = \frac{1425}{350 \times 400} = 0.01018 \approx 1.75 \rho_{frpb}$$

$$f_{frp} = 0.5 E_{frp} \varepsilon_{cu} \left[\left(1 + \frac{4 \alpha_1 \beta_1 \phi_c f'_c}{\rho_{frp} \phi_F E_{frp} \varepsilon_{cu}} \right)^{0.5} - 1 \right]$$

$$f_{frp} = 0.5 \times 47.6 \times 10^3 \times 0.0035$$

$$\times \left(\left[1 + \frac{4 \times 0.802 \times 0.89 \times 1 \times 32}{0.01018 \times 1 \times 47.6 \times 10^3 \times 0.0035} \right]^{0.5} - 1 \right) = 534 \text{ MPa}$$

$$\leq 728 \text{ MPa} \quad \text{ok}$$

$$\varepsilon_{frp} = \frac{534}{47.6 \times 10^3} = 0.0112$$

$$c = d \left(\frac{\varepsilon_{cu}}{\varepsilon_{cu} + \varepsilon_{frp}} \right)$$

$$c = 400 \times \left(\frac{0.0035}{0.0035 + 0.0112} \right) = 95 \text{ mm}$$

$$M_{nb} = \phi_F f_{frp} A_{frp} \left(d - \frac{\beta_1 c}{2} \right)$$

$$M_{nb} = 1 \times 534 \times 1425 \times \left(400 - \frac{0.89 \times 95}{2} \right) = 272 \text{ kN.m}$$

Design for shear

The stirrups spacing can be determined as the smallest of:

- Quarter of the section depth
- Eight times the diameter of the smallest longitudinal bars
- 300 mm

$$s = \text{smaller of} \left\{ \begin{array}{l} \frac{400}{4} = 100 \text{ mm} \\ 8 \times 19 = 152 \text{ mm} \\ 300 \text{ mm} \end{array} \right.$$

$$s = 100 \text{ mm}$$

Maximum acting shear, V , can be calculated from the nominal moment of the beam:

$$V = \frac{M_{nb}}{\text{Shear span}} = \frac{272}{2.00} = 136 \text{ kN}$$

$$V_c = 0$$

$$V_F = 1436 \times 10^3 = \frac{0.4 \phi_F A_v f_{u,v} d}{s}$$

$$A_v = \frac{136 \times 10^3 \times 100}{0.4 \times 1 \times 590 \times 400} = 144 \text{ mm}^2$$

$$A_{v,min} = \frac{0.3\sqrt{f'_c}bs}{f_{uv,frp}} = \frac{0.3 \times \sqrt{32} \times 350 \times 100}{0.004 \times 46.3 \times 10^3} = 321 \text{ mm}^2$$

Use 3 branches No.13 GFRP hoops

Column Design

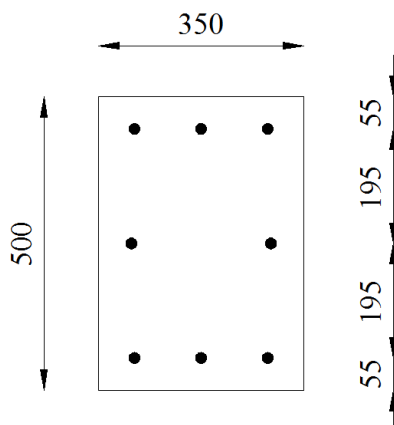
Flexural calculations

The clear cover in the column will be 45 mm (detailing requirements)

$$\text{Depth } (d_c) = 500 - 45 - \frac{19}{2} = 445 \text{ mm}$$

The actual M_R will be determined after satisfying the minimum detailing requirements and check, using the interaction diagram, the capacity of this cross section against the acting loads.

Using 8 bars No. 19 GFRP distributed around the section as shown:



Axial load calculations

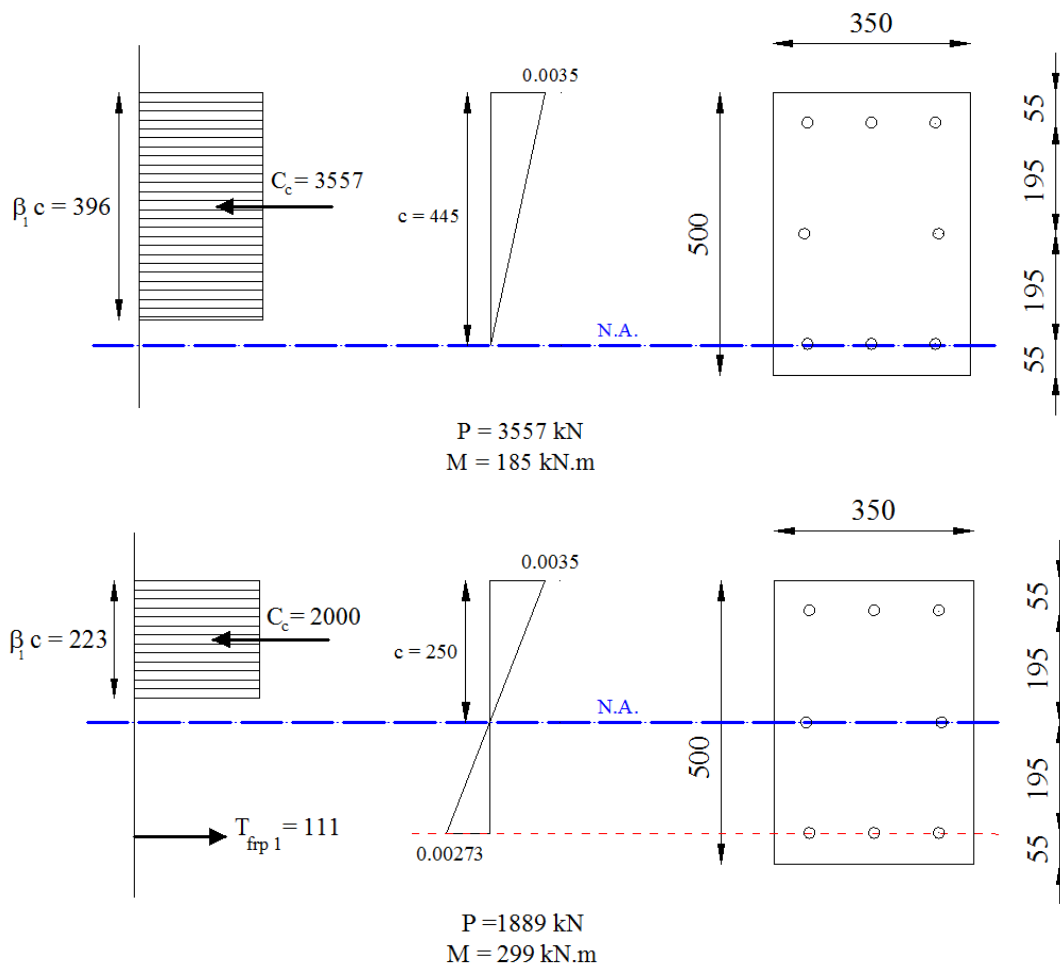
$$P_{ro} = 0.85\phi_c f'_c (A_g - A_{frp}) + \phi_F \varepsilon_{frpc} E_{frpc} A_{frp}$$

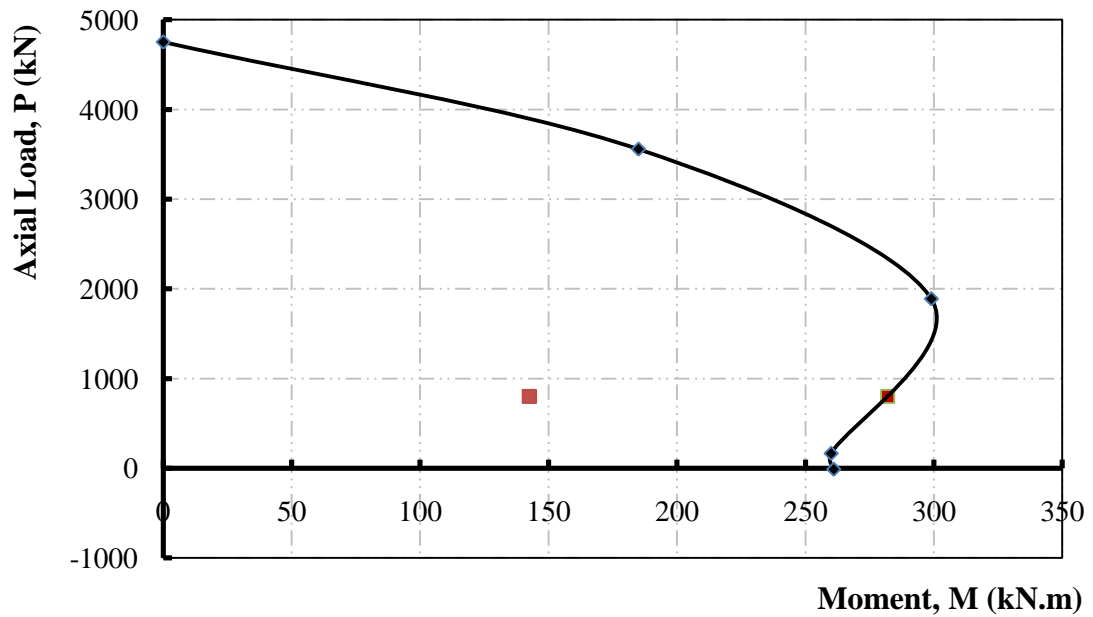
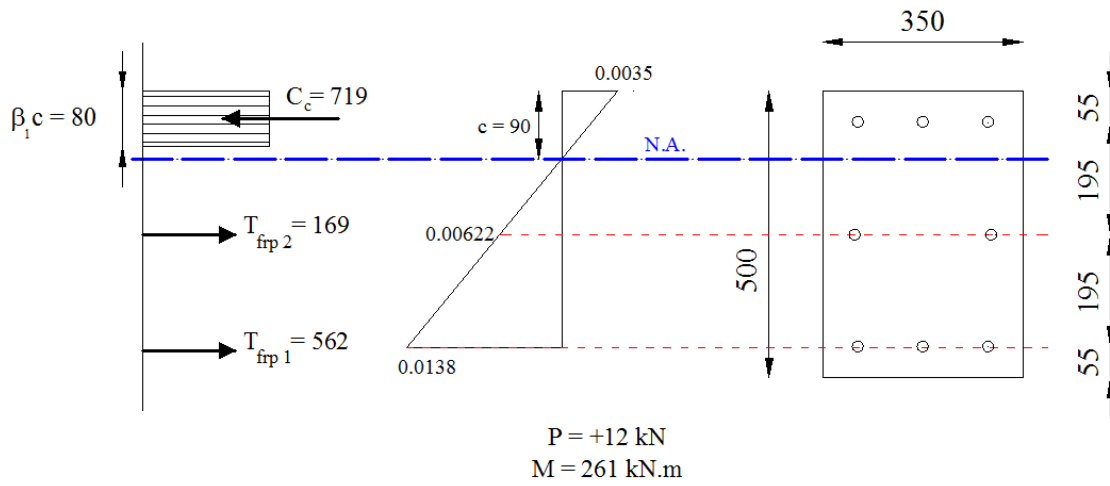
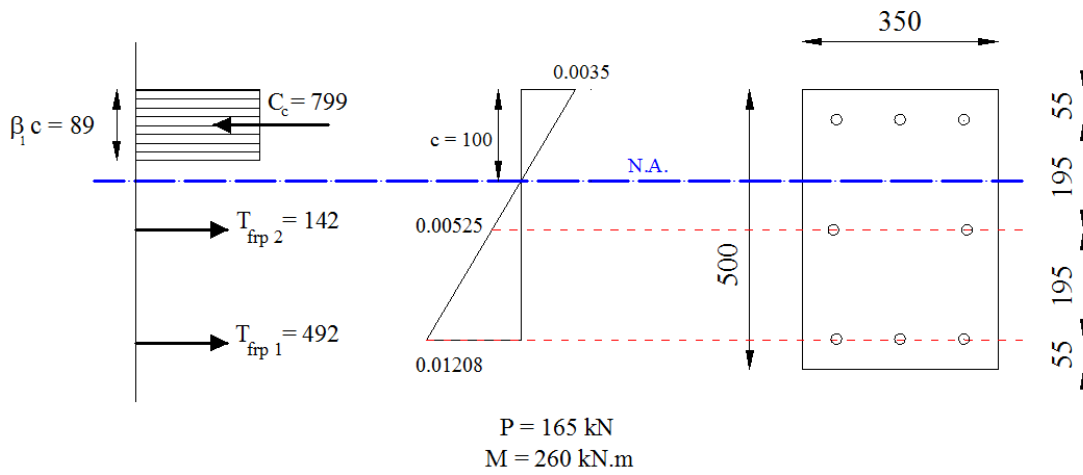
$$P_{ro} = 0.85 \times 1 \times 32 \times [(350 \times 500) - (8 \times 285)] +$$

$$0.002 \times 1 \times (0.25 \times 47.6 \times 10^3) \times (8 \times 285)$$

$$P_{ro} \approx 4752 \text{ kN}$$

$$P_{actual} \approx 15\% P_{ro} = 800 \text{ kN}$$

Axial load-moment interaction diagram



Checking the location on the interaction diagram:

$$(P = 800 \text{ kN}, \quad M = 136 \text{ kN.m})$$

Safe

Actual column nominal moment

$$M_{nc} \approx 283 \text{ kN.m}$$

Actual flexural strength ratio

$$M_R = \frac{2M_{nc}}{M_{nb}}$$

$$M_R = \frac{2 \times 283}{272} \approx 2.08 \geq 1.20 \quad \text{ok}$$

Shear calculations

stirrups spacing

= smaller of $\left\{ \begin{array}{l} \text{One – quarter of the minimum member dimension} \\ \text{six times the diameter of the smallest longitudinal bar} \end{array} \right.$

$$s = \text{smaller of } \left\{ \begin{array}{l} 0.25 \times 350 = 87.5 \text{ mm} \\ 6 \times 19 = 114 \text{ mm} \end{array} \right.$$

$$s = 90 \text{ mm}$$

Maximum acting shear, V_{col} , can be calculated from the actual nominal moment of the beam:

$$\text{Column design shear force (V)} = \frac{0.5 \times M_{nb}}{\text{Column shear span}} = \frac{0.5 \times 272}{1.500} = 91 \text{ kN}$$

$$V_c = 0$$

$$V_F = 91 \times 10^3 = \frac{0.4\phi_F A_v f_{f_{u,v}} d}{s}$$

$$A_v = \frac{91 \times 10^3 \times 100}{0.4 \times 1 \times 590 \times 445} = 87 \text{ mm}^2$$

$$A_{v,min} = \frac{0.3\sqrt{f'_c}bs}{f_{uv,frp}} = \frac{0.3 \times \sqrt{32} \times 350 \times 100}{0.004 \times 46.3 \times 10^3} = 321 \text{ mm}^2$$

Use hoops 3 branches No. 13 GFRP

Lateral confinement calculations

Column core dimensions are $\approx (447 \times 283)$

$$A_{FH} = (3 * 126.7) = 380.1 \text{ mm}^2$$

$$S_1 = 170 \text{ mm}$$

$$K_c = 0.15 \sqrt{\frac{h_c h_c}{s s_1}}$$

$$K_c = 0.15 \sqrt{\frac{283}{90} \times \frac{283}{170}} = 0.3432$$

$$A_{FH} = 14sh_c \frac{f'_c}{f_{FH}} \left(\frac{A_g}{A_c} - 1 \right) \frac{\delta}{\sqrt{K_c}} \frac{P_f}{P_{ro}}$$

$$380.1 = 14 \times 90 \times 283 \times \frac{32}{0.004 \times 46.3 \times 10^3} \times \left(\frac{500 \times 350}{447 \times 283} - 1 \right) \times \frac{\delta}{\sqrt{0.3432}} \times 0.15$$

$$\delta \approx 6 \% > 3 \% \quad \text{ok}$$

Joint Design

Design for shear

$$T_b = \varepsilon_{frp,nominal} E_{frp} A_{frp}$$

$$T_b = 0.0112 \times 47.6 \times 10^3 \times 1425 = 760 \text{ kN}$$

$$V_{nc} = \frac{M_{nc} = 0.5M_{nb}}{\text{column shear span}}$$

$$V_{nc} = \frac{0.5 \times 272 \times 10^6}{1500} = 91 \text{ kN}$$

$$V_j = T_b - V_{nc}$$

$$V_j = 760 - 91 \approx 669 \text{ kN}$$

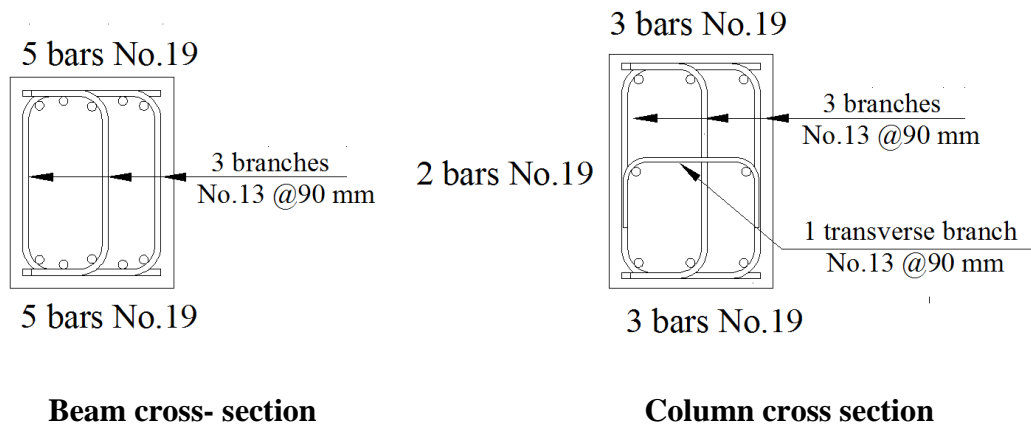
$$V_{jr} = 1.3\lambda\phi_c\sqrt{f'_c}A_j$$

$$V_{jr} = 1.3 \times 1 \times 1 \times \sqrt{32} \times (350 \times 500) = 1287 \text{ kN}$$

$$V_{jr} \geq V_j \quad \text{safe}$$

The hoops of the column shall be continue within the joint with the same spacing

Final Details of the Joint GG12-B11-J12



Design Procedures for Specimen CG12-B11-J12

Beam Design

Design for flexural

$$\text{Depth } (d) = 450 - 40 - \frac{10}{2} = 405 \text{ mm}$$

$$\alpha_1 = 0.85 - 0.0015 f'_c \geq 0.67$$

$$\alpha_1 = 0.85 - 0.0015(32) = 0.802$$

$$\beta_1 = 0.97 - 0.0025 f'_c \geq 0.67$$

$$\beta_1 = 0.97 - 0.0025(32) = 0.89$$

$$\rho_{frpb} = \alpha_1 \beta_1 \frac{\phi_c}{\phi_F} \frac{f'_c}{f_{frpu}} \left(\frac{\varepsilon_{cu}}{\varepsilon_{cu} + \varepsilon_{frpu}} \right)$$

$$\rho_{frpb} = \frac{A_{frpb}}{bd} = 0.802 \times 0.89 \times \frac{1}{1} \times \frac{32}{1596} \times \left(\frac{0.0035}{0.0035 + 0.014} \right) = 0.00286$$

$$A_{frpb} = 0.00286 \times 350 \times 405 = 406 \text{ mm}^2$$

$$\text{Number of bars} = \frac{406}{71} = 5.7$$

Use **7 bars No. 10 CFRP** top and bottom to ensure the concrete crushing failure mode

$$A_{frp} = 7 \times 71 = 497 \text{ mm}^2$$

$$\rho_{frp} = \frac{A_{frp}}{bd} = \frac{497}{350 \times 405} = 0.00351 \approx 1.23 \rho_{frpb}$$

$$f_{frp} = 0.5 E_{frp} \varepsilon_{cu} \left[\left(1 + \frac{4 \alpha_1 \beta_1 \phi_c f'_c}{\rho_{frp} \phi_F E_{frp} \varepsilon_{cu}} \right)^{0.5} - 1 \right]$$

$$f_{frp} = 0.5 \times 124 \times 10^3 \times 0.0035$$

$$\times \left(\left[1 + \frac{4 \times 0.802 \times 0.89 \times 1 \times 32}{0.00351 \times 1 \times 124 \times 10^3 \times 0.0035} \right]^{0.5} - 1 \right)$$

$$f_{frp} = 1477 \text{ MPa} \leq 1596 \text{ MPa} \quad \text{ok}$$

$$\varepsilon_{frp} = \frac{1477}{124 \times 10^3} = 0.0119$$

$$c = d \left(\frac{\varepsilon_{cu}}{\varepsilon_{cu} + \varepsilon_{frp}} \right)$$

$$c = 405 \times \left(\frac{0.0035}{0.0035 + 0.0119} \right) = 92 \text{ mm}$$

$$M_{nb} = \phi_F f_{frp} A_{frp} \left(d - \frac{\beta_1 c}{2} \right)$$

$$M_{nb} = 1 \times 1477 \times 497 \times \left(405 - \frac{0.89 \times 92}{2} \right) = 267 \text{ kN.m}$$

Design for shear

Maximum acting shear, V , can be calculated from the nominal moment of the beam:

$$V = \frac{M_{nb}}{\text{Shear span}} = \frac{267}{2.00} = 133.5 \text{ kN}$$

$$V_c = 0$$

$$V_F = 133.5 \times 10^3 = \frac{0.4 \phi_F A_v f_{u,v} d}{s}$$

$$A_v = \frac{133.5 \times 10^3 \times 100}{0.4 \times 1 \times 590 \times 400} = 141 \text{ mm}^2$$

$$A_{v,min} = \frac{0.3 \sqrt{f'_c} b s}{f_{uv,frp}} = \frac{0.3 \times \sqrt{32} \times 350 \times 100}{0.004 \times 46.3 \times 10^3} = 321 \text{ mm}^2$$

Use hoops 3 branches No. 13 GFRP

Column Design

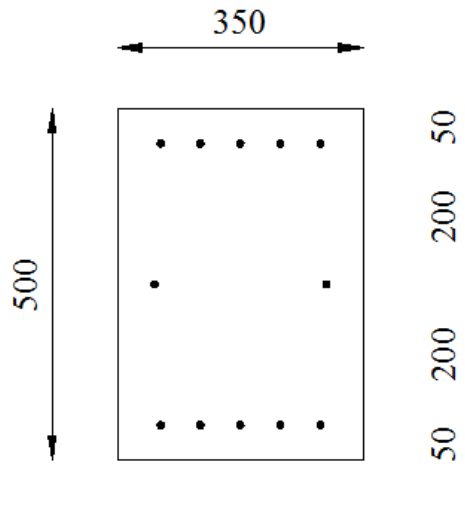
Flexural calculations

The clear cover in the column will be 45 mm (detailing requirements)

$$\text{Depth } (d_c) = 500 - 45 - \frac{10}{2} = 450 \text{ mm}$$

The actual M_R will be determined after satisfying the minimum detailing requirements and check, using the interaction diagram, the capacity of this cross section against the acting loads.

Using 12 bars No. 10 CFRP distributed around the section as shown:



Axial load calculations

$$P_{ro} = 0.85\phi_c f'_c (A_g - A_{frp}) + \phi_F \epsilon_{frpc} E_{frpc} A_{frp}$$

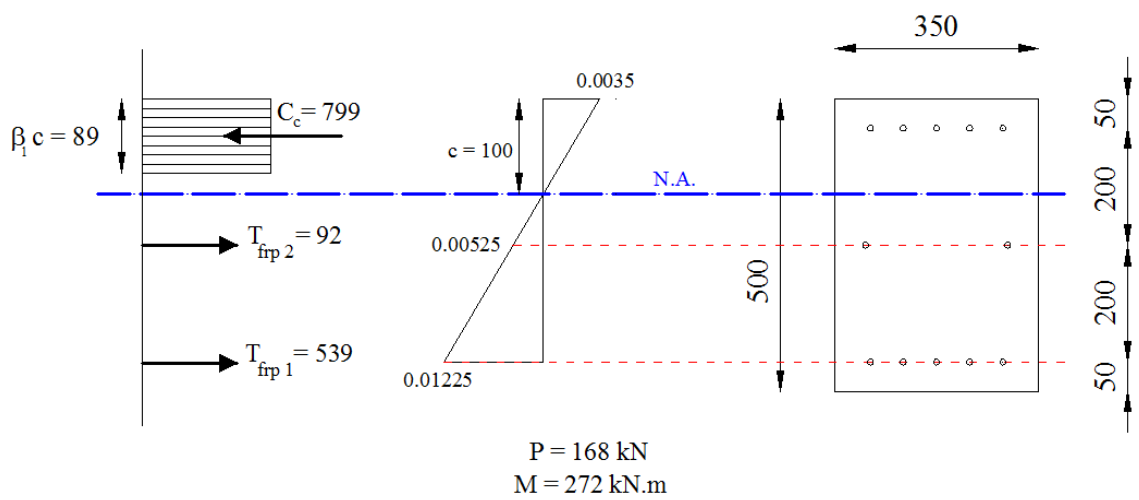
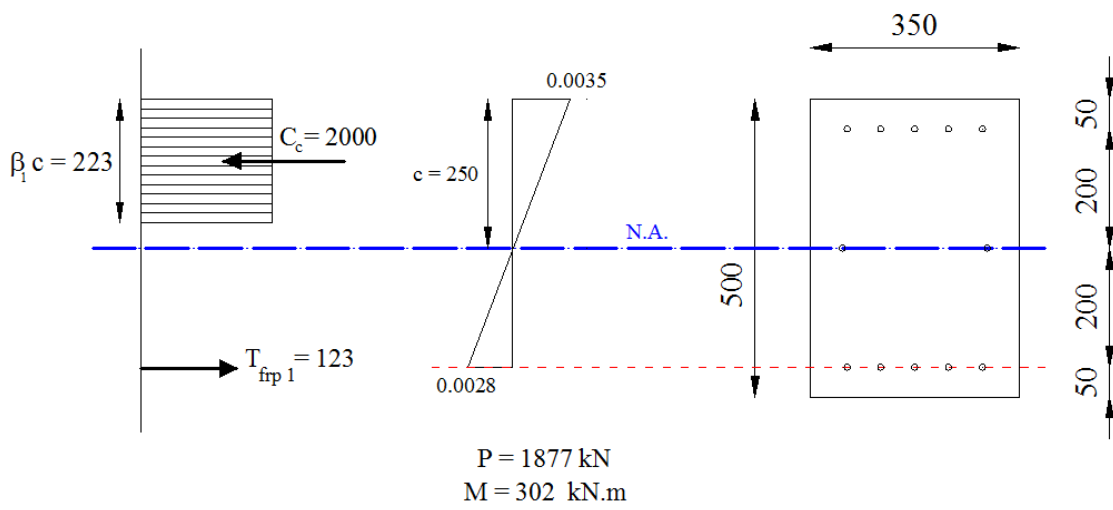
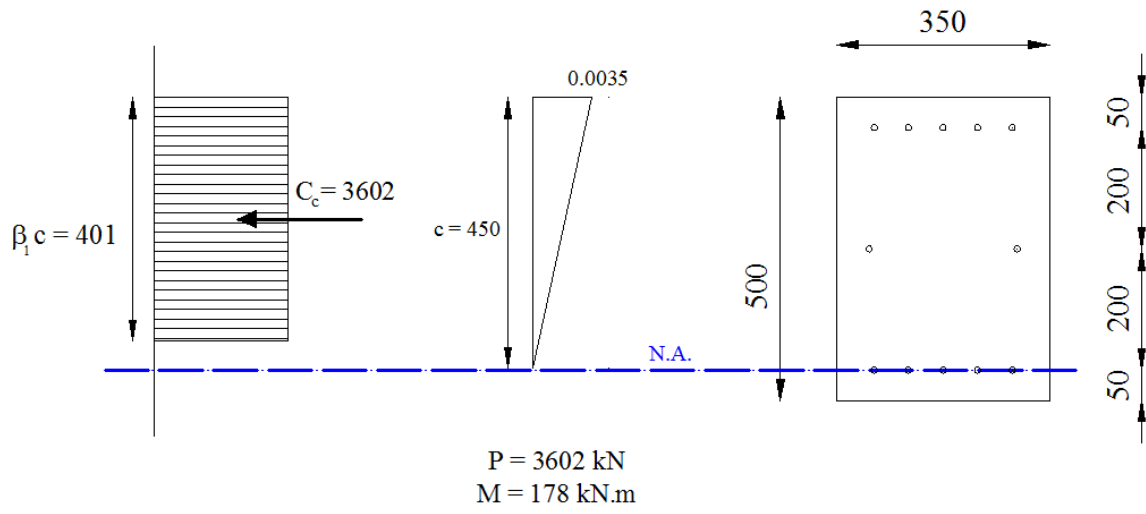
$$P_{ro} = 0.85 \times 1 \times 32 \times [(350 \times 500) - (12 \times 71)] +$$

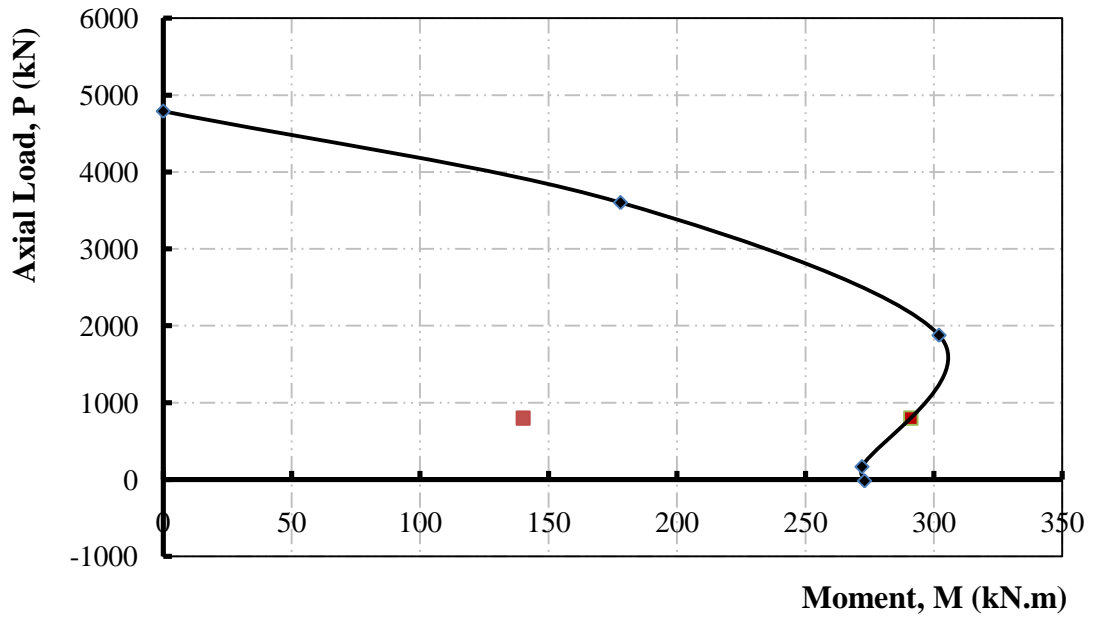
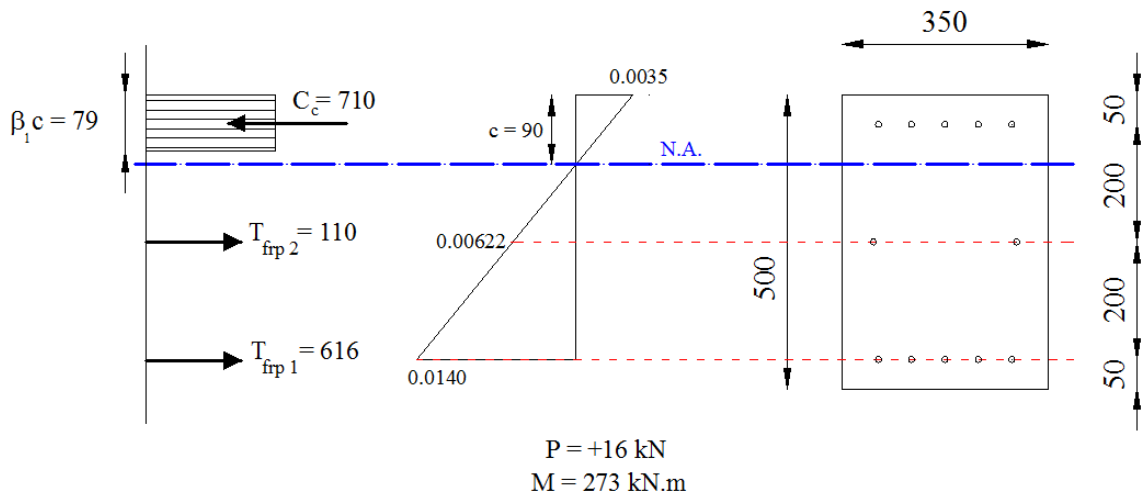
$$0.002 \times 1 \times (0.25 \times 124 \times 10^3) \times (12 \times 71)$$

$$P_{ro} \approx 4790 \text{ kN}$$

$$P_{actual} = 15\% P_{ro} = 720 \text{ kN}$$

Axial load-moment interaction diagram





Checking the location on the interaction diagram:

$$(P = 800 \text{ kN}, \quad M = 133.5 \text{ kN.m})$$

Safe

Actual column nominal moment

$$M_{nc} \approx 292 \text{ kN.m}$$

Actual flexural strength ratio

$$M_R = \frac{2M_{nc}}{M_{nb}}$$

$$M_R = \frac{2 \times 292}{267} \approx 2.18 \geq 1.20 \quad \text{ok}$$

Shear calculations

Maximum acting shear, V_{col} , can be calculated from the actual nominal moment of the beam:

$$\text{Column design shear force (V)} = \frac{0.5 \times M_{nb}}{\text{Column shear span}} = \frac{0.5 \times 267}{1.500} = 89 \text{ kN}$$

$$V_c = 0$$

$$V_F = 89 \times 10^3 = \frac{0.4\phi_F A_v f_{f_{u,v}} d}{s}$$

$$A_v = \frac{89 \times 10^3 \times 100}{0.4 \times 1 \times 590 \times 450} = 84 \text{ mm}^2$$

$$A_{v,min} = \frac{0.3\sqrt{f'_c}bs}{f_{uv,frp}} = \frac{0.3 \times \sqrt{32} \times 350 \times 100}{0.004 \times 46.3 \times 10^3} = 321 \text{ mm}^2$$

Use hoops 3 branches No. 13 GFRP

Lateral confinement calculations

Column core dimensions are $\approx (447 \times 283)$

$$A_{FH} = (3 * 126.7) = 380.1 \text{ mm}^2$$

$$S_1 = 170 \text{ mm}$$

$$K_c = 0.15 \sqrt{\frac{h_c h_c}{s s_1}}$$

$$K_c = 0.15 \sqrt{\frac{283}{90} \times \frac{283}{170}} = 0.3432$$

$$A_{FH} = 14sh_c \frac{f'_c}{f_{FH}} \left(\frac{A_g}{A_c} - 1 \right) \frac{\delta}{\sqrt{K_c}} \frac{P_f}{P_{ro}}$$

$$380.1 = 14 \times 90 \times 283 \times \frac{32}{0.004 \times 46.3 \times 10^3} \times \left(\frac{500 \times 350}{447 \times 283} - 1 \right) \times \frac{\delta}{\sqrt{0.3432}} \times 0.15$$

$$\delta = 6 \% > 3 \% \quad \text{ok}$$

Joint Design

Design for shear

$$T_b = \varepsilon_{frp,nominal} E_{frp} A_{frp}$$

$$T_b = 0.0119 \times 124 \times 10^3 \times 497 = 733 \text{ kN}$$

$$V_{nc} = \frac{M_{nc} = 0.5M_{nb}}{\text{column shear span}}$$

$$V_{nc} = \frac{0.5 \times 267 \times 10^6}{1500} = 89 \text{ kN}$$

$$V_j = T_b - V_{nc}$$

$$V_j = 733 - 89 \approx 644 \text{ kN}$$

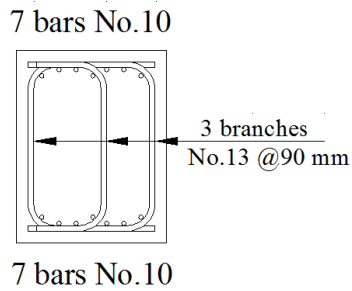
$$V_{jr} = 1.3\lambda\phi_c\sqrt{f'_c}A_j$$

$$V_{jr} = 1.3 \times 1 \times 1 \times \sqrt{32} \times (350 \times 500) = 1287 \text{ kN}$$

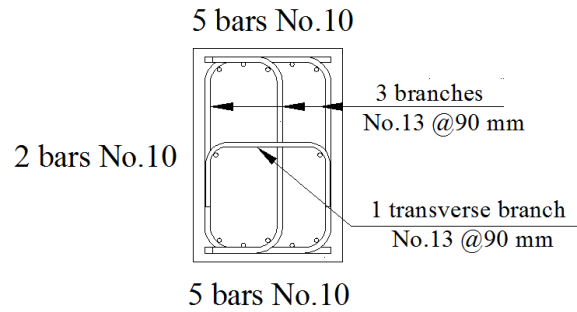
$$V_{jr} \geq V_j \quad \text{safe}$$

The hoops of the column shall be continue within the joint with the same spacing

Final Details of the Joint CG12-B11-J12



Beam cross- section



Column cross section

APPENDIX-B

Theoretical Forces and Deflections

Cracking cycle for specimen SS03-B06-J06

$$E_c = 4500\sqrt{f'_c} = 4500 \times \sqrt{32} = 25.5 \text{ GPa}$$

$$n = \frac{E_s}{E_c} = \frac{200}{25.5} = 7.8$$

$$M_{cr} = \frac{f_r \times I_{b \text{ gross}}}{y_{ct}}$$

$$f_r = 0.6 \times \sqrt{f'_c}$$

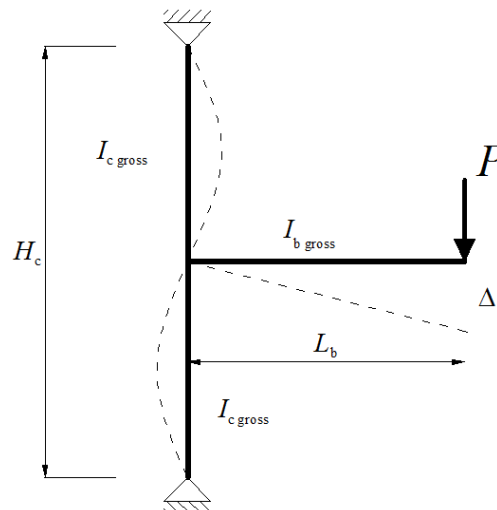
$$f_r = 0.6 \times \sqrt{32} = 3.4 \text{ MPa}$$

$$I_{b \text{ gross}} = \frac{bh^3}{12} + \left(2(n-1)A_s \left(\frac{h}{2} - d' \right)^2 \right)$$

$$I_{b \text{ gross}} = \frac{350 \times (450)^3}{12} + (2 \times (7.8 - 1) \times 1500 \times (175)^2) = 3282562500 \text{ mm}^2$$

$$M_{cr} = \frac{3.4 \times 3282562500}{225} = 49.6 \text{ KN.m}$$

$$P_{cr} = \frac{49.6}{2} = 24.8 \text{ KN}$$



$$\Delta = \frac{PL_b^3}{3EI_{b,gross}} + \frac{PL_b^2 H_c}{12EI_{c,gross}}$$

$$I_{c,gross} = \frac{350 \times (500)^3}{12} + (2 \times (7.8 - 1) \times 600 \times (200)^2) = 3972233333 \text{ mm}^2$$

$$\Delta = \frac{(24.8 \times 10^3) \times 2250^3}{3 \times 25.5 \times 10^3 \times 3282562500} + \frac{(24.8 \times 10^3) \times 2250^2 \times 3500}{12 \times 25.5 \times 10^3 \times 3972233333} = 1.49 \text{ mm}$$

Cracking cycle for specimen GG17-B11-J12

$$n = \frac{E_{frp}}{E_c} = \frac{47.6}{25.5} \approx 1.9$$

$$I_{b,gross} = \frac{350 \times (450)^3}{12} + (2 \times (1.9 - 1) \times 1425 \times (175)^2) = 2736365625 \text{ mm}^2$$

$$M_{cr} = \frac{3.4 \times 2736365625}{225} = 41 \text{ KN.m}$$

$$P_{cr} = \frac{43}{2} = 20.5 \text{ KN}$$

$$I_{c,gross} = \frac{350 \times (500)^3}{12} + (2 \times (1.9 - 1) \times 855 \times (195)^2) = 3704353808 \text{ mm}^2$$

$$\Delta = \frac{(20.5 \times 10^3) \times 2250^3}{3 \times 25.5 \times 10^3 \times 2736365625} + \frac{(20.5 \times 10^3) \times 2250^2 \times 3500}{12 \times 25.5 \times 10^3 \times 3704353808} = 1.44 \text{ mm}$$

Cracking cycle for specimen CG12-B11-J12

$$n = \frac{E_{frp}}{E_c} = \frac{124}{25.5} = 4.9$$

$$I_{b,gross} = \frac{350 \times (450)^3}{12} + (2 \times (4.9 - 1) \times 499 \times (175)^2) = 2777011125 \text{ mm}^2$$

$$M_{cr} = \frac{3.4 \times 2777011125}{225} = 42 \text{ KN.m}$$

$$P_{cr} = \frac{42}{2} = 21 \text{ KN}$$

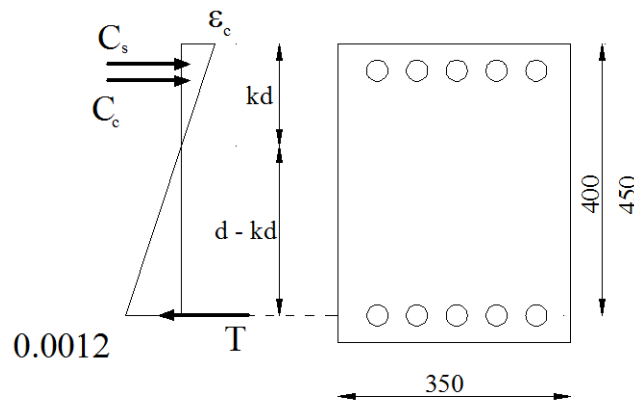
$$I_{c \text{ gross}} = \frac{350 \times (500)^3}{12} + (2 \times (4.9 - 1) \times 356.5 \times (200)^2) = 3757061333 \text{ mm}^2$$

$$\Delta = \frac{(21 \times 10^3) \times 2250^3}{3 \times 25.5 \times 10^3 \times 2777011125} + \frac{(21 \times 10^3) \times 2250^2 \times 3500}{12 \times 25.5 \times 10^3 \times 3757061333} = 1.45 \text{ mm}$$

Service cycle for specimen SS03-B06-J06

$$\varepsilon_s = 0.60 \varepsilon_y$$

$$\varepsilon_s = 0.60 \times 0.002 = 0.0012$$



$$T = 0.0012 \times 200 \times 10^3 \times 1500 = 360000 \text{ N}$$

According to CAC Concrete Design handbook:

$$B = \frac{b}{nA_s} = \frac{350}{7.8 \times 1500} = 0.03$$

$$r = \frac{(n-1)A'_s}{nA_s} = \frac{(7.8-1) \times 1500}{7.8 \times 1500} = 0.87$$

$$kd = \frac{\sqrt{2dB \left(1 + \frac{rd'}{d}\right) + (1+r)^2} - (1+r)}{B}$$

$$kd = \frac{\sqrt{2 \times 400 \times 0.03 \times \left(1 + \frac{0.87 \times 50}{400}\right) + (1 + 0.87)^2} - (1 + 0.87)}{0.03} \approx 120.5 \text{ mm}$$

$$C_s = 0.0012 \times \left(\frac{120.5 - 50}{400 - 120.5}\right) \times 200 \times 10^3 \times 1500 \approx 90805 \text{ N}$$

$$M_{service} = T \left(d - \frac{kd}{3}\right) + C_s \left(\frac{kd}{3} - d'\right)$$

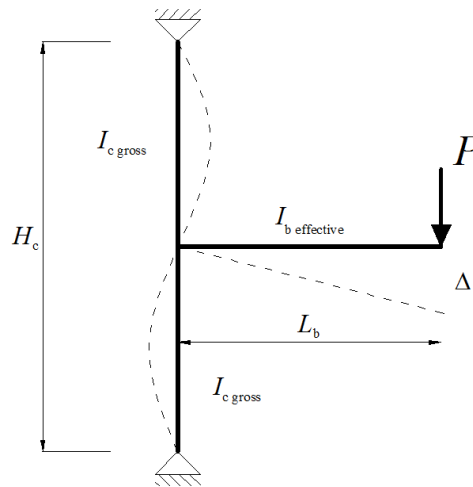
$$M_{service} = 360000 \times \left(400 - \frac{120.5}{3}\right) + 90805 \times \left(\frac{120.5}{3} - 50\right) = 128.65 \text{ KN.m}$$

$$P_{service} = \frac{128.65}{2} = 64.3 \text{ KN}$$

$$I_{cr} = \frac{b(kd)^3}{3} + nA_s(d - kd)^2 + (n - 1)A'_s(kd - d')^2$$

$$I_{cr} = \frac{350 \times (120.5)^3}{3} + 7.8 \times 1500 \times (400 - 120.5)^2 + (7.8 - 1) \times 1500 \times (120.5 - 50)^2$$

$$I_{cr} = 1168833990 \text{ mm}^4$$



$$\Delta = \frac{PL_b^3}{3EI_{b \text{ effective}}} + \frac{PL_b^2 H_c}{12 EI_{c \text{ gross}}}$$

According to CSA A23.3-04 (Clause 9.8.2.3) the effective moment of inertia I_{eff} can be calculated as:

$$I_{eff} = I_{cr} + (I_g - I_{cr}) \left(\frac{M_{cr}}{M_a} \right)^3$$

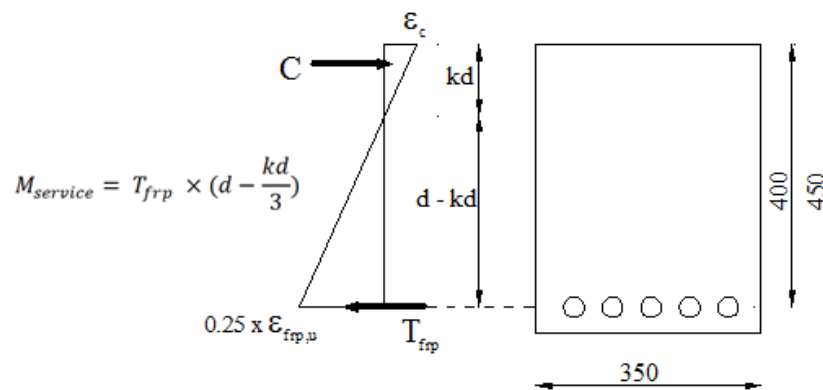
Where:

$$\begin{aligned} I_{eff} &= 1168833990 + (3282562500 - 1168833990) \times \left(\frac{49.6}{128.65} \right)^3 \\ &= 1289967657 \text{ mm}^4 \end{aligned}$$

$$\Delta = \frac{(64.3 \times 10^3) \times 2250^3}{3 \times 25.5 \times 10^3 \times 1289967657} + \frac{(64.3 \times 10^3) \times 2250^2 \times 3500}{12 \times 25.5 \times 10^3 \times 3972233333} = 8.4 \text{ mm}$$

Service cycle for specimen GG17-B11-J12

Based on the requirement of the CHBDC-CSA S6-09 (Clause 16.8.3) the maximum service strain in GFRP reinforcement should not exceed;



$$n = 1.9$$

$$\rho = 0.01018$$

$$k = 0.178$$

$$\varepsilon_{frp, maximum} = 0.25 \times 0.0153 = 3.8 \times 10^{-3}$$

Then; $f_{frp} = 181 \text{ MPa}$

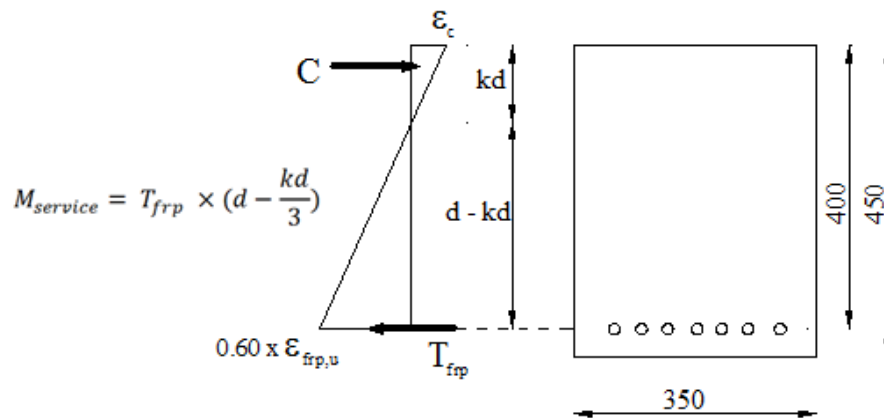
$$T_{frp} = 258 \text{ kN}$$

$$M_{service} = 97 \text{ kN.m}$$

$$P_{service} = \frac{M_{service}}{2} \approx 48.5 \text{ kN.m}$$

Service cycle for specimen CG12-B11-J12

Based on the requirement of the CHBDC-CSA S6-09 (Clause 16.8.3) the maximum service strain in CFRP reinforcement should not exceed;



$$n = 4.9$$

$$\rho = 0.00351$$

$$k = 0.17$$

$$\varepsilon_{\text{frp,maximum}} = 0.60 \times 0.014 = 8.4 \times 10^{-3}$$

Then;

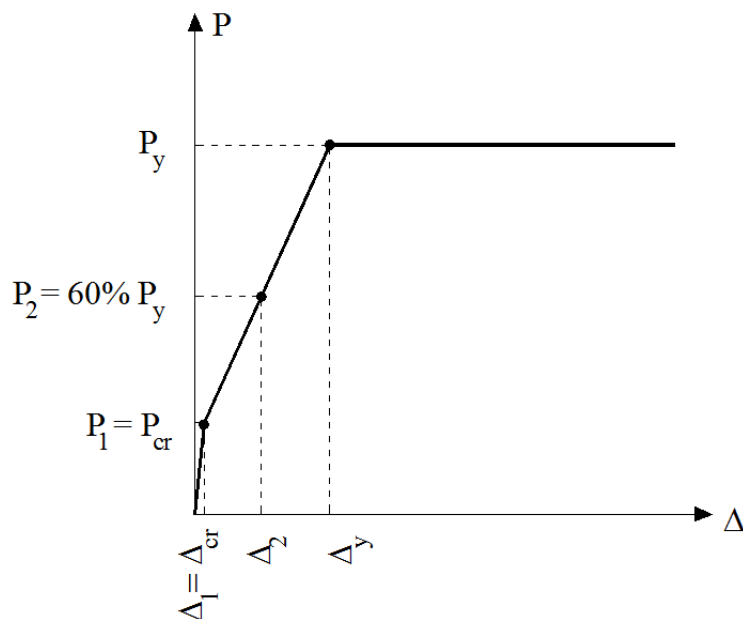
$$f_{\text{frp}} = 1041.6 \text{ MPa}$$

$$T_{\text{frp}} = 520 \text{ kN}$$

$$M_{\text{service}} = 196.2 \text{ kN.m}$$

$$P_{\text{service}} \approx 98.1 \text{ kN}$$

Yielding cycle for specimen SS03-B06-J06



By extrapolation;

$$\frac{P_y - P_2}{P_2 - P_1} = \frac{\Delta_y - \Delta_2}{\Delta_2 - \Delta_1}$$

Where:

$$P_y = \frac{P_2}{0.60}$$

So:

$$\Delta_y = \Delta_2 + \left((\Delta_2 - \Delta_1) \frac{0.67P_2}{P_2 - P_1} \right)$$

Theoretically;

$$\Delta_y = 8.4 + \left((8.4 - 1.49) \times \frac{0.67 \times 64.3}{64.3 - 24.8} \right) \approx 16 \text{ mm}$$

APPENDIX-C

Loading Procedure for All Specimens

First Phase: Load Control

Step 1

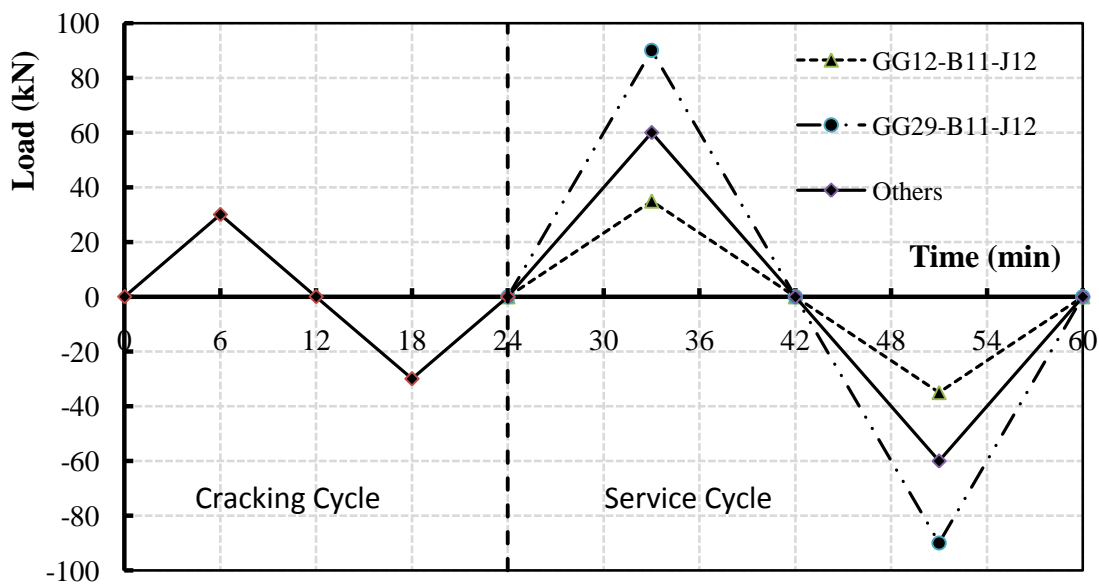
Cycle 1 (cracking step)

- Load amplitude = 25 kN for all specimens
- Loading rate 5 kN/min

Step 2

Cycle 2 (service state step)

- Load amplitude = 35 kN for specimen GG12-B11-J12
= 90 kN for specimen GG29-B11-J12
= 60 kN for all other specimens
- Loading rate 5 kN/min



Second Phase: Displacement Control**Step 1*****Cycles 1, 2& 3 (Corresponding to first yielding)***

- Displacement amplitude = $1 \times \Delta_y = 16.45$ mm
- Frequency = 0.01 Hz
- Cycle duration = 100 sec
- Displacement rate = $\left(\frac{16.45}{25}\right) = 0.658$ mm/sec
- Drift ratio = 0.75 %

Step 2***Cycles 4, 5& 6 (Ductility factor 1.3)***

- Displacement amplitude = 21.4 mm
- Frequency = 0.01 Hz
- Cycle duration = 100 sec
- Displacement rate = $\left(\frac{21.4}{25}\right) = 0.85$ mm/sec
- Drift ratio ≈ 1 %

Step 3***Cycles 7, 8& 9 (Ductility factor 1.8)***

- Displacement amplitude = 29.6 mm
- Frequency = 0.01 Hz
- Cycle duration = 100 sec
- Displacement rate = $\left(\frac{29.6}{25}\right) = 1.184$ mm/sec

- Drift ratio = 1.35 %

Step 4

Cycles 10, 11& 12 (Ductility factor 2.5)

- Displacement amplitude = 41.1 mm
- Frequency = 0.01 Hz
- Cycle duration = 100 sec
- Displacement rate = $\left(\frac{41.1}{25}\right) = 1.64$ mm/sec
- Drift ratio = 1.85 %

Cycle 13 (Service state stage)

- Load control cycle
- Load amplitude = 35 kN for specimen GG12-B11-J12
= 90 kN for specimen GG29-B11-J12
= 60 kN for all other specimens
- Loading rate 5 kN/min

Step 5

Cycles 14, 15& 16 (Ductility factor 3.35)

- Displacement amplitude = 55.1 mm
- Frequency = 0.01 Hz
- Cycle duration = 100 sec
- Displacement rate = $\left(\frac{55.1}{25}\right) = 2.20$ mm/sec
- Drift ratio = 2.50 %

Cycle 17 (Service state stage)

- Load control cycle
- Load amplitude = 35 kN for specimen GG12-B11-J12
= 90 kN for specimen GG29-B11-J12
= 60 kN for all other specimens
- Loading rate 5 kN/min

Step 6

Cycles 18, 19, 20& 21 (Ductility factor 4.17)

- Displacement amplitude = 68.5 mm
- Frequency = 0.01 Hz
- Cycle duration = 100 sec
- Displacement rate = $\left(\frac{68.5}{25}\right) = 2.74$ mm/sec
- Drift ratio = 3.10 %

Cycle 22 (Service state stage)

- Load control cycle
- Load amplitude = 35 kN for specimen GG12-B11-J12
= 90 kN for specimen GG29-B11-J12
= 60 kN for all other specimens
- Loading rate 5 kN/min

Step 7

Cycles 23 & 24 (Ductility factor 5.37)

- Displacement amplitude = 88.4 mm
- Frequency = 0.01 Hz
- Cycle duration = 100 sec

- Displacement rate = $\left(\frac{88.4}{25}\right) = 3.53$ mm/sec
- Drift ratio = 4.00 %

Cycle 25 (Service state stage)

- Load control cycle
- Load amplitude = 35 kN for specimen GG12-B11-J12
= 90 kN for specimen GG29-B11-J12
= 60 kN for all other specimens
- Loading rate 5 kN/min

Step 8**Cycles 26, 27& 28 (Ductility factor 6.7)**

- Displacement amplitude = 110.5 mm
- Frequency = 0.01 Hz
- Cycle duration = 100 sec
- Displacement rate = $\left(\frac{110.5}{25}\right) = 4.42$ mm/sec
- Drift ratio = 5.00 %

Cycle 29 (Service state stage)

- Load control cycle
- Load amplitude = 35 kN for specimen GG12-B11-J12
= 90 kN for specimen GG29-B11-J12
= 60 kN for all other specimens
- Loading rate 5 kN/min

Step 9**Cycles 30, 31& 32 (Ductility factor 6.7)**

- Displacement amplitude = 143.6 mm
- Frequency = 0.01 Hz
- Cycle duration = 100 sec
- Displacement rate = $\left(\frac{143.6}{25}\right) = 5.74$ mm/sec
- Drift ratio = 6.50 %

Cycle 33 (Service state stage)

- Load control cycle
- Load amplitude = 35 kN for specimen GG12-B11-J12
= 90 kN for specimen GG29-B11-J12
= 60 kN for all other specimens
- Loading rate 5 kN/min

